

LABORATOIRE CHARLES FABRY, EDF R&D

PHD MANUSCRIPT

Quantum simulation for strongly
interacting fermions with neutral atoms
array : towards the simulation of
materials of interest

Antoine MICHEL

Supervisors: Antoine BROWAEYS
et Christophe DOMAIN
Co-supervisor: Thierry LAHAYE

arXiv:2406.13343v1 [quant-ph] 19 Jun 2024

List of acronyms

AQS : Analog Quantum Simulation
AT : Adiabatic Theorem
BP : Barren Plateau
CDMFT : Cluster Dynamical Mean-Field Theory
CMFT : Cluster Mean Field Theory
DFT : Density Functional Theory
DFPT : Density Functional Perturbation Theory
DMFT : Dynamical Mean-Field Theory
DQS : Digital Quantum Simulation
EDF : Electricité de France
GGA : Generalized Gradient Approximation
HF : Hartree Fock
HPC : High Performance Computing
IASCC : Irradiated Assisted Stress Corrosion Cracking
LDA : Local Density Approximation
LTO : Long Term Operator
MF : Mean-Field
MIS : Maximum Independent Set
MOT : Magneto-Optical Trap
NISQ : Noisy Intermediate Scale Quantum
NPP : Nuclear Power Plant
PKA : Primary Knocked-on Atoms
PWR : Pressurized Water Reactor
PQC : Parametrized Quantum Circuit
QA : Quantum Annealing
QAOA : Quantum Approximate Optimization Algorithm
QC : Quantum Computing
QEC : Quantum Error Correction
QFT : Quantum Fourier Transform
QMC : Quantum Monte Carlo
QPU : Quantum Processor Unit
QuAltOA : Quantum Alternating Operator Ansatz
QUBO : Quadratic Unconstrained Binary Optimization
RQP : Rydberg Quantum Processor
SLM : Spatial Light Modulator
SSMF : Slave Spin Mean Field
STO : Slater Type Orbital
VQA : Variational Quantum Algorithm
VQE : Variational Quantum Eigensolver

Remerciements

C'est peut-être la partie la plus difficile à écrire pour moi, car je sais que c'est celle qui va être lue en premier, mais toute cette aventure n'aurait été possible sans la participation de beaucoup de personnes que je souhaite, par conséquent, remercier ici. Je souhaite tout d'abord remercier mon jury de thèse, Silke Biermann, Benoît Vermersch, Guido Pupillo, David Clément, Bruno Senjean et Thomas Ayral. Leur lecture approfondie de mon manuscrit ainsi que leurs retours et leurs commentaires sur mon travail m'ont permis de mettre en perspective ma recherche et sont des outils précieux pour la poursuivre.

Cette thèse étant CIFRE, je tiens à remercier la direction du laboratoire Charles Fabry pour son accueil, et notamment Patrick Georges, mais aussi EDF R&D et plus particulièrement Stéphane Taunier, Julien Stodolna et Marion Gorce pour m'avoir donné la chance d'évoluer au sein du groupe T27 du département MMC. Je tiens à remercier également Valérie Kervargant pour son aide très précieuse sur l'organisation de mes voyages en France et à l'étranger.

Je souhaite aussi remercier grandement Antoine Browaeys et Thierry Lahaye, mes deux directeurs de thèse, de m'avoir fait confiance pour ce projet ambitieux et d'avoir relevé le défi d'encadrer pour la première fois une thèse CIFRE, mais aussi une thèse théorique. Le mode d'encadrement était plus distendu qu'à l'accoutumé et la pandémie n'a pas aidé, mais vous avez toujours fait l'effort de garder le contact et un œil attentif sur mon travail. Vous avez toujours su être présent dans les moments charnières de la thèse et vos conseils et remarques ainsi que votre immense culture et expérience de la recherche m'ont été très utiles pour mener à bien mon travail et me suivront, j'en suis sûr, jusqu'à la fin de ma carrière. Je tiens aussi à remercier chaleureusement Christophe Domain, mon co-superviseur, avec qui j'ai passé la plupart de mon temps durant ces trois ans. Malgré la nouveauté du sujet, tu t'es investi avec moi pour essayer de comprendre et de relier les enjeux d'EDF sur le vieillissement des matériaux et la simulation quantique. Ta bienveillance et ta patience sont des qualités rares, surtout pour un doctorant à qui l'on doit expliquer encore au bout de trois ans comment fonctionne (et vieillit) une centrale nucléaire. Ta culture du numérique (je suis toujours friand de tes anecdotes sur le début du calcul HPC !) et de la physique m'a permis de prendre énormément de recul sur mon sujet et de comprendre les enjeux du calcul quantique. Merci de m'avoir introduit de la meilleure des manières à ce tout nouveau monde pour moi et je suis ravi de continuer avec toi sur ce sujet passionnant !

Cette thèse n'aurait tout simplement pas vu le jour sans le travail de Marc Porcheron (que je n'ai pas eu la chance de côtoyer longtemps), Stéphane Tanguy et Etienne Décossin qui ont lancé le programme quantique à EDF. Merci à vous d'avoir été aussi visionnaire et de croire en la physique ! Je tiens aussi à remercier tout particulièrement Joseph Mikael. Tu m'as tout de suite accueilli à bras ouverts dans le groupe même après un an de COVID et je m'y suis senti immédiatement dans mon élément. Je ne pense pas qu'il existe beaucoup de personnes aussi enthousiastes pour le monde du calcul quantique, et l'énergie que tu déploies pour faire vivre le projet m'impressionne un peu plus chaque jour. Je souhaite aussi remercier toute l'équipe qui gravite autour du quantique : Paulin, Pascale, Cyril, Cyril $\times 2$, Quentin, Rodolphe, Mohamed, Ulysse, Naomi (et j'en oublie certainement), nos échanges et diversités de compétences initiales furent un moteur pour ma thèse.

Durant toute la durée de ma thèse, j'ai pu compter sur le soutien de PASQAL et tout particulièrement de Loïc Henriot qui a suivi et participé à mon travail, merci pour la confiance !

Je souhaite aussi remercier grandement Sebastian Grijalva et Thomas Ayrat. Vous avez officieusement participé activement à l'encadrement de ma thèse et avez pris énormément de votre temps pour travailler avec un jeune doctorant que vous ne connaissiez pas et pour cela, je vous en serai éternellement reconnaissant.

Je tiens aussi à remercier Julien Villmejjane pour m'avoir fait confiance en me confiant des TP et des TD d'électronique en première année de l'IOGS malgré mes souvenirs qui étaient lointains.

Pendant les trois années de thèse (en fait les deux dernières), j'ai pu partager mes galères avec Clément, mon coloc' de bureau, ainsi qu'avec Clément bis, Lucie, Maxime et je les remercie pour cela. j'ai aussi fait de super rencontres à l'école des Houches que ce soit Andréas, Marion, Julien (j'espère que tu bats tout ton labo au ping maintenant !), Alexandre, Gabriel et d'autres que j'oublie !

En-dehors du monde quantique, le soutien de mes amis a été particulièrement important et je souhaite tout d'abord remercier Alexis, Sylvain et Anis qui ont fait le déplacement pour ma soutenance. C'est une amitié qui commence (la sauce) à bien durer dans le temps et j'espère que cela perdurera jusqu'à nos 80 ans quand on ouvrira une bonne bouteille... Mais j'ai aussi pu compter sur Laury, le chaleureux Antoine, Ambre, Antho, Thomas, Seddik (qui est le seul à s'être engagé dans la même galère que moi, merci pour la balade jusqu'au lac où on ne peut pas se baigner et pour les memes échangés), Alexandre et Amélie. Je voudrais aussi remercier Kamil pour m'avoir carry sur Ash (contrairement à Anis et Sylvain).

Parce qu'il est important de vider sa tête des codes Python et des équations, je souhaite remercier le club de tennis de table de Villemomble et tout particulièrement Nico, Jérèm, Loris, Lad, Cédric, Vibol, Yves et tout ceux que j'oublie pour m'avoir pris dans leurs équipes ! Promis les gars, on remonte en R3 bientôt.

Un grand merci aussi à ma famille (et ma belle-famille !) pour le soutien sans faille et surtout mes parents.

Enfin, je souhaite finir par toi qui me suis depuis maintenant 7 ans. De ma déprime d'école d'ingénieur à aujourd'hui, tu ne m'as jamais lâché. Ces trois années ont été très intenses avec de précieux moments de joie, mais aussi des moments difficiles. Néanmoins, nous sommes toujours restés soudés et pour rien au monde, je n'aurais souhaité vivre ces années avec quelqu'un d'autre. Tu es le dénominateur commun de toutes mes réussites, que tu le veuilles ou non. J'espère que l'on regardera The Big Bang Theory encore ensemble quand on sera vieux.

Contents

1	General introduction	7
1.1	Industrial material aging context	7
1.2	Quantum computing context	8
1.3	EDF projects	9
1.3.1	Multiscale modelling	10
1.3.2	The quantum project	10
1.4	Contributions of this work	11
1.5	Manuscript organization	11
2	Simulating correlated matter: from classical to quantum	13
2.1	Forewords	13
2.2	<i>Ab initio</i> or first principles methods	14
2.2.1	Hartree-Fock method	14
2.2.2	Fundamentals of density functional theory	15
2.2.3	The Local Density Approximation (LDA)	16
2.2.4	The generalized-gradient approximation (GGA)	17
2.2.5	The LDA + U method	17
2.2.6	Hybrid/metaGGA approach	17
2.2.7	Beyond DFT	17
2.2.8	Successes and limitations	18
2.3	Quantum approaches	18
2.3.1	The Hubbard model	18
2.3.2	The Mott physics: starting point of highly correlated electrons	19
2.3.3	The Dynamical Mean-Field Theory (DMFT)	19
2.3.4	Extensions of these methods	21
2.3.5	Quantum Monte Carlo	21
2.3.6	Conclusion	22
2.4	Overview of quantum computing	22
2.4.1	Basis	23
2.4.2	Many qubits system and entangled states	23
2.4.3	Density matrix and mixed states	24
2.4.4	Close system and quantum logic operators	25
2.4.5	Digital approach	26
2.4.6	Analog approach	28
2.4.7	Conclusion	30
2.5	Methods	30
2.5.1	The quantum phase algorithm	30
2.5.2	The Variational Quantum Algorithm (VQA)	32
2.5.3	Quantum Annealing	37
2.6	Quantum computing for chemistry and many-body physics	38

2.6.1	From qubits to fermions	38
2.6.2	Unitary coupled cluster ansatz	39
2.7	Conclusion	40
3	Quantum simulation with Rydberg atoms	42
3.1	Forewords	42
3.2	Neutral atom arrays	42
3.2.1	Initial state preparation	43
3.2.2	Generating spin-spin interactions	44
3.2.3	Register readout	45
3.3	Quantum simulation	46
3.3.1	Digital quantum simulation	46
3.3.2	Analog quantum simulation	47
3.4	Conclusion	49
4	Digital-analog variational quantum eigensolver for chemistry	50
4.1	Forewords	50
4.2	Introduction	50
4.3	Analog Variational Quantum Eigensolver with Rydberg atoms	52
4.3.1	Hamiltonians from Quantum Computational Chemistry	52
4.3.2	Rydberg Atom Quantum Processor	53
4.3.3	Variational Algorithms on a Rydberg atoms device	54
4.4	Description of the Protocols	55
4.4.1	UCC ansatz on an analog quantum processor: application on H_2	55
4.4.2	Alternating pulses	56
4.4.3	Optimized Register and Iteratively Parameterized Pulses	58
4.5	Numerical Results	61
4.5.1	Application on LiH and BeH_2 molecules	61
4.5.2	Roadmap for more complex molecules	63
4.6	Discussion	64
5	Using Rydberg platform to simulate strong fermionic correlations in the 2D-Hubbard model	69
5.1	Forewords	69
5.2	Introduction	69
5.3	Problem reduction through the slave-spin method.	70
5.3.1	Details of the main equations	72
5.3.2	Fulfillment of the constraint	73
5.3.3	Variants: Towards a multiorbital case	74
5.4	Solution of the two coupled subproblems	74
5.4.1	Solving the fermionic Hamiltonian H_f for J : Bogoliubov method	74
5.4.2	Solving the spin Hamiltonian via a cluster mean-field approach	75
5.4.3	Convergence of the self-consistent loop	76
5.5	Quantum algorithm for the spin Hamiltonian.	76
5.6	Solving the spin model with a Rydberg platform: details	78
5.6.1	Optimization of the geometry	78
5.6.2	Details of the annealing schedule	80
5.6.3	Experimental imperfections	80
5.7	Results at equilibrium	82
5.8	Dynamics of the Hubbard model with the slave-spin method	85
5.8.1	Dynamics in slave-spin theory	85
5.8.2	Frequency dependency on eigenenergies	86

5.8.3	Dynamics and constraint fulfillment	86
5.8.4	Results out of equilibrium	86
5.9	Conclusion	87
6	Summary and outlook	88
	Bibliography	90
A	LiH and BeH₂ Hamiltonians	107
B	Slave-spin theory for the Mott transition in the triangular lattice	109
B.1	Forewords	109
B.2	Solving the spin Hamiltonian H_S for Q : cluster mean-field	109
B.3	Self-consistent outer cycle	110
B.3.1	Solving the embedded model	111
B.4	Discussion on units	113
B.5	Results	114
B.5.1	Exact diagonalization method	114
B.5.2	Impact of experimental parameters	114
B.6	Discussion	115
B.6.1	Convergence of the method	115
B.6.2	Experimental feasibility	115
C	Discussion on the correlation length of the system	120
C.1	Forewords	120
C.2	Correlation length with the slave-spin method implemented in a RQP	120
D	Quasi-particle weight oscillations	124
D.1	Forewords	124
D.2	Data of the signal	124
D.3	Fourier transform	124
D.4	Effect of noise	124
E	Résumé en français	127

Chapter 1

General introduction

1.1 Industrial material aging context

The energy industry faces major challenges today with the threat of global warming, growth of raw material prices and political instabilities. Regarding this context, it is crucial for industries like Electricité de France EDF to deliver a sustainable source of electricity. In France, this electric power is mainly provided by nuclear energy (63% of the total production in 2022 ¹). This proportion dropped in 2022 due to the discovery of stress corrosion in Nuclear Power Plant (NPP). Global warming is expected to have a huge impact on our society (IPCC, 2022); therefore, reaching a zero carbon emission energy industry in 2050 is a major goal. From this standpoint, extending the lifetime of the nuclear power plant over 60 years (Long Term Operation-LTO) has been raised to be an important step ². All currently operating NPPs in France use the pressurized water reactor technology (PWR). One reactor is made of a pressure vessel containing the core internals supporting the fuel assemblies in which the fissile materials are, Fig. 1.1.

When operating, internal structures undergo harsh stresses: temperature locally up to 350°C, mechanical constraints, intense neutron irradiation up to 120 dpa (displacement per atom), corrosion. The combination of these factors induces creep, a potential risk of swelling (for which VVER or austenitic materials such as fuel cladding are concerned) but no evidence of this phenomena have been found in PWR reactors today, and thus changes the properties of materials inside the vessels. It has been shown that irradiation increases the formation of cracks in PWR components such as bolts (Christiaen, 2018). These phenomena are known as the Irradiation Assisted Stress Corrosion Cracking (IASCC). To anticipate materials aging of NPPs, it is needed to understand these phenomena at the atomic scale, where the formation of defects appears. Several works have been done to study defects evolution in austenitic steels (Paré, 2022) with *ab initio* method such as the Density Functional Theory (DFT) (Piochaud et al., 2014) or Monte-Carlo algorithms (kinetic Monte-Carlo or rate theory) (Fokt, 2021) with encouraging results. Nevertheless, simulating complex phenomena where quantum correlations are important, such as para-magnetism, is still difficult with these tools. Austenitic steels are in the para-magnetic phase in power plants conditions of temperature and pressure, and it is well known that magnetic phases play an important role in energies of mitigation and defects (Alling et al., 2010; Ekholm et al., 2010). Therefore, being able to simulate accurately strong quantum correlations could help, *in fine*, to increase NPP lifetime. Indeed, DFT is in a framework multiscale modelling approach and output data of atomic scale simulation can be used as input data of macroscopic scale simulations.

In addition, the aging of lithium-ion batteries is also a major issue to renew the car fleet or for

¹RTE bilan électrique 2022 <https://assets.rte-france.com/prod/public/2023-02/Bilan-electrique-2022-synthese.pdf>

²RTE futures énergétiques 2050 <https://assets.rte-france.com/prod/public/2021-12/Futurs-Energetiques-2050-principaux-resultats.pdf>

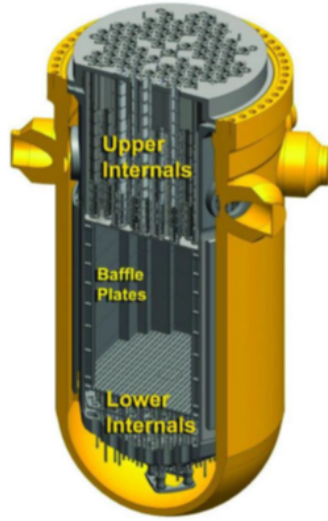


Figure 1.1: View of a vessel in PWR.

static energy storage, which is crucial to reduce greenhouse gas emissions. Oxides are very difficult to simulate because most of these materials have strong-correlated electrons that state-of-the-art methods struggle to design (Birkl et al., 2017). We are surrounded by batteries in our everyday life, and understanding how batteries age is decisive if an all electrical world is considered. Another field where simulations are important is solar cells. The difficulty is to reliably simulate excited states to understand the efficiency degradation. *Ab initio* methods reach their limits when it comes to study excited states of a material. The energy industry therefore needs new methods of simulation to understand how materials of interest age and to be able to avoid enormous costs like changing vessel internals after a cracking or an explosion of a battery following a great loss of the capacity. First principles computations have encountered great successes (Domain & Becquart, 2001; Piochaud et al., 2014; Zhang et al., 2011) but they are limited in great significance area and need to be improved or replaced because of quantum correlations being too important.

1.2 Quantum computing context

In 1982, the physicist Richard Feynman proposed to simulate quantum phenomena with a quantum computer (Feynman, 1982). This is the birth of quantum computing. The principle is to manipulate qubits, instead of classical bits, which lie in vectorial space. Thanks to the superposition of quantum states, it is possible to manipulate the coefficients a and b in a state $a|0\rangle + b|1\rangle$ where $|a|^2 + |b|^2 = 1$. We are not dealing only with the bit 0 or 1 but with both at the same time. In 1994, Peter Shor proposed an algorithm based on quantum computing and Quantum Fourier Transform (QFT) to factor any integer N in a polynomial time (Shor, 1994), threatening to break public-key cryptography schemes. In other words, if a quantum computer with enough noiseless qubits is built, it could break most of the internet security and the world internet network would be endangered. Thenceforth, a race for the universal quantum computer has begun and is still ongoing today. The number of applications is great: cryptography, optimization, differential partial equations, combinatorial problems and of course materials and chemistry. Several technologies are being tested with their own pros and cons all over the world (examples in Fig. 1.2). Researchers also focus on designing original quantum algorithms because it is impossible to convert a classical

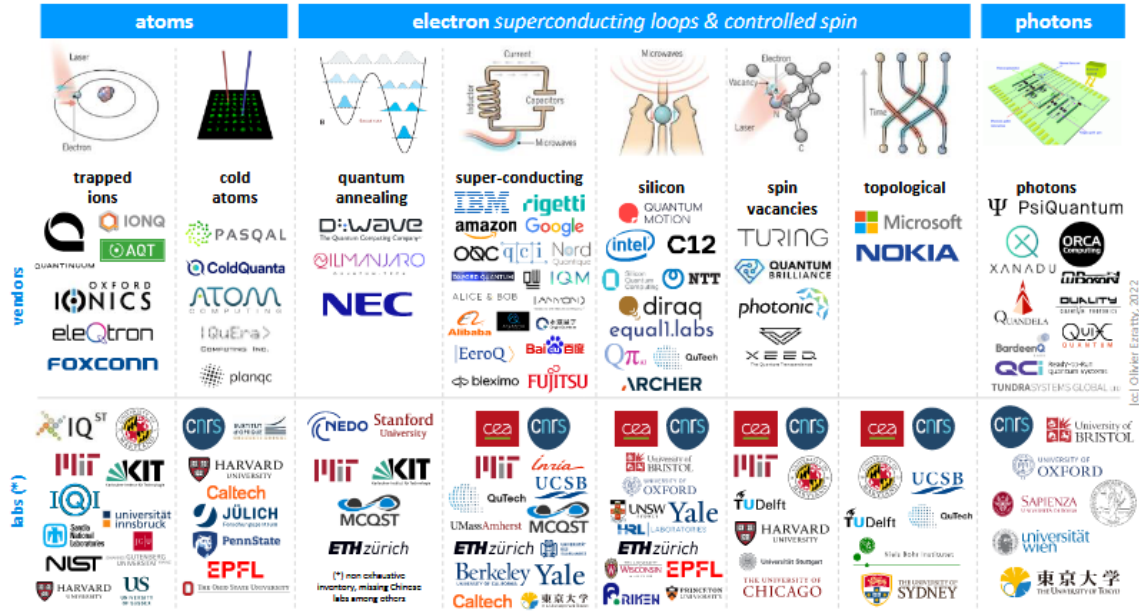


Figure 1.2: Overview of quantum computers builders in the world with the three main qubit carriers: the atoms, the electrons and the photons (figure taken from (Ezratty, 2022)).

algorithm into a quantum algorithm (Montanaro, 2016). Nevertheless, quantum computing is still a promise as no real quantum advantage has been shown up to date. Nowadays, we are in the Noisy Intermediate Scale Quantum Computer (NISQ) era, (Preskill, 2018) where noisy quantum simulators with a few qubits are available. Therefore, original algorithms considering noise have to be designed and a great amount of effort is put in the emulation of quantum computing. This means that High Performance Computing (HPCs) are used to numerically simulate the behavior of a quantum computer, considering noise and limitations. This very important step in the creation of an algorithm allows testing it with a few qubits to anticipate and to mitigate the effect of noise. Moreover, quantum algorithms are often in two parts:

- A quantum part which is supposed to be solved by a real quantum computer.
- A classical part that is tackled by a classical quantum computer.

The two parts are self-correlated and aim at minimizing an energy and finding the groundstate energy of a system through the variational principle, for instance.

The work presented in this manuscript lies between the energy industry challenges described above and the breakthroughs in quantum computing. We show how we can study strong-correlated electrons on realistic quantum simulators, having in mind the issue of aging materials for energy industry.

1.3 EDF projects

My PhD is part of a quantum project and contributing to a material modelling project:

- a multiscale modelling approach to understand and anticipate defects and develop aging models of materials in PWR (ULTIMATE project);
- a quantum project (SI quantique) which aims at studying potential applications of quantum computing for EDF.

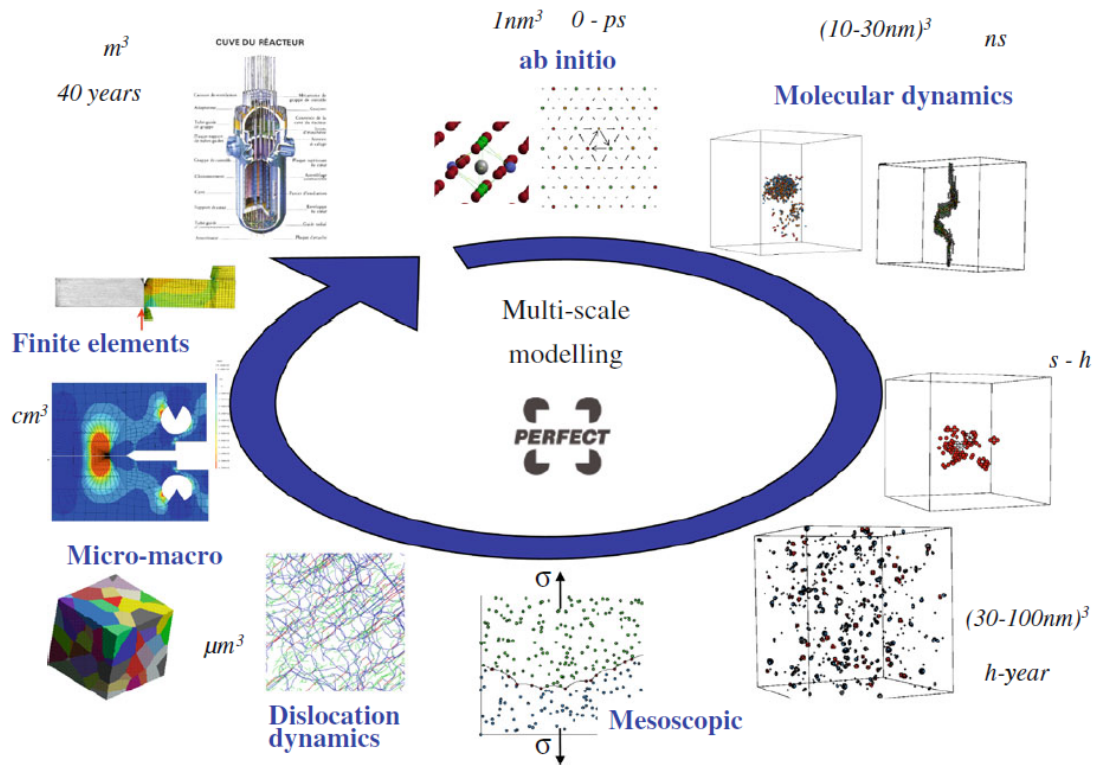


Figure 1.3: Multiscale modelling applied in the PERFECT project to the pressure vessel steels. Taken from (Becquart & Domain, 2011).

1.3.1 Multiscale modelling

Ab initio atomic simulations are a part of a wide modelling program at EDF, starting from simulating neutron irradiation to finite elements method. The idea of this multiscale modelling is to use data and results of atomic scale simulation to help modelling higher orders of magnitude problems, and so on until the macroscopic scale is reached. This encompasses simulating the energy distribution of the Primary Knocked-on Atoms (PKA) from the neutron spectrum, *ab initio* methods such as DFT, Molecular Dynamics to characterize elementary mechanisms at the atomic scale and also to simulate displacement cascades and dislocation-defect interactions, Monte-Carlo and rate theory to simulate microstructure evolution under irradiation, Dislocation Dynamics for plasticity modelling and so on (Adjanor et al., 2010; Becquart & Domain, 2011).

A schematic representation of multiscale modelling is shown in Fig. 1.3.

Therefore, quantum computing could help to improve results of all the loop of multiscale modelling by enhancing DFT materials modelling.

1.3.2 The quantum project

The Research and Development section of EDF is the biggest in Europe. Several crucial issues are studied there to deliver sustainable source of electricity in France (and other countries) and at the same time, keeping a balance in economy. Quantum computing holds the promise to solve numbers of relatable problems. The advent of QC could change everything in computing and simulation, and there is no mapping between classical simulations and the quantum world: one has to rewrite all algorithms to benefit QC. That was the starting point of the quantum project at EDF in 2018:

being active in this field and starting to design our own algorithms for our own use case. Several sector and direct applications have been identified such as partial differential equation (with the HHL algorithm see Sec. 2.5.1), post-quantum cryptography (Shor algorithm Sec. 2.5.1) the smart charging optimization problem (Dalyac et al., 2021) and, of course, material simulation. All use case can be seen in Tab. 1.1. The quantum group at EDF collaborated with a wide variety of actors from French start-ups to IBM in the United States of America.

R&D sectors	Direct application
Production	Materials simulation (internals, batteries) Probabilistic Safety Assessment studies Partial differential equations Quantum metrology networks
Network	Optimal power flow
Energy management	Optimisation/smart charging Machine learning
Information Technologies	Post-quantum cryptography

Table 1.1: Sectors and direct applications of quantum computing for EDF

1.4 Contributions of this work

The contributions of this work are the following:

First, I present the first hybrid digital-analog variational algorithm on the Rydberg Quantum Processor (RQP), a NISQ device, which aims at finding the groundstate of molecules. This algorithm encompasses all specificities from the device. I show a numerical implementation of this algorithm and prove that it can be run on an actual device in a reasonable amount of time. The efficiency of this algorithm is shown on molecules H_2 , LiH and BeH_2 . All steps of the algorithm are discussed. The transformation from a molecular algorithm to a qubits algorithm, the state preparation, the measurement process with the derandomization method are studied (Michel, Grijalva, et al., 2023). We propose a roadmap for bigger molecules and an experimental implementation. This work results from a strong collaboration with the start-up PASQAL.

Secondly, I introduce a new hybrid algorithm to observe the Mott transition on 2D-Hubbard model on a RQP. The slave-spin method is used to transfer the complexity of the strongly-correlated electrons of Hubbard model on Ising-like Hamiltonian coupled to a free electron's system via a mean-field mapping. We study the feasibility of this algorithm on an experimental device by exploring the impact of all sources of error known up to date. I show that the Mott transition can be observed on a RQP. I also demonstrate that we can observe the effect of a quantum quench on the quasi-particle weight of the system on RQP. This algorithm is the first step toward simulation of bulk materials on a noisy quantum simulator. This work results from a strong collaboration with the EVIDEN/ATOS company.

1.5 Manuscript organization

This work is structured as follows:

In chapter 2, I give an overview of state-of-the-art methods to simulate electrons and magnetism "classically". Successes and limitations of these tools are presented. Then, after an introduction of theoretical quantum principles, I present some of the most recent NISQ quantum algorithms and their applications with a focus on methods to simulate fermionic systems.

In chapter 3, I present the Rydberg platform, the physics behind it and how to perform quantum computing with it. The digital and the analog approaches are presented.

In chapter 4, I give the method and results of a digital-analog quantum eigensolver designed for the RQP. After a presentation of the molecular to qubits Hamiltonian mapping, we present an analog simulation implementation to find the groundstate of the H_2 molecule, which is inspired from the Unitary coupled-cluster ansatz. Finally, I present the protocol for bigger molecules and the results we obtain numerically.

In chapter 5, I introduce the slave-spin method and I show how it can be employed to predict the Mott metallic-insulator transition and the out of equilibrium behavior in the 2D-Hubbard model on a RQP. All the protocol and theory behind the algorithm are described. The numerical simulation of a realistic implementation on a noisy quantum simulator is shown and discussed.

Chapter 6 presents the conclusion and outlook of this work.

Chapter 2

Simulating correlated matter: from classical to quantum

2.1 Forewords

The famous citation of Richard Feynman "Nature isn't classical, dammit, and if you want to make a simulation of nature, you'd better make it quantum mechanical, and by golly it's a wonderful problem, because it doesn't look so easy" reminds us that simulating nature with a quantum computer seems to be a good idea but most importantly, it is not straightforward. Indeed, there are $\approx 10^{23}$ interacting electrons in all pieces ($\approx 1 \text{ cm}^3$) of all the matter surrounding us. Even if only one-half spin degree of freedom is considered, it means that $\approx 2^{10^{23}}$ states are allowed for a small piece of matter, which is more than the number of particles in the universe. Therefore, in front of this unreachable complexity, humans had to be creative. The first step is attributable to Erwin Schrödinger and Werner Heisenberg who first described the behavior of non-relativist quantum particles with the Schrödinger equation (and matrix calculation):

$$i\hbar \frac{\partial \psi(t, \vec{r})}{\partial t} = -\frac{\hbar^2}{2m} \Delta \psi(t, \vec{r}) + V(t, \vec{r}) \psi(t, \vec{r}) \quad (2.1)$$

with \hbar the Planck constant divided by 2π , $\psi(t, \vec{r})$ the wavefunction of the particle, m its mass, and $V(t, \vec{r})$ all external potentials the particle undergoes. This equation combined with periodic boundaries condition (PBC) has led to the first quantum revolution with the band theory (Kittel & Holcomb, 1967) which is at the heart of all today's electronic devices. Nevertheless, approximations can not stand when considering certain class of materials. For instance, complex alloys can not be described with this theory. With the democratization of computers, the idea of solving the Schrödinger equation with an algorithm to describe and understand complex phenomena has been more and more studied. Indeed, as Richard Feynman said, the world is quantum and if we want to improve our lives and our society, the quantum world has to reveal all its secrets. Since particles are in interaction and the complexity of materials is huge, approximations have to be made to hope for an advancement. In this section, I review some of the most ubiquitous methods to simulate strongly correlated electrons and spins. They all consider approximations, but they have allowed to understand a large part of complex materials. These methods are used today at EDF for instance to improve and anticipate material aging. I discuss successes but also limitations of these methods. These limitations can be really bounding in some fields where quantum correlations are very strong (Abrikosov et al., 2016; Ho et al., 2018). Quantum computing (QC) holds the promise to solve really hard materials' problem unreachable today. In the second part of this chapter, I give an overview of the theoretical bases of QC and how to simulate interacting electrons on a quantum computer. The last part of this bibliography is dedicated to modern methods to perform quantum

computing on NISQ device and how to simulate fermionic problems on them.

2.2 *Ab initio* or first principles methods

The challenge of simulating materials relies on solving the Schrödinger equation (Eq. 2.1). It is only possible in specific cases (the harmonic oscillator for instance with $\hat{H} = \frac{\hat{P}^2}{2m} + \frac{1}{2}k\hat{X}^2$). In general, approximations are necessary to reach observable values. In this section, I describe the Hartree-Fock method and the Density Functional Theory (DFT), electronic structure-calculation methods widely used all around the world and state-of-the-art methods in a large part of chemistry and material simulation at the atomic level.

The Born-Oppenheimer approximation

Let us consider a periodic material. It is composed of electrons and nuclei in interactions. The Hamiltonian of such a system can be written:

$$H_{\text{mat}} = \sum_{k=1}^M \nabla_{\vec{R}_k}^2 - \sum_{i=1}^N \nabla_{\vec{r}_i}^2 + \frac{1}{2} \sum_{i_1 \neq i_2=1}^N \frac{e^2}{|\vec{r}_{i_1} - \vec{r}_{i_2}|} + \frac{1}{2} \sum_{k_1 \neq k_2=1}^M \frac{Z_{k_1} Z_{k_2}}{|\vec{R}_{k_1} - \vec{R}_{k_2}|} - \sum_i^N \sum_k^M \frac{Z_k e}{|\vec{r}_i - \vec{R}_k|} \quad (2.2)$$

with M and N being the number of nucleus and electrons respectively, \vec{R}_k and \vec{r}_i the coordinates in 3D-space of nucleus and electrons respectively. e is the electric charge and Z_k the number of protons inside the nucleus. The first two terms are the kinetic energy of protons and electrons, and the other terms are the Coulomb interaction energy. The first approximation to simplify this equation was proposed by Max Born and Robert Oppenheimer in 1927. It relies on the ratio of mass between nucleus and electrons being equal to ≈ 2000 . It is therefore possible to consider that electrons see the nucleus moving adiabatically. The kinetic energy of the nucleus is then neglected, and the Coulomb interaction between protons is a constant. From electron's point of view, they undergo the following Hamiltonian:

$$H_e = E + U + V \quad (2.3)$$

where E is the kinetic energy of electrons, U is the interaction between electrons and V the interaction of electrons with the stationary external potential (protons interaction). The purpose now is to find the groundstate of such a Hamiltonian for a well-defined V . It can actually be solved for small systems in small basis set but obviously, trying to solve this equation with the vectorstate $|\psi_0\rangle$ for a material is out of reach for classical computer and will always be.

2.2.1 Hartree-Fock method

The Hartree-Fock (HF) method (Echenique & Alonso, 2007) is based on finding a good approximation of the wave-function of the system to compute the ground state energy. The method often assumes that the N-body wave-function describing the ground state of a system is what we called a Slater determinant:

$$\Psi(\mathbf{r}_1, \mathbf{r}_2, \dots, \mathbf{r}_N) = \frac{1}{\sqrt{N!}} \begin{vmatrix} \psi_1(\mathbf{r}_1) & \psi_2(\mathbf{r}_1) & \dots & \psi_N(\mathbf{r}_1) \\ \psi_1(\mathbf{r}_2) & \psi_2(\mathbf{r}_2) & \dots & \psi_N(\mathbf{r}_2) \\ \vdots & \vdots & \ddots & \vdots \\ \psi_1(\mathbf{r}_N) & \psi_2(\mathbf{r}_N) & \dots & \psi_N(\mathbf{r}_N) \end{vmatrix} \quad (2.4)$$

with orthogonality relations:

$$\delta_{i,j} = \int \psi_i^\dagger(\mathbf{x}) \psi_j(\mathbf{x}) d\mathbf{x} \quad (2.5)$$

where $\mathbf{x} = (\mathbf{r}, \sigma)$. The next approximation is to find how to express these spatial-spin wave-functions. In general, linear combinations of Gaussian functions (STO-nG) are chosen as basis set. This leads to good approximations without too much complexity (Stewart, 2003). The variational principle is then used to solve the HF equations.

This principle states that all approximations of ground state will lead to an energy greater or equal to the exact ground state energy. The Rayleigh Ritz wave-function variational principle can be expressed as:

$$E_0 = \min_{|\psi\rangle} \langle \Psi | H_e | \Psi \rangle \quad (2.6)$$

where $\langle \psi | \psi \rangle = 1$.

The HF method is at the center of many quantum chemistry numerical simulations today (Helgaker et al., 2001).

2.2.2 Fundamentals of density functional theory

Finding a good wave-function for the system can be complicated and can lead to huge approximations. Another approach is to focus on the one-particle density of the system. Indeed, this observable gives a lot of information of the system and can be easier to compute than the wave-function. This is the very first step of the Density Functional Theory (DFT).

The variational theorem can be reformulated in terms of one-electron density defined as:

$$n(\mathbf{r}) = N \int \cdots \int |\psi(\mathbf{x}_0 \mathbf{x}_1 \dots \mathbf{x}_N)|^2 d\mathbf{x}_0 d\mathbf{x}_1 \dots d\mathbf{x}_N. \quad (2.7)$$

Indeed, the Hohenberg-Kohn theorem states that:

- the external potential is a unique functional of the electronic density up to a constant;¹
- the functional that gives the energy of the system gives the ground state energy if and only if the density is the ground-state density.

This is the foundation of the density functional theory. If we define the universal density functional,

$$F[n] = \langle \psi[n] | E + U | \psi[n] \rangle, \quad (2.8)$$

The variational principle can be written:

$$E_0 = \min_n \left(F[n] + \int V(\mathbf{r})n(\mathbf{r})d\mathbf{r} \right). \quad (2.9)$$

The final step is to map this interacting functional of energy onto N non-interacting one-electron systems with an effective external potential $V_{\text{eff}}(\mathbf{r})$ generating the same density $n(\mathbf{r})$ as the real system. The state of such a system can be described as a Slater determinant of one-body wave functions $\phi_i(\mathbf{r})$. Therefore, for the free-electrons (or Kohn-Sham) system, the density is $n(\mathbf{r}) = \sum_i |\phi_i(\mathbf{r})|^2$ where i browses all occupied orbitals and the ground-state energy is $E_0 = \min_{\phi} \left(\langle \phi | T_0 | \phi \rangle + \langle \phi | V_{\text{eff}} | \phi \rangle \right)$ With T_0 the kinetic energy of the free-electrons system. By

¹Proof: let's consider two external potentials $V_1(\mathbf{r})$ and $V_2(\mathbf{r})$ such as $V_1(\mathbf{r}) \neq V_2(\mathbf{r}) + \text{cst}$. The two corresponding Hamiltonians $H_1(V_1)$ and $H_2(V_2)$ have therefore different groundstates $|\psi_1\rangle$ and $|\psi_2\rangle$ and groundstate energies E_1 and E_2 but let's suppose the same one-electron density $n(\mathbf{r})$. We have $E_1 = \langle \psi_1 | H_1 | \psi_1 \rangle = \langle \psi_1 | H_2 + V_1 - V_2 | \psi_1 \rangle > E_2 + \langle \psi_1 | V_1 - V_2 | \psi_1 \rangle = E_2 + \int (V_1(r) - V_2(r))n(r)dr$ and $E_2 = \langle \psi_2 | H_2 | \psi_2 \rangle = \langle \psi_2 | H_1 + V_2 - V_1 | \psi_2 \rangle > E_1 + \int (V_2(r) - V_1(r))n(r)dr$. This leads to $E_1 + E_2 > E_1 + E_2$ which is absurd. So, the one-electron density has to be different for the two Hamiltonians.

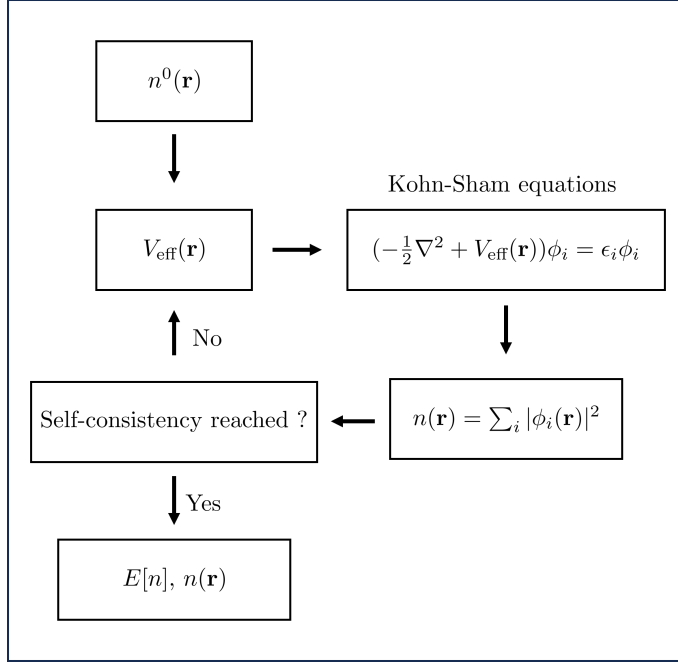


Figure 2.1: Self-consistency loop to solve Kohn-Sham equations.

decomposing $F[n]$ as $\langle \phi | T_0 | \phi \rangle + E_{\text{Hxc}}[n]$ with $E_{\text{Hxc}}[n] = \frac{1}{2} \int \int \frac{n(\mathbf{r}_1)n(\mathbf{r}_2)}{|\mathbf{r}_1 - \mathbf{r}_2|} d\mathbf{r}_1 d\mathbf{r}_2 + E_{\text{xc}}[n]$, one can obtain:

$$E[n] = T_0[n] + \frac{1}{2} \int \int \frac{n(\mathbf{r}_1)n(\mathbf{r}_2)}{|\mathbf{r}_1 - \mathbf{r}_2|} d\mathbf{r}_1 d\mathbf{r}_2 + E_{\text{xc}}[n] + \int V(\mathbf{r})n(\mathbf{r})d\mathbf{r} \quad (2.10)$$

with $T_0[n] = \sum_i \int \phi_i^*(\mathbf{r})(-\frac{\nabla^2}{2})\phi_i(\mathbf{r})d\mathbf{r}$. As a result, $V_{\text{eff}}(\mathbf{r}) = V(\mathbf{r}) + \int \frac{n(\mathbf{r}')}{|\mathbf{r}' - \mathbf{r}|} d\mathbf{r}' + \frac{\delta E_{\text{xc}}[n]}{\delta n(\mathbf{r})}$.

We obtain the Kohn-Sham equations:

$$\left(-\frac{1}{2}\nabla^2 + V(\mathbf{r}) + \int \frac{n(\mathbf{r}')}{|\mathbf{r}' - \mathbf{r}|} d\mathbf{r}' + \frac{\delta E_{\text{xc}}[n]}{\delta n(\mathbf{r})} \right) \phi_i(\mathbf{r}) = \epsilon_i \phi_i(\mathbf{r}). \quad (2.11)$$

This equation can be solved by a self-consistent loop described in Fig. 2.1. One starts from a first guess for the density $n^0(\mathbf{r})$. From this density, one can calculate $V_{\text{eff}}(\mathbf{r})$ and solve the Kohn-Sham equation, Eq. 2.11. We then recover $n^k(\mathbf{r})$ from wave-functions $\phi_i(\mathbf{r})$ and we compare it to the previous density $n^{k-1}(\mathbf{r})$. The loop goes on until self-consistency is reached. Everything in the DFT is exact except that E_{xc} and $\frac{\delta E_{\text{xc}}[n]}{\delta n(\mathbf{r})}$ are unknown and must be approximated. I will give a few examples of common approximations used in this theory.

2.2.3 The Local Density Approximation (LDA)

A strong but simple approximation is to consider that E_{xc} depends on the density the same way as an electron gas:

$$E_{\text{xc}}[n] = \int \epsilon_{\text{xc}}(n(\mathbf{r}))n(\mathbf{r})d\mathbf{r} \quad (2.12)$$

and

$$\frac{\delta E_{\text{xc}}[n]}{\delta n(\mathbf{r})} = \epsilon_{\text{xc}} + n(\mathbf{r}) \frac{\delta \epsilon_{\text{xc}}^{\text{LDA}}(n(\mathbf{r}))}{\delta n(\mathbf{r})} \quad (2.13)$$

where ϵ_{xc} is the exchange-correlation term of a uniform electron gas of density $n(\mathbf{r})$. This approximation relies on empirical results and on powerful transferability and universality properties of

interaction, leading to successful results during the last decades. It is easy to consider spinfull model with the Local Spin Density Approximations where densities of spins up $n_{\uparrow}(\mathbf{r})$ and spins down $n_{\downarrow}(\mathbf{r})$ are added in the term:

$$E_{xc}^{\text{LSDA}}[n_{\uparrow}, n_{\downarrow}] = \int \varepsilon_{xc}(n_{\uparrow}, n_{\downarrow})n(\mathbf{r}) \, d\mathbf{r} \quad (2.14)$$

2.2.4 The generalized-gradient approximation (GGA)

Another approach consists in considering gradients $\nabla n(\mathbf{r})$, $\nabla^2 n(\mathbf{r})$ and so on, of the density. whereas results can be worse than LDA in some cases (like describing gas-phase reaction barriers), it is used to describe metals and molecule-metal surface reactions (Gerrits et al., 2020; Lazzeri et al., 2008). In certain cases, LDA can have better results than GGA (Barrera et al., 2005).

2.2.5 The LDA + U method

The LDA method is blind to the orbital dependency of the Coulomb and exchange interaction. In (Anisimov et al., 1997), the authors proposed to add an interaction term, for localized electrons, driven by an interaction U just as proposed by P.W Anderson (Anderson, 1961). This method gives a correct description of the Mott insulators (see Sec. 2.3.2) and oxides such as NiO (Anisimov et al., 1997; Bengone et al., 2000) and UO_2 (Dorado et al., 2013; Shi et al., 2010; Yu et al., 2009) which are materials of interest for EDF.

2.2.6 Hybrid/metaGGA approach

metaGGA methods includes a part in the exchange-correlation function which depends on the kinetic energy, and higher order of gradients of the density. In addition, one, can mix a Hartree-Fock (HF) and a Kohn-Sham exchange to obtain better results (Toulouse & Adamo, 2002).

2.2.7 Beyond DFT

In many DFT works, paramagnetic phases are modeled as non-magnetic which can lead to erroneous conclusions (Abrikosov et al., 2016). A realistic treatment of magnetism in materials can be crucial to perform a predictive description of some properties, like defect's energies in austenitic steels. Two orthogonal pictures were first proposed to simulate magnetism:

- the itinerant model,
- the local magnetic moment model.

The first one is based on the band theory of electrons whereas the latter assumes localized electrons on atoms which carry therefore a local moment. The answer lies in mixing these two approaches (Abrikosov et al., 2016). For instance, the spin dynamics is based on the equivalence between a strongly interacted system with onsite interactions and an electron living in a system with fluctuating charge and spin fields. For instance, the Disordered Local Moment (DLM) model considers that the full electrons model does not cover its phase space in time. Indeed, each of the spins can flip after a time denotes the spin-flip time and points in more or less random direction. An example of magnetic interactions for this type of model is the longitudinal spin-fluctuation Hamiltonian H_{lsf} :

$$H_{\text{lsf}} = NJ^{(0)}(\overline{M}) + \sum_i J^{(1)}(\overline{M}, M_i) - \sum_{i,j \neq i} J_{i,j}(\overline{M}, M_i, M_j) \mathbf{M}_i \mathbf{M}_j \quad (2.15)$$

with \mathbf{M}_i being the magnetization vector and M_i its norm, $J^{(0)}(\overline{M})$ is the energy of the magnetically disordered system where the mean value of the local magnetic moment is $\overline{M} = 1/N \sum_i M_i$. $J^{(1)}(\overline{M}, M_i)$ is the energy needed to alter the value of the spin i into M_i from the imposed average value \overline{M} . Finally, $J_{i,j}$ is the interaction energy between two spins where all other local moments are disordered.

Many other approaches exist, (Abrikosov et al., 2016), and choosing the good magnetic model strongly depends on the problem.

2.2.8 Successes and limitations

The potency of the DFT relies on its simplicity and its polynomial complexity. When it first came out, the method exceeded all previous methods in terms of efficiency and duration of computation. Despite being quite simple, the LDA approximations have shown his efficiency and has confirmed a lot of experimental results (Burke, 2012). Several improvements have been done such as Density Functional Perturbation Theory (DFPT) to study phonons in crystals and periodic materials (Baroni et al., 2001). However, several complex systems remain unreachable for DFT.

- In practice, computing excited energies is still difficult with this method as it relies on variational principle which is efficient to find the ground state. Therefore, computing gap in semiconductor or photovoltaic materials are still out of reach (Burke, 2012).
- In batteries, complex phenomena can happen, especially for oxides (for instance Li-ion batteries or NiO materials (Rohrbach & Hafner, 2005)) and *ab initio* simulations struggle to recover good results corresponding to experimental data (Birkl et al., 2017; Y. Ma, 2018). Simple and empirical approximations of the exchange-correlation terms are not enough to encompass all phenomena observed experimentally, especially when electrons tend to be delocalized (Burke, 2012).
- In magnetic materials, spins have a quantum behavior and the simulation of a paramagnetic material suffers from too many approximations (Abrikosov et al., 2016). An example is the austenitic steel in nuclear power plant: it has been shown (Piochaud et al., 2014) that simulating paramagnetism with DFT (and molecular dynamics as DFT works at 0 K) leads to find the antiferromagnetic phase the most stable one to study defects, whereas it is known the paramagnetic phase is the most stable. In that specific case, one must go further to properly study magnetic phases in materials.

2.3 Quantum approaches

2.3.1 The Hubbard model

Starting from first principles methods is not the only way to describe the quantum world. Another approach to study strongly correlated electrons system is to describe it with quantum mechanics formalism. By considering second quantization (Coleman, 2015), one can express states and observables in the Fock state, which is much more convenient when the number of particle is big (such as in materials). Electrons are described by quantum mechanics and then tend to be delocalized to minimize their energy (wave behavior) but as charged particles, they repel one another and thus try to be as localized as possible in order to avoid paying this potential energy price. The minimal way of describing this strive is the famous example of the toy model called “the Hubbard model”. The system is simple: we consider fermions (or bosons) on a lattice where particles have a probability to jump on nearest-neighbors sites (tight-binding) and interact locally when they see each other on the same site (Arovas et al., 2022):

$$\begin{aligned}
H_{\text{Hubbard}} = & \sum_{i,j,\sigma} t_{i,j} d_{i\sigma}^\dagger d_{j\sigma} + U \sum_i n_{i,\uparrow} n_{i,\downarrow} \\
& + \mu \sum_i (n_{i,\uparrow} + n_{i,\downarrow})
\end{aligned} \tag{2.16}$$

where $t_{i,j}$ is the hopping term between sites i and j , $d_{i,\sigma}^\dagger$ ($d_{i,\sigma}$) the fermionic creation (annihilation) operator following anticommutation rule $\{d_{i,\sigma}^\dagger, d_{j,\sigma'}\} = \delta_{i,j,\sigma,\sigma'}$, $n_{i,\sigma} = d_{i,\sigma}^\dagger d_{i,\sigma}$, U the onsite interaction (describing the Coulomb interaction) and μ the chemical potential. This is the single-band Hubbard model (only one orbital per site). This model in 2 dimensions is conjectured to be describing (reasonably) high-temperature superconductors (Anderson, 1987). The doping and several orbital cases are still active fields of research in 2D and 3D. Solving this model could lead to major discoveries and breakthroughs in fields of experimental and theoretical physics (“The Hubbard model at half a century”, 2013).

The ratio U/t controls the importance of interaction energy over kinetic energy. If $U/t \rightarrow 0$, this means that we are dealing with free electrons and the Hamiltonian can be diagonalized in the Fourier space by setting $c_{k,\sigma}^\dagger = \sum_i e^{i.k.R_i} d_{i,\sigma}^\dagger$ such that $H_{\text{Hubbard}} = \sum_k \epsilon_k c_k^\dagger c_k$. The many-body ground state is a Slater determinant made up of these modes of energy $< \epsilon_f$ (Fermi energy) propagating with the dispersion relation $\epsilon(k)$. On the other hand, if $U/t \rightarrow \infty$, the Hamiltonian is diagonal in the real space and eigenstates are of the form $|n_{(0,\sigma)}, \dots, n_{(i,\sigma)}, \dots, n_{(N,\sigma)}\rangle$ where $n_{i,\sigma} = 0$ or 1. In the case of half-filling, each site is populated with one particle and the first excited state (so one site double-occupied) costs an energy of U . We can therefore observe two regimes: one where electrons can move freely such as in a metal and the other where the kinetic energy is negligible, and the system is an insulator. This describes what we call the Mott physics.

2.3.2 The Mott physics: starting point of highly correlated electrons

Back in the early 1900s, band’s theory was one of the greatest breakthroughs discovered thanks to the quantum theory. It is the starting point of transistors discovery which has led to the huge establishment of computers in our lives (for instance the one on which I am typing these lines) and the Moore’s law (Moore, 2006). Still, while band theory provided a good classification for many solids at the time, Verwey and de Boer (Verwey & de Boer, 1936) discovered in 1936 that some materials such a nickel oxide (NiO), an oxide with 3D valence electrons, were very poor conductors. From this postulate, Mott and Peierls (Mott & Peierls, 1937) proposed in 1937 to hypothesize that in these materials, “the electrostatic interaction between the electrons prevents them from moving at all”, explaining their insulating behavior. Mott’s paper was the opening remark of the field of strongly correlated materials.

2.3.3 The Dynamical Mean-Field Theory (DMFT)

The mean-field approximation Let’s consider the toy model of statistical physics, the Ising model:

$$H_{\text{Ising}} = J \sum_{i,j} \sigma_i \sigma_j + h \sum_j \sigma_j \tag{2.17}$$

with $\sigma = \{-1; +1\}$ and z the coordination number of the lattice. This model is exactly solvable in 1D and 2D (Onsager, 1944). Nevertheless, a first approach to solve such a model is the single-site Mean-Field (MF) method (Weiss, 1907). This means that we only consider one site interacting with a MF obtained by a self-consistent loop. Mathematically, $\sigma_i \sigma_j \approx \langle \sigma_i \rangle \sigma_j + \langle \sigma_j \rangle \sigma_i - \langle \sigma_i \rangle \langle \sigma_j \rangle$. We can define $m = \langle \sigma \rangle$ and as a result, Eq. 2.17 can be written (neglecting constant terms):

$$H_{\text{Ising}} \approx (mJz + h) \sum_i \sigma_i. \tag{2.18}$$

$h_{\text{eff}} = mJz + h$ is called the Weiss field and must be found by the self-consistency condition $m = \tanh(\beta mJz + h)$. m is the relevant degree of freedom, as known as the order parameter. The dynamical mean-field theory is based on the same reasoning. In this section, I describe the basis of the DMFT following (Georges, 2004).

The Green function Treating interacting particles is very hard, and the complexity of such a system grows exponentially with the number of particle (or size of the system in the Fock space). We therefore need some general way of examining the change of the system in response to external effects (potential, temperature...) even though we can not diagonalize the Hamiltonian. One of the mathematical tools often used in many-body physics is the Green's function. It is defined as:

$$\mathcal{G}(\mathbf{r}, \mathbf{r}', t - t') = -i \langle \phi | T d_{i,\sigma}(\mathbf{r}, t) d_{j,\sigma'}^\dagger(\mathbf{r}', t') | \phi \rangle \quad (2.19)$$

where $|\phi\rangle$ is the many-body groundstate and \mathbf{r}, t are space coordinates, time coordinates respectively. T is the ordering operator, such as:

$$\begin{aligned} T d_{i,\sigma}(\mathbf{r}, t) d_{j,\sigma'}^\dagger(\mathbf{r}', t') &= d_{i,\sigma}(\mathbf{r}, t) d_{j,\sigma'}^\dagger(\mathbf{r}', t') \quad (t > t') \\ T d_{i,\sigma}(\mathbf{r}, t) d_{j,\sigma'}^\dagger(\mathbf{r}', t') &= \pm d_{j,\sigma'}^\dagger(\mathbf{r}', t') d_{i,\sigma}(\mathbf{r}, t) \quad (t < t'). \end{aligned} \quad (2.20)$$

In the case of periodic system, \mathcal{G} only depends on $(\mathbf{r} - \mathbf{r}')$. In the Hubbard model, fermionic operators only depends on time and site number. We can define the *local* Green's function at a given lattice site:

$$\mathcal{G}^\sigma(\tau - \tau') = -\langle T d_{i,\sigma}(\tau) d_{i,\sigma'}(\tau') | \phi \rangle \quad (2.21)$$

where τ is the imaginary time defined as $\tau = -it$. In the classical mean-field theory, the local magnetization m_i is represented as a single spin on site i coupled to an effective Weiss field h_{eff} . The reasoning is rigorously analog in the DMFT (Georges, 2004). Let's consider the Hamiltonian of an Anderson impurity model, $H_{\text{And}} = H_{\text{atom}} + H_{\text{bath}} + H_{\text{coupling}}$ in which:

$$\begin{aligned} H_{\text{atom}} &= U n_\uparrow^c n_\downarrow^c - \mu(n_\uparrow^c + n_\downarrow^c) \\ H_{\text{bath}} &= \sum_{l,\sigma} \epsilon_l a_{l,\sigma}^\dagger a_{l,\sigma} \\ H_{\text{coupling}} &= \sum_{l,\sigma} V_l (a_{l,\sigma}^\dagger c_\sigma + c_\sigma^\dagger a_{l,\sigma}). \end{aligned} \quad (2.22)$$

with μ the chemical potential of the impurity/atom. This Hamiltonian is describing free fermions (a bath described by the a_l^\dagger 's) coupled (via the interaction V_l) to a single-site (the "impurity"). The idea is to consider that the Green's function of this model coincides with the local Green's function of the lattice Hubbard model under consideration. The parameters V_l and ϵ_l are only taken into account in the hybridization function

$$\Delta(i\omega_n) = \sum_l \frac{|V_l|^2}{i\omega_n - \epsilon_l}. \quad (2.23)$$

The Weiss dynamical field (as known as the self-energy of the impurity model) of this method is then defined as:

$$\begin{aligned} \hat{\Sigma}_{\text{imp}}(i\omega_n) &= \hat{\mathcal{G}}_{0,\text{imp}}^{-1} - \hat{G}_{\text{imp}}^{-1}(i\omega_n) \\ &= i\omega_n + \mu - \Delta(i\omega_n) - \hat{G}_{\text{imp}}^{-1}(i\omega_n) \end{aligned} \quad (2.24)$$

with \mathcal{G}_0 being the Green's function of the impurity model when $U = 0$ and G the interacting Green's function. Let's now consider the Green's function of the original lattice model (the Hubbard model):

$$\hat{G}(\mathbf{k}, i\omega_n) = \frac{1}{i\omega_n + \mu - \epsilon_{\mathbf{k}} - \hat{\Sigma}(\mathbf{k}, i\omega_n)}. \quad (2.25)$$

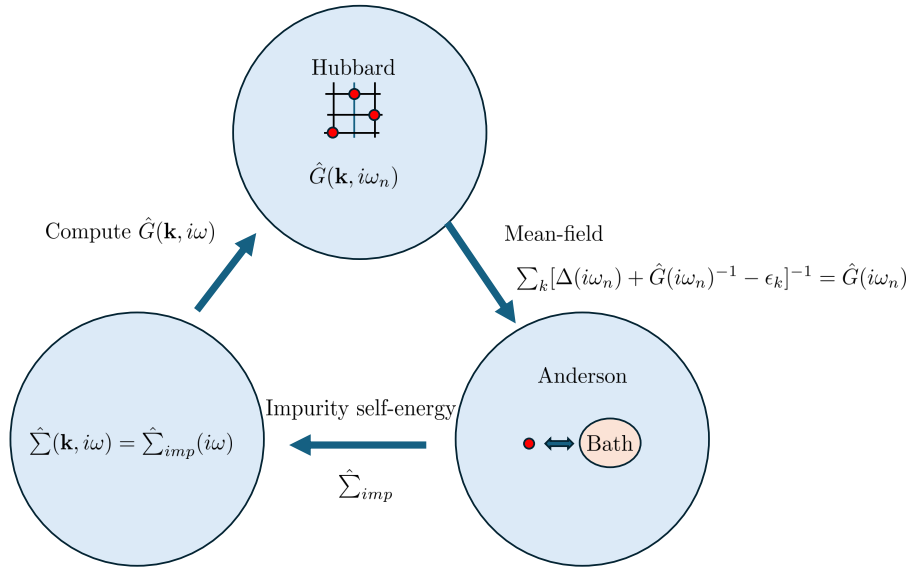


Figure 2.2: The DMFT loop (inspire from (Ayral, 2015))

The approximation relies now on considering that the lattice self-energy coincides with the impurity. This means that:

$$\hat{\Sigma}_{i,i} \approx \hat{\Sigma}_{imp}, \quad \hat{\Sigma}_{i \neq j} \approx 0. \quad (2.26)$$

As a result, we obtain the self-consistency relation:

$$\sum_{\mathbf{k}} \frac{1}{\Delta(i\omega_n) + \hat{G}(i\omega_n)^{-1} - \epsilon_{\mathbf{k}}} = \hat{G}(i\omega_n). \quad (2.27)$$

A schematic representation of DMFT loops is shown in Fig. 2.2. The DMFT is exact in the limit of infinite coordination lattices. This is also true for the mean-field in classical mechanics. It is also true in the extreme cases $U = 0$ and $t_{i,j} = 0$. The DMFT has encountered many successes in the calculation of Mott transition (see (Georges et al., 1996) for more details).

2.3.4 Extensions of these methods

The major weakness of the DMFT is the lack of correlations due to considering a single site. The Cluster DMFT (CDMFT) has been developed to consider a cluster of sites coupled to a bath resulting in a better comprehension of Mott transitions (“Chapter 3 Dynamical, extended dynamical, and cluster dynamical mean-field theories”, 2008; Park et al., 2008). In addition, the DFT and DMFT can be combined (Biermann et al., 2005; Haule & Birol, 2015; Lechermann, 2018; Park et al., 2014; Paul & Birol, 2019; J.-H. Sim et al., 2023) which enables an efficient calculation of the total energy of realistic correlated electron systems (see Fig. 2.3).

2.3.5 Quantum Monte Carlo

To end this section, I will talk a bit about Quantum Monte Carlo (QMC) methods. This approach aims at solving complex many-body problems by estimating explicitly the groundstate wave-function of the system. To this aim, a stochastic numerical integration is performed with

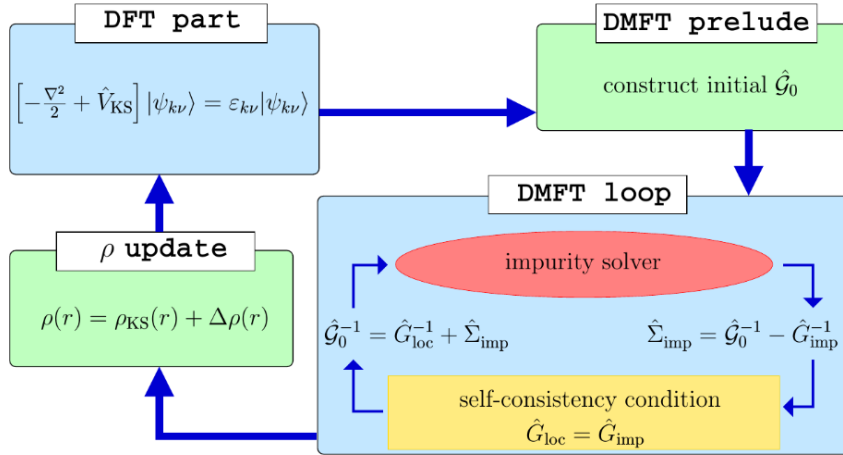


Figure 2.3: Double loop in the DFT+DMFT method. Taken from (Lechermann, 2018).

the famous Metropolis algorithm (Metropolis et al., 2004; Wessel, 2013). These algorithms have a polynomial complexity ($O(N^3) - O(N^4)$) and are widely used to solve and simulate spins model (Sandvik & Kurkijärvi, 1991; Stapmanns et al., 2018). Some works also study materials (Esler et al., 2012; Wagner, 2007). A mix between *Ab initio* approaches and QMC is possible (Wagner, 2014). However, the famous sign problem arises for fermionic systems (Pan & Meng, 2022) but also for frustrated spin systems (Alet et al., 2016; Henelius & Sandvik, 2000). QMC approaches are methods used for decades with a lot of successes but some strong limitations exist.

2.3.6 Conclusion

In this section, I have briefly described first principles methods, Green function methods and quantum Monte-Carlo approaches to many-body systems. These approaches are at the center of modern numerical methods to understand properties of materials at the atomic scale. During the last decades, these methods have contributed to understand and design complex phenomena in materials in academic and industry research. Investigations on improving them are still ongoing. Nevertheless, describing correlations in strong correlated systems seems to be out of reach without approximations. A spark in the dark has appeared with the promise of quantum computing.

2.4 Overview of quantum computing

Whether quantum theory is exact or holds hidden variables has been a thorny debate among physicists in the early 1900s. Albert Einstein said that “gods don’t play dice” and there was room for doubt. Nevertheless, the quantum theory was confirmed with many experiments during all the century until the final hit, the Aspect’s experiment that has violated Bell’s inequalities in 1982 (Aspect et al., 1982). Since this major breakthrough awarded by the Nobel Prize in 2022, researchers and industrials invest a huge amount of money and energy to build what we call a quantum computer. In this section, I describe the foundation of quantum computing principles and some advanced methods to use it. I also describe the impact of this research and the promise of quantum computing for materials and chemistry, which could change our society.

In “classical” computing, the smallest unit of information is stored in Bits “0” or “1”. Thanks to transistors and their reduced size (\approx few nm), it is possible to apply millions of operations per second in modern computers, such as the ‘AND’ or the ‘XOR’ operators. In the quantum world,

the information is stored in vector states. The combination of such states allows performing this kind of operation to bits '0' and '1' at the same time. We are not dealing with bits anymore, but with qubits. These two states are distinguishable, and we will use the Dirac notation in the following $|0\rangle = \begin{pmatrix} 1 \\ 0 \end{pmatrix}$ and $|1\rangle = \begin{pmatrix} 0 \\ 1 \end{pmatrix}$ (equivalent to $|\uparrow\rangle$ and $|\downarrow\rangle$ or $|g\rangle$ and $|r\rangle$ in our notations).

These states can be created via photons, excited states in atoms or superconducting devices. One of the main properties of these states is their dynamical behavior, being driven by the Schrödinger equation. It is then possible to apply unitary operators to evolve the system through time. We have therefore access to a new algebraic set of "quantum gates" replacing the "classical gates" of qubit. In the following, $\hbar = 1$. Most of this section is inspired from (Nielsen & Chuang, 2011).

2.4.1 Basis

Let's start with a pure state. One can write the state of a qubit as:

$$|\psi\rangle = a|0\rangle + b|1\rangle \quad (2.28)$$

where a and b are complex coefficients and $|a|^2 + |b|^2 = 1$. A qubit is always written in the z basis. A qubit can evolve under the application of operators. A very important set of such operators are the Pauli matrices,

$$\mathcal{I} = \begin{pmatrix} 1 & 0 \\ 0 & 1 \end{pmatrix}, \quad S^x = \begin{pmatrix} 0 & 1 \\ 1 & 0 \end{pmatrix}, \quad S^y = \begin{pmatrix} 0 & -i \\ i & 0 \end{pmatrix}, \quad S^z = \begin{pmatrix} 1 & 0 \\ 0 & -1 \end{pmatrix}. \quad (2.29)$$

It is a basis for the 2×2 Hermitian matrices real vector. This means that any hermitian operator U ($U^\dagger = U$) is a linear combination of these 4 matrices. They are also unitary ($U^\dagger U = \mathcal{I}$). Usually, a qubit is represented on a Bloch sphere, Fig. 2.4. Indeed, in the z basis, any state can be written $\cos(\frac{\theta}{2})|0\rangle_z + e^{i\phi}\sin(\frac{\theta}{2})|1\rangle_z$ with $\phi \in [0, 2\pi]$ and $\theta \in [0, \pi]$ up to a global phase. As an example, $|0\rangle_x$ (the eigenstate of S^x with the corresponding eigenvalue 1) can be read on the Bloch sphere

$$\cos\left(\frac{\pi}{4}\right)|0\rangle + e^0\sin\left(\frac{\pi}{4}\right)|1\rangle = \frac{1}{\sqrt{2}}(|0\rangle + |1\rangle) = |0\rangle_x \quad (2.30)$$

but also $|1\rangle_y$ (the eigenstate of S^y with the corresponding eigenvalue -1)

$$\cos\left(\frac{\pi}{4}\right)|0\rangle + e^{-i\frac{\pi}{2}}\sin\left(\frac{\pi}{4}\right)|1\rangle = \frac{1}{\sqrt{2}}(|0\rangle - i|1\rangle) = |1\rangle_y. \quad (2.31)$$

2.4.2 Many qubits system and entangled states

Considering only one qubit is not very useful but it is possible to deal with several qubits (let's note N qubits) by considering the tensor product of states. For instance, if we suppose that a system A is in the state $\psi_A = a_A|0\rangle + b_A|1\rangle$ and a system B is in the state $\psi_B = a_B|0\rangle + b_B|1\rangle$, we can describe the full system AB by the separable state

$$|\psi_A\rangle \otimes |\psi_B\rangle = a_A a_B |00\rangle + a_A b_B |01\rangle + b_A a_B |10\rangle + b_A b_B |11\rangle. \quad (2.32)$$

Separable means that the state of the whole system can be written as a tensor product of the state of the two sub-systems. One can generalize with $|\Psi\rangle_{\text{tot}} = \bigotimes_{i=1}^N |\psi\rangle_i$ but also for any operator $\hat{O}_{\text{tot}} = \bigotimes_{i=1}^N \hat{O}_i$. What makes quantum physics distinct from other physics fields is the strange property of entanglement. If we go back to the two qubits system, it can be, for instance, in what are called Bell states:

$$\frac{|00\rangle + |11\rangle}{\sqrt{2}} \quad \text{or} \quad \frac{|01\rangle + |10\rangle}{\sqrt{2}}. \quad (2.33)$$

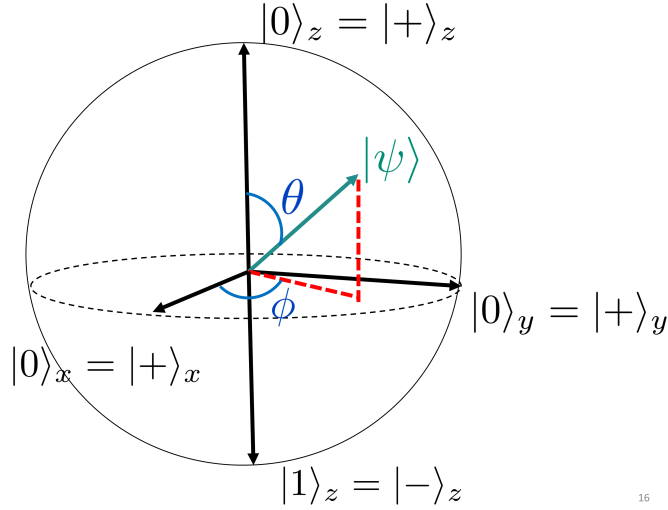


Figure 2.4: The Bloch sphere is a graphical tool to represent a qubit. A state ψ lies on the surface of the sphere and can entirely be described by the two angles θ and ϕ .

These states can not be written as a tensor product $|\psi_A\rangle \otimes |\psi_B\rangle$. In addition, performing a measurement on one system imposes the state of the other system instantly. This counter-intuitive concept is described by Albert Einstein as “a spooky action at a distance” and is at the center of the promises of quantum computing. One can remark that the amount of information to store to be able to fully describe a quantum state grows exponentially (2^N) with the number of qubit.

2.4.3 Density matrix and mixed states

The most general way of representing the state of a quantum system is with the density matrix representation:

$$\rho = \sum_i p_i |\psi\rangle_i \langle\psi|_i. \quad (2.34)$$

In this representation, we consider a statistical ensemble of N_s system, each one being in a pure state $|\psi\rangle_i$. p_i is the probability of finding the quantum system in a pure state $|\psi_i\rangle$ and $\sum_i p_i = 1$. This state is called a mixed state. Using density matrices and mixed states is useful when the state prepared is not fully known. For instance, if we consider two ensembles of one qubit with one ensemble in the state $|0\rangle$ and the other in the state $|1\rangle$, the corresponding density matrix will be:

$$\rho = \begin{pmatrix} \frac{1}{2} & 0 \\ 0 & \frac{1}{2} \end{pmatrix}. \quad (2.35)$$

The state described here is a fully mixed state. Non-zero off-diagonal elements in the density matrix identify the presence of quantum coherence in a system. One interesting value to compute is the purity of the system, *i.e* $P = \text{Tr}(\rho^2)$. If $P = 1$ the system is in a pure state and, on the other hand, if $P = \frac{1}{2^N}$, we have a fully mixed state. The density matrix representation is very useful to describe open system, as it is very difficult to know the state of the whole system: (system \otimes environment).

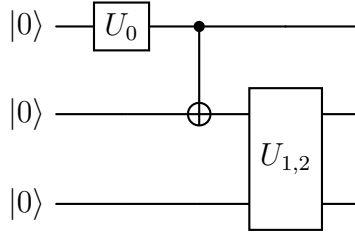


Figure 2.5: Example of a quantum circuit with three qubits. The initial state is $|000\rangle$

2.4.4 Close system and quantum logic operators

For a closed system, the evolution of a quantum state is driven by the Schrödinger equation, leading to:

$$i\hbar \frac{\partial |\psi(\tau)\rangle}{\partial \tau} = H(\tau) |\psi(\tau)\rangle \quad (2.36)$$

where $H(\tau)$ is the time dependent Hamiltonian of the system. A direct consequence is the unitary nature of any evolution operator acting on a close system (a unitary operator means $U^\dagger U = \mathcal{I}$). Therefore, only unitary operators can be used to evolve a quantum state. This can be interpreted as the norm preservation of a quantum state. To know the state after the time-evolution, one must measure the state (so the operator S^z in the z basis) several times. Indeed, if the system is in the state $\frac{|0\rangle+|1\rangle}{\sqrt{2}}$, performing on measurement of S^z one time will give -1 with probability $|a|^2 = 1/2$ and 1 with probability $|b|^2 = 1/2$. One has to perform many measurement repetitions to obtain these probabilities. The mean value of S^z is obtained by probability of mean value $-\frac{N_0}{N_m} + \frac{N_1}{N_m}$ and a standard-deviation proportional to $1/\sqrt{N_m}$ where N_0 is the number of 1 obtained after measurement, N_1 is the number of -1 obtained after measurement and $N_m = N_0 + N_1$ is the total number of measurements. This is a direct consequence of the quantum projection principle (or collapse of the wave-function), and it is called the quantum projection noise as it brings errors to the computation of an observable (this will be called shot noise in the following).

The quantum computing is based on applying unitary operators or quantum logical gates (abbreviated as gates) on the system, just as in classical computing. The procedure to perform quantum computing is the following:

- start with a register of N qubits in a well-known initial state;
- a quantum circuit which carries all time-ordered gates to apply to the register is defined;
- at the end of the quantum circuit, a measurement is performed to obtain a set of N classical bits (due to the quantum projection noise).

An example of a quantum circuit is shown in Fig. 2.5. A quantum circuit allows manipulating 2^N coefficients, whereas only N bits are controlled at a time in classical computing. Single qubit operators $U = \begin{pmatrix} U_{11} & U_{12} \\ U_{21} & U_{22} \end{pmatrix}$ are then 2×2 unitary matrices. It changes coefficient a and b in $|\psi\rangle = a|0\rangle + b|1\rangle$ into a' and b' such as:

$$U |\psi\rangle = \begin{pmatrix} U_{11} & U_{12} \\ U_{21} & U_{22} \end{pmatrix} \begin{pmatrix} a \\ b \end{pmatrix} = \begin{pmatrix} a' \\ b' \end{pmatrix}, \quad |a'|^2 + |b'|^2 = 1 \quad (2.37)$$

This means that any quantum evolution on a quantum circuit is reversible (contrary to classical circuit). More generally, applying a unitary matrix to a qubit is like moving the quantum state on the surface of the Bloch sphere. One performs rotations in all directions while conserving the norm. Thus, any arbitrary single qubit unitary operator can be written in the form:

$$U = e^{i\alpha} R_{\mathbf{n}}(\theta) \quad (2.38)$$

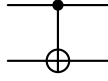


Figure 2.6: Graphical, a representation of a CNOT gate in a quantum circuit

with $R_{\mathbf{n}}(\theta) = \exp(-i\theta(\mathbf{n} \cdot \mathbf{S})/2) = \cos \frac{\theta}{2} \mathcal{I} - i \sin \frac{\theta}{2} (n_x S^x + n_y S^y + n_z S^z)$ and α a real number $\in [0, 2\pi]$. Here, $\mathbf{n} = (n_x, n_y, n_z)$ is a real unit vector in three dimensions and $\mathbf{S} = (S^x, S^y, S^z)$. Some very useful gates can be pointed out, such as the Hadamard gates (denoted H) or the phase shift gate (denoted R_ϕ):

$$H = \frac{1}{\sqrt{2}} \begin{pmatrix} 1 & 1 \\ 1 & -1 \end{pmatrix} = ie^{-i\frac{\pi}{2}(S^x - S^z)/\sqrt{2}}, \quad R_\phi = \begin{pmatrix} 1 & 0 \\ 0 & e^{i\phi} \end{pmatrix} = e^{i\frac{\phi}{2}} e^{-i\phi S^z} \quad (2.39)$$

Still, considering only one-qubit operators is not very useful as we can not create entangled states. Two-qubit gates can do the job. The idea is to make two qubits interact. For instance, the CNOT gate considers two input qubits: one is the control qubit and the other is the target qubit such as if the control qubit is in the state $|1\rangle$, the other qubit "flips" $|0\rangle \rightarrow |1\rangle$ and $|1\rangle \rightarrow |0\rangle$, otherwise it remains the same. The matrix representation of the CNOT gate is

$$\text{CNOT} = \begin{pmatrix} 1 & 0 & 0 & 0 \\ 0 & 1 & 0 & 0 \\ 0 & 0 & 0 & 1 \\ 0 & 0 & 1 & 0 \end{pmatrix} \quad (2.40)$$

and it is graphically represented in Fig. 2.6. Combining 1-qubit and 2-qubit gates can bring entanglement in the system. For instance, if the target qubit is in state $|0\rangle$ and the control qubit is in state $|1\rangle$ at the start of the circuit, applying a Hadamard gate to the control qubit and then a CNOT creates a Bell state for the target qubit $\frac{|00\rangle - |11\rangle}{\sqrt{2}}$. Some other 2-qubit gates are widely used, such as the *SWAP* gate

$$\text{SWAP} = \begin{pmatrix} 1 & 0 & 0 & 0 \\ 0 & 0 & 1 & 0 \\ 0 & 1 & 0 & 0 \\ 0 & 0 & 0 & 1 \end{pmatrix}. \quad (2.41)$$

We can also think of N-qubit gates, but they are very difficult to implement in practice. Hopefully, universal quantum gates sets exist, which means that only with specific finite size sets of 1-qubit and 2-qubit gates, one can approximately reproduce any unitary operation. The error on the approximation reduces to 0 when the number of gates is infinite. For example, the rotation operator $R_{\mathbf{n}}(\theta)$, the phase shift gate R_ϕ and the CNOT gate are commonly used to form a universal quantum gate set.

The quantum computing is then based on the evolution through time of a state of a closed system thanks to 1-qubit and 2-qubits unitary operators. In practice, two very different approaches exist (Georgescu et al., 2014): the digital and the analog approaches.

2.4.5 Digital approach

Following the fact that any unitary operator can be (approximately) decomposed in product of 1-qubit and 2-qubit gates, it is possible to emulate the evolution of any Hamiltonian with a quantum circuit. This is the Digital Quantum Simulation (DQS). In the following, this Hamiltonian is called the **target** Hamiltonian. In quantum computing, the ansatz is a way to prepare a specified quantum state with a circuit. It encompasses the initial state preparation, but also the circuit itself. The purpose of a good ansatz is to reach the desire quantum state with the fewer gates or measurements as possible.

Preparing the initial state of an ansatz can be very difficult if some specific properties are needed. In the case of fermionic computation, it can be very useful to start with a state that respects antisymmetries in the quantum state. Usually, the state $|0\rangle^{\otimes N}$ is the easiest to prepare as it is the native state of the device, and it has been proven that one can prepare a fermionic state with all possible permutations with polynomial resources (Abrams & Lloyd, 1997). Ancilla qubit can also be useful to prepare the initial state (H. Wang et al., 2011). An ancilla qubit is a qubit acting in the circuit but which is not a qubit describing the original problem. It is added to the quantum circuit only to help the algorithm to run faster. It does not contain properties of the wanted state, but it helps in the quantum computation.

DQS is not easy because sometimes the number of gates needed grows exponentially with the size of the system but for most Hamiltonians with local terms, this number grows in a polynomial way (Nielsen & Chuang, 2011). Let us consider that the target Hamiltonian is a sum of constant local interaction terms $H = \sum_l H_l$. Therefore, mimicking the evolution of H in time means that the circuit must be as close as possible of $U(t) = e^{-i\sum_l H_l t}$. Two cases are possible:

- Either, for all indices l and l' , $[H_l, H_{l'}] = 0$ and $U = \prod_l e^{-iH_l t}$ and the decomposition in gates is direct.
- Either, and that is the vast majority of cases, $[H_l, H_{l'}] \neq 0$ and one need to use the Trotter decomposition.

The idea is to cut the total time of evolution in infinitesimal slices, such as $U(t) \approx (e^{-i\sum_l H_l \Delta t})^{\frac{t}{\Delta t}}$. Therefore, we obtain (Nielsen & Chuang, 2011)

$$U(t) \approx \prod_{N_t = \frac{t}{\Delta t}} \left(\prod_l e^{-iH_l \Delta t} \right)^{N_t} + O((\Delta t)^2) \quad (2.42)$$

and when $\Delta t \rightarrow 0$ we recover a product of local terms. Similarly, one can decompose $e^{i(A+B)\Delta t}$, where $[A, B] \neq 0$, into:

$$e^{i(A+B)\Delta t} = e^{iA\Delta t/2} e^{iB\Delta t} e^{iA\Delta t/2} + O((\Delta t)^3). \quad (2.43)$$

In some cases, the goal is to reach a specific state with specific properties instead of mimicking the evolution of a specific Hamiltonian. The Shor algorithm (Shor, 1994) is a perfect example of this. Details about this algorithm will be provided in Sec.2.5. For this type of algorithm, the QFT is very useful. The idea is the same as for the classical discrete Fourier transform, where we take a vector of complex numbers $(x_0, x_1, \dots, x_{N-1})$ as inputs, and it outputs the transformed data as a vector of complex numbers $(y_0, y_1, \dots, y_{N-1})$ defined as:

$$y_k = \frac{1}{\sqrt{N}} \sum_{j=0}^{N-1} x_j e^{2i\pi jk/N} \quad (2.44)$$

The QFT is exactly the same transformation applying on an orthonormal basis. We define states $|0\rangle, \dots, |n-1\rangle$ with $|0\rangle = |0\rangle^{\otimes N}$, $|1\rangle = |0\rangle^{\otimes (N-1)} \otimes |1\rangle, \dots, |n-1\rangle = |1\rangle^{\otimes N}$ and $n = 2^N$. Considering a state $|\psi\rangle = \sum_{j=0}^{n-1} \alpha_j |j\rangle$ The QFT is the defined as:

$$\begin{aligned} |\psi\rangle &\rightarrow \sum_{k=0}^{n-1} \beta_k |k\rangle \\ \beta_k &= \frac{1}{\sqrt{n}} \sum_{j=0}^{n-1} e^{2i\pi jk/n} \alpha_j |j\rangle. \end{aligned} \quad (2.45)$$

The digital approach is based on the fact that "anything" can be simulated with only a universal set of gates. The gates are applied with in an ordered-time sequence. The last step is the measurement of the state at the output of the circuit.

As described in previous sections (Sec. 2.4.4), measuring a quantum state means getting the eigenvalue λ_k of a hermitian operator \hat{O} (measurement tool) corresponding to the eigenstate $|k\rangle$ with the probability $|\langle\psi|k\rangle|^2$ where $|\psi\rangle$ is the state just before the measurement. If $|\psi\rangle$ is not an eigenstate of \hat{O} but a linear combination of its eigenstates, N_m measurements are needed to reconstruct statistically the value of $\langle\hat{O}\rangle$ with an error of $\approx 1/\sqrt{N_m}$. In general, Quantum State Tomography (QST) can be used to characterize a quantum state but it requires resources that grow exponentially with the size of the system, making it inefficient for large quantum systems (D'Ariano et al., 2003). The measurement can also be performed in the quantum circuit and not only at the end, that the case for protective measurements (Choi et al., 2020), to perform Quantum Error Correction (QEC). The QEC for digital quantum computing is out of the scope of this thesis but it is a crucial part of digital quantum computing today (Roffe, 2019).

The measurement procedure is therefore a major step of quantum computing, and a good measurement procedure is needed to reduce the cost of computation.

In practice, we do not have access to perfect qubits but to what is called **physical** qubits *i.e.* qubits with errors. In classical computing, the system is repeated a great amount of time in parallel to avoid errors but in the quantum world, the no-cloning theorem (Wootters & Zurek, 1982) prevents this method. Two types of error can appear in qubits:

- the bit-flip error $|0\rangle \rightarrow |1\rangle$ and $|1\rangle \rightarrow |0\rangle$
- the phase-flip error $\frac{|0\rangle+|1\rangle}{\sqrt{2}} \rightarrow \frac{|0\rangle-|1\rangle}{\sqrt{2}}$ and $\frac{|0\rangle-|1\rangle}{\sqrt{2}} \rightarrow \frac{|0\rangle+|1\rangle}{\sqrt{2}}$.

A contrario, **logical** qubits are noiseless qubits and can be directly used for computation. QEC allows to count the number of effective logical qubits that are available for an algorithm from the number of physical qubits available in the device. Another source of error is the gate fidelity and most importantly the fidelity of entangling gates. The fidelity \mathcal{F} of a gate is a number between 0 and 1 which measures the capacity of an experimental gate to reproduce the theoretical expected state. If the fidelity is $\mathcal{F} = 0$, it always reproduces an orthogonal state whereas if $\mathcal{F} = 1$ (impossible in practice), it reproduces exactly the target state at each application.

2.4.6 Analog approach

That being said, a "perfect" quantum computer or simulator (without noise or with very efficient QEC) does not exist today and the number of qubits or gates is limited. As an example, the Shor algorithm would need several thousands logical qubits which means millions of physical qubits... which is far from being reached. John Preskill (Preskill, 2018) has defined this era as the Noisy Intermediate Scale Quantum (NISQ) era where only few number of noisy qubits are available and, unfortunately, DQS boils down to the number of logical qubits and the fidelity of gates. Nevertheless, some quantum devices can simulate quantum mechanics by quantum means. This means that the intrinsic physics of the device follows a quantum behavior and, therefore, can mimic another system of interest. The Hamiltonian of the system is called the *resource* Hamiltonian and the Hamiltonian to mimic is still the *target* Hamiltonian. Here, the challenge is to map the resource Hamiltonian onto the target Hamiltonian. It is not always possible, and in most cases, only a partial mapping can be done with, for instance, symmetries in common. An important advantage of Analog Quantum Simulation (AQS) is the fidelity of the simulation of the resource Hamiltonian. Usually, this type of device can control more qubits with a better fidelity than for digital quantum computing. In addition, even in the presence of noise, one can recover physical properties of interest. For instance, when looking at a quantum phase transition, the qualitative behavior with not all quantitative quantities can be enough. At first glance, AQS seems simpler than DQS, but it comes with major inconveniences. First, the mapping between the resource and the target Hamiltonian is not always direct. For instance, qubits are not fermions and therefore looking at properties of a fermionic system with a driven qubits Hamiltonian needs several steps. Second, AQS is way less flexible than DQS and not anything can be simulated. In most cases, states reached by AQS are

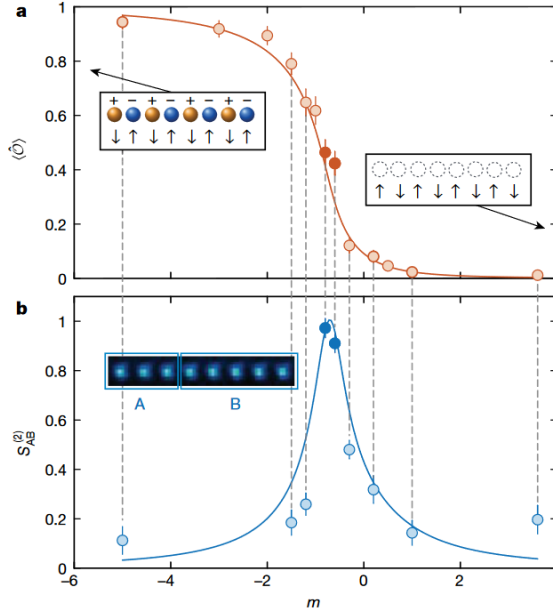


Figure 2.7: Quantum phase transition observed on trapped-ions device with Analog Quantum Simulation. (a) is the order parameter of the phase transition and (b) is the second-order Rényi entanglement entropy. Experimental data are represented by circles, and solid lines are theoretical results from exact diagonalization. The error bars are standard errors of the mean $\langle \hat{O} \rangle$ and $S_{AB}^{(2)} = \text{tr}(\rho_A^2)$ (with the A–B bipartition shown in the inset), respectively. Taken from (Kokail et al., 2019)

not known and problems which are hard to describe with a physical Hamiltonian (such as the Shor algorithm) can not be solved with analog simulators. An example of the success of AQS has been done on trapped-ions simulator (Kokail et al., 2019). They have investigated the physics of the Schwinger model — a toy problem for lattice quantum electrodynamics by leveraging the similarity between the symmetries of a 20-ions quantum simulator and those of the Schwinger model. The resource Hamiltonian is the 'XY' Hamiltonian

$$H_R = \sum_{i=1}^{N-1} \sum_{j=i+1}^N J_{i,j} (S_i^+ S_j^- + S_i^- S_j^+) + B \sum_{i=1}^N S_i^z \quad (2.46)$$

with $J_{i,j}$ the long-range antiferromagnetic interaction term. This term is controllable and $J_{i,j} \approx J_0/|i-j|^\alpha$ with $0 < \alpha < 3$. B is an effective, uniform magnetic field. $S_i^+ = (S_i^x + iS_i^y)/2$ and $S_i^- = (S_i^+)^{\dagger} = (S_i^x - iS_i^y)/2$. On the other hand, the target Hamiltonian (Schwinger model) is

$$H_T = w \sum_{j=1}^{N-1} (S_j^+ S_{j+1}^- + S_{j+1}^- S_j^+) + \frac{m}{2} \sum_{j=1}^N (-1)^j S_j^z + \bar{g} \sum_{j=1}^N L_j^2 \quad (2.47)$$

where L_j depends on S^z . The crucial point, here, is the shared symmetries of the two Hamiltonians: in both cases, $[H, S_{\text{tot}}^z] = 0$. This helps to reduce the complexity of the "quantum circuit" and the number of parameters in the quantum computation (see Sec. 4.4.1). The result is the observation of a quantum phase transition up to 20 qubits despite all the noise and errors in the system (Fig. 2.7) with a divergent derivative for one observable and a divergence for the other. Because of the finite size system, these divergences do not go to infinity. Nevertheless, the behavior of the target Hamiltonian is reproduced at least qualitatively.

2.4.7 Conclusion

Quantum computing can be performed in two different ways:

- A digital approach with the possibility to simulate any Hamiltonian at a cost of a high number of gates and qubits needed to reach an advantage.
- An analog approach leading to simulate with a better precision specific Hamiltonian feasible in practice.

The promises could be world changing or at least improve drastically the search of solutions for certain classes of problems and, hence, overcome classical limitations. Despite many public and private investments, it is far from a forgone conclusion that quantum computing will be inevitable one day because of noise and errors. A new field has therefore emerged: the hybrid algorithms. The quantum algorithms are divided in two parts: one quantum part where the quantum simulator or computer solves a very specific quantum problem and one classical part which helps the quantum part to reach his target. More globally, many hybrid and fully quantum algorithms are developed today to mitigate errors and being implemented on today's devices. In the next section, I will present some of these methods with their success and also the improvements needed to reach the famous "quantum supremacy" or, more realistically, "quantum advantage".

2.5 Methods

In this section, I describe some of state-of-the-art methods of quantum computing. I also depict the slave-spin theory and how to implement it on a Rydberg Quantum Processor (RQP) leading to an hybrid quantum-classical algorithm.

2.5.1 The quantum phase algorithm

In many quantum problems, the goal is to find the eigenstates of an operator U . When N is too big, classical computer struggles to diagonalize a $2^N \times 2^N$ matrix. The quantum phase algorithm proposes to overcome this. The first thing to notice is that an eigenvector of a unitary operator is only defined by its phase as its modulus square is 1. If λ is an eigenvalue corresponding to the eigenstate $|\psi\rangle$ of a unitary operator, $\langle\psi|U^\dagger U|\psi\rangle = \langle\psi|\psi\rangle \lambda^* \lambda = |\lambda|^2$ and because $U^\dagger U = \mathcal{I}$, $|\lambda|^2 = 1$. Therefore, any eigenstate is of the form $\lambda = e^{2i\pi\phi}$ with $\phi \in [0, 1]$. As $\phi \in [0, 1]$, one can write it in binary notation $\phi = 0.\phi_1\phi_2\dots\phi_N = \phi_1 \times 2^{-1} + \phi_2 \times 2^{-2} + \dots\phi_N \times 2^{-N}$. Let's consider the circuit, Fig. 2.8. After the Hadamard gate, the state is $(|0\rangle|\psi\rangle + |1\rangle|\psi\rangle)/\sqrt{2}$. Then the $C_{U^{2^j}}$ gate is applied: this means that if the control qubit is $|1\rangle$, the gate U^{2^j} , with j an integer, is applied to $|\psi\rangle$, otherwise it is not. The power of 2^j will be explained later. Here, $j = 0$ and hence, the state at the end of the circuit is $(|0\rangle|\psi\rangle + e^{2i\pi\phi}|1\rangle|\psi\rangle)/\sqrt{2}$.

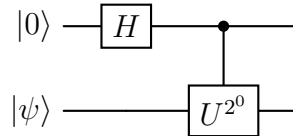


Figure 2.8: Quantum circuit for the quantum phase estimation at first order.

Let's now consider Fig. 2.10. It is straightforward to see that $U^2|\psi\rangle = e^{2\pi(2\phi)}$ and more generally, $U^{2^j}|\psi\rangle = e^{2\pi(2^j\phi)}$. In addition, $\phi = 0.\phi_1\phi_2 = \phi_1 \times 2^{-1} + \phi_2 \times 2^{-2}$, $2\phi = \phi_1.\phi_2$ and therefore, $e^{i2\pi(2\phi)} = e^{i2\pi(\phi_1)}e^{i2\pi(0.\phi_2)} = e^{i2\pi(0.\phi_2)}$ because ϕ_1 is an integer. More generally, $e^{i2\pi(2^j\phi)} = e^{i2\pi 0.\phi_{j+1}\phi_{j+2}\dots}$. Going back to the case $j = 1$, the output state is $\left(|0\rangle +$

$e^{2i\pi 0.\phi_1\phi_2} |1\rangle (|0\rangle + e^{2i\pi 0.\phi_2} |1\rangle) |\psi\rangle) / 2$ if $\phi = 0.\phi_1\phi_2$ is assumed. For an arbitrary n , the output state is

$$\frac{1}{\sqrt{2^n}} \sum_{k \in \{0,1\}^n} e^{2i\pi(\phi \times k)} |k\rangle |\psi\rangle \quad (2.48)$$

with k a binary number. The final step is to consider the inverse Fourier transform (QFT^{-1}) in the canonical basis $|x\rangle$, $x \in \{0,1\}^n$. The QFT is defined as

$$|x\rangle \rightarrow |x_{QTF}\rangle = \frac{1}{\sqrt{2^n}} \sum_{k \in \{0,1\}^n} e^{2i\pi(x \times k)/2^n} |k\rangle \quad (2.49)$$

and looks very much like Eq. 2.48. Finally, applying the inverse Fourier transform leads to the state $|\phi\rangle = |\phi_n\rangle |\phi_{n-1}\rangle \dots |\phi_1\rangle$ which can be directly measured (ignoring the state $|\psi\rangle$ which remains the same). Thanks to this method, one can estimate the n first digits of the phase and therefore the eigenvalue of any unitary operator. A strong asset of this method is the state $|\psi\rangle$ can be unknown. Indeed, one can decompose the state $|\psi\rangle$ in the basis of eigenvalue of U and thus recover the result described above for all eigenstates.

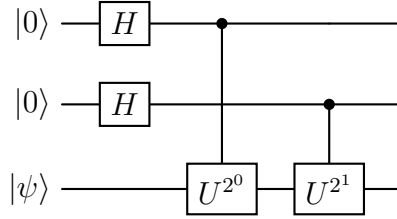


Figure 2.9: Quantum circuit for the quantum phase estimation at second order.

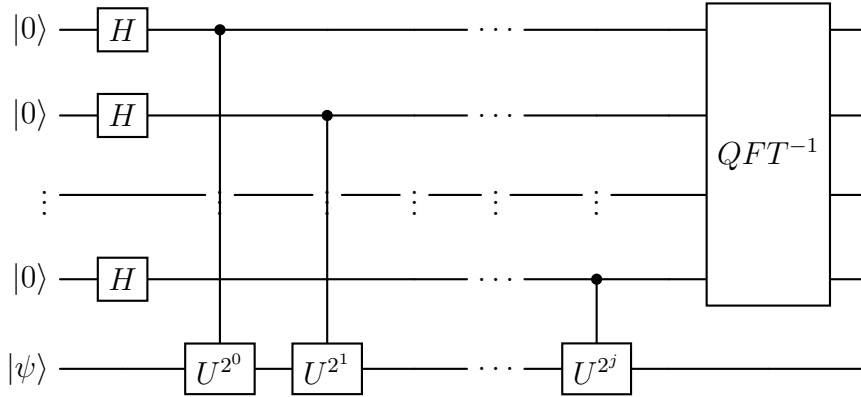


Figure 2.10: Complete quantum circuit for the quantum phase estimation.

This algorithm and the QFT are at the heart of several algorithms which are candidate to show quantum supremacy : the Shor algorithm to decompose any number into prime numbers (Shor, 1994) with polynomial resources, the HHL (stands for Harrow, Hassidim and Lloyd, the authors of the original article) (Harrow et al., 2009) algorithm which solves linear equations with a complexity of $O(\log(N))$ where N is the number of variables in the system and the Grover algorithm (Grover, 1996) for unstructured search that finds with high probability the unique input to a black box function that produces a particular output value. For instance, consider a function $f\{0, 1, \dots, N - 1\} \rightarrow \{0, 1\}$ and you want to find out the relation between inputs and outputs of

the function. Classically, the fastest way to do so is to test all possibilities, which means $O(N)$ measurement. The Groover algorithm proposes to find the solution with a probability higher than $1/2$ with only $O(\sqrt{N})$ measurements.

Despite being very promising, these algorithms need a lot of qubits and high fidelity gates that are not accessible today, and we do not know when they will be. The challenge is very hard and it is a long journey before being able to show a quantum advantage over classical algorithms but the reward would be to crack most communication encryption of our modern world, so maybe it is worth it. But it remains a bet. Only the number 15 was decomposed into prime numbers thanks to the Shor algorithm (Monz et al., 2016). Because no one wants to wait several decades, some other methods have been explored.

2.5.2 The Variational Quantum Algorithm (VQA)

As described in Sec. 2.2, computing the groundstate of strongly-correlated many-body Hamiltonians would help researchers but also companies in energy, chemistry, health, drugs and therefore change the society. The good news is that, it often relies on finding the groundstate of such a Hamiltonian. In all minds, quantum computing aims at exceeding classical computing. However, classical algorithms benefit from several decades of development, and they are far from being obsolete. The idea to combine both quantum and classical worlds was first proposed by Alberto Peruzzo *et al.* in (Peruzzo et al., 2013). Such an algorithm which combines quantum and classical realms is called a hybrid quantum-classical algorithm. More specifically, one specific algorithm is well suited to find the groundstate of an operator: the Variational Quantum Algorithm (VQA). The principle is to prepare a state with a gate-parametrized quantum circuit. This means that parameters can be manually adjusted in gates of the circuit (such as angle θ in rotation matrix $R_n(\theta)$) to change the output as a function of parameters. The aim is to be able to span the most of Hilbert space possible with the different parameters. One starts with an input state and a unitary parametrized gate (called Parametrized Quantum Circuit PQC) $U(\theta)$ is applied to it. The state is measured at the end of the circuit, and the target operator (often the target Hamiltonian, noted as H_T in the following) is measured in this state by statistical repetition of the measurement. When the goal of VQA is to find the lower eigen value of an operator, it is often called the Variational Quantum Eigensolver (VQE). The key point is that now a classical optimizer looks for the parameters to minimize the measured value. Then the computation is done again with the new parameters and the loop goes on until a criterion is reached. At the end, the energy measured in the state obtained should be close to the real ground state energy of the target operator. A graphical example of the VQA algorithm is shown in Fig. 2.11. In the following, I describe each step of this algorithm and how to leverage them to increase the performance of VQA.

One of the main advantages of VQA methods is that they provide a general framework that can be used to solve a wide array of problems. Indeed, the basic elements are always the same, whereas the structure can be different from a problem to another. VQA algorithm is an active field of research (Bharti et al., 2022; Y. Cao et al., 2019; Cerezo, Arrasmith, Babbush, Benjamin, Endo, et al., 2021; McArdle et al., 2020; McClean et al., 2016) and have been performed on a lot of architectures (Colless et al., 2018; Kandala et al., 2017; Nam et al., 2020; O'Malley et al., 2016; Peruzzo et al., 2013). It is at the center of quantum computing today and the most promising way to show a quantum advantage in the next few years.

The first step of VQA is to encode our problem as a cost function to minimize C . This cost function is usually the mean value of a Hamiltonian:

$$\langle \psi_{\text{init}} | U(\theta)^\dagger H_T U(\theta) | \psi_{\text{init}} \rangle = \langle H_T \rangle_\theta \quad (2.50)$$

where $|\psi_{\text{init}}\rangle$ is the initial state and $U(\theta)$ the PQC describing the circuit. Other cost functions can be chosen, such as the Gibbs objective function (L. Li et al., 2020)

$$G = -\ln \langle e^{-\eta H_T} \rangle \quad (2.51)$$

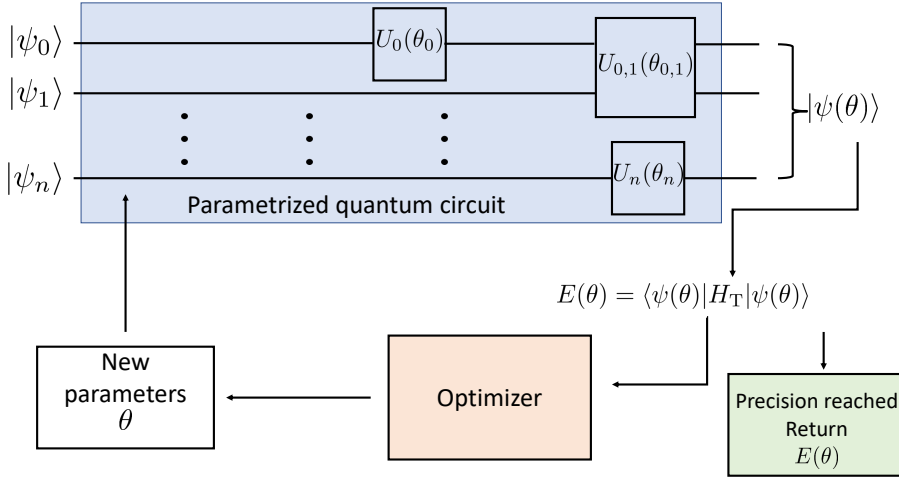


Figure 2.11: The Variational Quantum Algorithms loop. An initial state is prepared as an input. Then time-ordered parametrized (the parameters are regrouped in a vector θ) gates are applied to this state. The output is a vector state depending on parameters. This state is measure to obtain a bitstring and the target Hamiltonian is measured in this bitstring state. This procedure is repeated N times to estimate the mean value $E(\theta_{\text{tot}}) = \langle H_T \rangle$. Then a classical optimizer looks for new parameters to minimize this mean value. The procedure is done again with the new parameters. These loops are performed until a criteria is reached on the value of $\langle H_{\text{target}} \rangle$ is reached or a fixed number of loops is exceeded. The final value of $\langle H_T \rangle$ is expected to be very close to the real ground-state energy.

where the parameter η has to be tuned. But in the end, when η is small, it reduces to the problem Eq. 2.50. Another target of VQA can be a specific state, $|\Psi\rangle$ and then this algorithm is used to test the fidelity of a circuit. The cost function is then

$$\langle \psi_{\text{init}} | U(\theta)^\dagger | \Psi \rangle \langle \Psi | U(\theta) | \psi_{\text{init}} \rangle = | \langle \Psi | U(\theta) | \psi_{\text{init}} \rangle |^2. \quad (2.52)$$

That is the case in (Barison et al., 2021; Cerezo, Sone, et al., 2021; Havlíček et al., 2019) for specific problems. However, one needs to know the target state to use this cost function, and it is often not the case in materials where the groundstate is obviously not known. The main goal of VQA is to find the set of parameters θ to reach:

$$\min_{\theta} (C(\theta)) \quad (2.53)$$

and therefore the ground-state energy of the target Hamiltonian through the variational principle (see 2.6) in the specific case of a VQE algorithm for instance.

One has to ensure that the target Hamiltonian can be measured in the computational basis, *i.e.* it is a sum of Pauli strings

$$H_T = \sum_{s=1}^{N_S} \mathbf{c}_s \left(\bigotimes_{j=1}^N S_j^{(s)} \right) \quad (2.54)$$

with N_S the number of Pauli strings and N the number of qubits. S_j are the Pauli matrices. If H_T is expressed this way, the measurement in the computational basis is straightforward. Unfortunately, the original problem is not always described with qubits and therefore, one must find a way to map the initial Hilbert space into the qubit Hilbert space. Depending on the problem considered, this step can be easy or can need a mapping (see Sec. 4.3.1). Then an expectation value of H_T is

the sum of expectation values of Pauli operators

$$\langle H_T \rangle_\theta = \sum_{s=1}^{N_S} \mathbf{c}_s \left(\bigotimes_{j=1}^N S_j^{(s)} \right)_\theta. \quad (2.55)$$

The next essential building block is of course the quantum circuit or the ansatz. The common definition of all VQA algorithm is the state obtained at the end of the circuit:

$$|\psi(\theta)\rangle = U(\theta) |\psi_{\text{init}}\rangle \quad (2.56)$$

where $|\psi_{\text{init}}\rangle$ is the initial state of the circuit. The initial state preparation strongly relies on the problem and the circuit. A good start offers better performance with for instance an initial state that follows problem symmetries or is easy to prepare on the quantum hardware. The choice of $U(\theta)$ will greatly impact the success of the VQA. From the perspective of the problem, the *ansatz* influences both the convergence speed and the closeness of the final state to a state that optimally solves the problem. On the other hand, one can have to take into account the hardware on which the VQA is performed: gates, parameters, errors, and even the method (digital or analog) can differ a lot between architectures. For instance, some entangling gates such as CNOT can have a great fidelity in some hardwares, but it would be better to choose the SWAP gate on another ones. In practice, most of the ansatz developed can be classified as problem-inspired or hardware efficient, depending on their structure and application.

Problem-inspired ansatz The idea here is to draw from the target Hamiltonian to get the circuit. One example is the Trotter decomposition, Eq. 2.42. Chemists have developed their own ansatz way before the advent of the VQA. It is called the *Unitary coupled cluster ansatz* (Bartlett et al., 1989) and will be developer deeper in Sec. 2.6 and Sec. 4. In a simpler manner, the variational Hamiltonian ansatz aims at reducing the number of parameters and accelerate the convergence (McClellan et al., 2016; Wecker et al., 2015) by considering terms of the fermionic target Hamiltonian itself. For this purpose, we consider that $H_T = \sum_l H_l$ and the ansatz is then

$$U = \prod_{l=1} e^{i\theta_l H_l}. \quad (2.57)$$

A very promising algorithm of the NISQ era is the Quantum Approximate Optimization Algorithm (QAOA) (Farhi et al., 2014). It aims at approximate solutions to combinatorial optimization problems. The cost function is designed to encode a combinatorial problem by means of bit strings that form the computational basis. A key point of this algorithm is a theoretical guarantee of convergence when the depth of the quantum circuit increases. It consists of applying p times two layers of non commutating operators C (the operator of the cost function) and M the mixing operator. Mathematically, the prepared wave function is of the form (taking notations from (Dalyac et al., 2021)):

$$|Z_{\gamma,\beta}\rangle = e^{-i\beta_p M} e^{-i\gamma_p C} \dots e^{-i\beta_0 M} e^{-i\gamma_0 C} |\psi_{\text{init}}\rangle. \quad (2.58)$$

(γ, β) are sets of parameters to optimize and p is called the QAOA level or depth. The performance of the QAOA algorithm improves with this value in a perfect case (in the absence of noise). For satisfying constraints of the original problem or experimental device limitations, penalties can be added to the cost function. Nevertheless, it is often not sufficient and thinking on how to encode the constraints directly in the ansatz seems to be the most promising way (Nguyen et al., 2023). This approach was implemented on a quantum emulator considering Rydberg atoms device on Maximum Independent Set (MIS) and max-k-cut problems with promising results (Dalyac et al., 2021). The two problems are drawn from the rapidly growing sector of smart-charging of electrical vehicles, in which EDF is strongly involved. The QAOA method can be compared with a Trotterisation of the annealing method (see 2.5.3). One can generalize this method with layers of two unitary

operators $U(\gamma)$ (phase-separation) and $V(\beta)$ (mixing) which do not necessarily emerge from the time evolution of a specific Hamiltonian. This is called the Quantum Alternating Operator Ansatz (Hadfield et al., 2020) (also QAOA in the literature). Following (Bharti et al., 2022), we will abbreviate this ansatz as QuAltOA. In my work, I have tested this ansatz for chemistry problems with Rydberg atoms device and compared it with a new hardware-efficient digital-analog ansatz and I have shown that in this case, hardware-ansatz is more efficient.

Hardware-efficient ansatz Problem-inspired ansatz seems great theoretically with good symmetries between the problem and the unitary operator, reduced parameters number, better efficiency... But when it comes to implement it on a real quantum computer, reality is catching up to us. Indeed, each architecture can implement gates with more or less efficiency (some gates are impossible to implement on some devices) and errors, decoherence, limited fidelity impose to use hardware-efficient circuits. That is hardware-efficient ansatz. Even if the circuit is not well suited for the original problem, choosing gates that can be well implemented on a specific device can lead to better results than with a problem-inspired device. The first example of this is in (Kandala et al., 2017) where IBM chose to build a parametrized circuit with specific gates that can be well implemented on a superconductor device. Back then, it was one of the most impressive results of quantum computing for chemistry and spin system. Often, hardware efficient ansatz relies on only one or two entangling gates and just a few single-qubit gates. For the specific case of superconducting qubit, the lack of connectivity between qubits leads to choose specific gates that are not linked with the original problem. All the difficulty of studying VQA in The NISQ era is to balance the two ansatz. As explained in the previous section, it is possible to map a circuit with specific gates into another circuit with another gates, with the same results. Most of the studies take the problem-inspired ansatz and implement it with a hardware efficient circuit (Hempel et al., 2018; Nam et al., 2020). In addition, one can choose a specific architecture to solve a problem as symmetries of implementable gates match with symmetries of the problem (Kokail et al., 2019). In fact, it seems that choosing the architecture with respect to problem symmetries to reduce the complexity and length of the circuit is one of the major challenges of the NISQ era (and maybe beyond).

Classical optimization The quantum part of VQA is very important and challenging, but the optimization of parameters is also an active field of research. Thus far, the effect of noise and errors have only been considered for the quantum part, but the impact on the optimizer is huge. Even natural laws of physics themselves limit the efficiency of the optimization: one have to perform many measurements to obtain the mean value of an observable with a great precision. Thus, a good optimizer should try to minimize the number of measurements or function evaluations. Last but not least, it should be resilient to noisy values coming from limited fidelity, quantum decoherence and so on. In other words, the perfect optimizer should converge toward the minimum value of an observable with only few noisy sets of data which is not an easy task. Therefore, choosing a good optimizer is crucial (Lavrijsen et al., 2020). The first idea is to use gradient descent algorithm, which is a local based research algorithm. It is based on the postulate that one can have access to the derivative of the cost function $\frac{\partial C(\theta)}{\partial \theta_i}$. This value indicates the direction in which the objective function shows the greatest change (Piskor et al., 2022). More sophisticated or free-gradient algorithms have been tried such as the genetic algorithm (Michel, Grijalva, et al., 2023; Wakaura et al., 2021) which is a global optimizer (it aims at finding a global minimum) at a cost of more function evaluations. Finding the good optimizer for different problems is still an active field of research (Bonet-Monroig et al., 2023; Gacon et al., 2021) that I will not develop here, but useful insights can be found in (Bharti et al., 2022; Cerezo, Arrasmith, Babbush, Benjamin, Endo, et al., 2021; Wecker et al., 2015).

Measurements Once the state is obtained at the output of the circuit, one must measure the state in the most efficient way to facilitate the work of the quantum optimizer and reduced the number of total measurements. The most direct approach is to decompose the output state in the basis of the target operator O . To proceed, a unitary operation can be applied to project the state into the diagonal basis of the observable. Let's consider an example: we have a state $|\psi(\theta)\rangle_z$ of N qubits at the output of the circuit, diagonal in the z basis, and we want to know the mean value of the operator $\bigotimes^N Y$. One needs to perform a rotation at the end of the circuit to project the state in the y basis:

$$Y = R_x^\dagger(\pi/2)ZR_x(\pi/2) \quad (2.59)$$

and

$$\langle Y \rangle = \langle \psi(\theta) | R_x^\dagger(\pi/2)ZR_x(\pi/2) | \psi(\theta) \rangle. \quad (2.60)$$

Therefore, the rotation $R_x(\pi/2)$ must be applied to all qubits at the end of the circuit. This example is quite simple, but let's now consider a general target Hamiltonian $H_T = \sum_{s=1}^{N_s} \mathbf{c}_s \left(\bigotimes_{j=1}^N S_j^{(s)} \right)$ where S can be either S^z , S^x or S^y . For each Pauli string, a specific tensor product of rotations is needed. This means that the number of gates to apply to each qubit is proportional to the number of different Pauli strings in the Hamiltonian. In many-body and chemistry target Hamiltonian, the number of terms can grow rapidly and therefore the number of measurement can become considerable (keeping in mind that for each Pauli strings, N_s measurements are needed to have an error of $1/\sqrt{N_s}$ on the mean value). For one Pauli string, the number of measurement samples needed to estimate $\bigotimes_j^N S_j$ with an additive error of at most ϵ with a failure probability of at most δ is bounded by Hoeffding's inequality (H.-Y. Huang et al., 2019)

$$N_s \geq \frac{2}{\epsilon^2} \log\left(\frac{2}{\delta}\right). \quad (2.61)$$

The first idea is to group Pauli strings that can be measured simultaneously to minimize the number of measurements (Kandala et al., 2017; McClean et al., 2016) but this can be a NP-hard problem.

One of the most powerful methods is the classical shadow method with randomized (H.-Y. Huang et al., 2020) and derandomized (H.-Y. Huang et al., 2021) measurement (details about this method is shown in 4.4.3).

One advantage of VQA algorithm is the possibility to implement it with AQS (Kokail et al., 2019; Michel, Grijalva, et al., 2023) and DQS (Kandala et al., 2017; Nam et al., 2020).

Limitations and challenges VQA algorithm offers a good alternative to full quantum algorithm and many promising results have yet been shown theoretically and experimentally in this paradigm. Yet, theoretical limitations (so not considering device limitations and errors) have been demonstrated recently. The first one is the Barren Plateau (BP) (McClean et al., 2018). In this article, it has been shown that the expectation value of the gradient of the cost function decays exponentially to zero as a function of the number of qubits. This is true for Randomized Parameterized Quantum Circuit (RPQC) but also for a wide class of reasonable parameterized quantum circuits. As a result, the parameters landscape is essentially flat. Hence, in a BP, one needs an exponentially large precision to resolve against finite sampling noise and determine a cost-minimizing direction. This phenomenon is true for free-gradient methods (Arrasmith et al., 2021) and of course gradient-based methods. Even noise has been shown to be a source of BP regardless of the ansatz employed (S. Wang et al., 2021). This could annihilate any hope on the much anticipated quantum advantage, and methods to overcome this issue have to be found.

Other challenges remain, such as the expressibility of the ansatz (the capability of the parametrized quantum gates to explore all vector states of the Hilbert space) or the reachability (whether it is

easy to find a quantum state that minimize the cost function). Even the effects of noise are still studied today (Fontana et al., 2022; Gentini et al., 2020; Kübler et al., 2020).

VQA algorithms pave the way to reach a quantum advantage. Combining High-performance computing (HPC) and Quantum Processor Unit (QPU) is a hot topic, and this could help to overcome difficulties described above. One can also think of parallelization of quantum device, just as the start-up Welingq proposes (Welingq, 2022).

Many challenges remain but in the NISQ era, variational algorithms seem to be the most promising way to show that quantum computing can surpass most advanced classical methods in specific problems.

2.5.3 Quantum Annealing

Another possible approach with NISQ is the Quantum Annealing (QA) (Apolloni et al., 1990; Finnila et al., 1994; Kadowaki & Nishimori, 1998). The idea is to use quantum fluctuation to reach a specific state of a Hamiltonian. In practice, the Adiabatic Theorem (AT) is often used (Albasha & Lidar, 2018). Starting from a well-known eigenstate of a realizable Hamiltonian H_0 , one can slowly tune the parameters of the device to reach a more complicated Hamiltonian (the target Hamiltonian H_T). The adiabatic theorem stipulates that the state of the system at the end of annealing is (approximately) the corresponding eigenstate of the target Hamiltonian (the eigenstate with the same level of excited energy). For instance, if the system is in the groundstate of H_0 at the beginning, it will be in the groundstate of H_T at the end. If it starts in the first excited state of H_0 , it will end in the first excited state of H_T and so on for all eigenstates to the most excited state. Mathematically, a time-dependent parameter $s(t)$ is slowly tuned from 0 to 1

$$H(s) = s(t)H_T + (1 - s(t))H_0 \tag{2.62}$$

where $s(t = 0) = 0$ and $s(t = T_{\text{final}}) = 1$ and T_{final} is the final time of the procedure. QA has been performed with DQS on the D-Wave machine (Kairys et al., 2020). It attempts to solve problems in a particular form called Quadratic Unconstrained Binary Optimization (QUBO) with the Ising Hamiltonian (Lucas, 2014). However, no quantum advantage or speed-up over classical simulations have yet been found (Amin, 2015; Cho, 2014). AT is well suited for AQS if the problem can be translated into finding the groundstate of the resource Hamiltonian. A recent success of quantum annealing is with Rydberg Quantum Processor where an anti-ferromagnetic has been built up to 196 spins (or qubits) (Scholl et al., 2021) by dynamically tuning the parameters of the Hamiltonian quasi-adiabatically whereas numerical simulations struggle at calculating ground state of a quantum Ising Hamiltonian for more than 32 spins.

The adiabatic theorem is not really flexible in terms of problems that can be tackled, but if a solvable problem with this method is found, it can provide good results and a potential path towards a quantum advantage (see Sec. 5).

Conclusion on methods We have seen the limitations of full-quantum algorithm such as QPE on today’s device. Reaching a quantum advantage with the Shor algorithm is only conceivable in a distant future, hence, many other tools have been developed to run algorithms on NISQ computers. One of them are hybrid algorithms, which combine a quantum part with few gates and qubits and a classical part helping the quantum part to reach its target. Despite having theoretical challenges that remain, hybrid algorithms are the most promising way to solve real-world problems. Materials and chemistry simulation could help to find room temperature superconductor, new drugs, new materials are to anticipate materials aging. In the next section, I present modern methods to apply quantum computing to solve many-body physics problems.

2.6 Quantum computing for chemistry and many-body physics

2.6.1 From qubits to fermions

In atoms, electrons are assumed to be in a fixed potential created by nucleus (Born-Oppenheimer approximation). Therefore, we can describe them with a kinetic potential and the Coulomb interaction between electrons. In the second quantization, the electronic Hamiltonian is used to rewrite Eq. 2.2 as:

$$H = \sum_{p,q} h_{pq} a_p^\dagger a_q + \frac{1}{2} \sum_{p,q,r,s} h_{pqrs} a_p^\dagger a_q^\dagger a_r a_s. \quad (2.63)$$

where the coefficients h_{pq} and h_{pqrs} encode the spatial and spin configuration of each of the electrons and depend on the inter-nuclear and inter-electron distances \mathbf{R}, \mathbf{r} :

$$\begin{aligned} h_{pq} &= \int d\mathbf{x} \phi_p^*(\mathbf{x}) \left(-\frac{\nabla^2}{2} - \sum_i \frac{Z_i}{|\mathbf{R}_i - \mathbf{r}|} \right) \phi_q(\mathbf{x}) \\ h_{pqrs} &= \int d\mathbf{x}_1 d\mathbf{x}_2 \frac{\phi_p^*(\mathbf{x}_1) \phi_q^*(\mathbf{x}_2) \phi_r(\mathbf{x}_1) \phi_s(\mathbf{x}_2)}{|\mathbf{r}_1 - \mathbf{r}_2|}. \end{aligned} \quad (2.64)$$

Next, we map the fermionic a^\dagger operators acting on Fock states of n orbitals to a Hilbert space of operators acting on spin states of N qubits. This corresponds to the quantum processors' effective interaction Hamiltonians, quantum gates and measurement basis. In my work, I have studied VQA algorithms applied to electrons system and so on, fermions. As it is well-known, fermions follow the Pauli principle and fermionic wave-functions have to be antisymmetrized to respect this fundamental principle. Qubits (or spin) do not have the same statistics, and the corresponding states are not naturally antisymmetrized. Hopefully, several methods have been developed to map qubits to fermions and vice versa. Here, I describe the ones I have used during my PhD: the Jordan-Wigner transform (Jordan & Wigner, 1928) and the Bravyi-Kitaev transform (Bravyi & Kitaev, 2002). Let's consider a many-body electrons system. The annihilation c and creation c^\dagger operators follow an anticommutation rule $\{c_i, c_j^\dagger\} = \delta_{i,j}$. The system's Hamiltonian is written with this type of operator. For Pauli operators $\{S^i, S^j\} = 2\delta_{i,j}\mathcal{I}$ where i and $j \in \{0, x, y, z\}$ and, therefore, it is not easy to describe the target Hamiltonian in terms of Pauli operators. To alleviate this issue, Pascual Jordan and Eugene Wigner proposed the following transformation (Seeley et al., 2012)

$$\begin{aligned} c_1^\dagger &= (S^-) \otimes I \otimes I \cdots \otimes I \\ c_2^\dagger &= \sigma^z \otimes (S^-) \otimes I \otimes I \cdots \otimes I \\ &\vdots \\ c_n^\dagger &= \sigma^z \otimes \sigma^z \otimes \cdots \otimes \sigma^z \otimes (S^-). \end{aligned} \quad (2.65)$$

where $S^- = \frac{S^x + iS^y}{2}$ and $S^{-\dagger} = S^+ = \frac{S^x - iS^y}{2}$. Therefore, the relations

$$\{c_i, c_j^\dagger\} = \delta_{i,j}, \quad \{c_i, c_j\} = 0, \quad \{c_i^\dagger, c_j^\dagger\} = 0 \quad (2.66)$$

are well fulfilled. The main advantage of this mapping is its simplicity, but as a result, any fermionic operator becomes a Pauli string of N Pauli matrices, and we lost locality properties of the original Hamiltonian. It is therefore really hard to emulate such a Hamiltonian as $H_T \neq \sum_l H_l$. In addition, this transformation needs $O(N)$ operations on qubits to perform one fermionic operation. In JW transform, the occupation stays local but parity of the wave-function is delocalized.

The **parity** mapping is the exact inverse (Seeley et al., 2012). In this mapping, the parity is stored locally. The idea is to consider the occupation number basis state (fermionic state)

$|f_n, f_{n-1}, \dots, f_0\rangle$ (in the following, all sums of binary variables are taken modulo 2) and apply the transformation:

$$p_i = \sum_j [\pi_n]_{i,j} f_j \quad (2.67)$$

where n is the number of orbitals and π_n is upper triangular matrix:

$$[\pi_n]_{i,j} = 1 \text{ if } i < j, \quad [\pi_n]_{i,j} = 0 \text{ otherwise.} \quad (2.68)$$

Unlike the JW transform, one can not represent the creation and annihilation operators of a particle in an orbital j simply by applying S_j^\pm because one qubit does not store the occupation of an orbital. It is needed to look at qubit $(j-1)$. If the qubit $(j-1)$ is in the state $|0\rangle$, then it represents accurately the occupation orbital j and then one needs to apply S^+ to the parity basis to simulate a^\dagger on the fermionic basis. On the other hand, if the qubit $(j-1)$ is in the state $|1\rangle$, the qubit j inverts parity and the operator S^+ needs to be applied. The same reasoning applied for the annihilation operator. The equivalent of S^\pm in the parity basis is:

$$P_j^\pm = S_j^\pm \otimes |0\rangle \langle 0|_{j-1} - S_j^\mp \otimes |1\rangle \langle 1|_{j-1} = \frac{1}{2}(S_j^x \otimes Z_{j-1} \mp iS_j^y) \quad (2.69)$$

Furthermore, creating or annihilating a particle in orbital j implies a change in the parity data and we must update the cumulative sums for all $k > j$ by applying the operator S^x . It corresponds to add 1 to all qubits $k > j$ modulo 2.

At the end of the day, the creation and annihilation operators in the parity mapping are written:

$$\begin{aligned} a^\dagger &= S_n^x \otimes S_{n-1}^x \otimes \dots \otimes S_{j+1}^x \otimes P_j^+ \\ a &= S_n^x \otimes S_{n-1}^x \otimes \dots \otimes S_{j+1}^x \otimes P_j^-. \end{aligned} \quad (2.70)$$

As it is clearly seen, we just replaced the loss of locality with matrices Z in the JW transform with the loss of locality with matrices X in the parity basis. Thus, the total operation to apply on each qubit is still $O(N)$.

In the middle of both transforms, there is the Bravyi-Kitaev mapping (BK) (Bravyi & Kitaev, 2002). The idea is to store the parity and occupation non-locally. A qubit j stores the occupation only if j is even. If j is odd, the corresponding qubit holds a partial sum of the occupation set of orbitals less than index j . The transformation is quite complicated and I refer to (Seeley et al., 2012) for more details. What is important is the BK transform only needs $O(\log_2(N))$ transformation to go from fermions to qubits and therefore is the simplest transform from a digital circuit complexity point of view.

2.6.2 Unitary coupled cluster ansatz

The simplest approximation for a complete basis of Fock space for fermions is the set of Slater Determinants (Eq. 2.4). In other words, we approximate the eigenstates of the target Hamiltonian to be of the form:

$$|\psi\rangle = \prod_j (a_j^\dagger)^{\gamma_j} |00\dots 0\rangle \quad (2.71)$$

where $\gamma_j = 0, 1$ and a_j^\dagger creates a particle in the orbital j . The corresponding state with the JW transform is

$$|\psi\rangle_{\text{JW}} = \prod_j (S_j^x)^{\gamma_j} |00\dots 0\rangle \quad (2.72)$$

Usually, the method to generate Slater determinants is the Thouless algorithm (Thouless, 1960). Starting from a Slater determinant $|\psi_0\rangle$ one can generate an ensemble of new determinants given by (GOOGLE AI QUANTUM AND COLLABORATORS et al., 2020):

$$|\psi(Z)\rangle = e^{i \sum_{i,j} Z_{i,j} a_i^\dagger a_j} |\psi_0\rangle \quad (2.73)$$

where Z is hermitian. In VQA algorithms (GOOGLE AI QUANTUM AND COLLABORATORS et al., 2020), this matrix is optimized with a PQC to minimize $\langle \psi_Z | H_T | \psi_Z \rangle$.

Thus far, we did not take into account correlations which are at the heart of the goal of quantum computing. Starting from the Thouless algorithm, one can extend it to gradually insert excitation into the system. This is the Unitary Coupled Cluster (UCC) ansatz.

It is constructed from a parametrized cluster operator $T(\theta)$ which is a sum of particle-hole excitations of different orders:

$$\begin{aligned} T(\theta) &= T^1(\theta) + T^2(\theta) + \dots \\ T^1(\theta) &= \sum_{i,j} \theta_{i,j} a_i^\dagger a_j \\ T^2(\theta) &= \sum_{i,jkl} \theta_{i,jkl} a_i^\dagger a_j^\dagger a_k a_l. \end{aligned} \tag{2.74}$$

The sum is truncated due to the decrease impact of higher order terms.

The ansatz of the PQC is then:

$$|\psi(\theta)\rangle = e^{(T(\theta) - T^\dagger(\theta))} |\psi_{\text{init}}\rangle. \tag{2.75}$$

UCCSD refers to the truncation after the double excitation and *UCCSDT* to the truncation after the triple excitation. The next step is transforming the operators T into qubits operators with methods describe in Sec. 2.6.1. Finally, the Trotter decomposition can be used to decompose $e^{T(\theta) - T^\dagger(\theta)}$ into a sequence of gates. This method is very well suited for DQS.

This method is quite old and has been proposed decades ago (Helgaker et al., 2000) and has been consequently widely applied. A good summary of implementations of the UCC ansatz can be found in (Anand et al., 2022). These problems often concern small molecules, as this method is still benchmarked on NISQ computers.

Thus far, we only discussed the quantum part of the algorithm and how to leverage it for molecular and fermionic many-body problems but the problem can be directly simplified with chemistry and theoretical simplifications. For instance, molecular wave-functions in Eq. 2.64 have to be chosen. They often constructed from linear combinations of atomic orbitals, themselves considered as linear combination of Gaussian functions (STO-NG) basis. The more common ones are the STO-3G (for three gaussians) or STO-6G (for six gaussians) (Hehre et al., 2003). Therefore, choosing 3 or 6 functions can reduce or increase the complexity of the target Hamiltonian and thus, the efficiency of the VQA algorithm. But in the other hand, choosing a more accurate representation of orbitals leads to a better description of correlations in molecules or materials. The difficulty lies in finding the balance between chemical accuracy and VQA efficiency. In addition, some low energy orbitals can be considered as "frozen" whereas high energy orbitals can be considered as unoccupied just as in (Hempel et al., 2018) where they only focused on a subspace of the orbitals in the lithium molecule. With all these approximations, they reduced the target Hamiltonian from 12 qubits and 200 Pauli strings to an effective Hamiltonian of only 3 qubits and 13 Pauli strings.

In conclusion, efforts have to be done in optimizing the quantum algorithm but also in the chemistry side where approximations are really important to simplify the problem.

2.7 Conclusion

Simulating matters at atomic scale is at the center of much research since the advent of computing. It enables to anticipate the behavior of complex system and even creating new materials. Several methods (DFT, DMFT, QMC) have encountered great successes and are used all around the world for fundamental physics or applications. Recently, a new approach has emerged to help or even surpass these "classical" approaches: the quantum computing. Many methods theoretically exist to provide a quantum advantage on a quantum computer. Yet, noiseless computers with

thousands of logical qubits and high fidelity gates do not exist and it is not even sure they will one day. What do exist today are NISQ device, with experimental proofs of their utility. Therefore, hybrid methods such as VQA have been developed to show a quantum advantage on these devices. There have been some successes but also failures with the discovery of Barren Plateau for instance. Today, a real quantum advantage on important problems for the society has not been found. The field of quantum computing is an experimental and theoretical exploration where industrial giants are involved with the promise to revolutionize the world and many architectures have their pros and cons. Among this emulation, one technology has proven a quantum advantage in theoretical physics problems: the neutral atoms (or Rydberg Quantum Processor RQP) (Browaeys & Lahaye, 2020). Groundbreaking results have emerged from this technology, considering digital (Cong et al., 2022; Evered et al., 2023; Kalinowski et al., 2023) or analog (Chen et al., 2023; Scholl et al., 2022; Scholl et al., 2021) quantum computing. RQP is one of the best candidates to simulate many-body physics. Regarding the goal of my PhD to perform quantum simulation of fermionic many-body physics, it has appeared to me that RQP is an excellent candidate to get closer to a quantum advantage in this field and, most importantly, being able to implement my algorithms on a real device soon.

Chapter 3

Quantum simulation with Rydberg atoms

3.1 Forewords

In this chapter, I give an overview of the experimental apparatus of the Rydberg Quantum Processor (RQP) (first section) and the protocol to perform digital and analog quantum computing (second section). Most of the contents of are adapted from (Browaeys & Lahaye, 2020; Henriet et al., 2020; Scholl, 2021).

3.2 Neutral atom arrays

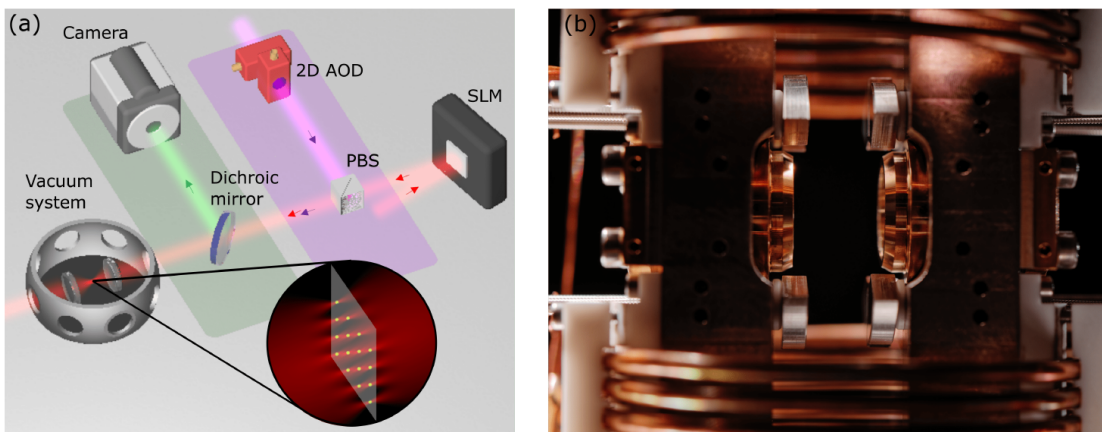


Figure 3.1: (a) Schematic representation of the main hardware components constituting the RQP. In red, the trapping laser is modulated by the Spatial Light Modulator (SLM) to produce microtraps *i.e.* optical tweezers with the geometry desired (see inset). In purple, the moving tweezers allow reorganizing the atoms after the first fluorescence picture. They are controlled by a 2D acousto-optic laser beam deflector (AOD). In green, the fluorescence light is captured by a camera to obtain a bitstring. (b) Picture of the heart of experimental apparatus. The register is prepared at the center of the photography. Taken from (Henriet et al., 2020).

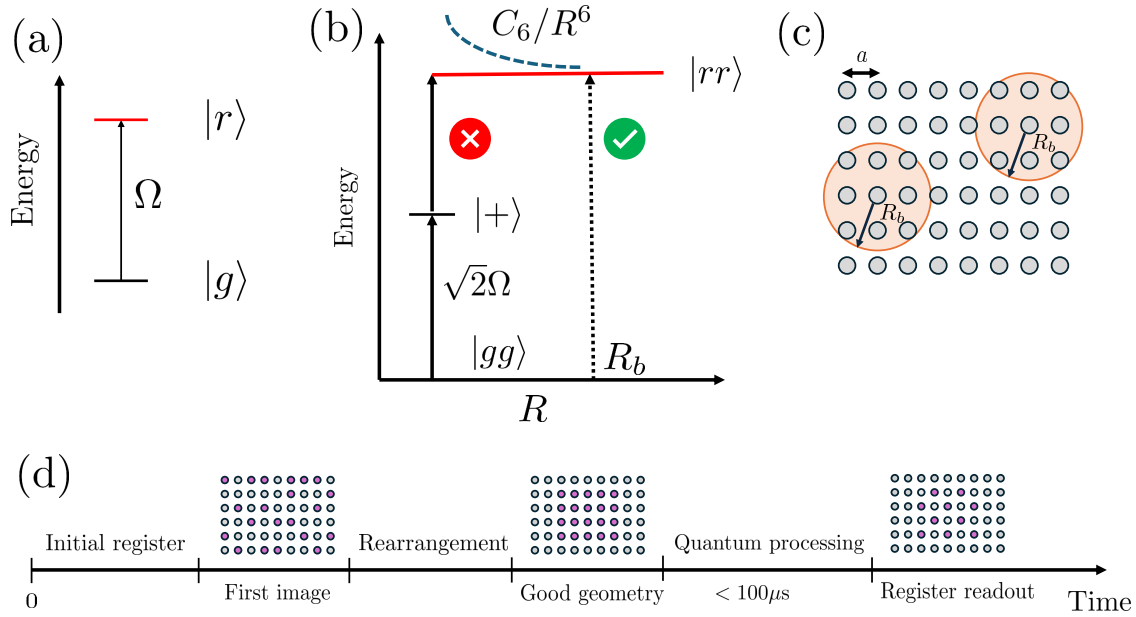


Figure 3.2: *The Rydberg blockade and computation cycle* (a) The two chosen electronic states of atoms are coupled via the Rabi frequency Ω . (b) Two atoms separated by a distance $R < R_b$ are only coupled to the state $|+\rangle = (|rg\rangle + |gr\rangle)/\sqrt{2}$ and not $|rr\rangle$. If the distance is greater than R_b , the state $|rr\rangle$ is accessible. (c) Graphical representation of Rydberg blockade. A regular array with spacing a is created with the SLM, each of the atoms prevent the atoms in the circle of radius R_b from its center to be in the state $|r\rangle$ with it. (d) Temporal sequence of one computational cycle. The register is initialized with atoms trapped in a tweezer with a probability $1/2$. The atoms are then rearranged in the desired geometry. The quantum processing can now start and the cycle end with a picture of atoms: the register readout. All the process has to be done again for each measurement. The three first figures are inspired from Fig. B1 of (Browaeys & Lahaye, 2020) and the last figure is inspired from Fig. 5B of (Henriet et al., 2020).

3.2.1 Initial state preparation

Quantum computing is by definition the manipulation of individual quantum objects (qubits) by experimental techniques. Quantum objects can take various forms such as gazes, dots, ions, photons, Josephson junctions and atoms. Until the end of the 1900s, controlling qubits with enough precision to entangle and apply logic operations on them was still a theoretical idea. Today, many platforms are able to control up to several hundreds of qubit at the same time and thus, give a hope to simulate quantum systems better than classical methods. RQP is based on ensembles of individual atoms trapped in optical lattices. In this section, I give an overview of breakthrough methods which have led to being able to manipulates hundreds of neutral atoms individually and make them interact.

RQP is fully controlled by light, from the state preparation and the set-up of the register to the quantum processing part and finally to readout the register. Each step needs different type of lights with different wavelengths and power. At the same time, electronic components and software stack monitor steps like rearranging atom tweezers or tune the magnitude of lasers achieving desired Hamiltonian. The first step to generate arrays of neutral atoms is to prepare a diluted atomic vapor inside an ultra-high vacuum system (to isolate atoms from the environment). To do so, one gram of solid rubidium (Rb) is heated up in an oven to transform it into a vapor. Contrary to other architectures such as superconductors, the device operates at room-temperature, leveraging the

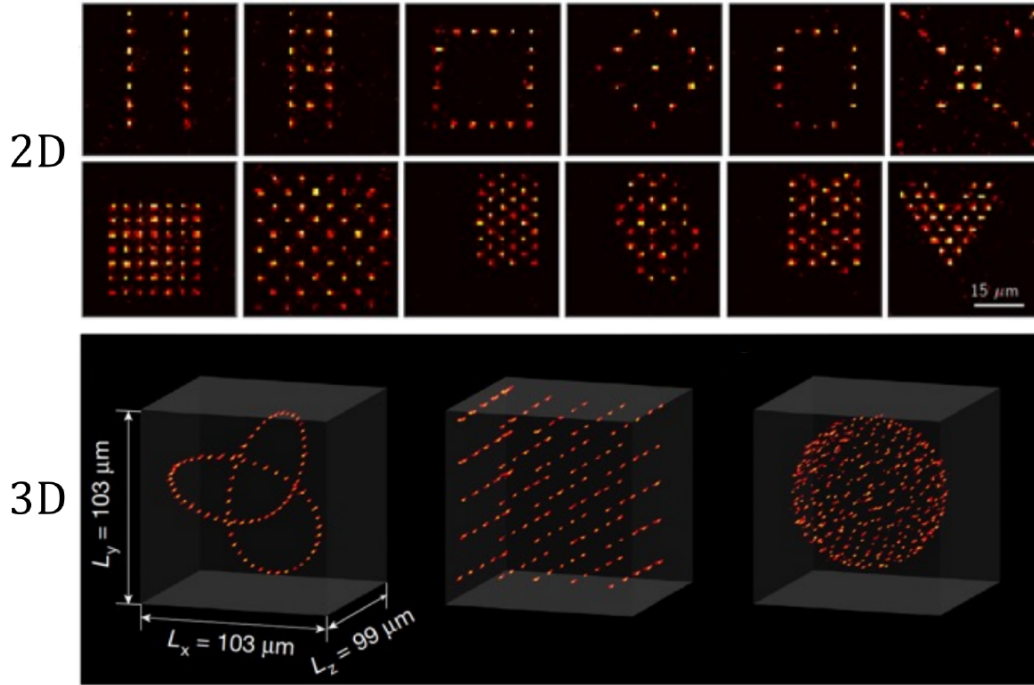


Figure 3.3: Examples of geometry in 2D and 3D experimentally feasible. Taken from (Barredo et al., 2018).

complications of a cooling system. At the output of the oven, atoms are slowed down to reach ≈ 10 m/s. The atoms of gas are then trapped inside a 3D magneto-optical trap (3D MOT). These atoms are the reservoir to a second trapping laser system which isolates each individual atoms, the so-called optical tweezers (Schlosser et al., 2001). Two very useful characteristics of optical tweezer can be pointed out: at first, each tweezer contains at most 1 atom. This is ensured by the very fast light-assisted collision which happens if two atoms are in the trap. The number of tweezers and their arrangement in the 2D or 3D space is controlled by a Spatial Light Modulator (SLM) (Nogrette et al., 2014) which is a "mask" that modulates the phase of the light into a desired intensity pattern (see Fig. 3.3). A strong asset of RQP is to fully control the geometry of the array and therefore connectivity between atoms (more details in the next section, Sec. 3.2.2). Nevertheless, the occupation of a trap is not deterministic: this means that a trap is filled with one atom with a probability of $p \sim 0.5$. To palliate this issue, a picture of atoms is taken by looking at their fluorescence and tweezers are moved one by one to arrange atoms in the desired way. This procedure has a success rate of 99% and takes few tens of milliseconds. This is enabled by an algorithm calculating the optimal moves for each tweezer from the first picture. After all of this, the register is ready for the quantum processing. A schematic representation of the experimental apparatus is shown in Fig. 3.1 with also a picture of the heart of the device.

3.2.2 Generating spin-spin interactions

In this subsection, I describe the physics behind the QRP and the tunable Hamiltonians that can be simulated thanks to this physics. In order to perform quantum computing, atoms have to interact. To this aim, two electronic states are chosen to be the qubit $|0\rangle$ and $|1\rangle$: the groundstate and a high excited state of the atoms. A key asset of Rydberg atoms for quantum computing is the Rydberg blockade (Saffman et al., 2010). The strong van der Waals interactions between two

atoms in the Rydberg state can be used to prevent simultaneous excitations of two atoms. In an isolated atom, a laser field is coupling the ground state and the Rydberg state of an atom with a Rabi frequency, Ω Fig. 3.2(a). In the case of two atoms separated by a distance R , they undergo a van der Waals interaction for the state $|rr\rangle$ and therefore there is a shift in energy by the quantity C_6/R^6 to reach this state. Thus, one can define the blockade radius defined by:

$$R_b = (C_6/\hbar\Omega)^{1/6}. \quad (3.1)$$

If the blockade condition is fulfilled $\hbar\Omega \ll C_6/R^6$ *i.e.* $R \ll R_b$, the state $|rr\rangle$ is non-resonant and the two atoms evolve from the state $|gg\rangle$ to the state $|+\rangle = (|rg\rangle + |gr\rangle)/\sqrt{2}$ with a coupling $\sqrt{2}\Omega$ Fig. 3.2(b). More precisely, it will oscillate between these two states at a frequency of $\sqrt{2}\Omega$, this is a Rabi oscillation. Depending on the geometry, it is possible to bring N atoms to a fully entangled state $\sum_{i=1}^N |gg \dots r_i \dots g\rangle / \sqrt{N}$. If the system size is bigger than the Rydberg radius, some atoms can be excited and some not, leading to complex many-body states interesting for quantum simulation. Mathematically, the Rydberg blockade is written:

$$\sum_{i,j} \frac{C_6}{R_{i,j}^6} n_i n_j \quad (3.2)$$

where $n_i = (1 + Z_i)/2$. There is a second way to make atom interact. To do, two Rydberg states are chosen to be state $|g\rangle$ and $|r\rangle$. These two states are dipole-coupled and separated by a transition of typically 10 GHz. The dipole-dipole interaction leads to a coherent exchange between the two Rydberg states. Contrary to van der Waals interaction, this scales like C_3/R^3 (Barredo et al., 2015; Orioli et al., 2018). In addition, $C_3 \propto 1 - 3\cos^2\theta$ where θ is the angle of the separation between the two atoms. Physically, the atoms reproduce a "XY" interaction, which is described by:

$$\sum_{i,j} \frac{C_3}{R_{i,j}^3} (S_i^+ S_j^- + S_i^- S_j^+) = 2 \sum_{i,j} \frac{C_3}{R_{i,j}^3} (S_i^x S_j^x + S_i^y S_j^y) \quad (3.3)$$

These two interactions (van der Waals and dipole-dipole) are the building blocks of quantum computing with RQP. Indeed, they depend on the distance between atoms, and they can bring entanglement in the system. As a result, depending on the geometry we choose, one can generate very complex many-body states. More details about Hamiltonian one can generate with this device will be given in Sec. 3.3.2.

The quantum processing is quite quick ($< 100 \mu\text{s}$) compared to the whole process which lasts around 200 ms. After having done the quantum process, one needs to extract information on the system with a measurement.

3.2.3 Register readout

The last part of a quantum algorithm is the measurement of the system state. As we have seen before, it is crucial to optimize this step because it is the moment we extract the information from all the quantum processing sequence. In the RQP, it is quite "easy" because it only involves taking a final fluorescence image. Indeed, atoms in the state $|g\rangle$ will appear dark in the image, whereas atoms in the excited Rydberg state $|r\rangle$ will appear bright (see Fig.3.2(d)). The efficiency of this method is of 98.6% or more as reported in (Fuhrmanek et al., 2011). One obtains a bit string from the readout register. After the measurement, all the process of register preparation, quantum processing and register readout has to be done again to obtain another bit string. As the total process takes $\approx 200 - 300$ ms, the device rate is of $2 - 3$ Hz and one can obtain several hundred measurements in a few minutes. In the next section, we see how one can perform quantum simulation and computing with this device and the possible applications.

3.3 Quantum simulation

The quantum processing part is the one which changes depending on the problems and the algorithm we implement. In this section, I will describe how to perform digital and analog quantum simulation on a RQP and the possibilities the platform can offer in these two paradigms.

3.3.1 Digital quantum simulation

DQS needs a great quantum coherence to work, *i.e.* with the minimum of interaction with the environment. In addition, it has to be possible to perform at least single-qubit rotations and CNOT gates to be able to generate a universal gate set (Nielsen & Chuang, 2011). Hopefully, RQP is able to perform these gates.

The first point is ensured by taken qubit $|0\rangle$ and $|1\rangle$ as the two hyperfine groundstates $F = 1$ and $F = 2$ of the rubidium atom. Indeed, they both have a very long lifetime (several years) and it therefore avoids quantum decoherence. This means that Rydberg states $|r\rangle$ are only intermediate states to perform gates, whereas they are used for the Rydberg blockade effect. Arbitrary rotation around the Bloch sphere can be performed by driving the qubit transition with a control field (Bluvstein et al., 2021; Yavuz et al., 2006). The laser-atoms interaction is characterized by the Rabi frequency Ω , the detuning δ and its phase ϕ . I will not go into experimental details, but these parameters are driven to perform rotations around (x, y, z) axis with angles $(\tau\Omega \cos \phi, \tau\Omega \sin \phi, \tau\delta)$ with τ the duration of the controlled sequence. Thus, any rotation around the Bloch sphere can be performed by controlling these four parameters. For instance, a pulse of area equal to π where $\delta = 0$ will lead to a change $|0\rangle \rightarrow |1\rangle$. The same pulse on $|1\rangle$ will lead to $|0\rangle$ (the phase here is not important). This is the NOT gate:

$$\text{NOT} = \begin{pmatrix} 0 & 1 \\ 1 & 0 \end{pmatrix} \quad (3.4)$$

It corresponds to half a Rabi oscillation and will also be called a π pulse. The Hadamard gate is performed by a π pulse but where $\delta = \Omega$ and the phase $\phi = 0$. The fidelity of single-qubit gates is more than 99.5%.

In order to perform a CNOT gate, one must decompose it into tensor products of Hadamard and CZ gates (Fig. 3.4) because CZ gates are implementable with a specific sequence.

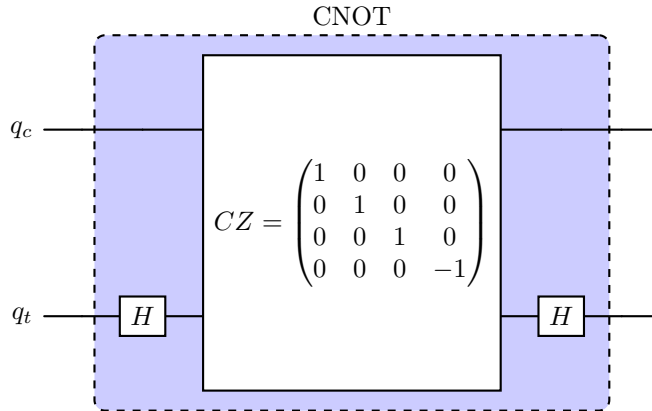


Figure 3.4: Decomposition of the CNOT gate into tensor product of Hadamard and CZ gates.

We consider two atoms in the state $|0\rangle$ or $|1\rangle$. We consider that the state $|1\rangle$ is coupled with the state $|r\rangle$ whereas the state $|0\rangle$ is not. Finally, they are separated by a distance such that the Rydberg blockade condition is fulfilled. The protocol is then the following:

- A π pulse is applied to the control atom with a controlled phase.

- Then, a 2π pulse is applied to the target atom.
- Finally, a π pulse is applied on the control atom again.

Therefore, if the state is $|00\rangle$, these states are off-resonant and the state remains the same.

If the state is $|10\rangle$ or $|01\rangle$, only the qubit in the state $|1\rangle$ will undergo a 2π pulse with a phase $e^{i\pi} = -1$. If the state is $|11\rangle$, the first pulse will bring the control atom to the state $|r\rangle$ and because of the Rydberg blockade, the state $|r\rangle$ is off resonant for the target atom, and it stays in the state $|1\rangle$ after the 2π pulse. Finally, the last π pulse swaps the state of the control atom to $|0\rangle$ again. The whole state picks up a factor $e^{i\pi} = -1$.

Finally, we have applied the gate:

$$\begin{pmatrix} -1 & 0 & 0 & 0 \\ 0 & -1 & 0 & 0 \\ 0 & 0 & -1 & 0 \\ 0 & 0 & 0 & 1 \end{pmatrix} = e^{i\pi} CZ \quad (3.5)$$

which is the CZ gate up to a phase. We will call this method the H – CZCNOT method following (Isenhower et al., 2010). Other protocols can be used to generate a CNOT gate (Isenhower et al., 2010). For a long time, the measured fidelity of the CNOT gate built this way was the major issue (94.1% in 2018 (Levine et al., 2018)) but recently, the Lukin’s group has shown a fidelity of 99.5% on up to 60 atoms in parallel, surpassing the surface code threshold for error correction (Evered et al., 2023) (see also Fig. 3.5). Theoretically, achieving error correction is also at the center of interest for gates with RQP (Jandura et al., 2023; S. Ma et al., 2023). The high connectivity of Rydberg atoms and the growing fidelity of entangling gates pave the way toward digital quantum computing on a Rydberg device.

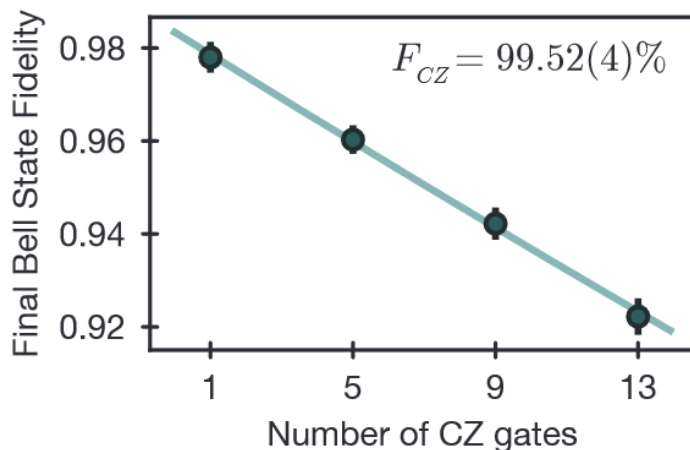


Figure 3.5: Fidelity of Bell’s state as a function of number of CZ gates. Error bars represent 68% confidence intervals. Taken from (Evered et al., 2023).

3.3.2 Analog quantum simulation

Neutral atoms arrays are mostly known for their results as analog quantum processor. Actually, it is possible to implement the Ising model by combining the van der Waals interaction and the tunable parameters: the Rabi frequency and the detuning. The resulting time-dependent Hamiltonian

realized is (following the notation of (Henriet et al., 2020)):

$$H_{\text{Rydberg}} = \sum_{i \neq j} \frac{C_6}{|\mathbf{r}_i - \mathbf{r}_j|^6} n_i n_j + \frac{\hbar \Omega(\tau)}{2} \sum_i S_i^x - \hbar \delta(\tau) \sum_i n_i \quad (3.6)$$

with τ the time. In practice, the Rabi frequency and the detuning are driven by a magnetic field (Ω is proportional to the transverse component whereas δ depends on the longitudinal component). The Ising Hamiltonian is the "toy" model to study magnetism and can help to tackle many problems from condensed matter, materials, chemistry to optimization problems for instance (Lucas, 2014). Recently, a "quantum advantage" of many-body problems has been demonstrated with the Ising model. An antiferromagnetic state is constructed from a parameters sequence with more than 200 spins/qubits (Scholl et al., 2021) (See Fig. 3.6). Moreover, different phases of matter have been explored in (Ebadi et al., 2021) with this Hamiltonian on 256-atom programmable quantum simulator.

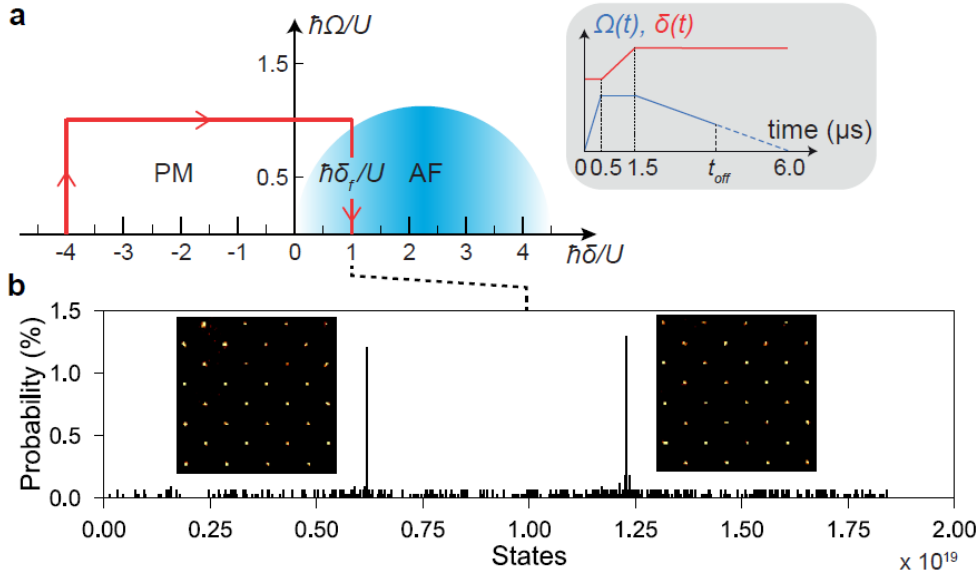


Figure 3.6: (a) Phase diagram of the Rabi frequency and the detuning to reach an antiferromagnetic state superposition. (b) State histogram for an 8×8 array at the end of the procedure. Antiferromagnetic states have a probability to be measured of 2.5% among more than 10^9 states possible. Taken from (Scholl et al., 2021).

In addition, one can use the dipole-dipole interaction to implement the "XY" Hamiltonian (following notation of (Henriet et al., 2020)):

$$H = \frac{\hbar}{2} \Omega \sum_j S_j^x - \frac{\hbar}{2} \delta \sum_j S_j^z + 2 \sum_{i \neq j} \frac{C_3}{r_{i,j}^3} (S_i^x S_j^x + S_i^y S_j^y). \quad (3.7)$$

This Hamiltonian is another "simple" model to study magnetism in systems such that frustrated quantum magnets (Balents, 2010) or topological materials (de Léséleuc et al., 2019). In both cases, many applications are possible in the field of materials or chemistry but also in optimization, machine learning and so on. In addition, combining cleverly the capacity to drive the parameters and choose the geometry can lead to create effective XXZ models (Signoles et al., 2021) or non-spin conserving terms (Whitlock et al., 2017).

AQS is a strong asset of the RQP with results showing a "quantum advantage" over classical simulation for a specific theoretical physics problem (Nielsen & Chuang, 2011; Scholl, 2021). The Rabi frequency and the detuning being driven through time, it is possible to implement VQA with AQS where Ω, δ and τ are the parameters (see Sec. 4 for an example). Eventually, if the problem can be mapped into finding the groundstate of exactly Eq. 3.6 or Eq. 3.7, one can directly use the adiabatic theorem. Starting from a state which is the known ground state of a realizable Hamiltonian (for instance, the groundstate of Eq. 3.6 for $\Omega = 0$ and $\delta \ll -|C_6|/R^6$, the groundstate is $|00\dots 0\rangle$ meaning that all atoms are in their electronic groundstate), one can tune the parameters slowly to reach (approximately) the many-body groundstate of the Ising Hamiltonian with the desired parameters. The same protocol applied for the XY Hamiltonian. This method is more efficient than VQA because measurements do not have to be repeated to feed a classical optimizer, the measurements are directly useful to get the groundstate.

3.4 Conclusion

RQP is based on a well established technology allowing to perform digital and analog quantum simulation. The whole process of quantum computing is enabled and fully optimized by light control, electronic components and software stacks. The Hamiltonians and gates implementable benefits from the good coherence time of Rydberg states (in the order of a hundred of microseconds) and the wide space of the parameters Ω and δ can explore. The device rate is between 2 – 3 Hz (sometime it can go to 5 Hz): it means that one can obtain "only" 2 – 3 bitstrings per second. The information is important if one wants to design an algorithm which can be experimentally implementable and only needs to run during a few days. RQP is a NISQ device and, therefore, is limited by several sources of noise. During my PhD, I tried to take into account all advantages but also limitations of the device to extract the full potential of it. For instance, in Chap. 4, the total number of measurements or shots is the criteria to stop the variational procedure whereas in Chap. 5, most source of noise are described and implemented to test the robustness of the algorithm.

Chapter 4

Digital-analog variational quantum eigensolver for chemistry

4.1 Forewords

This chapter contains exactly my first publication available on arxiv and published in *Physical Review A* (Michel, Grijalva, et al., 2023). It is the result of the first half of my PhD work. It has resulted from a strong collaboration with the start-up PASQAL and all simulations are performed with the python library pulser (Silvério et al., 2022). In this chapter, I propose a new digital-analog variational algorithm to find groundstate of molecules on a Rydberg atom device and show numerically the result on H_2 , LiH and BeH_2 molecules. To this aim, we take into account characteristics of the platform to optimize the VQA algorithm and increase its efficiency. We propose a complete protocol from the register preparation to a measurement method. The stopping criteria of the algorithm is the number of measurements to fulfill feasible experiment today.

4.2 Introduction

Quantum simulation holds the promises to solve outstanding questions in many-body physics, in particular finding the ground state of strongly interacting quantum systems (Georgescu et al., 2014; McClean et al., 2016). The determination of the ground state energies of complex molecules, one of the main tasks in quantum chemistry, is therefore an example of application where quantum simulation could be of interest. Along this line, proof-of-principle demonstrations were obtained using photons (Lanyon et al., 2010; Peruzzo et al., 2013), ions (Hempel et al., 2018; Shen et al., 2017) or quantum circuits (Kandala et al., 2017). The last two examples used a hybrid approach where a classical computer optimizes in an iterative way the results obtained by a quantum device that was operating in a digital mode, *i.e.* as a series of one and two-qubit gates.

Rydberg quantum simulators are another example of promising quantum simulation platforms, thanks to their potential for scaling the number of qubits and their programmability (Browaeys & Lahaye, 2020). They rely on individual atoms trapped in arrays of optical tweezers that can interact when promoted to Rydberg states. The platform naturally implements spin Hamiltonians. Analog quantum simulation with hundreds of atoms has now been achieved (Chen et al., 2023; Ebadi et al., 2022; Scholl et al., 2021).

One appealing feature of this platform is the ability to place the atoms in arbitrary position in two and three dimensions, thus allowing large flexibility in their connectivity. Another feature is their ability to prepare different initial product states as heuristic trials before the unitary evolution (whether it is by a set of digital gates or the action of an analog Hamiltonian evolution). However,

this freedom in register preparation has a significant time cost that adds to the repetition clock rate (Henriet et al., 2020).

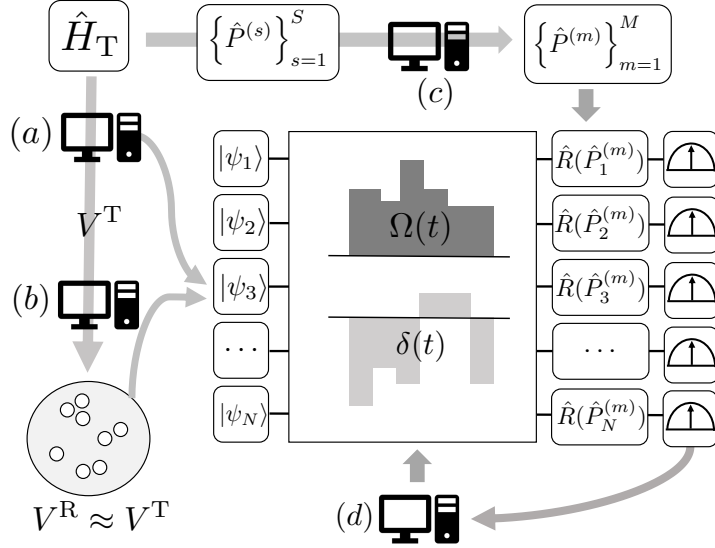


Figure 4.1: Digital-Analog VQE on Rydberg atoms studied in this paper. The computer icons indicate where classical processing enhances and informs the cycle. First, a target molecular Hamiltonian H_T is passed to computer (a). This computer extracts a subset of terms that define a target interaction matrix V^T . Computer (b) then optimizes atom positions (with interaction matrix V^R) to approximate V^T . With a chosen register, computer (a) tests virtually some product states that can be experimentally implemented, warm-starting the algorithm. Meanwhile, computer (c) takes the Pauli strings $\{\hat{P}^{(s)}\}$ that constitute H_T and outputs a *derandomized* set of Pauli measurement basis $\{\hat{R}(\hat{P}^{(m)})\}$ that will be used at the end of the circuit where the prepared state is measured in the Z -axis. A parameterized pulse acts on the initial state, and the readout data is used by computer (d) to estimate the expectation value of the target Hamiltonian $\langle H_T \rangle$. Finally, computer (d) calculates new pulse parameters to update the quantum evolution. When a desired precision or some stopping criteria is reached, the best energy value is returned.

Neutral atom devices are naturally suited for *analog quantum algorithms*, where the analog blocks are represented by control pulses that drive the system (or subsets of it). Given a prepared state, the parameterized pulses can be adjusted to variationally improve on a given score of the state. Methods for the optimization of parameters have been the subject of intense exploration in recent years (Banchi & Crooks, 2021; Barkoutsos et al., 2020; Cerezo, Sone, et al., 2021; Cerezo et al., 2020; Gacon et al., 2021; McClean et al., 2016, 2018; Meitei et al., 2021; Piskor et al., 2022; Wakaura et al., 2021; Wecker et al., 2015). Additionally, the information and “cost functions” from the prepared quantum system are obtained by repeatedly measuring the state in the computational basis, which constitutes an operational overhead. Recent results (Dalyac et al., 2020; Ebadi et al., 2022; Elben et al., 2019; H.-Y. Huang et al., 2021; Kokail et al., 2019; Nam et al., 2020) on

protocols for the estimation of quantum observables are available and have helped to establish efficient measurement procedures based on generalized random measurements and a series of post-processing steps that are performed on a classical computer and that alleviate the measurement overhead. The types of randomized measurements that we shall describe in this paper require local rotations on the qubits of the register, thus constituting another “digital” layer, from a quantum circuit perspective. In fact, *digital-analog* algorithms (Parra-Rodriguez et al., 2020), benefit from the fact that analog operations can be performed with much higher fidelities than when using digital gates, while local single-qubit gates can be added explicitly in crucial steps of the process (state preparation and measurement).

In this paper, we explore the implementation of a digital-analog VQE algorithm in a Rydberg quantum simulator. We account for typical constraints of the platform: the local action is restrained to the initial state preparation and measurement, with Hamiltonian time-evolution acting on the entire system as a “global” gate. We study numerically this version of a VQE for the H_2 molecule using common ansatz, followed by a more efficient protocol for larger molecules. We discuss the embedding of the Hamiltonian in the atom register, the way in which the optimization of the pulse sequence can be performed and the necessity of including an efficient estimation of energies (namely, we explore the effect of a *derandomization* estimation (H.-Y. Huang et al., 2021)) at each iteration step. We apply this numerically to the examples of LiH and BeH_2 . The manuscript is organized as follows: In section II we recall how the Variational Quantum Eigensolver (VQE) estimates the energy of the ground state of a molecular-based Hamiltonian. We then describe the basic ingredients of Rydberg Atom Quantum Processors and the Hamiltonians that they implement. We end the section by explaining the optimization cycle of variational quantum algorithms on these devices. In section III we describe the strategies for implementation of the VQE, going from a direct application of a Unitary Couple Cluster Ansatz, to the Quantum Alternating Operator ansatz and finally to a more hardware-oriented approach that combines elements of register preparation, pulse optimization and observable estimation. This is followed in section IV by numerical results of the error in energy obtained as a function of the number of repetitions of the experiment, an informative measure of the performance of hybrid classical-quantum implementations.

4.3 Analog Variational Quantum Eigensolver with Rydberg atoms

The Variational Quantum Eigensolver (or VQE) is a hybrid quantum-classical algorithm designed to find the lowest eigenvalue of a given Hamiltonian (Fedorov et al., 2022). We describe below the origin of the Hamiltonians that we consider and how VQE can be studied with a Rydberg Quantum Processor.

4.3.1 Hamiltonians from Quantum Computational Chemistry

We first recall the method used to express the electronic Hamiltonian as a spin model (see e.g. (Hempel et al., 2018)). We start from the Born-Oppenheimer approximation of the Hamiltonian of the system, which considers the nuclei of the molecules as classical point charges:

$$H = -\sum_i \frac{\nabla_i^2}{2} - \sum_{i,I} \frac{Z_I}{|\mathbf{r}_i - \mathbf{R}_I|} + \frac{1}{2} \sum_{i \neq j} \frac{1}{|\mathbf{r}_i - \mathbf{r}_j|} \quad (4.1)$$

(in atomic units) where ∇_i is the kinetic energy term for the i -th electron, Z_I is the charge of the I -th nucleus, and \mathbf{r} , \mathbf{R} denote the distance of the i -th electron and the I -th nucleus with respect to the center of mass, respectively. We aim to obtain the ground state energy of (4.1).

One needs to define a basis set in which to represent the electronic wavefunctions. We shall concentrate on the Slater-type orbital approximation for the basis set, with three Gaussian functions, STO-3G. This minimal basis set $\{\phi_i(\mathbf{x}_i)\}$ (where $\mathbf{x}_i = (\mathbf{r}_i, \sigma_i)$ encodes the i -th electron's spatial and spin coordinates) includes the necessary orbitals to represent the valence shell of an atom. Moreover, the wavefunctions need to be anti-symmetric under the exchange of electrons. This can be achieved through *second quantization*, where one defines anticommuting fermionic creation/annihilation operators $\{a_p^\dagger\}, \{a_p\}$ and rewrites the initial Slater determinant form of the wavefunction as $|\Psi\rangle = \prod_p (a_p^\dagger)^{\phi_p} |\text{vacuum}\rangle$, representing the occupation of each molecular orbital.

The fermionic operators are used to rewrite (4.1) as:

$$H = \sum_{p,q} h_{pq} a_p^\dagger a_q + \frac{1}{2} \sum_{p,q,r,s} h_{pqrs} a_p^\dagger a_q^\dagger a_s a_r. \quad (4.2)$$

where the coefficients h_{pq} and h_{pqrs} encode the spatial and spin configuration of each of the electrons and depend on the inter-nuclear and inter-electron distances \mathbf{R}, \mathbf{r} :

$$\begin{aligned} h_{pq} &= \int d\mathbf{x} \phi_p^*(\mathbf{x}) \left(-\frac{\nabla^2}{2} - \sum_i \frac{Z_i}{|\mathbf{R}_i - \mathbf{r}|} \right) \phi_q(\mathbf{x}) \\ h_{pqrs} &= \int d\mathbf{x}_1 d\mathbf{x}_2 \frac{\phi_p^*(\mathbf{x}_1) \phi_q^*(\mathbf{x}_2) \phi_r(\mathbf{x}_1) \phi_s(\mathbf{x}_2)}{|\mathbf{r}_1 - \mathbf{r}_2|}. \end{aligned} \quad (4.3)$$

Next, we map the fermionic operators acting on Fock states of n orbitals to a Hilbert space of operators acting on spin states of N qubits. This corresponds to the quantum processors' effective interaction Hamiltonians, quantum gates and measurement basis. Useful maps of this kind include the Jordan-Wigner (JW) (Jordan & Wigner, 1928) or the Bravyi-Kitaev (BK) (Bravyi & Kitaev, 2002) transformations. The obtained Hamiltonian is a sum of tensor products of single-qubit Pauli matrices:

$$H_T = \sum_{s=1}^S \mathbf{c}_s \left(\bigotimes_{j=1}^N S_j^{(s)} \right) \quad (4.4)$$

where $S_j \in \{\mathbb{1}, S^z, S^y, S^x\}$, S is the number of Pauli strings in the Hamiltonian and N the number of qubits.

4.3.2 Rydberg Atom Quantum Processor

Rydberg atom arrays are now well-established quantum simulation platforms (Browaeys & Lahaye, 2020; Henriot et al., 2020). Briefly, atoms are trapped in optical tweezers, each containing exactly one atom. The tweezers may be arranged in any 1D, 2D or 3D geometrical configurations. The register can be rebuilt after each computational cycle. To perform quantum processing, we use the fact that the platform implements spin-like Hamiltonians, where the interactions originate from strong dipole-dipole couplings between atoms laser-excited to Rydberg states.

Depending on the choice of atomic levels, the atoms experience different effective interactions. In the case of the Ising mode, $|0\rangle$ is a "ground" state prepared by optical pumping (Browaeys & Lahaye, 2020) and $|1\rangle$ is a Rydberg state of the atom. The Hamiltonian term for this interaction is:

$$H_{\text{Ising}} = \sum_{i>j} \frac{C_6}{r_{i,j}^6} n_i n_j, \quad (4.5)$$

with $\hat{n}_i = |1\rangle_i \langle 1| = (\mathbb{1}_i + S_i^z)/2$ the projector on the Rydberg state and $r_{i,j}$ the distance between atoms. Here and below, S_i^x, S_i^y and S_i^z indicate the local Pauli operators.

If instead the two states chosen are two dipole-coupled Rydberg states (for example $|0\rangle = |nS\rangle$ and $|1\rangle = |nP\rangle$ for large n), the interaction is resonant and realizes a so-called “XY” or “flip-flop” term:

$$H_{XY} = \sum_{i \neq j} \frac{C_3}{r_{i,j}^3} (S_i^x S_j^x + S_i^y S_j^y), \quad (4.6)$$

where C_3 depends on the chosen Rydberg orbitals and their orientation with respect to the interatomic axis. It corresponds to a coherent exchange of neighboring spin states $|10\rangle$ to $|01\rangle$.

In addition, we can include time-dependent terms on the Hamiltonian, by means of a laser pulse (Ising mode) or a microwave field (XY mode) targeting the transition between the ground and excited states. This is represented by the following “drive” terms:

$$H_{\text{drive}} = \frac{\hbar}{2} \sum_{i=1}^N \Omega_i(t) S_i^x - \hbar \sum_{i=1}^N \delta_i(t) n_i. \quad (4.7)$$

Here, $\Omega(t)$ is Rabi frequency and $\delta(t)$ the detuning of the field with respect to the resonant transition frequency. The addressing can be either global or local. In the procedure used in this work, the local addressing is restricted to the initial state preparation and the register readout stages.

4.3.3 Variational Algorithms on a Rydberg atoms device

In the analog VQE algorithm, we seek to estimate the energy of the ground state of a qubit Hamiltonian called the *target* Hamiltonian, H_T , by using an iterative method. The *resource* Hamiltonian is the one realized by the hardware, and can be configured with different types of interactions (H_{inter}) (4.5, 4.6) and driving fields (H_{drive}):

$$H_R = H_{\text{inter}} + H_{\text{drive}}. \quad (4.8)$$

Experimentally, the transition from the ground to the excited state is typically generated by a two-photon process, from which an approximate two level system is extracted, driven by an effective Rabi frequency Ω and detuning δ during the quantum processing stage. We use their values as parameters in our analog presentation of a VQE algorithm: The first step is to prepare the register of N atoms with a geometry that determines the interaction terms H_{inter} and then to initialize the system in a state $|\psi_0\rangle$. Then, a pulse sequence is applied to evolve the system under the resource Hamiltonian $H_R(\Omega(t), \delta(t))$ whose corresponding time-ordered unitary evolution operator is $U(t) = \mathcal{T} \exp(-i \int_0^t H_R(\Omega(\tau), \delta(\tau)) d\tau)$. The final prepared state is:

$$|\psi(\Omega, \delta, t)\rangle = U(t) |\psi_0\rangle. \quad (4.9)$$

The energy of a prepared state will be calculated with respect to the target Hamiltonian:

$$E(\Omega, \delta, t) = \langle \psi(\Omega, \delta, t) | H_T | \psi(\Omega, \delta, t) \rangle. \quad (4.10)$$

After each cycle, a classical optimizer adjusts the parameters $\Omega \rightarrow \Omega'$, $\delta \rightarrow \delta'$ and $t \rightarrow t'$ and we repeat the evolution of the initial quantum state $|\psi_0\rangle$ with the new parameter set $U(\Omega', \delta', t')$. We aim to obtain for each iteration $E(\Omega', \delta', t') \leq E(\Omega, \delta, t)$ ¹. After several iterations of this loop, the variational scheme attempts to prepare a state whose energy is a good approximation of the ground state energy of H_T (McClellan et al., 2016).

¹This classical optimization problem can be addressed for example by obtaining the gradient of the energy function.

4.4 Description of the Protocols

In this section, we describe two analog variational quantum algorithms for the estimation of the ground state energy and apply them to quantum chemistry problems. The protocols differ mainly by the choice of ansatz: one is the *Unitary Coupled Cluster* (UCC) ansatz (Bartlett et al., 1989), while the other is an adaptation of a *hardware-efficient ansatz* (Kandala et al., 2017), based on repeating alternating values of amplitude, frequency or phase of the applied pulses. We verify numerically the performance of these two types of ansatz in a Rydberg-based Quantum Processor (QP). Next we discuss a protocol for larger molecules tailored after the hardware capabilities. We begin by considering the prototypical example of the H_2 molecule.

4.4.1 UCC ansatz on an analog quantum processor: application on H_2

Numerous implementations of the VQE algorithm rely on the use of digital gates. Recent experimental implementations for the H_2 , LiH and BeH_2 molecules have been realized in (Hempel et al., 2018; Kandala et al., 2017), with superconducting and trapped ions devices respectively. For the analog version of this algorithm on H_2 , we consider the target Hamiltonian and the ansatz as in (Hempel et al., 2018). The Jordan-Wigner and Bravyi-Kitaev transformations lead to two different spin Hamiltonians of this molecule:

$$\begin{aligned}
 H_{JW} = & \mathbf{c}_0 \mathbb{1} + \mathbf{c}_1 (S_0^z + S_1^z) + \mathbf{c}_2 (S_2^z + S_3^z) + \\
 & \mathbf{c}_3 S_3^z S_2^z + \mathbf{c}_4 S_2^z S_0^z + \mathbf{c}_5 (S_2^z S_0^z + S_3^z S_1^z) + \\
 & \mathbf{c}_6 (S_2^z S_1^z + S_3^z S_0^z) + \mathbf{c}_7 (S_3^x S_2^y S_1^y S_0^x + \\
 & S_3^y S_2^x S_1^x S_0^y - S_3^x S_2^x S_1^y S_0^y + S_3^y S_2^y S_1^x S_0^x)
 \end{aligned} \tag{4.11}$$

and

$$\begin{aligned}
 H_{BK} = & \mathbf{f}_0 \mathbb{1} + \mathbf{f}_1 S_0^z + \mathbf{f}_2 S_1^z + \mathbf{f}_3 S_2^z + \mathbf{f}_4 S_1^z S_0^z + \\
 & \mathbf{f}_5 S_2^z S_0^z + \mathbf{f}_6 S_3^z S_1^z + \mathbf{f}_7 S_2^x S_1^z S_0^x + \mathbf{f}_8 S_2^y S_1^z S_0^y + \\
 & \mathbf{f}_9 S_2^z S_1^z S_0^z + \mathbf{f}_{10} S_3^z S_2^z S_0^z + \mathbf{f}_{11} S_3^z S_2^z S_1^z + \\
 & \mathbf{f}_{12} S_3^z S_2^x S_1^z S_0^x + \mathbf{f}_{13} S_3^z S_2^y S_1^z S_0^y + \mathbf{f}_{14} S_3^z S_2^z S_1^z S_0^z
 \end{aligned} \tag{4.12}$$

where the coefficients $\{\mathbf{c}_i\}$ and $\{\mathbf{f}_j\}$ are calculated from (4.3). Since in (4.12) qubits 1 and 3 are only affected by the operators $\mathbb{1}$ and Z one can actually work with the following two-qubit effective Hamiltonian (O'Malley et al., 2016):

$$\begin{aligned}
 H_{BK}^{(\text{eff})} = & \mathbf{g}_0 \mathbb{1} + \mathbf{g}_1 S_0^z + \mathbf{g}_2 S_1^z + \mathbf{g}_3 S_0^z S_1^z + \\
 & \mathbf{g}_4 S_0^x S_1^x + \mathbf{g}_5 S_0^y S_1^y.
 \end{aligned} \tag{4.13}$$

Usually, a good ansatz $|\psi(\boldsymbol{\theta})\rangle = U(\boldsymbol{\theta})|\psi_0\rangle$ requires a balance between hardware constraints and symmetries in target Hamiltonian. However, using the ‘knobs’ available on the hardware is often not efficient, and one thus needs additional guidance to reach the states we are looking for in a potentially very large Hilbert space. In this sense, the well-established Unitary Coupled Cluster (UCC) ansatz allows one to perform an unitary operation while keeping advantages of coupled cluster ansatz from chemistry (Helgaker et al., 2000).

In most cases, implementing the UCC ansatz in a quantum processor requires constructing a digital quantum circuit with full local addressing. An example where global addressing is sufficient is the H_2 molecule. The initial guess of the molecular wave function is a product state obtained from the classical Hartree-Fock calculation performed to determine the coefficients $\{\mathbf{c}_i\}$ and $\{\mathbf{f}_j\}$. Considering only relevant single and double excitations in the unitary coupled-cluster operator (UCC-SD) yields the following one-parameter unitary:

$$U_{\text{UCC-SD}}(\theta) = e^{\theta(c_2^\dagger c_3^\dagger c_1 c_0 - c_0^\dagger c_1^\dagger c_3 c_2)} \tag{4.14}$$

where the minimal set of orbitals are represented by the fermionic annihilation and creation operators c, c^\dagger (Hempel et al., 2018). A Jordan-Wigner transformation on these operators leads to the UCC ansatz $|\psi(\theta)\rangle = \exp(-i\theta S_3^x S_2^x S_1^x S_0^y) |0011\rangle$, where $|0011\rangle$ is the Hartree-Fock state. In the case of the (effective) Bravyi-Kitaev transform (4.13), we obtain the simpler UCC ansatz $|\psi(\theta)\rangle = \exp(-i\theta S_1^x S_0^y) |01\rangle$.

Since the evolution Hamiltonian commutes with the XY Hamiltonian (4.6), one can use the latter ansatz and attempt to drive the Rydberg QP in the XY mode, using $\Omega = 0$ and non-zero local detunings, leaving the rest of the parameters to be set by variational optimization:

$$\begin{aligned} |\psi(\delta_0, \delta_1, t)\rangle &= \exp\left(-it(\delta_0 S_0^z + \delta_1 S_1^z + H_{XY})\right) |01\rangle \\ &= a(\delta_0, \delta_1, t) |01\rangle + b(\delta_0, \delta_1, t) |10\rangle, \end{aligned} \quad (4.15)$$

which coincides with the subspace reached with the UCC ansatz:

$$\exp(-i\theta S_1^x S_0^y) |01\rangle = a(\theta) |01\rangle + b(\theta) |10\rangle. \quad (4.16)$$

A numerical implementation of this protocol is shown in Fig. 4.2, where the classical optimization was performed with a differential evolution algorithm (Storn & Price, 1997). We observe that the ground-state energy can be obtained with an error smaller than 5% using less than 36500 shots for each point.

Such examples of a UCC ansatz implementable with an analog approach, often rely on finding symmetries between target and resource Hamiltonians (Kokail et al., 2019). Nevertheless, this kind of protocol remains impractical for larger molecules because of the increasingly higher number of qubits and Pauli strings in the Hamiltonian. In order to use the analog approach for larger encodings, we explore other approaches below.

4.4.2 Alternating pulses

We now describe an alternating operator approach, based on the QAOA algorithm (Farhi et al., 2014). Let $|\psi_0\rangle$ be the state composed of all qubits in the ground state. The whole sequence is composed by alternating constant (global) pulses, corresponding to two non-commuting Hamiltonians H_a, H_b :

$$H_a = \frac{\hbar}{2} \sum_{i=1}^N \left(\Omega S_i^x - \delta S_i^z \right) + H_{\text{inter}} \quad (4.17)$$

$$H_b = \frac{\hbar}{2} \sum_{i=1}^N \Omega S_i^x + H_{\text{inter}}. \quad (4.18)$$

These Hamiltonians define evolution operators $U_a(t)$ and $U_b(t)$, during a certain time t (see (4.9)). The ansatz of L layers is written as:

$$|\psi(\mathbf{t}_a, \mathbf{t}_b)\rangle = \prod_{\ell=1}^L U_a(t_a^\ell) U_b(t_b^\ell) |\psi_0\rangle, \quad (4.19)$$

where the arrays of parameters $\mathbf{t}_k = (t_k^1, \dots, t_k^\ell, \dots, t_k^L)$, $k \in \{a, b\}$, fix the duration of each pulse in the layer, as described in (Dalyac et al., 2021). As another example, a different choice of parameters was used in (Ebadi et al., 2022), considering a single Hamiltonian:

$$H = \frac{\hbar}{2} \sum_{i=1}^N \left(\Omega(t) e^{i\phi(t)} |0\rangle_i \langle 1| + \text{h.c.} \right) + H_{\text{inter}} \quad (4.20)$$

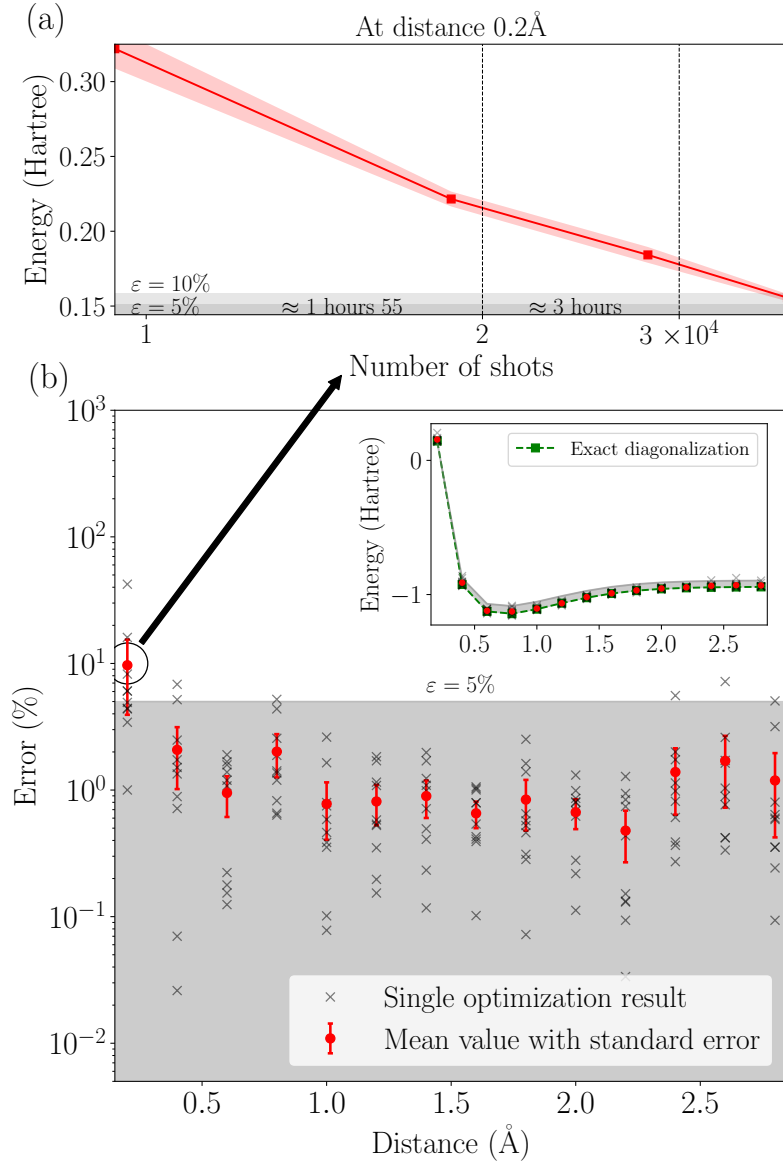


Figure 4.2: *Numerical implementation of an analog VQE algorithm using a UCC ansatz.* (a) A zoom on the smallest inter-atomic distance (0.2 Å) shows the evolution of the optimization with respect to the number of shots. The differential evolution was set to perform at most 4 iterations (red squares). The red scale shows the errorbar over 20 realizations. It takes approximately 3.5 hours of runtime for a QP operating at 3 Hz to achieve $\epsilon = 10\%$ (light grey scale) of error and 4 hours to achieve $\epsilon = 5\%$ (dark grey scale). (b) Relative error in percentage (red circles) between the mean VQE result and the numerically computed lowest eigenvalue of the target Hamiltonian (in STO-3G basis) over 10 realizations (gray crosses). The expected error is below $\epsilon = 5\%$ (grey area). The inset depicts the same result on an energy scale and compares it with the exact solution (green squares). The result is drawn as a function of hydrogen inter-atomic distance.

with different time $\mathbf{t} = (t^1, \dots, t^\ell, \dots, t^L)$ and phase $\phi = (\phi^1, \dots, \phi^\ell, \dots, \phi^L)$ arrays defining L segments of the pulse. The corresponding ansatz is then:

$$|\psi(\mathbf{t}, \phi)\rangle = \prod_{\ell=1}^L U(t^\ell, \phi^\ell) |\psi_0\rangle. \quad (4.21)$$

The two approaches can be implemented in existing experimental setups, especially when the target Hamiltonian is equal to the resource Hamiltonian (such as the case of the Maximal Independent Set problem with Unit Disks, which is native to the Rydberg atoms setting). However, these methods struggle to minimize the molecular target Hamiltonian energies within a limited number of iterations and measurement repetitions. The alternating pulse ansatz assumes an initial register configuration and initial guesses for the durations of the pulses in each layer, two tasks that are the subject of active research. The expectation is that a properly chosen register and an optimized pulse will drive the system to a low-energy state. In Fig. 4.3, we compare numerically the performance of the two alternating pulse ansätze discussed above ((Dalyac et al., 2021), (Ebadi et al., 2022)). We also included the procedure described in Sec. 4.4.3, which addresses the embedding of the problem in the register and an estimation protocol for the observables. Comparing the required number of shots for these approaches highlights the necessity of including an efficient estimation protocol for the observables.

4.4.3 Optimized Register and Iteratively Parameterized Pulses

In this section, we present a more refined approach to deal with larger systems, aiming at exploiting the capabilities already available in Rydberg simulators. To exemplify the procedure, we consider in the following the Ising mode with the resource Hamiltonian (4.5).

Atom register and initial state

Even though we only consider global pulses for the processing stage, there still remains freedom in the choice of the positions of the atoms. This determines the strength of pairwise interactions and defines a connectivity graph whose edges correspond to the atoms that experience a blockade effect (Henriet et al., 2020) (a different graph structure can be defined for the XY mode (4.6)).

In order to find suitable atomic positions, the coordinates are optimized in the plane so that the associated interaction energy matrix resembles as much as possible the information contained in the target Hamiltonian. Since the latter contains general Pauli strings, we consider a subset of terms whose coefficients can be expressed in terms of the coordinates of the atoms². A simple choice consists in selecting the terms that can be directly compared with the Ising-like interaction of the atoms: Let the matrix V^T be given by the positive coefficients of the terms with only two Z operators in the molecular target Hamiltonian and V^R (our “register” matrix) the resulting values of interaction strength $C_6/r_{i,j}^6$ for each pair i, j of atom positions in the register. This defines a score function $\sum_{i,j} (V_{i,j}^T - V_{i,j}^R)^2$ that we minimize numerically by varying the atom coordinates.

The set of atomic positions that arises from this minimization will be our optimized register. Its geometry will be used to simulate the target Hamiltonian, but has no intrinsic chemical meaning. The information that is taken from the Hamiltonian can be chosen from other subsets of the Pauli strings (e.g. terms with 3 or more Z operators) and different interpretations of how the coefficients constitute a register matrix. A different resource Hamiltonian, such as one with XY interactions, would imply a different choice of subset. In Fig. 4.4, we summarize graphically the procedure for the case of the H_2 molecule with the Jordan-Wigner transformation. It turns out that we obtain at a geometry very similar to the one heuristically picked for the alternating pulse ansatz.

²A broader series of techniques for embedding the problem information into the atom register has been considered in (Coelho et al., 2022; Leclerc et al., 2022)

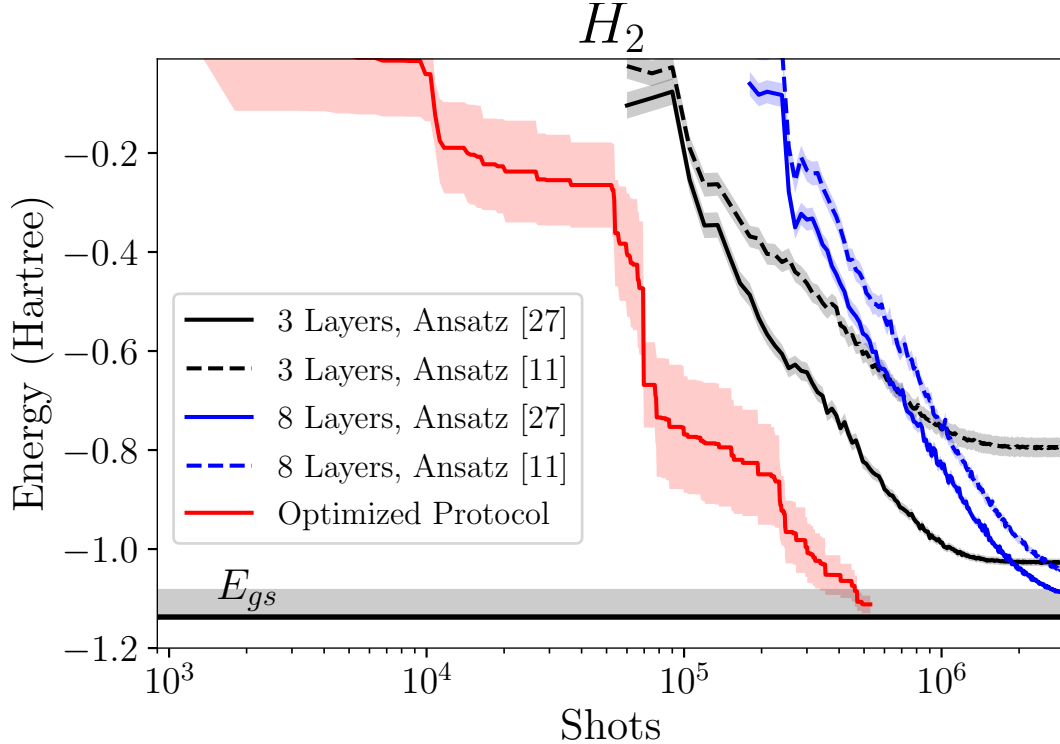


Figure 4.3: Evolution of the ground-state energy as a function of the accumulated number of shots for the H_2 molecule at a fixed inter-nuclear distance. We have averaged numerically 200 realizations of VQE with 3 and 8 layers using the two alternating pulse ansatz, (Dalyac et al., 2021) (straight line), and (Ebadi et al., 2022) (dashed line). In the alternating operator approach, each Pauli string mean value is performed with 1000 shots, which for the H_2 Hamiltonian represents 1.5×10^4 shots before obtaining the first energy data point. Achieving energy errors below 5% (gray area) requires at least $\mathcal{O}(10^6)$ shots in total. For the optimized procedure (adding more control over atom positions, pulse shaping and derandomization estimation), the same energy error typically requires $\mathcal{O}(10^5)$ shots.

Optimization of the parameterized pulse sequence

We constructed a variation of the so-called `ctrl1-VQE` protocol (Meitei et al., 2021) for the case of a global pulse on the register, in which the number of parameters increases at every optimization iteration, while the total time t_{tot} remains fixed:

Consider a set of Rabi frequencies $\{\Omega_i\}_{i=1}^K$ and detunings $\{\delta_i\}_{i=1}^K$ defined discretely over a set of time labels $0 < t_1 < \dots < t_K = t_{\text{tot}}$. Then, at iteration k , a new time label $0 < t_k < t_{\text{tot}}$ is generated at random, lying between two previous time labels, $t_{i-1} < t_k < t_i$. To avoid labels too close to each other, we will accept t_k if the intervals $|t_{i-1} - t_k|, |t_k - t_i|$ are large enough compared to the response time of the waveform generator of the machine (in the order of a few ns). The corresponding Rabi frequency Ω_i and detuning δ_i from the parent interval $[t_{i-1}, t_i]$ are then split into two independent parameters Ω'_i, Ω'_k and δ'_i, δ'_k whose initial values are set equal to their parent parameters (see Fig. 4.5). Finally, the new set of parameters $\{\Omega_1, \dots, \Omega'_i, \Omega'_k, \dots, \Omega_K\}$ (likewise for $\{\delta_i\}_{i=1}^K$) is optimized starting from the previous iteration values. This algorithm acts therefore

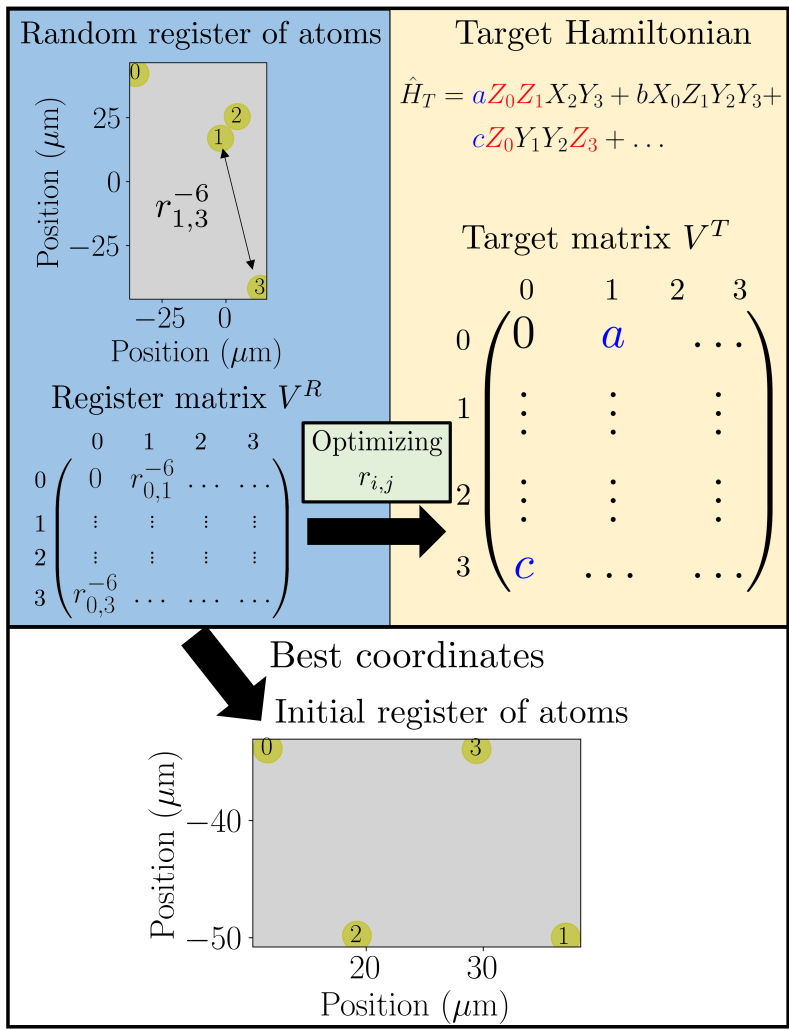


Figure 4.4: Protocol to optimize the positions of the atoms in a register based on a target Hamiltonian. Blue: we begin with a register of randomly placed atoms and all the Ising interaction terms are entered in a $N \times N$ matrix. Yellow: all positive coefficients before the Pauli strings with only two Z operators in the target Hamiltonian are combined in another (target) matrix $N \times N$. The coordinates of the atoms are optimized to minimize the distance between the two matrices. We then obtain a new register on which we will apply the VQE sequence.

as a pulse shaping process. From time t_{i-1} to t_i the acting Hamiltonian is:

$$H_i = \frac{\hbar}{2} \left(\Omega_i \sum_{j=1}^N S_j^x - \delta_i \sum_{j=1}^N S_j^z \right) + H_{\text{inter}} \quad (4.22)$$

and our ansatz, for K iterations, becomes:

$$|\psi(\boldsymbol{\Omega}, \boldsymbol{\delta})\rangle = \mathcal{T} \prod_{i=1}^K \exp \left[-i \int_{t_i}^{t_{i+1}} H_i(\tau) d\tau \right] |\psi_0\rangle \quad (4.23)$$

Note that while the interval involves a constant Hamiltonian, we include a time-dependent integration at each interval, to indicate that the waveforms that compose the pulse can be adapted to hardware conditions (e.g. by being interpolated, or by adapting the shape with an envelope function).

Energy estimation by derandomization

In our algorithm implementation, we take as a figure of performance of the variational optimization run the *total* number of shots required to achieve a given error threshold ϵ for the energy. A bounded number of processing cycles is required to remain within a realistic time lapse for the entire implementation process. Rather than measuring several times each of the Pauli observables in the Hamiltonian, we use an estimation protocol (derandomization (H.-Y. Huang et al., 2021)) based on fixing local Pauli measurements from an originally random set. This allows to efficiently predict the energy of the prepared state $|\psi\rangle$, $\langle H_{\text{T}}(\psi)\rangle$, at each loop of the optimization of the parameters.

More specifically, the derandomization algorithm starts with an initial measurement set of M random Pauli strings $\{S^{(m)}\}_{m=1}^M$. A greedy algorithm improves the overall expected performance of the measurement set, effectively “derandomizing” the operators of each random Pauli string in sequence. The improvement is quantified by the average of the *confidence bound*, which ensures that the empirical average $^3 \omega_p$ corresponding to the p -th term of H_{T} is within a desired accuracy $|\omega_s - \langle S^{(p)}\rangle| / |\langle S^{(p)}\rangle| < \epsilon$ and with a high probability. The total energy is finally estimated as $\langle H_{\text{T}}(\psi)\rangle \approx \sum_{p=1}^P \omega_p$.

While the pulses that prepare the state are global, the measurement itself requires the implementation of local rotations on the qubits. This can be achieved experimentally by using a toolbox such as the one described in (Notarnicola et al., 2021), thus emphasizing the digital-analog interplay that is now within reach for next-generation neutral atom devices.

4.5 Numerical Results

4.5.1 Application on LiH and BeH₂ molecules

We have applied the method described in section 4.4.3 to the LiH and BeH₂ molecules. Using the `Qiskit` (Qiskit contributors, 2023) framework combined with `Pyquante` (Muller, 2022), we

³A Pauli string A *hits* B , if by changing some operators in A to $\mathbb{1}$, we form B (for example $ZX\mathbb{1}$ hits $\mathbb{1}X\mathbb{1}$ and $Z\mathbb{1}\mathbb{1}$). The empirical average is obtained using those Pauli measurement basis $\{S^{(m)}\}$ that hit an observable $S^{(p)}$, with the relevant measured bits expressed as \pm :

$$\omega_s = \frac{1}{N_{\text{h}}} \sum_{\substack{m: \\ S^{(m)} \text{ hits } S^{(p)}}}^M \left(\prod_{j: S_j^{(p)} \neq \mathbb{1}}^N \mathbf{b}_j^{(m)} \right),$$

where N_{h} counts how many Pauli strings in the set $\{S^{(m)}\}$ hit $S^{(p)}$, and $\mathbf{b}^{(m)} = \mathbf{b}_1^{(m)} \dots \mathbf{b}_N^{(m)}$ is the bitstring measured with the basis $S^{(m)}$

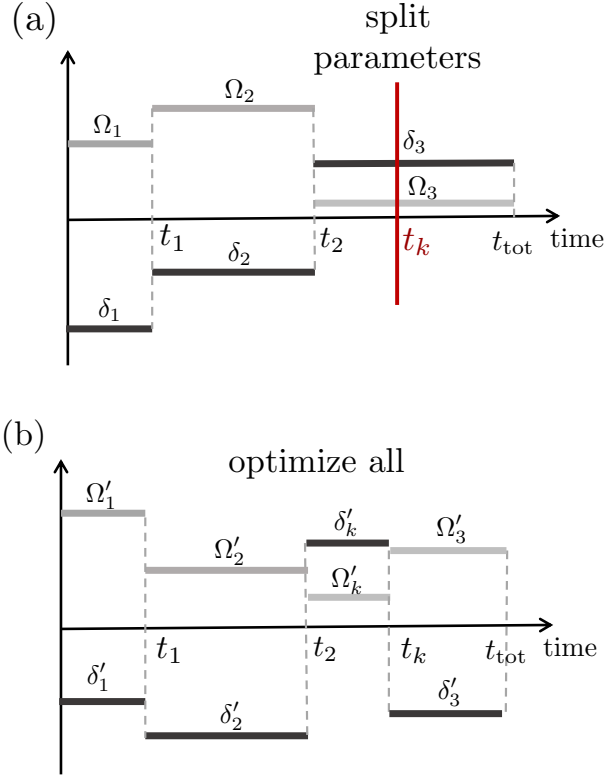


Figure 4.5: Iterative splitting and optimization of the pulse parameters: (a) Choose at random a time t_k , which will fall in the interval (t_{i-1}, t_i) , and accept it if $|t_{i-1} - t_k|$ and $|t_k - t_i|$ conform to the device response time. Split the corresponding Ω_i into two parameters Ω'_i, Ω'_k with initial value equal to Ω_i . Do the same to the set $\{\delta_i\}$. (b) Optimize the new set of parameters to lower the energy of the prepared state (4.10).

calculate the one and two-body integrals of (4.3), encoding the problem into 6 qubits using the Bravyi-Kitaev method. The Hamiltonians contain 118 and 165 Pauli strings respectively. To design the pulse sequence and include realistic device constraints into the simulations we used the open source package **Pulsar** (Silvério et al., 2022). The Powell algorithm (Powell, 1964) was used for the classical optimization of the pulse values with 20 function evaluations for each iteration. The two initial Rabi frequency and detuning are chosen randomly in the interval $[0, 2 \times 2\pi]$ MHz for each optimization procedure. During the optimization, Rabi frequencies are bounded to this interval to remain within experimentally accessible values (Scholl et al., 2021), while the interval for the detuning was taken as $[-2 \times 2\pi, 2 \times 2\pi]$ MHz. We ran the algorithm five times for four different inter-nuclear distances R yielding the results shown in Fig. 4.6. The algorithm converges with small errors in most cases, but we notice the impact of the initial parameters on the obtained energies. For instance at $R = 1.5 \text{ \AA}$ for the BeH_2 molecule, the obtained energy values are up to

0.4 Hartree apart.

To optimize the register geometry, we took the coordinates as parameters, starting from random positions and minimized the score function described in Sec. 4.4.3. We optimized the atom register based on the Nelder-Mead method (Nelder & Mead, 1965), with a few thousands function evaluations, and we also compared to several heuristic choices obtained by a term-by-term comparison with the interaction matrix (a well-performing choice of positions is shown for LiH in Fig. 4.6)

We define our error as

$$\varepsilon = |E_{\text{exact}} - E_{\text{estimated}}|/|E_{\text{exact}}|, \quad (4.24)$$

where $E_{\text{exact}} = \langle H_T \rangle$ is the exact diagonalization solution with respect to the target Hamiltonian and $E_{\text{estimated}}$ is the energy calculated with the optimized geometry, the optimized pulse sequence, and the derandomization estimation. The optimized configurations, together with optimized pulse parameters and energies estimated at each iteration with derandomized measurements give rise to energy errors typically below the $\varepsilon = 5\%$ threshold in less than 350000 shots.

The implementation of the derandomization algorithm allows us to choose the number of measurements that we wish to take (our budget), for a given target accuracy of estimation, which we set to correspond to our $\varepsilon = 5\%$ benchmark. The resulting “derandomized” Pauli measurements included typically close to 20 different Pauli strings, calculated from the minimization of the average confidence bound that ensures an empirical average within the chosen ε . Since some derandomized Pauli strings have more operators in common with the terms in the target Hamiltonian (they “hit” more target observables), we adjusted the measurement repetitions to be spent proportionally more in them, which improved statistics. We also verified that the obtained accuracy improves upon increasing the allowed number of shots, although we don’t expect a full convergence, given the incomplete information used to define H_T .

4.5.2 Roadmap for more complex molecules

We discuss in this section some observations about the presented protocol for larger molecules and more complex basis sets, where the number of terms in the Hamiltonian and the required qubits to encode it grows quickly. Currently available neutral-atom devices can load hundreds of traps (Schymik et al., 2022), but the available space on the register will eventually become a resource limitation. In Fig. 4.7 we show the register optimization results for H_2O and CH_4 in different basis sets, where thousands of terms would need to be measured. Our simple restriction to Z -terms captures limited features of the Hamiltonian, mostly concentrating atoms where the largest values need to be reproduced. In fact, as the system size grows, we observe that most of the atoms in the register act as a “background” for these clusters. Choosing different terms from the Target Hamiltonian will bring forward other features, highlighting the opportunities of using learning methods to find more performing atom positions. We have not addressed here the possibilities offered by three-dimensional registers (Barredo et al., 2018), which allow for more complex embeddings and have been already studied for graph-combinatorial problems (Dalyac & Henriot, 2022), although they can be straightforwardly included in the protocol.

Two aspects of the optimization that rely on classical computation can be further refined: the choice of initial state and the selection of parameters: initializing the optimization with a product state from a Hartree-Fock state approximation can help exploring a lower energy set of output states. In Fig. 4.8 we have scanned through all product states of an 8-qubit system to select those who benefit the most from the first step of the pulse-optimization protocol presented above. The best choice of initial product state can then be used for the Rydberg QP implementation⁴. Comparing the energy $\langle \psi_0 | U(\theta)^\dagger H_T U(\theta) | \psi_0 \rangle$ of a candidate initial product state $|\psi_0\rangle$ evolving under a constant pulse parameterized by θ can be performed for example using tensor-network techniques over an HPC backend (Bidzhiev et al., 2023; Rudolph et al., 2022). On the other hand,

⁴Preparing the initial product state requires for example masking atoms with the help of a spatial light modulator.

the number of parameters can be chosen at will, and do not depend on the number of qubits. More advanced control techniques can be applied here, and there is large choice of techniques and numerical tools in the subject of quantum optimal control. We recall that the optimization of the pulse sequence is not dependent on the embedding itself – it is a global property of the system evolution, where nearby atoms constitute blockade regions that characterize the final state.

4.6 Discussion

In this work, we have numerically studied a digital-analog quantum algorithm in the context of quantum chemistry using an ideal Rydberg quantum processor as a hardware. We have considered small molecules with resource Hamiltonians of two qubits for the H_2 molecule and six qubits for the LiH and BeH_2 molecules to demonstrate the applicability of our methods. Our purpose was to describe the construction of such an algorithm, discussing the cost of each stage in terms of the number of measurement repetitions. Our numerical results should be viewed as a first benchmark and should trigger further explorations. Besides, it provides a roadmap for the improvement of Rydberg quantum processor, in particular in terms of cycle time.

By considering the symmetries of H_2 Hamiltonian, we show how the UCC method efficiently and accurately approximates the ground state energy. However, finding a two-body Hamiltonian which commutes with a more general molecular target Hamiltonian is a hard problem. We therefore proposed another protocol for larger molecules: we optimized the geometries of the atomic array, pulse sequences and included an estimation method (derandomization) for the energy measurement. We targeted 5% of accuracy compared to the exact diagonalization method for Hamiltonian with 6 qubits and more than a hundred Pauli strings.

We observed that the geometry of the array has a significant impact on the result: In the case of LiH , where the target matrix V^T does not provide much information due to the few terms with only two Z operators, the optimized positions underperform with respect to a careful choice of positions, although scaling the heuristics that gives rise to such a geometry for molecules with large number of qubits in their encoding is impractical. This calls for the design of more advanced embedding algorithms. Indeed, for the case of BeH_2 , the register optimization achieves rather small energy errors, especially for larger distances.

Previous studies (Wecker et al., 2015) have quantified the demanding resource requirements for practical VQE applications. After several iterations of pulse optimization with energy estimation via derandomization, the error on the average energy of the final prepared state descends to $\varepsilon < 5\%$, and expected to be obtained within a day of measurement in a typical current-day Rydberg QP.

In the numerical implementation we have used out-of-the-box optimizers with limitations for the numerical task at hand. Other possibilities include the use of an interpolated waveform for each set of parameters and shaping the pulse using bayesian optimization routines as explored in (Coelho et al., 2022) for the study of combinatorial graph problems. Note that experimentally, one could clone several times the atom layout in spatially separated regions of the register (at least for a small number of qubits), multiplying the obtained number of bitstrings. To achieve close to 1% relative error, we expect that at least a week of Rydberg QP runtime would be necessary (see extrapolation shown in Fig. 4.6). The capacity of a circuit ansatz to construct a desired quantum state while keeping a small depth and number of parameters is studied by its *expressibility* (Holmes et al., 2022; S. Sim et al., 2019). In the case of analog systems, this is an emerging topic of research (Tangpanitanon et al., 2020), with the goal of ensuring that a given ansatz could potentially lead to a good approximation of the ground state and achieve chemical accuracy.

The impact of experimental errors in a real-life implementation will also lead to performance reductions. SPAM (State Preparation And Measurement) errors are typically the largest source of discrepancy for the neutral atom devices (de Léséleuc et al., 2018), but the energy errors observed in numerical simulations remain low as long as the failure rates are small, given that the variational nature of the algorithm shows robustness to several types of errors (Henriet, 2020). Recently (Guo

et al., 2022), VQE was experimentally implemented in a superconducting quantum processor for H_2 , LiH and F_2 with 4, 6 and 12 qubits, respectively, using the UCC ansatz and a different flavor of measurement protocol (Wu et al., 2023). The readouts went through an error mitigation post-processing routine, which showed that these techniques can greatly compensate the noise effects from their quantum processor, with an error reduction of up to two orders of magnitude and leading to chemical accuracy in some circumstances. We expect that such mitigation can be added to the protocols considered in this paper and will help experimental implementations in Rydberg QP.

To tackle quantum simulation algorithms for energy estimation, more developments in both quantum and classical parts of the hybrid algorithm are needed. Reaching chemical accuracy for molecules with a few tens of qubits remains an open challenge that can now begin to be explored in experimental devices. This will provide evidence to generate new and fundamental insights to understand under what conditions a computational advantage can be achieved.

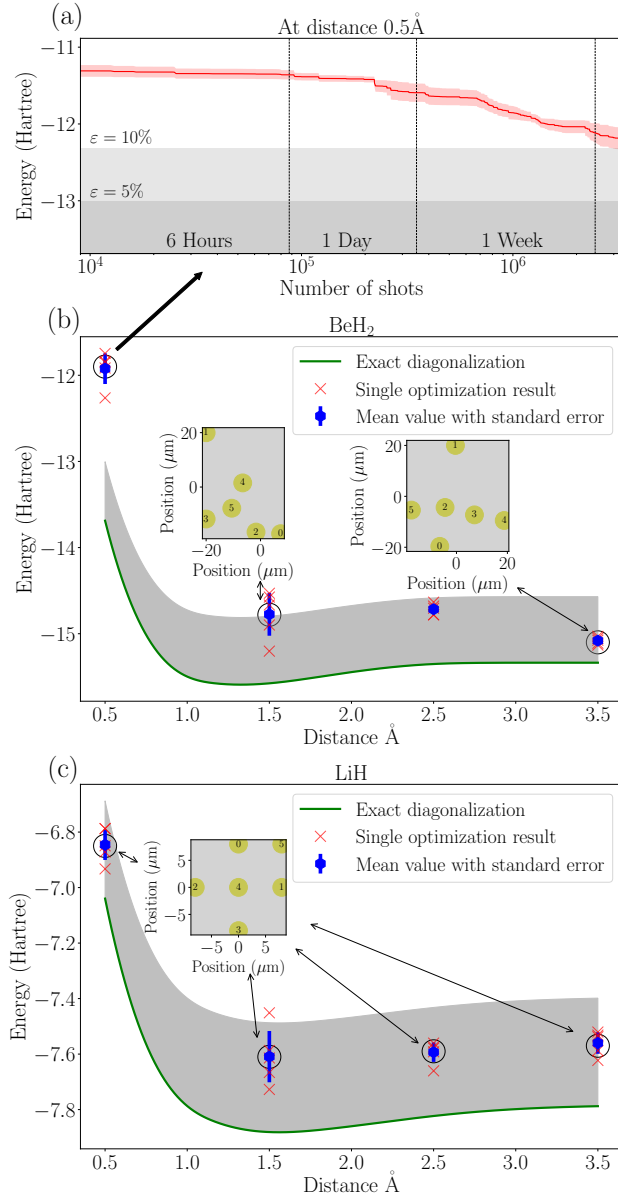


Figure 4.6: Numerical results of the VQE algorithm with our digital-analog protocol (a) for BeH₂ at an intermolecular distance of 0.5 Å where we increased the number of shots beyond 1 day of experiment and observed the expected improvement over several days of calculations. The light grey shade and the dark grey shade indicate respectively $\epsilon = 10\%$ and $\epsilon = 5\%$ error benchmark. The red line shows the improvement mean value over 100 run. (b) Result of BeH₂ molecule with an encoding of 6 qubits and 165 Pauli strings and (c) result of LiH molecule result with an encoding of 6 qubits and 118 Pauli strings. The insets show the register geometry at specific inter-nuclear distances. For the case of LiH a single heuristic choice was used, while for BeH₂ an optimized geometry was prepared at each inter-nuclear distance, minimizing the distance between selected terms of the target Hamiltonian and the interaction energies of the atoms in the register (see Sec. 4.4.3). Blue squares: mean value for several simulations. Green line: result from exact diagonalization. The gray shade indicates an $\epsilon = 5\%$ error benchmark. The total number of shots for each optimization result (red crosses) is set to 350000, corresponding roughly to a day of processing in a Rydberg QP.

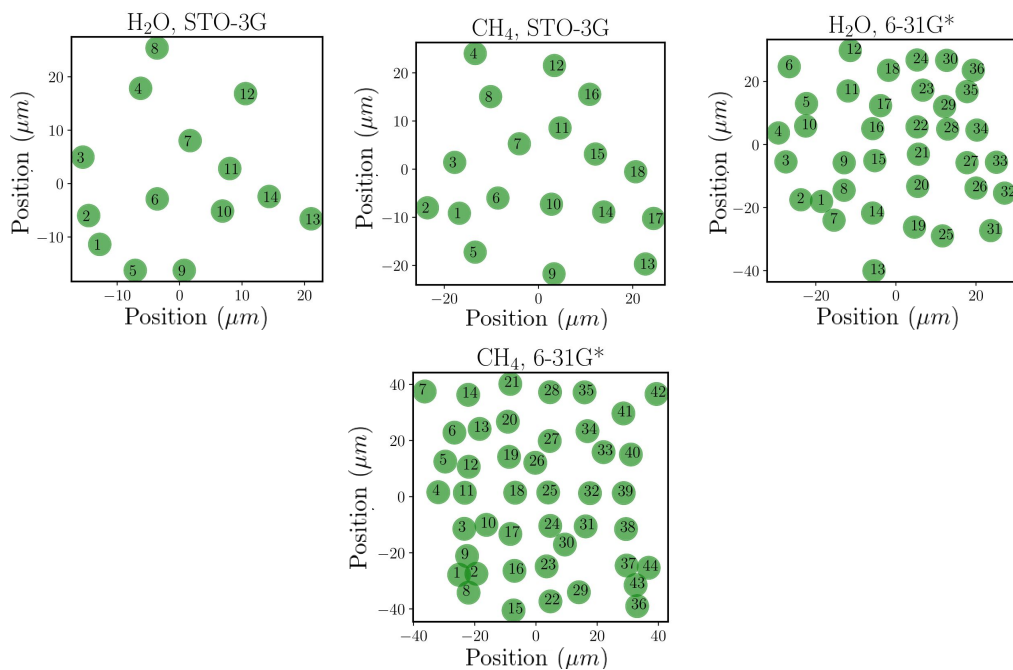


Figure 4.7: Example embeddings for the H_2O and CH_4 molecules. Using a Jordan-Wigner encoding, for two different basis, our H_2O Hamiltonian (left column) consisted of 14 qubits and 2110 terms (STO-3G basis), of which 595 were chosen as features for the reference Hamiltonian. Choosing a 6-31G* basis gives 36 qubits, with 83003 terms and 5594 of them relevant. For CH_4 (right column), the STO-3G basis gives 18 atoms and 6892 Pauli terms, of which 1359 terms were used for the embedding. The 6-31G* basis requires 44 qubits, 297075 terms and we have picked an embedding with 11772 terms.

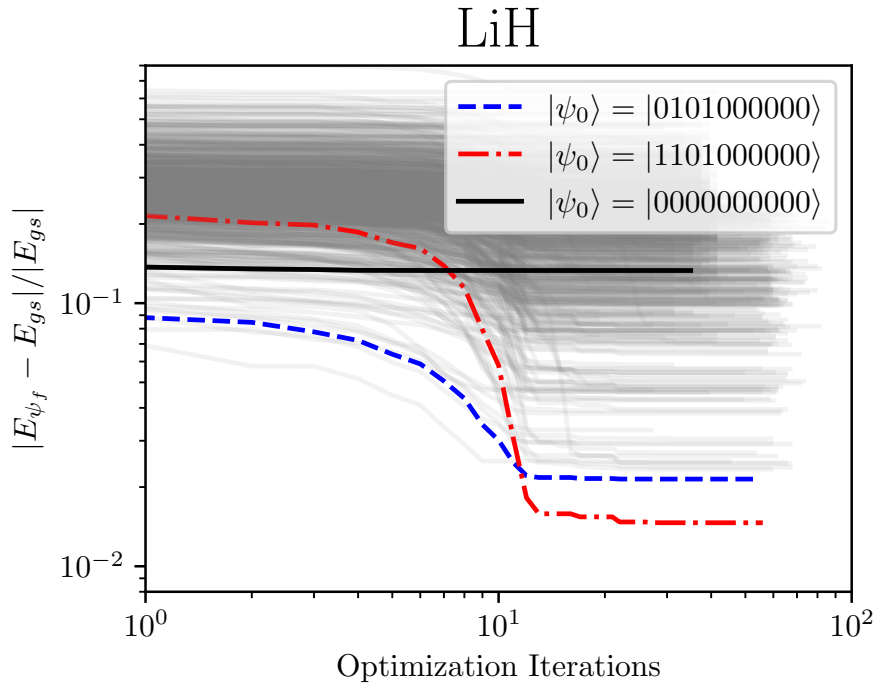


Figure 4.8: Relative error ε after the first step of the pulse optimization 4.4.3, using different initial product states. While the default $|\psi_0\rangle = |0\rangle^{\otimes N}$ (black line) barely improves its ε by the optimization step, other product states (blue, dashed line and red, dashed-dotted line) achieve a very low error. We have used an 10-qubit Jordan-Wigner encoding of the LiH Molecular Hamiltonian under the STO-3G basis (276 terms), and averaged several instances for each product state.

Chapter 5

Using Rydberg platform to simulate strong fermionic correlations in the 2D-Hubbard model

5.1 Forewords

This chapter is a mix of the main text and the supplementary material of a preprint (Michel, Henriot, et al., 2023) submitted to a peer-reviewed journal. It is the result of a collaboration with ATOS/EVIDEN.

5.2 Introduction

Decades of theoretical efforts have led to tremendous progress in the understanding of the exotic phases of strongly correlated electron systems. For instance, lots is known about the physics of their minimal model, the Hubbard model (LeBlanc et al., 2015; Schäfer et al., 2021). Yet, the exponential difficulty of the underlying many-body problem still poses formidable challenges in low-temperature, doped phases relevant to cuprate superconductors, in multi-orbital settings relevant, for instance, to iron-based superconductors (Si et al., 2016) and the recent Moiré superconductors (Andrei et al., 2021), or in out-of-equilibrium situations like sudden quenches that lead to a fast growth of entanglement.

Quantum processors, i.e., controllable, synthetic quantum many-body systems (Aryal et al., 2023), are promising to solve these outstanding challenges (Feynman, 1982). Ultracold fermionic atoms trapped in optical lattices were already implemented more than a decade ago (Boll et al., 2016; Cheuk et al., 2016; Esslinger, 2010; Hart et al., 2015; Jördens et al., 2008; Mazurenko et al., 2017; Schneider et al., 2008; Schneider et al., 2012; Schreiber et al., 2015; Tarruell & Sanchez-Palencia, 2018) as the most direct, or "analog", quantum processors of fermions. They allowed to observe signatures of, for instance, Mott physics, while operating—so far—at temperatures too high to gain insights into pseudogap or superconducting phases.

In contrast, universal "digital" quantum processors rely on quantum bits encoded on two-level or "spin-1/2" systems, and operate logic gates on them. They in principle enable the simulation of the second-quantized fermionic problems explored in materials science (Bauer et al., 2020) or chemistry (Y. Cao et al., 2019).

Yet, early attempts are facing the physical limitations of these processors in terms of the number of qubits and number of gates that can be reliably executed before decoherence sets in. Fermionic systems are particularly demanding due to the loss of locality of the Hamiltonian (Bravyi & Kitaev,

2002; Jordan & Wigner, 1928) or the need for auxiliary qubits (Derby & Klassen, 2020; Setia et al., 2019; Verstraete & Cirac, 2005) that come with translating to a qubit language. Both constraints generically lead to longer quantum programs, and hence an increased sensitivity to imperfections. To alleviate those issues, hybrid quantum-classical methods (Bharti et al., 2022; Endo et al., 2021) such as the Variational Quantum Eigensolver (VQE, (Peruzzo et al., 2013)) were proposed, with many developments but without clear-cut advantage so far.

Despite remarkable recent progress towards large-size digital quantum processors, "analog" quantum processors remain a serious alternative to explore fermionic problems. Beyond the aforementioned ultracold atoms, platforms include systems of trapped ions and cold Rydberg atoms. The lesser degree of control of these machines—with a fixed, specific "resource" Hamiltonian that does not necessarily match the "target" Hamiltonian of interest — is compensated by the large number of particles that can be controlled, with now up to a few hundreds of particles (Chen et al., 2023; Ebadi et al., 2021; Scholl et al., 2021). In addition, the parameters of the resource Hamiltonian are usually precisely controlled in time (Bloch et al., 2008; Bluvstein et al., 2021; Browaeys & Lahaye, 2020; Glaetzle et al., 2015; González-Cuadra et al., 2023; Scholl et al., 2021). This has enabled the use of analog quantum processors to study many-body problems in several recent works (Argüello-Luengo et al., 2019; Bloch et al., 2008; González-Cuadra et al., 2023; Kokail et al., 2019; Michel, Grijalva, et al., 2023). For instance, (Kokail et al., 2019) have investigated the physics of the Schwinger model—a toy problem for lattice quantum electrodynamics—by leveraging the similarity between the symmetries of a 20-ion quantum simulator and those of the Schwinger model. In general, however, such a similarity between target and resource Hamiltonians is rare. In particular, the question of how to tackle a fermionic many-body problem with a spin-based, analog simulator is an open problem.

In this Letter, we propose a method to address this problem using a specific processor, namely an analogue Rydberg quantum processors (Browaeys & Lahaye, 2020; Henriot et al., 2020). By using a self-consistent mapping between the fermionic problem and a "slave-spin" model, we circumvent the nonlocality issues related to fermion-to-spin transformations. We show that the method allows one to compute key properties of the Hubbard model in and out of equilibrium. We show, through realistic numerical simulations, that it does so even in the presence of hardware imperfections like decoherence, readout error and shot noise coming from the finite number of repetitions of the experiment.

5.3 Problem reduction through the slave-spin method.

As a proof of concept, we tackle the single-band, half-filled Fermi-Hubbard model on a square lattice. Its Hamiltonian:

$$H_{\text{Hubbard}} = \sum_{i,j,\sigma} t_{i,j} d_{i\sigma}^\dagger d_{j\sigma} + \frac{U}{2} \sum_i (n_i^d - 1)^2 \quad (5.1)$$

contains creation (resp. annihilation) operators $d_{i\sigma}^\dagger$ (resp. $d_{i\sigma}$) that create (resp. annihilate) an electron of spin σ on lattice site i , with a hopping amplitude $t_{i,j}$ between two sites (we will focus on nearest-neighbor hopping only, $t_{i,j} = -t\delta_{\langle i,j \rangle}$) and an on-site interaction U . (The chemical potential was set to $\mu = U/2$ to enforce half-filling.)

This prototypical model of strongly-correlated electrons is generically hard to solve on classical computers, especially in out-of-equilibrium phases where the most advanced methods are usually limited to short-time dynamics. Instead of directly tackling this fermionic model, we resort to a kind of separation of variables that singles out two important degrees of freedom of the model, namely spin and charge. Technically, this is achieved by resorting to a "slave-particle" method known as Z_2 slave-spin theory (de'Medici et al., 2014; Rüegg et al., 2010). We replace the fermionic operator $d_{i\sigma}^\dagger$ by the product of a pseudo-fermion operator $f_{i\sigma}^\dagger$ and an auxiliary spin field S_i^z ($S_i^{a=x,y,z}$ denote the Pauli spin operators), namely $d_{i\sigma}^\dagger = S_i^z f_{i\sigma}^\dagger$. The ensuing enlargement of the Hilbert space

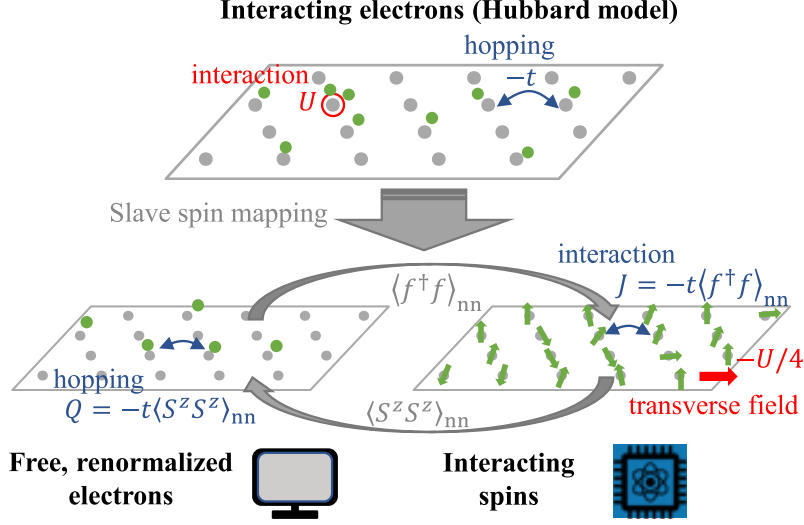


Figure 5.1: *Slave spin mapping*. The Hubbard Hamiltonian (top) is mapped to two self-consistently determined simpler problems: an efficiently solvable free fermionic Hamiltonian with a renormalized hopping (bottom left, $H_f(Q)$ in the text), and a transverse field Ising Hamiltonian (bottom right, $H_s(J)$ in the text), which we tackle using a quantum Rydberg processor.

is compensated for by imposing constraints $\frac{S_i^x + 1}{2} = (n_i^f - 1)^2$ on each site. In the particle-hole symmetric case studied here, these constraints will be fulfilled automatically (Schiró & Fabrizio, 2011).

We then perform a mean-field decoupling of the pseudo-fermion and spin degrees of freedom $S_i^z S_j^z f_{i,\sigma}^\dagger f_{j,\sigma} \approx \langle S_i^z S_j^z \rangle f_{i,\sigma}^\dagger f_{j,\sigma} + S_i^z S_j^z \langle f_{i,\sigma}^\dagger f_{j,\sigma} \rangle - \langle S_i^z S_j^z \rangle \langle f_{i,\sigma}^\dagger f_{j,\sigma} \rangle$. We obtain a sum of two self-consistent Hamiltonians $H \approx H_f + H_s$:

$$H_f = \sum_{i,j,\sigma} Q_{i,j} f_{i,\sigma}^\dagger f_{j,\sigma} \quad (5.2a)$$

$$H_s = \sum_{i,j} J_{i,j} S_i^z S_j^z + \frac{U}{4} \sum_i S_i^x, \quad (5.2b)$$

with $Q_{i,j} = t_{i,j} \langle S_i^z S_j^z \rangle$ and $J_{i,j} = \sum_\sigma t_{i,j} \langle f_{i,\sigma}^\dagger f_{j,\sigma} \rangle$.

Solving the Hubbard model within slave spin theory amounts to solving these two self-consistently defined problems. This is done in an iterative fashion, as illustrated in Fig. 5.1: starting from an initial guess for the renormalized hopping Q to initiate the self-consistent computation, (i) the correlation function $\langle f_{i,\sigma}^\dagger f_{j,\sigma} \rangle$ of the pseudo-fermion problem, needed to define the spin interaction $J_{i,j}$, can be computed efficiently on a classical computer using a Bogoliubov transformation (see Suppl. Mat 5.4.1 for more details), (ii) the spin problem, on the other hand, is harder to tackle on classical computers. We thus set out to compute its spin-spin correlation function with a quantum processor. Since H_s is of infinite size, we first reduce it to a finite-size problem by using a cluster mean-field approximation, as done in e.g. (Hassan & de'Medici, 2010): we solve

$$H_s^C = \sum_{i,j \in C} J_{i,j} S_i^z S_j^z + \frac{U}{4} \sum_{i \in C} S_i^x + \sum_{i \in C} h_i S_i^z, \quad (5.3)$$

where C denotes the set of N cluster sites and $h_i = 2z_i \bar{J} \bar{m}$ is the self-consistent mean field that mimics the influence of the infinite lattice. Here, z_i is the number of neighbors of site i outside the

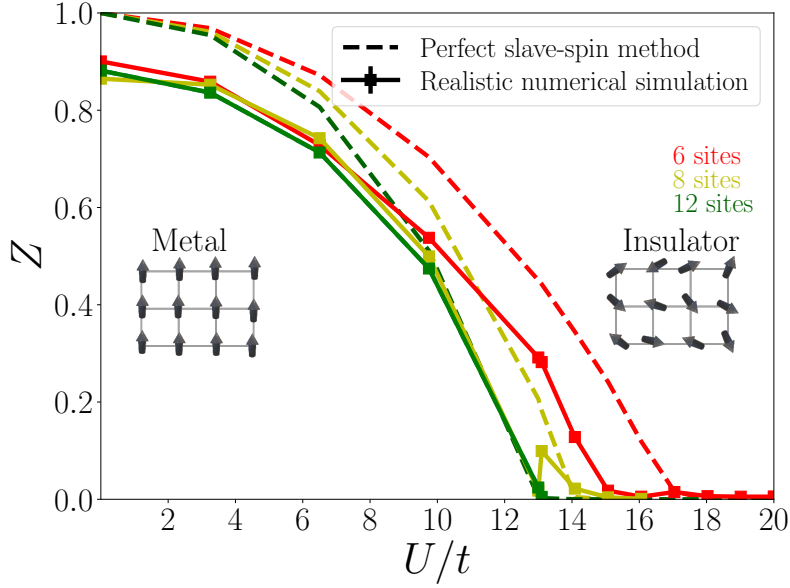


Figure 5.2: *Mott transition observed with the slave-spin method on a realistic numerical simulation of Rydberg atoms device.* The characteristics of the device considered are $t_{\max} = 4 \mu\text{s}$, $\gamma = 0.02$ MHz, $N_s = 150$, $\epsilon = \epsilon' = 3\%$ and $k = 5$. The error bar is calculated from the errors of ϵ and N_s .

cluster, $\bar{J} = \frac{1}{N_p} \sum_{\langle i,j \rangle \in \mathcal{C}} J_{i,j}$ is the average nearest-neighbor coupling (N_p is the number of nearest-neighbor links inside the cluster) and $\bar{m} = \frac{1}{N} \sum_{i \in \mathcal{C}} \langle S_i^z \rangle$ is the average magnetization. This model needs to be solved iteratively by starting from a guess for the mean field \bar{m} . For a given value of this mean field, the finite spin problem defined by $H_s^{\mathcal{C}}$ is solved using a quantum algorithm (described below). This yields the correlation function $\langle S_i^z S_j^z \rangle$ and closes the self-consistent loop, which runs until convergence. At convergence, we can extract useful observables of the original Hubbard model. For instance, the quasiparticle weight Z of the original model, which measures the quantum coherence of the fermionic excitations, can be obtained via the spin model's magnetization: $Z = \bar{m}^2$ (we also have access to site-resolved magnetizations $\langle S_i^z \rangle$ and hence site-resolved quasiparticle weights).

5.3.1 Details of the main equations

We choose the most simple form of slave spins, introduced in (Rüegg et al., 2010). We recall its main steps below. We replace the fermionic operator d^\dagger by the tensor product of a pseudo fermion operator (that follows the same anticommutation rules as d^\dagger) and an auxiliary spin field

$$d_{i\sigma}^\dagger = S_i^z f_{i\sigma}^\dagger, \quad (5.4)$$

where S_i^z is the Pauli-Z operator at site i (later S_i^a , with $a \in \{x, y, z\}$, will denote the Pauli spin operators), and $f_{i\sigma}^\dagger$ and $f_{i\sigma}$ denote fermionic operators called pseudo-fermions. The d and f operators obey fermionic anticommutation relations due to the spin commutation relations.

By substituting, in H_{Hubbard} , the original fermionic operators by new spin and pseudo fermion degrees of freedom, we effectively enlarge the Hilbert space where the new Hamiltonian, H'_{Hubbard} , acts. In practice, we want to map the original problem H_{Hubbard} to a Hilbert space of same size by looking at a restriction of the new Hamiltonian, H'_{Hubbard} , on a restricted portion of the new Hilbert state, which is called the physical subspace. This is achieved by imposing a constraint: on

each site i , we impose the relation (Rüegg et al., 2010):

$$\left(n_{i\uparrow}^f + n_{i\downarrow}^f - 1\right)^2 = \frac{S_i^x + 1}{2} \quad (5.5)$$

to hold for the "physical states". Among the eight possible local states, only four states (*i.e.* the same number of original local states) verify this constraint:

$$|n_i^d = 0\rangle = |S^x = 1, n_i^f = 0\rangle, \quad (5.6a)$$

$$|n_{i,\sigma}^d = 1\rangle = |S^x = -1, n_{i,\sigma}^f = 1\rangle, \quad \sigma = \uparrow, \downarrow \quad (5.6b)$$

$$|n_i^d = 2\rangle = |S^x = 1, n_i^f = 2\rangle. \quad (5.6c)$$

Assuming this constraint is satisfied in the physical subspace, we can transform the original Hubbard Hamiltonian, expressed as

$$\begin{aligned} H_{\text{Hubbard}} &= \sum_{i,j,\sigma} t_{i,j} d_{i\sigma}^\dagger d_{j\sigma} + \frac{U}{2} \sum_i (n_i^d - 1)^2 \\ &+ \left(\mu - \frac{U}{2}\right) \sum_i n_i^d, \end{aligned} \quad (5.7)$$

to the following transformed Hamiltonian:

$$\begin{aligned} H'_{\text{Hubbard}} &= \sum_{i,j,\sigma} t_{i,j} S_i^z S_j^z f_{i,\sigma}^\dagger f_{j,\sigma} + \frac{U}{2} \sum_i \left(\frac{S_i^x + 1}{2}\right) \\ &+ \left(\mu - \frac{U}{2}\right) \sum_i (n_{i,\uparrow}^f + n_{i,\downarrow}^f), \end{aligned} \quad (5.8)$$

via substitution of equality (5.5) in the interaction term of (5.7). It is straightforward to see that $n_i^d = n_i^f$ considering (5.6). At this point, no approximations have been made.

The next step is then to decouple fermions and spins with a mean-field approach

$$\begin{aligned} S_i^z S_j^z f_{i,\sigma}^\dagger f_{j,\sigma} &\approx \langle S_i^z S_j^z \rangle f_{i,\sigma}^\dagger f_{j,\sigma} + S_i^z S_j^z \langle f_{i,\sigma}^\dagger f_{j,\sigma} \rangle - \\ &\langle S_i^z S_j^z \rangle \langle f_{i,\sigma}^\dagger f_{j,\sigma} \rangle. \end{aligned} \quad (5.9)$$

Therefore, Eq. (5.8) can be expressed as a sum of two Hamiltonians (neglecting constant terms and considering half-filling) $H'_{\text{Hubbard}} = H_s + H_f$ with $H_s = \sum_{i,j} t_{i,j} \langle f_{i,\sigma}^\dagger f_{j,\sigma} \rangle S_i^z S_j^z + \frac{U}{4} \sum_i S_i^x$, an Ising-like transverse-field Hamiltonian (TFIM) and $H_f = \sum_{i,j,\sigma} t_{i,j} \langle S_i^z S_j^z \rangle f_{i,\sigma}^\dagger f_{j,\sigma}$ describing the free renormalized electrons. The correlators $\langle f_{i,\sigma}^\dagger f_{j,\sigma} \rangle$ and $\langle S_i^z S_j^z \rangle$ are obtained via auto-coherent loops until convergence is reached.

5.3.2 Fulfillment of the constraint

When performing loops described above, one must ensure that the constraint Eq. 5.5 is imposed on each site. In practice, the mean-field simplification leads to

$$\langle (n_{i,\uparrow}^f + n_{i,\downarrow}^f - 1)^2 \rangle_f = \left\langle \frac{S_i^x + 1}{2} \right\rangle_s. \quad (5.10)$$

This equality can be enforced on all sites by using a Lagrange multiplier λ_i : one adds a term $H_\lambda = \sum_i \lambda_i ((n_i - 1)^2 - \frac{S_i^x + 1}{2})$ to $H_s + H_f$ and optimizes the corresponding cost function.

In particle-hole symmetric cases (which includes our setting, namely the single-orbital, half-filled Hubbard model on a square—*i.e.* bipartite—lattice), λ_i should be zero to respect the symmetry of the energy spectrum around 0 (Schiró & Fabrizio, 2011; W.-W. Yang et al., 2019).

5.3.3 Variants: Towards a multiorbital case

The Z_2 slave spin theory used here is one among others.

Another related slave-spin approach (de'Medici et al., 2005; Hassan & de'Medici, 2010) consists in enlarging the Hilbert space with the spin operator $S_{i,\sigma}^z$ such as

$$d_{i,\sigma}^\dagger = f_{i,\sigma}^\dagger S_{i,\sigma}^z \quad (5.11)$$

In this method, the physical states are $|n_{i,\sigma}^d = 1\rangle \Leftrightarrow |n_{i,\sigma}^f = 1, S_{i,\sigma}^z = 1\rangle$ and $|n_{i,\sigma}^d = 0\rangle \Leftrightarrow |n_{i,\sigma}^f = 0, S_{i,\sigma}^z = -1\rangle$. The constraint to be satisfied to only span physical states is then $n_{i,\sigma} = S_{i,\sigma}^z + \frac{1}{2}$.

While this method lends itself quite naturally to multiorbital models (see e.g (de'Medici et al., 2005)), the additional σ dependency of the slave-spin operators (compared to the Z_2 slave spins considered in our work) leads to an effective model which is more difficult to relate to existing experimental platforms.

5.4 Solution of the two coupled subproblems

In this section, we show how we solve numerically Eq. (5.2a) and Eq. (5.2b) to obtain matrices J and Q . For H_s , we describe the embedding of the cluster mean-field theory.

5.4.1 Solving the fermionic Hamiltonian H_f for J : Bogoliubov method

To compute $J_{i,j}$, we need to compute the one-particle density matrix

$$G_{i,j}^\sigma =_{\text{f}} \langle \psi_0 | f_{i,\sigma}^\dagger f_{j,\sigma} | \psi_0 \rangle_{\text{f}}. \quad (5.12)$$

H_f can be rewritten as a matrix product:

$$H_f = F^\dagger Q F \quad (5.13)$$

with $F^\dagger = (f_{1,\downarrow}^\dagger, f_{1,\uparrow}^\dagger, f_{2,\downarrow}^\dagger, \dots)$ and Q a Hermitian, $N \times N$, matrix. Q can be diagonalized numerically: $Q = LDL^\dagger$, with $D = \text{diag}\{\lambda_1, \lambda_2, \dots, \lambda_N\}$. If the number of sites is even, the trace of D vanishes and we obtain as many $\lambda_i < 0$ as $\lambda_i > 0$. It leads to define $C^\dagger = F^\dagger L \iff C = L^\dagger F$ and a diagonal form of H_f is obtained

$$H_f = \sum_{i,\sigma} \lambda_i c_{i,\sigma}^\dagger c_{i,\sigma}. \quad (5.14)$$

The ground-state energy of this Hamiltonian is the sum of negative λ_i and the groundstate is then a Slater determinant $|0101\dots 01\rangle_C$ in the c basis with 1 corresponding to negative energies and 0 otherwise. To go back in the f basis, one can use the L matrices:

$$G_{i,j}^\sigma = \langle \psi_0 | \sum_{k,k',\sigma} L_{k,i}^\dagger L_{j,k'} c_{k,\sigma}^\dagger c_{k',\sigma} | \psi_0 \rangle \quad (5.15)$$

$$= \sum_{k,k',\sigma} \delta_{k,k'} L_{k,i}^\dagger L_{j,k'} \langle c_{k,\sigma}^\dagger c_{k',\sigma} \rangle \quad (5.16)$$

$$= \sum_{k,\sigma} L_{i,k}^* n_{k,\sigma} L_{k,j}^t. \quad (5.17)$$

with $n_{k,\sigma}$ equal to 1 for k indices where $\lambda_k < 0$. Numerically, it means that only matrices L and eigenvalues λ_i are needed to compute J . This part can be dealt with a classical quantum computer

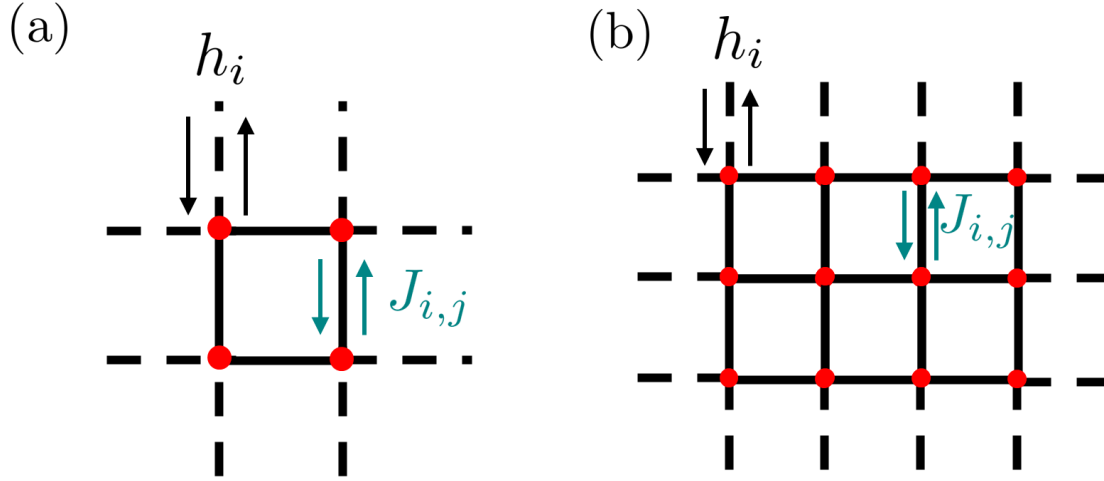


Figure 5.3: Schematic representation of the cluster geometry for (a) $N = 4$ sites and (b) 12 sites. The dashed black lines represent the interaction with the surrounding mean-field whereas the full black line show the interactions within the cluster. In the twelve sites lattice, the two sites inside the cluster do not interact with the mean-field.

as it has a polynomial complexity. Going into the thermodynamic limit makes it easier as the system is really translation invariant and the Hamiltonian is then diagonal in the Fourier space. In our work, we choose to solve H_f considering boundaries to show the effect of a finite-size system on the method. Further developments could be done to simplify this step and consider an infinite-size system.

5.4.2 Solving the spin Hamiltonian via a cluster mean-field approach

We now focus on the computation of $Q_{i,j}$. It requires the computations of the spin-spin correlation function $\langle S_i^z S_j^z \rangle$.

We consider a cluster of N_x columns and N_y rows (see Fig. 5.3 for an example) surrounded by a mean field. The number of sites in the cluster is then $N = N_x \times N_y$.

The cluster mean-field approximation leads to

$$S_i^z S_j^z \approx \langle S_i^z \rangle S_j^z + \langle S_j^z \rangle S_i^z - \langle S_i^z \rangle \langle S_j^z \rangle, \quad (5.18)$$

where i (j) is inside the cluster at the border of it and j (i) is not. The mean-field parameter $\langle S_i^z \rangle$ is the same for all sites in the thermodynamic limit. As we consider finite-size systems, we numerically compute

$$\bar{m} = \frac{1}{N} \sum_{i=1}^N \langle S_i^z \rangle. \quad (5.19)$$

This mean magnetization will be the one outside the cluster following a self-consistent loop.

Therefore, $\sum_{i,j} J_{i,j} S_i^z S_j^z = \sum_{i,j} J_{i,j} (m S_j^z + m S_i^z) = m \sum_{i,j} J_{i,j} (S_j^z + S_i^z)$, neglecting constant terms. However, the matrix element $J_{i,j}$ is not known for a site i inside the cluster and a site j outside of it. In the thermodynamic limit, all $J_{i,j}$ are equals as it is the one-particle density matrix of a free fermionic system. We can thus take the mean value of all $J_{i,j}$ for nearest neighbors inside the cluster to guess the interaction between sites inside and outside the cluster. Let's then define

$$\bar{J} = \frac{1}{N_p} \sum_{\langle i,j \rangle} J_{i,j} \quad (5.20)$$

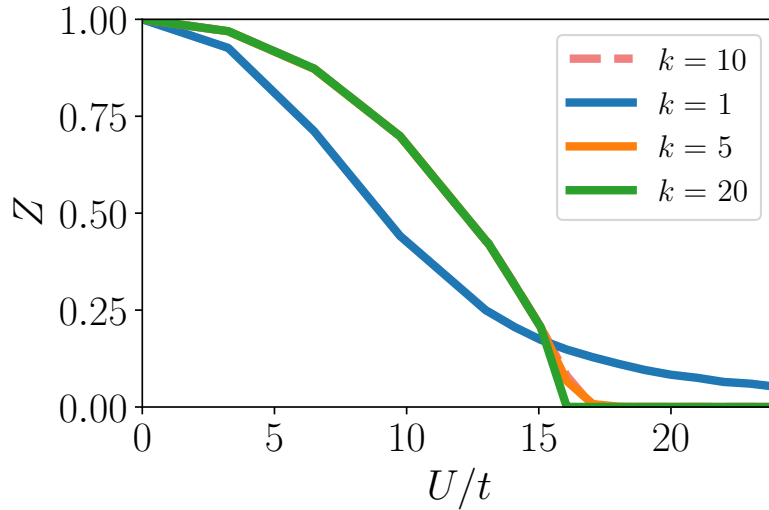


Figure 5.4: *Impact of imposed number of loops k in the slave-spin mean-field theory for a cluster of $N = 4$ sites. The resolution method is annealing and all sources of error are neglected.*

where the sum goes all over nearest neighbors in the cluster and N_p is the number of such pairs. In the square lattice, each site has 4 nearest neighbors. We can define a number z_i which is the number of neighbors outside the cluster for site i . For example, this number is equal to 0 for a site which has 4 neighbors inside the cluster.

Finally we obtain a mean-field term

$$\sum_{i \in \mathcal{C}} h_i S_i^z = 2\bar{J}\bar{m} \sum_{i \in \mathcal{C}} z_i S_i^z \quad (5.21)$$

and we obtain Eq. (5.3).

5.4.3 Convergence of the self-consistent loop

The self-consistent procedure to solve the inner loop is first to guess an initial value for the magnetization m_0 , then to solve Eq. (5.3) and calculate $\bar{m} = \frac{1}{N} \sum_i \langle S_i^z \rangle$ in the groundstate obtained. The loop goes on until a convergence criteria is reached. In our simulation, two criteria are used: the number of inner loop and outer loop can be narrowed by a number k (so the total number of loop allowed is $k \times k$). The second criteria is the norm of the difference between Q at step $l-1$ and Q at step l for the outer loop and the norm of the difference between \bar{m} at step $l-1$ and \bar{m} at step l for the inner loop. We choose a value η such as the loop stop if one of the two norm is lower than η . in our simulation we choose $\eta = 0.01$. The evolution of Z as a function of iterations is shown in Fig. 5.5 for a cluster of $N = 6$ sites, $k = 10$ and $\eta = 10^{-6}$. Different initial guess for \bar{m} are tested and they all converge toward the same value which states for the robustness of the method. The convergence takes more time close to the transition value. The impact of the number of loops k imposed is shown in Fig. 5.4.

5.5 Quantum algorithm for the spin Hamiltonian.

Let us turn to the solution of the (cluster) spin problem, $H_s^{\mathcal{C}}$. It is nothing but the transverse-field Ising model, which has recently been claimed to be a potential candidate problem for reaching quantum advantage using gate-based quantum processors (Kim et al., 2023). As it turns out, its

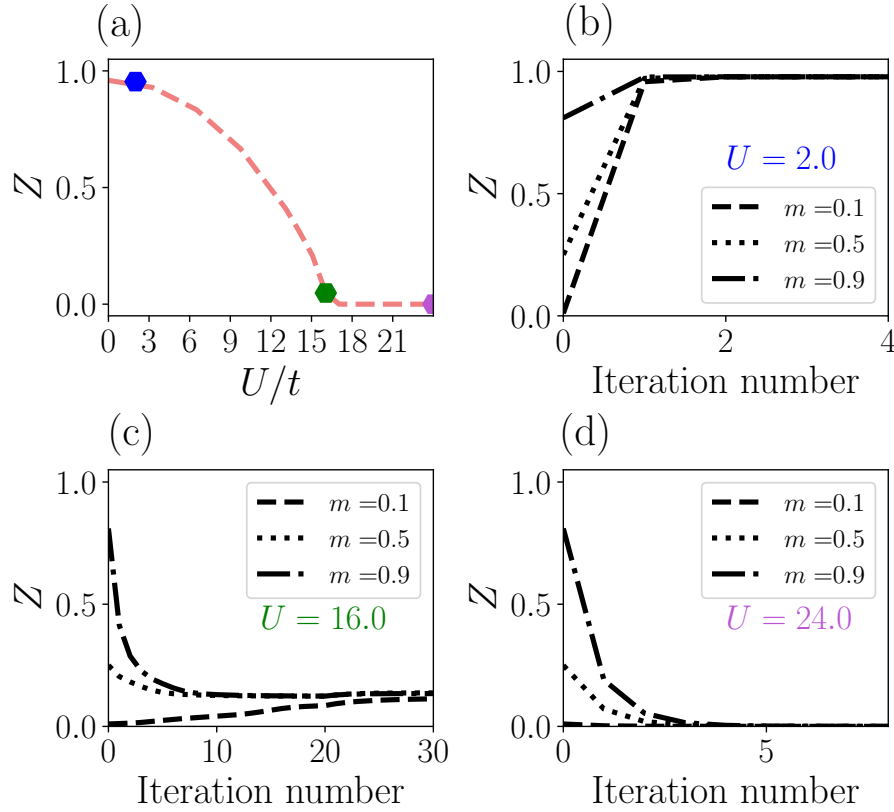


Figure 5.5: *Evolution of Z as a function of loop iterations for a 6 sites embedding.* (a) Mott transition for a 3×3 cluster where three points are highlighted. The convergence of these points ((b) $U/t = 2.0$, (c) $U/t = 16.0$ and (d) $U/t = 24.0$) during the slave-spin mean-field procedure is shown for different initial guess of the mean field \bar{m} (0.1, 0.5 and 0.9). The solving method is annealing where all source of noise are neglected. The number of allowed iteration is increased to 100 but the x-axis are limited to convergence in the three panels for sake of clarity and the error accepted is $\eta = 10^{-5}$.

form is very similar to the Hamiltonian realized experimentally by Rydberg atoms trapped with optical tweezers (Browaeys & Lahaye, 2020):

$$H_{\text{Rydberg}} = \sum_{i \neq j} \frac{C_6}{|\mathbf{r}_i - \mathbf{r}_j|^6} \hat{n}_i \hat{n}_j + \frac{\hbar \Omega(\tau)}{2} \sum_i \hat{S}_i^x - \hbar \delta(\tau) \sum_i \hat{n}_i, \quad (5.22)$$

where $\Omega(\tau)$ and $\delta(\tau)$ are the time-dependent Rabi and detuning drives, and C_6 the magnitude of the interatomic van der Waals interactions; $\hat{n}_i = (I + S_i^z)/2$. The main difference between H_{Rydberg} and H_s^C is the sign of the interaction: it is positive for Rydberg atoms, negative (since usually $t_{i,j} < 0$) for the slave spin problem. We can nevertheless make use of the Rydberg platform: instead of looking for its ground state, we are going to be looking for its most excited state, which we attain using an annealing procedure: we start from drive parameters $\Omega(\tau = 0) = 0$ and a large negative $\delta(\tau = 0)$ so that the system's native initial state $|\psi_{\text{start}}\rangle = |g\rangle^{\otimes N}$ is the most excited state of the initial Hamiltonian. We then, over a long enough annealing time, linearly ramp the Rabi and detuning drives to reach the final values $\hbar \Omega(\tau_{\text{max}}) = \frac{U}{2}$, $\hbar \delta_i(\tau_{\text{max}}) = \sum_{j \neq i} \frac{C_6}{r_{i,j}^6} + 4\bar{J}\bar{m}z_i$. Provided we can, in addition, optimize the atom positions in such a way that $\frac{C_6}{r_{i,j}^6} \approx -4J_{i,j}$ (details about this optimization are in Sec. 5.6.1), the final Hamiltonian will be $-H_s^C$. Hence, following the adiabatic theorem (applied to the most excited state), the procedure should (approximately) bring the system to the most excited state of $-H_s^C$ and hence the ground state of H_s^C . We can finally measure the spin-spin correlation function on this state.

5.6 Solving the spin model with a Rydberg platform: details

In order to solve Eq. (5.3), we propose to use the Ising Hamiltonian Eq. (5.22) generated by Rydberg atoms device.

As discussed in the main text, this is achieved via an annealing procedure whose final Hamiltonian is supposed to be as close as possible to the Hamiltonian whose ground state correlations functions we want to compute.

In this section, we discuss in more detail the annealing procedure and the deviations from the ideal case that we take into account.

5.6.1 Optimization of the geometry

The Hamiltonian we are considering, Eq. (5.3), displays a self-consistently determined spin coupling matrix $J_{i,j}$, while the Hamiltonian that is controlled in the experiment displays a van der Waals interaction term $\sum_{j \neq i} \frac{C_6}{r_{i,j}^6}$. This section explains how we optimize the atom positions to make both couplings match as much as possible.

Our goal is to minimize the cost function

$$\mathcal{D} = \sqrt{\sum_{i,j} \left(\frac{C_6}{|r_{i,j}|^6} + 4J_{i,j} \right)^2}. \quad (5.23)$$

We use the conjugate gradient descent algorithm from the `scipy` library (Virtanen et al., 2020) with the following initial guess for the geometry: we place the atoms on a square lattice where the distance between nearest-neighbor atoms is $r_{\text{init}} = \max_{i,j} \left(\frac{C_6}{|4J_{i,j}|} \right)^{\frac{1}{6}}$.

The evolution of \mathcal{D} as a function of the number of sites in the cluster is shown Fig. 5.6. The optimization of the positions does not lead to a vanishing \mathcal{D} . In practice, the gradient descent algorithm can be trapped in numerous local minima, leading to a poor approximation of $-4J_{i,j}$ by the interaction matrix element. In addition, difficulties can arise directly from the symmetries of

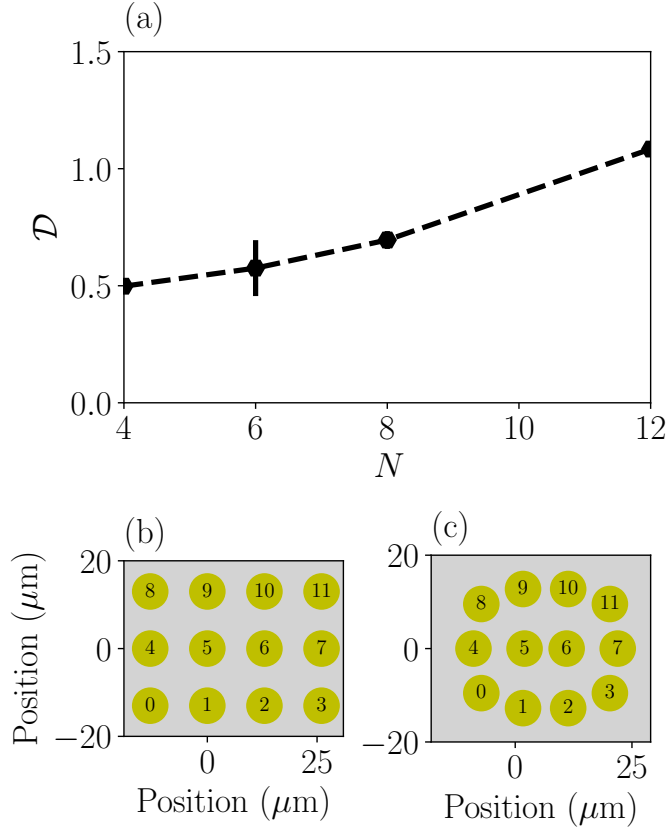


Figure 5.6: *Optimization of geometry for an implementation on real device.* (a) Mean value of the cost function \mathcal{D} (Eq. 5.23) for different cluster size at $U = 13.1$ MHz. The error bar shows the standard deviation over all \mathcal{D} values encountered during loops. (b) Initial position of the atoms before optimization for a $N = 12$ sites cluster in the last outer loop of the slave-spin mean-field method at $U = 13.1$ MHz. (c) Position of atoms after the optimization of the geometry to minimize \mathcal{D} .

the initial cluster guess. For instance, in the case of a 2×2 cluster, if distance between nearest-neighbors is called a , the distance between next nearest neighbors is always $a/\sqrt{2}$ whereas it should be 0 for our model since $J_{i,j} = 0$ for next nearest neighbors. Therefore, in most cases, \mathcal{D} is not exactly zero and finding the best geometry is not an easy task.

Despite these imperfections, it seems that the impact of considering an imperfect optimization of the geometry (leading to a nonzero \mathcal{D}) does not lead to significant changes. In Fig. 5.8, we show the outcome of the equilibrium and out-of-equilibrium computations with a "perfect geometry" (assuming the coupling is actually $J_{i,j}$) and an imperfect geometry. For the Mott transition, differences can be seen to be negligible for $N = 4$ cluster sites. For the dynamical behavior, we can observe a change in amplitude but the frequency remains the same as for the slave-spin mean-field interactions. To illustrate the outcome of the optimization procedure, we also show an example of initial and optimized position for $N = 12$ cluster sites in Fig. 5.6. One can observe that the final pattern is slightly distorted compared to the translation-invariant initial pattern. This is due to the fact that the couplings at the edges of the cluster differ from the ones in the "bulk" of the cluster to account for the cluster's environment. As the cluster size grows, these edge effects will have less and less influence, and the optimization will become easier and easier.

Thus, we can conclude that the geometry optimization yields reasonably faithful interactions.

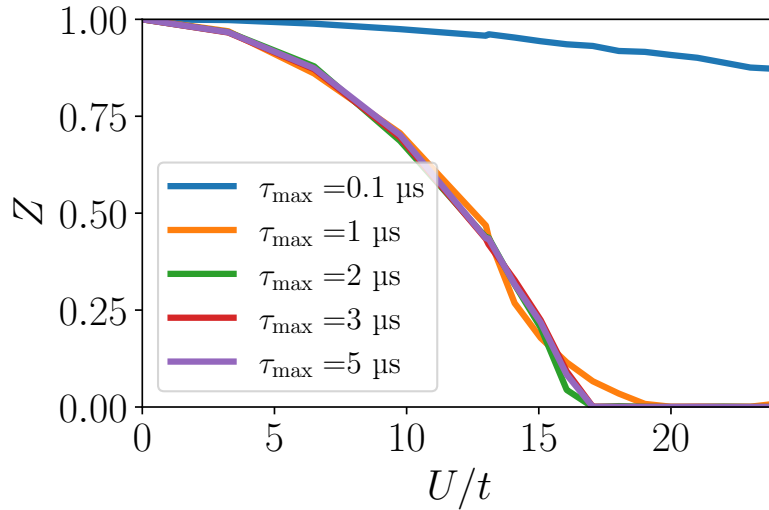


Figure 5.7: *Impact of total annealing time for a cluster of $N = 4$ sites. All other sources of error are neglected.*

5.6.2 Details of the annealing schedule

Once the geometry is found, the atoms are prepared in the state $|\psi_{\text{start}}\rangle = |g\rangle^{\otimes N}$. The following Hamiltonian is the one applied at $\tau = 0$

$$H_{\text{start}} = \sum_{i \neq j} \frac{C_6}{|\mathbf{r}_i - \mathbf{r}_j|^6} \hat{n}_i \hat{n}_j - \hbar \delta_{\text{start}} \sum_i n_i \quad (5.24)$$

where δ_{start} is set to -5 MHz so that $|\psi_{\text{start}}\rangle$ is the most excited state of (5.24). The Rabi frequency and the detuning are then driven during a time τ_{max} to reach the Hamiltonian $-H_s^C$. A global addressing is performed for the Rabi frequency and for the detuning.

Following the procedure described in the main text, the Rabi frequency starts at 0 MHz and is driven linearly to $\frac{U}{2}$ ($\hbar\Omega(\tau_{\text{max}}) = \frac{U}{2}$). Similarly, the detunings are all prepared at a value δ_{start} and are driven separately to values $\hbar\delta_i(\tau_{\text{max}}) = \sum_{j \neq i} \frac{C_6}{r_{i,j}^6} + 4\bar{J}\bar{m}z_i$.

The effect of annealing time is shown in Fig. 5.7. Starting from $\tau_{\text{max}} = 3 \mu\text{s}$, the impact seems to be insignificant. In our simulations, we choose $\tau_{\text{max}} = 4 \mu\text{s}$ to ensure a good convergence.

To perform the study of the dynamics in the Hubbard model, we need to quench the value of the Rabi term. In practice, the quench is not instantaneous. In Fig. 5.9, we investigate the effect of the finite switch-on time τ_{ramp} on the Rabi and detuning. We see that this time impacts the frequency of the signal for $\tau_{\text{ramp}} \geq 0.3 \mu\text{s}$. At the actual device specifications $\tau_{\text{ramp}} \approx 0.05 \mu\text{s}$, the effects are negligible.

5.6.3 Experimental imperfections

The algorithm described in the main text is designed to work on actual neutral atoms devices. As they are NISQ computer, it is necessary to evaluate effects of noise and limitations on the results of the method. In the following, methods to emulate noise are described and implemented in our code.

All numerical simulations are performed with the library QuTiP (Johansson et al., 2013) (exact diagonalization) and the Quantum Learning Machine. The SPAM error is implemented with a code from Pulser (Silvério et al., 2022).

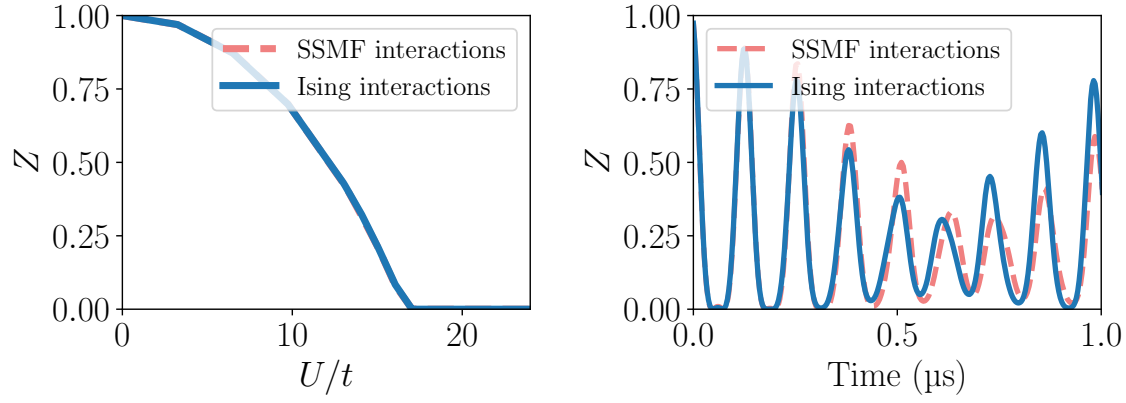


Figure 5.8: *Impact of considering a realistic geometry on a cluster of $N = 4$ sites. Left: Comparison of Z values between method with the real matrix J and the optimized one for 4 sites. Right: Z dynamics after a quench $U_f = 13$ MHz with the same comparison. All other sources of noise are neglected.*

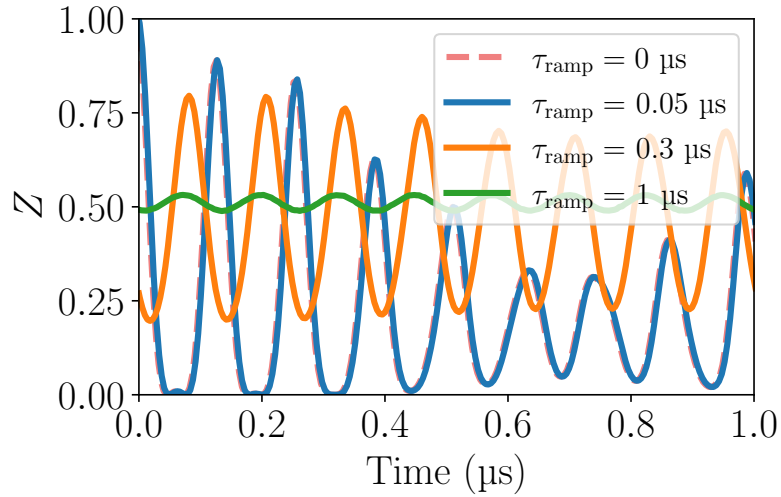


Figure 5.9: *Impact of switch-on time τ_{ramp} in the quench dynamic for a cluster of $N = 4$ sites. We consider $U_f = 13$ MHz. All other sources of error are neglected.*

Dephasing noise

Decoherence during the annealing procedure is described via the Lindblad master equation (following (Lienhard et al., 2018)):

$$\frac{d\rho}{d\tau} = -i[H(\tau), \rho] - \frac{1}{2} \sum_{i=1}^N \gamma_i \left[\{L_i^\dagger L_i, \rho\} - 2L_i \rho L_i^\dagger \right] \quad (5.25)$$

where ρ is the density matrix describing the mixed state of the system and $H(\tau)$ is the resource Hamiltonian at a time τ during the annealing. The jump operators L_i corresponding to dephasing are equal to n_i . We choose to simplify the problem by taking a single dephasing parameter $\gamma_i = \gamma$.

The effect of this noise is shown as a function of dephasing parameters in Fig. 5.10. For the quench dynamics, the dephasing damps the oscillations but do not change the frequency. We can see this behavior on the Mott transition where it is shifted for small values of U/t for larger γ .

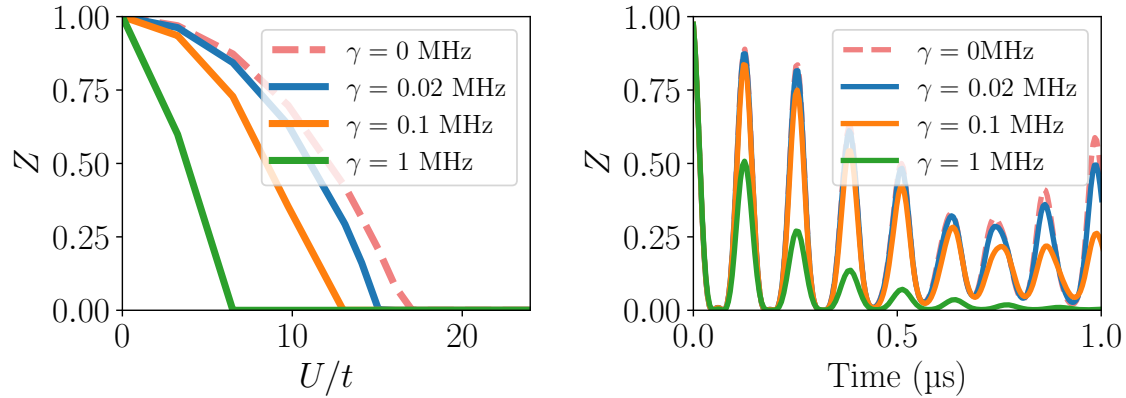


Figure 5.10: *Effect of dephasing noise on the result of for a cluster of $N = 4$ sites. Left: Impact on the Mott phase transition. All other sources of noise are neglected. Right: Impact on the quench dynamic for $U_f = 13$ MHz. The color code is the same as for the top panel.*

Sampling and measurement error

We simulate the sampling of states as in Rydberg atoms device by picking randomly N_s times a bitstring with a probability equal to the probability to measure this bitstring in the z -basis on the device. The impact of such a procedure is shown Fig. 5.12 at equilibrium and out of equilibrium. The impact is negligible starting from $N_s \approx 100$. We model the readout error by a probability (in %) of error ϵ of detecting an atom in a state $|r\rangle$ instead of its real state $|g\rangle$ and ϵ' of not detecting an excited atom. Experimentally, these values are around $2 \sim 3\%$ (de Léséleuc et al., 2018). We choose $\epsilon = \epsilon' = 3\%$ for both values in the main text. The impact of such error for $\epsilon = \epsilon'$ is shown in Fig. 5.11. Until $\epsilon \approx 5\%$, the behavior of the system remains the same.

5.7 Results at equilibrium

We implemented this self-consistent procedure with a realistic numerical simulation of the annealing algorithm used to solve the spin problem with Rydberg atoms. We repeated the computation for several values of the local Hubbard interaction U to obtain the evolution of the quasiparticle weight Z as a function of U , as shown in Fig. 5.2, for cluster sizes, and hence number of atoms, of 4, 6, 8 and 12. The major experimental limitations were considered in order to account for the

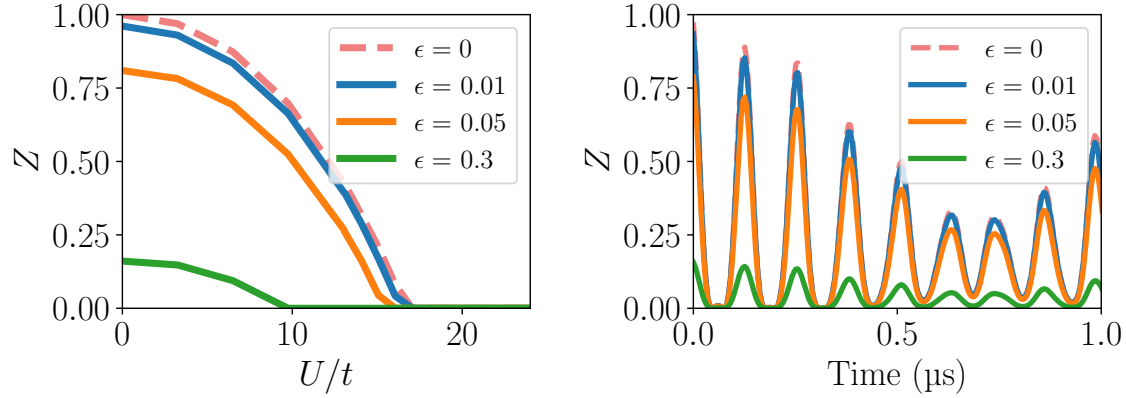


Figure 5.11: *Impact of measurement error for a cluster of $N = 4$ sites. Left:* shows the effect of $\epsilon = \epsilon'$ at equilibrium and *right:* out of equilibrium for $U_f = 13$ MHz. The number of shots considered for each measurement is 10^6 . All other sources of noise are neglected.

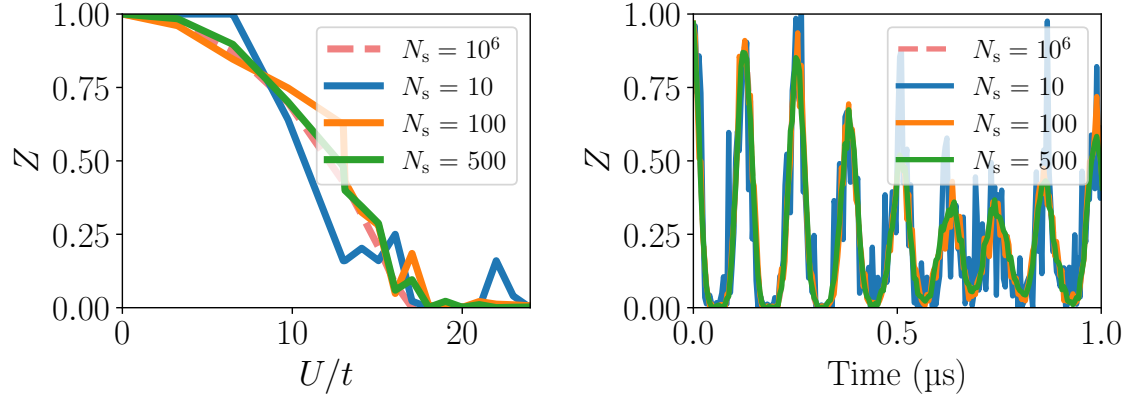


Figure 5.12: *Impact of different sampling rate N_s on measured states for a cluster of $N = 4$ sites. Left:* at equilibrium and *right:* out of equilibrium ($U_f = 13$ MHz). All other sources of error are neglected.

true potential of current devices: dephasing noise, shot noise, measurement error, global detuning, finite annealing times τ_{max} and imperfect positioning of the atoms to reproduce the right magnetic coupling (see Sec. 5.6 for more details). Despite these limitations, leading to few points being far from the noiseless result due to error repetitions within all loops, the quasiparticle weight we obtain (solid lines) is fairly close to the one obtained with a perfect solution of the spin model (dashed lines). The Rydberg platform can thus be used to get a reasonable estimate of the Mott transition, i.e the value U_c when Z vanishes and the systems turns Mott insulating. While for the half-filled, single-band model studied in this proof-of-concept example, classical methods can be implemented to efficiently solve the spin model (see e.g (Schuler et al., 2016)), other regimes are less readily amenable to a controlled classical computation: doped regimes, multi-orbital models, and dynamical regimes. We investigate the latter regime in the next paragraph.

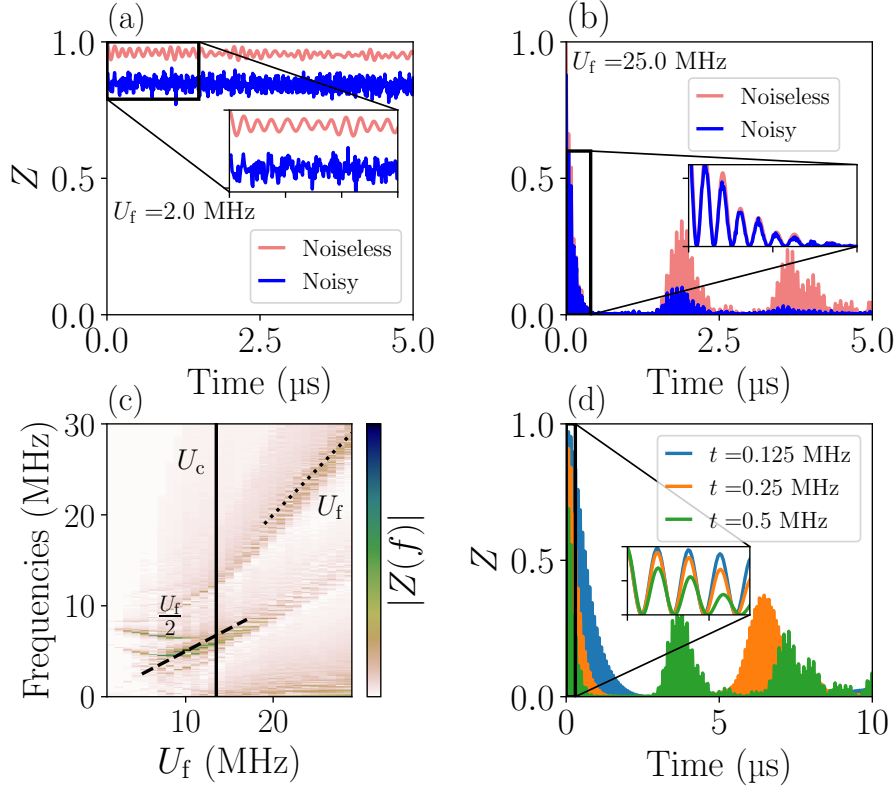


Figure 5.13: *Dynamical response of the quasiparticle weight after an interaction quench.* $N = 12$ spin cluster. Time evolution of Z for (a) $U_f = 2$ MHz and (b) $U_f = 25$ MHz. The red line shows the noiseless annealing solution and the blue line a realistic numerical simulation on Rydberg atoms device ($\gamma = 0.02$ MHz, $\epsilon = \epsilon' = 3\%$, $N_s = 150$ shots, realistic Ising interactions and a global detuning are imposed). (c) Fourier transform amplitude $|Z(f)|$ for several U_f . The vertical black line shows the equilibrium critical value U_c as computed from Fig. 5.2. (d) Impact of the hopping terms t on the damping of the response of Z after a quench ($U_f = 13 \approx U_c$). The blue, orange and green lines represent the result for $t = 0.125$, 0.25 and 0.5 MHz, respectively.

5.8 Dynamics of the Hubbard model with the slave-spin method

We thus turn to a dynamical setting to emphasize the potential advantage brought by the use of quantum processors when used within this slave-spin framework. Starting from a noninteracting ground state ($U = 0$), we suddenly switch on the value of the local interaction to a final value U_f . Our goal is to validate that the method solved with a physically realizable quantum processor can recover the phenomenology observed in previous experimental and theoretical studies of quenched Hubbard systems (Eckstein et al., 2009; Greiner et al., 2002; Iyer et al., 2014; Kollath et al., 2007; Lacki & Heyl, 2019; Riegger et al., 2015; Schachenmayer et al., 2011; Schiró & Fabrizio, 2011; Will et al., 2015; W.-W. Yang et al., 2019), to wit: collapse and revival oscillations of various observables in the $U_f \gg U_c$ regime, with a $2\pi/U_f$ period, and a damping that increases with bandwidth. In the $U_f \ll U_c$ regime, overdamped oscillations have been observed (see (Eckstein et al., 2009) for instance).

5.8.1 Dynamics in slave-spin theory

In this subsection, we review how the slave-spin formalism extends to the time-dependent case.

After the introduction of the slave variables, we are considering the Hamiltonian:

$$H'_{\text{Hubbard}} = \sum_{i,j} S_i^z S_j^z f_i^\dagger f_j + \frac{U}{4} \sum_i S_i^x \quad (5.26)$$

(Eq. (5.8) at half-filling and neglecting the constants). At the mean-field level, the time-dependent solution of the Schrödinger equation is of the form $|\Psi(\tau)\rangle = |\Phi_f(\tau)\rangle |\Psi_s(\tau)\rangle$ with $|\Phi_f(\tau)\rangle$ (the time will be defined as τ to avoid confusion with the hopping) governed by a Schrödinger evolution with time-dependent Hamiltonians:

$$\begin{aligned} H_f(t) &= \sum_{i,j} t_{i,j} \langle S_i^z S_j^z \rangle(\tau) f_i^\dagger f_j \\ H_s(\tau) &= \sum_{i,j} t_{i,j} S_i^z S_j^z \langle f_i^\dagger f_j \rangle(\tau) + \frac{U}{4} \sum_i S_i^x. \end{aligned} \quad (5.27)$$

The initial state is of the form $|\Psi(\tau=0)\rangle = |\Phi_f(\tau=0)\rangle |\psi_s(\tau=0)\rangle$ with $|\Phi_f(\tau=0)\rangle$ (respectively $|\psi_s(\tau=0)\rangle$) the ground states of $H_f(\tau < 0)$ (respectively $H_s(\tau < 0)$) found with the mean-field slave-spin procedure. To solve these coupled equations, we a priori need to compute correlators $\langle S_i^z S_j^z \rangle(\tau)$ and $\langle f_i^\dagger f_j \rangle(\tau)$ and use them to construct $H_f(\tau)$ and $H_s(\tau)$. We should then evolve the wavefunctions to obtain correlators for a time $\tau + d\tau$ and so on.

In fact, as stated in (Schiró & Fabrizio, 2011), the dynamics of the pseudo-fermions is trivial if our system is translation invariant (i.e. $t_{i,j} = t_{i-j}$). In this case, indeed, $\langle S_i^z S_j^z \rangle(\tau) = g_{i-j}(\tau)$. Thus,

$$H_f(\tau) = \sum_{i,j} t_{i-j} g_{i-j}(\tau) f_i^\dagger f_j. \quad (5.28)$$

This Hamiltonian is then diagonal in the Fourier space

$$H_f(\tau) = \sum_k \epsilon_k(\tau) f_k^\dagger f_k, \quad (5.29)$$

with $\epsilon_k(\tau)$ the Fourier transform of $t_{i-j} g_{i-j}(\tau)$, and $n_k = f_k^\dagger f_k$, with $f_k \propto \sum_i e^{ikR_i} f_i$. We denote as $|\Phi_\alpha\rangle$ the Fock states of the system associated with the transformed operators, f_k . They are the eigenstates of $H_f(\tau)$ at any time τ .

The initial state $|\Phi_{\alpha_0}\rangle$ is the ground state of the system. Let's consider the time evolution of an arbitrary state $|\Phi_f(\tau)\rangle$, we can decompose $|\Phi_f(\tau)\rangle = \sum_{\alpha} c_{\alpha}(\tau) |\Phi_{\alpha}\rangle$. Therefore,

$$\begin{aligned} \sum_{\alpha} i\partial_t c_{\alpha}(\tau) |\Phi_{\alpha}\rangle &= \sum_{\alpha} c_{\alpha}(\tau) H_f(\tau) |\Phi_{\alpha}\rangle \\ &= \sum_{\alpha} c_{\alpha}(\tau) E_{\alpha}(\tau) |\Phi_{\alpha}\rangle \end{aligned} \quad (5.30)$$

One can project onto $\langle \Phi_{\alpha}(\tau) |$:

$$i\partial_t c_{\alpha}(\tau) = c_{\alpha}(\tau) E_{\alpha}(\tau). \quad (5.31)$$

Thus, $c_{\alpha}(\tau) = c_{\alpha}(\tau = 0) e^{-i \int_0^{\tau} E_{\alpha}(\tau') d\tau'}$.

Therefore, starting from the groundstate, for $\alpha \neq \alpha_0$, $c_{\alpha}(\tau) = 0$ and $c_{\alpha_0}(\tau) = e^{-i\phi(\tau)}$. At the end of the day,

$$|\Phi_f(\tau)\rangle = e^{-i\phi(\tau)} |\Phi_f(\tau = 0)\rangle \quad (5.32)$$

and the renormalized fermionic system remains in the groundstate up to global phase, meaning that $\langle f_i^{\dagger} f_j \rangle(\tau) = \langle f_i^{\dagger} f_j \rangle_0$ is independent of time. This enables us to only consider the correlator $\langle S_i^z S_j^z \rangle(\tau)$ during the quench.

5.8.2 Frequency dependency on eigenenergies

The link between eigenenergies of $H(U_f)$ and the frequency of oscillations can be derived: the initial state is $|\psi_s(\tau < 0)\rangle$, the groundstate of $H_s(U = 0)$. We can decompose it in the basis of $H(U_f)$ eigenstates: $|\psi_s(\tau < 0)\rangle = \sum_k a_k |E_k\rangle$ where $|E_k\rangle$ are eigenstates of $H(U_f)$ corresponding to an eigenenergy E_k . Let's now consider the value of an observable \hat{O} through time. We obtain:

$$\begin{aligned} \langle \hat{O} \rangle(\tau) &= \langle \psi_s(\tau < 0) | e^{iH(U_f)\tau} \hat{O} e^{-iH(U_f)\tau} | \psi_s(\tau < 0) \rangle \\ &= \sum_{k,k'} a_k^* a_{k'} \langle E_k | e^{iH(U_f)\tau} \hat{O} e^{-iH(U_f)\tau} | E_{k'} \rangle \\ &= \sum_{k,k'} a_k^* a_{k'} e^{i(E_k - E_{k'})\tau} \langle E_k | \hat{O} | E_{k'} \rangle \end{aligned} \quad (5.33)$$

Therefore, frequencies of oscillations of any observable only depend on differences between eigenenergies of $H(U_f)$.

5.8.3 Dynamics and constraint fulfillment

In the Z_2 slave-spin theory, one can define the projector $Q_i = \left(\frac{S_i^x + 1}{2} - (n_i - 1)^2 \right)^2 = \frac{1 + S_i^x e^{i\pi n_i}}{2}$ such that $Q_i |\Psi\rangle = 0$ iff $|\Psi\rangle$ respects the constraint Eq. (5.6). Using the fact that $[H'_{\text{Hubbard}}, \prod_i Q_i] = 0$, the constraint is fulfilled during the quench dynamics because $\prod_i Q_i |\Psi(\tau = 0)\rangle = 0$ (see (Rüegg et al., 2010; Schiró & Fabrizio, 2011) for more details).

5.8.4 Results out of equilibrium

Here, we look for this phenomenology in the time evolution of the quasiparticle weight Z . Within slave-spin applied to the single-site Hubbard model at half-filling, interaction quenches are particularly simple to implement: translation invariance on the lattice makes the dynamics of pseudo-fermions trivial when starting from an eigenstate (Schiró & Fabrizio, 2011). Thus, only the dynamics of the spin model are of interest: the procedure boils down to quenching the value of the transverse field in Eq. (5.3) from 0 to $U_f/4$. On our target Rydberg platform, this means switching the Rabi frequency from zero up to the desired value to obtain U_f . In practice, the switch-on

time is not instantaneous but very fast (about 50 ns to switch from 0 MHz to $U_f = 2$ MHz). One can directly measure $\langle S_i^z \rangle$ on the device for different evolution times. The main limiting factor is thus the measurement rate, in addition to the aforementioned sources of noise. In Fig. 5.13, we show the oscillations we observe numerically for a cluster of 12 sites, with and without noise. The upper panels present the oscillation of Z as function of time after a quench to $U_f = 13$ MHz (a) and to $U_f = 25$ MHz (b). From Fig. 5.2, we know that the phase transition for such a cluster is $U_c \approx 13.5$. In the case of $U_f = 25$ MHz ($U_f \gg U_c$), we clearly observe the damped oscillations, whether in the noiseless or the noisy setting. Because of dephasing noise of the experiment, the agreement between the noiseless and noisy curve becomes worse with time. However, during the first μ s of observations, we recover the perfect signal and the estimation of the oscillation frequency is possible (insets in (a) and (b)). For $U_f = 13$ MHz ($U_f \approx U_c$), we see that Z quickly reaches a value ≈ 0.1 (slightly higher than the Z obtained for this value of U at equilibrium), around which it oscillates. Panel (c) exhibits the Fourier transform of $Z(\tau)$ for various U_f for the exact slave-spin method (namely with an exact solution of the spin model). For $U_f < U_c$, components at $\omega = U_f/2$ can be identified along with other contributions, while for $U_f > U_c$, $\omega = U_f$ end up dominating the spectrum. This is expected from the physics of the Mott transition in the Hubbard model: above the transition, the single-particle spectrum displays a Mott gap of U_f , while below it excitations between the quasiparticle band and the emerging Hubbard bands (with energy $U_f/2$), and within the quasiparticle band, are possible. Finally, panel (d) confirms the expected increase of the damping of oscillations with the hopping strength t .

5.9 Conclusion

In this work, we introduced a hybrid quantum-classical method to study the equilibrium and dynamics of a prototypical model for strongly correlated fermions, the Hubbard model. Our method makes use of a spin-based quantum processor but does not suffer from the usual overheads of translating fermionic problems to spin problems, namely long quantum evolutions (due to nonlocal spin terms) or auxiliary quantum degrees of freedom. This is made possible by the use of an existing advanced mapping, the slave-spin method, that turns the difficult fermionic problem at hand into a free, and thus efficiently tractable, fermion problem that is self-consistently coupled to an interacting, yet *local* spin problem. This locality makes this spin problem well suited for current quantum processors based on spins (aka qubits).

Here, to solve the spin problem, we turned to an *analog* quantum processor made of Rydberg atoms, as opposed to a *gate-based* quantum processor. Despite being a priori restricted—because of the limited number of knobs in the Hamiltonian—in the class of the problems that it can deal with, the Rydberg platform is particularly well suited for the spin problem at hand because its Hamiltonian can be made to almost exactly coincide with the effective spin Hamiltonian to be solved. Moreover, its analog character allows one to circumvent the usual issues associated with gate-based algorithms, like trotterization when performing time evolution, or the variational aspects inherent to many NISQ algorithms like VQE or its temporal counterparts. Finally, the number of Rydberg atoms that can be controlled in current experiments allow to tackle problem sizes that are very hard to reach using classical methods.

This proposal calls for many further investigations. An important step is an experimental validation with larger atom numbers than the 12 atoms we simulated here. Other future improvements involve the slave-spin method itself: doped regimes (relevant to cuprate materials), multiorbital models (relevant to iron-based superconductors, where orbital-selective effects may appear (de’Medici et al., 2005)) pose various technical difficulties that warrant further theoretical developments. In particular, the fulfillment of the constraint to ensure the states remain in the physical subspace becomes more difficult in these regimes than in the half-filled, single-band case that we studied here. Going beyond the mean-field decoupling of the pseudo-fermion and spin variables is also another interesting avenue.

Chapter 6

Summary and outlook

Quantum simulation is a potential very strong tool to solve plenty of problems. One of the most promising field is the simulation of materials and many-body systems. Indeed, quantum simulator are often using many-body system to perform computation and the first idea that comes to mind is to map real-life materials problem onto the many-body system of the simulator. The digital approach, despite being very flexible and promising for all types of problems, is still limited to small number of noisy qubit and the gates fidelity has not reached yet the famous three "9" (99.9%) when several gates are piled up. For all these reasons, I choose to develop analog quantum algorithm during my thesis having in mind an experimental realization during or soon after my PhD.

The Rydberg platform offers a way to simulate many-body physics up to hundreds of spins with a great fidelity. The two Hamiltonian one can implement on it are at the center of the study of magnetism and spin dynamics. It is therefore a logical choice to develop quantum algorithm on this platform for simulating materials and electronic systems of interest.

Quantum chemistry During the course of my PhD, I have strongly collaborated with the company PASQAL. From this collaboration we have proposed a new hybrid algorithm which combines a digital and an analog approach. This algorithm has been numerically tested on the H_2 , LiH and BeH_2 molecules. For the H_2 molecule, we are using the "XY" interaction of the neutral atoms as it shares common symmetries with the molecular Hamiltonian. This leads to obtain the groundstate of the molecule with a great precision. For the two other molecules, the geometry of the atom array is optimized with respect to selected features of the molecular Hamiltonian transformed into a qubit Hamiltonian with a qubit-fermion mapping. The pulse sequence is designed to have a constant duration and to increase the number of parameters. This leads to enhance the expressibility of the quantum "circuit" during the whole procedure and at the same time, avoid the impact of the choice of the initial parameters. Each step of the variational procedure performs a derandomization energy estimation. This method allows to reduce drastically the number of measurement needed to estimate the energy of an Hamiltonian. We show that one can estimate the groundstate energy of the molecules for several molecular inter-atomic distances to a few percent points of error ($\approx 5\%$).

Simulating strong fermionic correlations in the 2D-Hubbard model The second half of my PhD was dedicated to develop an new hybrid algorithm to simulate a Fermi-Hubbard model at and out of equilibrium on a RQP. This work is the result of a strong collaboration with the company EVIDEN/ATOS and PASQAL. The algorithm is based on the slave-spin approach: a condensed-matter method to map the complexity of the Fermi-Hubbard model into an Ising-like model. To this aim, the original problem Hilbert space is enlarged by adding a "slave" spin to each site of the model. In order to restrain the problem to the physical space, a constraint on the

occupation and slave-spin values on each site has to be fulfilled. The crucial part is now to perform a mean-field approximation to decouple fermionic and slave spin degrees of freedom. This leads to approximate the original Hamiltonian as a sum of a free-fermions Hamiltonian and an Ising-like Hamiltonian. This two Hamiltonian are self-correlated. We choose to solve this model on a square bipartite lattice to elude the constraint. The free-fermions system can be solved classically with a polynomial complexity. The Ising-like Hamiltonian is solved by a cluster mean-field approach. Spin-spin correlators are computed to obtain a new kinetic term for the fermionic Hamiltonian. Fermionic correlators are then computed to obtain the new spin interaction term of the Ising Hamiltonian. The self-correlated loop goes on until convergence.

This method is used to compute numerically the Mott transition of the Hubbard model at equilibrium. We show that we can simulate the Ising-like Hamiltonian on RQP to calculate the correlators and one can recover the Mott transition even if a noisy experimental implementation is considered. The dynamical behavior of the Hubbard model can also be studied in the slave-spin paradigm. The observation of out-of-equilibrium Fermi-Hubbard behavior is very difficult classically and being able to do it on a RQP could be a proof of a quantum advantage.

Perspectives Our work paves the way of quantum computing for electronic structure simulation with a quantum simulator. The two proposed hybrid algorithms are implementable on a NISQ computer, the RQP, and therefore can be run on real device really soon. This work is one of the first step toward simulation of fermionic many-body problems on analog quantum simulators made of arrays of neutral atoms.

Experimentally, both algorithms developed in this manuscript could be implemented on real device today. The digital-analog eigensolver for chemistry is bounded by the number of measurements and therefore sticks to the constraint of a RQP. The next step could be to anticipate and mitigate well known errors (de Léséleuc et al., 2018) of the architecture to ensure the success of an experimental implementation. In addition, more complex molecules could be treated with the hundreds of atoms available on today's devices. The slave-spin method should be run experimentally really soon and I look forward the result as it could bring a potential quantum advantage in this field. I show in appendix B that this method can be implemented for a triangular lattice if the constraint is fulfilled and the half-filling condition is imposed. In addition, it is possible to add orbitals to site (see Sec. 5.3.3) and hence, distinguish sites by the number of orbitals and obtain "effective" atoms. One can therefore think of placing several multiorbitals 2D layers in parallel and as a result, modelling an effective 3D material. This could be a way to simulate paramagnetism in austenitic steel for instance.

On the theoretical side, improving the efficiency of the digital-analog variational eigensolver for chemistry could lead to being able to reach the ground-state energy of any Hamiltonian which can be described as sum of Pauli strings. Therefore, one can think of time-dependent Hamiltonian for instance and solve it with this method at each time step. This is a path toward simulating chemical reaction in oxides or in PV. A lot of work can still be done with the slave-spin approach in understanding more deeply the involvement of performing a mean-field approximation between electrons and slave spins degrees of freedom. The constraint is also a major point to ensure the theoretical validity of the method and further studies could be done to generalize its fulfillment on every lattices.

Beyond that, it is far from a forgone conclusion that QC will replace actual "classical" simulation methods of electronic structures which benefit from dozen of years of studies and improvements. Therefore, a smart use of QC could be to improve this classical method in terms of precision and/or computing capacity. For instance, QC results for small or medium systems with only few dozens qubits could be use as input parameters of a DFT computation, provided that "good" physical quantities can be extracted from the quantum simulation. Another approach would be to compute a large part of the system's Hamiltonian with DFT and add corrections with QC which simulates a small part of the systems with more correlations. This embedding approach is an active field of research (C. Cao et al., 2023; B. Huang et al., 2022; W. Li et al., 2022; Rossmannek et al., 2023;

Tilly et al., 2021; Vorwerk et al., 2022; H. Wang et al., 2011) and results of the work presented here could be a first step to improve ab initio simulations in chemistry and materials. Finally, QC could help directly classical simulations by computing directly Green's function (Endo et al., 2020) in DMFT or encoding the occupation number in orbitals in DFT (Senjean et al., 2023).

Bibliography

- Abrams, D. S., & Lloyd, S. (1997). Simulation of Many-Body Fermi Systems on a Universal Quantum Computer. *Physical Review Letters*, *79*(13), 2586–2589. <https://doi.org/10.1103/PhysRevLett.79.2586> (cit. on p. 27).
- Abrikosov, I. A., Ponomareva, A. V., Steneteg, P., Barannikova, S. A., & Alling, B. (2016). Recent progress in simulations of the paramagnetic state of magnetic materials. *Current Opinion in Solid State and Materials Science*, *20*(2), 85–106. <https://doi.org/10.1016/j.cossms.2015.07.003> (cit. on pp. 13, 17, 18).
- Adjanor, G., Bugat, S., Domain, C., & Barbu, A. (2010). Overview of the RPV-2 and INTERN-1 packages: From primary damage to microplasticity. *Journal of Nuclear Materials*, *406*, 175–186. <https://doi.org/10.1016/j.jnucmat.2009.09.006> (cit. on p. 10).
- Albash, T., & Lidar, D. A. (2018). Adiabatic quantum computation. *Reviews of Modern Physics*, *90*(1), 015002. <https://doi.org/10.1103/RevModPhys.90.015002> (cit. on p. 37).
- Alet, F., Damle, K., & Pujari, S. (2016). Sign-Problem-Free Monte Carlo Simulation of Certain Frustrated Quantum Magnets. *Physical Review Letters*, *117*(19), 197203. <https://doi.org/10.1103/PhysRevLett.117.197203> (cit. on p. 22).
- Alling, B., Marten, T., & Abrikosov, I. A. (2010). Effect of magnetic disorder and strong electron correlations on the thermodynamics of CrN. *Physical Review B*, *82*(18), 184430. <https://doi.org/10.1103/PhysRevB.82.184430> (cit. on p. 7).
- Amin, M. H. (2015). Searching for quantum speedup in quasistatic quantum annealers. *Physical Review A*, *92*(5), 052323. <https://doi.org/10.1103/PhysRevA.92.052323> (cit. on p. 37).
- Anand, A., Schleich, P., Alperin-Lea, S., Jensen, P. W. K., Sim, S., Díaz-Tinoco, M., Kottmann, J. S., Degroote, M., Izmaylov, A. F., & Aspuru-Guzik, A. (2022). A quantum computing view on unitary coupled cluster theory. *Chemical Society Reviews*, *51*(5), 1659–1684. <https://doi.org/10.1039/D1CS00932J> (cit. on p. 40).
- Anderson, P. W. (1961). Localized Magnetic States in Metals. *Physical Review*, *124*(1), 41–53. <https://doi.org/10.1103/PhysRev.124.41> (cit. on p. 17).
- Anderson, P. W. (1987). The Resonating Valence Bond State in La₂CuO₄ and Superconductivity. *Science*, *235*(4793), 1196–1198. <https://doi.org/10.1126/science.235.4793.1196> (cit. on p. 19).
- Andrei, E. Y., Efetov, D. K., Jarillo-Herrero, P., MacDonald, A. H., Mak, K. F., Senthil, T., Tutuc, E., Yazdani, A., & Young, A. F. (2021). The marvels of moiré materials. *Nature Reviews Materials*, *6*(3), 201–206. <https://doi.org/10.1038/s41578-021-00284-1> (cit. on p. 69).
- Anisimov, V. I., Aryasetiawan, F., & Lichtenstein, A. I. (1997). First-principles calculations of the electronic structure and spectra of strongly correlated systems: The LDA+ U method. *Journal of Physics: Condensed Matter*, *9*(4), 767. <https://doi.org/10.1088/0953-8984/9/4/002> (cit. on p. 17).
- Apolloni, B., Cesa-Bianchi, N., & De Falco, D. (1990). A numerical implementation of “quantum annealing”. *Stochastic Processes, Physics and Geometry: Proceedings of the Ascona-Locarno Conference*, 97–111 (cit. on p. 37).
- Argüello-Luengo, J., González-Tudela, A., Shi, T., Zoller, P., & Cirac, J. I. (2019). Analogue quantum chemistry simulation. *Nature*, *574*(7777), 215–218 (cit. on p. 70).

- Arovas, D. P., Berg, E., Kivelson, S. A., & Raghu, S. (2022). The hubbard model. *Annual Review of Condensed Matter Physics*, *13*(1), null. <https://doi.org/10.1146/annurev-conmatphys-031620-102024> (cit. on p. 18).
- Arrasmith, A., Cerezo, M., Czarnik, P., Cincio, L., & Coles, P. J. (2021). Effect of barren plateaus on gradient-free optimization. *Quantum*, *5*, 558. <https://doi.org/10.22331/q-2021-10-05-558> (cit. on p. 36).
- Aspect, A., Grangier, P., & Roger, G. (1982). Experimental realization of einstein-podolsky-rosen-bohm gedankenexperiment: A new violation of bell’s inequalities. *Phys. Rev. Lett.*, *49*, 91–94. <https://doi.org/10.1103/PhysRevLett.49.91> (cit. on p. 22).
- Ayral, T. (2015, September). *Nonlocal Coulomb Interactions and Electronic Correlations: Novel Many-Body Approaches* [Doctoral dissertation, Ecole Polytechnique]. (Cit. on p. 21).
- Ayral, T., Besserve, P., Lacroix, D., & Guzman, E. A. R. (2023). Quantum computing with and for many-body physics, 1–51 (cit. on p. 69).
- Balducci, F., Gambassi, A., Lerosé, A., Scardicchio, A., & Vanoni, C. (2023). Interface dynamics in the two-dimensional quantum Ising model. *Physical Review B*, *107*(2), 024306. <https://doi.org/10.1103/PhysRevB.107.024306> (cit. on p. 117).
- Balents, L. (2010). Spin liquids in frustrated magnets. *Nature*, *464*(7286), 199–208. <https://doi.org/10.1038/nature08917> (cit. on p. 48).
- Banchi, L., & Crooks, G. E. (2021). Measuring Analytic Gradients of General Quantum Evolution with the Stochastic Parameter Shift Rule. *Quantum*, *5*, 386. <https://doi.org/10.22331/q-2021-01-25-386> (cit. on p. 51).
- Barison, S., Vicentini, F., & Carleo, G. (2021). An efficient quantum algorithm for the time evolution of parameterized circuits. *Quantum*, *5*, 512. <https://doi.org/10.22331/q-2021-07-28-512> (cit. on p. 33).
- Barkoutsos, P. K., Nannicini, G., Robert, A., Tavernelli, I., & Woerner, S. (2020). Improving Variational Quantum Optimization using CVaR. *Quantum*, *4*, 256. <https://doi.org/10.22331/q-2020-04-20-256> (cit. on p. 51).
- Baroni, S., de Gironcoli, S., Dal Corso, A., & Giannozzi, P. (2001). Phonons and related crystal properties from density-functional perturbation theory. *Reviews of Modern Physics*, *73*(2), 515–562. <https://doi.org/10.1103/RevModPhys.73.515> (cit. on p. 18).
- Barredo, D., Labuhn, H., Ravets, S., Lahaye, T., Browaeys, A., & Adams, C. S. (2015). Coherent Excitation Transfer in a Spin Chain of Three Rydberg Atoms. *Physical Review Letters*, *114*(11), 113002. <https://doi.org/10.1103/PhysRevLett.114.113002> (cit. on p. 45).
- Barredo, D., Lienhard, V., de Léséleuc, S., Lahaye, T., & Browaeys, A. (2018). Synthetic three-dimensional atomic structures assembled atom by atom. *Nature*, *561*(7721), 79–82. <https://doi.org/10.1038/s41586-018-0450-2> (cit. on pp. 44, 63).
- Barrera, G. D., Colognesi, D., Mitchell, P. C. H., & Ramirez-Cuesta, A. J. (2005). LDA or GGA? A combined experimental inelastic neutron scattering and ab initio lattice dynamics study of alkali metal hydrides. *Chemical Physics*, *317*(2), 119–129. <https://doi.org/10.1016/j.chemphys.2005.04.027> (cit. on p. 17).
- Bartlett, R. J., Kucharski, S. A., & Noga, J. (1989). Alternative coupled-cluster ansätze II. The unitary coupled-cluster method. *Chemical Physics Letters*, *155*(1), 133–140. [https://doi.org/10.1016/S0009-2614\(89\)87372-5](https://doi.org/10.1016/S0009-2614(89)87372-5) (cit. on pp. 34, 55).
- Bauer, B., Bravyi, S., Motta, M., & Kin-Lic Chan, G. (2020). Quantum Algorithms for Quantum Chemistry and Quantum Materials Science. *Chemical Reviews*, *120*(22), 12685–12717. <https://doi.org/10.1021/acs.chemrev.9b00829> (cit. on p. 69).
- Becquart, C. S., & Domain, C. (2011). Modeling Microstructure and Irradiation Effects. *Metallurgical and Materials Transactions A*, *42*(4), 852–870. <https://doi.org/10.1007/s11661-010-0460-7> (cit. on p. 10).
- Bengone, O., Alouani, M., Blöchl, P., & Hugel, J. (2000). Implementation of the projector augmented-wave LDA + U method: Application to the electronic structure of NiO. *Physical Review B*, *62*(24), 16392 (cit. on p. 17).

- Bharti, K., Cervera-Lierta, A., Kyaw, T. H., Haug, T., Alperin-Lea, S., Anand, A., Degroote, M., Heimonen, H., Kottmann, J. S., Menke, T., Mok, W.-K., Sim, S., Kwek, L.-C., & Aspuru-Guzik, A. (2022). Noisy intermediate-scale quantum algorithms. *Rev. Mod. Phys.*, *94*, 015004. <https://doi.org/10.1103/RevModPhys.94.015004> (cit. on pp. 32, 35, 70).
- Bidzhiev, K., Wennersteen, A., Beji, M., Dagrada, M., D’Arcangelo, M., et al. (2023). Cloud on-demand emulation of quantum dynamics with tensor networks. *arXiv:2302.05253* (cit. on p. 63).
- Biermann, S., Poteryaev, A., Lichtenstein, A. I., & Georges, A. (2005). Dynamical Singlets and Correlation-Assisted Peierls Transition in VO₂. *Physical Review Letters*, *94*(2), 026404. <https://doi.org/10.1103/PhysRevLett.94.026404> (cit. on p. 21).
- Birkel, C., Roberts, M., McTurk, E., Bruce, P., & Howey, D. (2017). Degradation diagnostics for lithium ion cells. *Journal of Power Sources*, *341*, 373–386. <https://doi.org/10.1016/j.jpowsour.2016.12.011> (cit. on pp. 8, 18).
- Bloch, I., Dalibard, J., & Zwirger, W. (2008). Many-body physics with ultracold gases. *Reviews of modern physics*, *80*(3), 885 (cit. on p. 70).
- Blöte, H. W. J., & Deng, Y. (2002). Cluster Monte Carlo simulation of the transverse Ising model. *Physical Review E*, *66*(6), 066110. <https://doi.org/10.1103/PhysRevE.66.066110> (cit. on p. 117).
- Bluvstein, D., Omran, A., Levine, H., Keesling, A., Semeghini, G., Ebadi, S., Wang, T. T., Michailidis, A. A., Maskara, N., Ho, W. W., Choi, S., Serbyn, M., Greiner, M., Vuletić, V., & Lukin, M. D. (2021). Controlling quantum many-body dynamics in driven Rydberg atom arrays. *Science*, *371*(6536), 1355–1359. <https://doi.org/10.1126/science.abg2530> (cit. on pp. 46, 70).
- Boll, M., Hilker, T. A., Salomon, G., Omran, A., Nespolo, J., Pollet, L., Bloch, I., & Gross, C. (2016). Spin- and density-resolved microscopy of antiferromagnetic correlations in Fermi-Hubbard chains. *Science*, *353*(6305), 1257–1260. <https://doi.org/10.1126/science.aag1635> (cit. on p. 69).
- Bonet-Monroig, X., Wang, H., Vermetten, D., Senjean, B., Moussa, C., Bäck, T., Dunjko, V., & O’Brien, T. E. (2023). Performance comparison of optimization methods on variational quantum algorithms. *Physical Review A*, *107*(3), 032407. <https://doi.org/10.1103/PhysRevA.107.032407> (cit. on p. 35).
- Bravyi, S. B., & Kitaev, A. Y. (2002). *Fermionic quantum computation*. *Ann. Phys.*, *298*, 210. <https://doi.org/10.1006/aphy.2002.6254> (cit. on pp. 38, 39, 53, 69).
- Browaeys, A., & Lahaye, T. (2020). Many-body physics with individually controlled Rydberg atoms. *Nature Physics*, *16*(2), 132–142. <https://doi.org/10.1038/s41567-019-0733-z> (cit. on pp. 41, 42, 43, 50, 53, 70, 78).
- Brown, P. T., Guardado-Sanchez, E., Spar, B. M., Huang, E. W., Devereaux, T. P., & Bakr, W. S. (2020). Angle-resolved photoemission spectroscopy of a Fermi-Hubbard system. *Nature Physics*, *16*(1), 26–31. <https://doi.org/10.1038/s41567-019-0696-0> (cit. on p. 109).
- Burke, K. (2012). Perspective on density functional theory. *The Journal of Chemical Physics*, *136*(15), 150901. <https://doi.org/10.1063/1.4704546> (cit. on p. 18).
- Cao, C., Sun, J., Yuan, X., Hu, H.-S., Pham, H. Q., & Lv, D. (2023). Ab initio quantum simulation of strongly correlated materials with quantum embedding. *npj Computational Materials*, *9*(1), 1–11. <https://doi.org/10.1038/s41524-023-01045-0> (cit. on p. 89).
- Cao, Y., Romero, J., Olson, J. P., Degroote, M., Johnson, P. D., Kieferová, M., Kivlichan, I. D., Menke, T., Peropadre, B., Sawaya, N. P. D., Sim, S., Veis, L., & Aspuru-Guzik, A. (2019). Quantum Chemistry in the Age of Quantum Computing. *Chemical Reviews*, *119*(19), 10856–10915. <https://doi.org/10.1021/acs.chemrev.8b00803> (cit. on pp. 32, 69).
- Cerezo, M., Arrasmith, A., Babbush, R., Benjamin, S. C., Endo, S., et al. (2020). Variational quantum algorithms. *quant-ph arXiv*, (2012.09265) (cit. on p. 51).
- Cerezo, M., Arrasmith, A., Babbush, R., Benjamin, S. C., Endo, S., Fujii, K., McClean, J. R., Mitarai, K., Yuan, X., Cincio, L., & Coles, P. J. (2021). Variational quantum algorithms.

- Nature Reviews Physics*, 3(9), 625–644. <https://doi.org/10.1038/s42254-021-00348-9> (cit. on pp. 32, 35, 117).
- Cerezo, M., Sone, A., Volkoff, T., Cincio, L., & Coles, P. J. (2021). Cost function dependent barren plateaus in shallow parametrized quantum circuits. *Nature Communications*, 12(1), 1791. <https://doi.org/10.1038/s41467-021-21728-w> (cit. on pp. 33, 51).
- Chapter 3 Dynamical, extended dynamical, and cluster dynamical mean-field theories: (DMFT, EDMFT, and cluster DMFT). (2008, January). In P. Misra (Ed.), *Handbook of Metal Physics* (pp. 23–49, Vol. 2). [https://doi.org/10.1016/S1570-002X\(08\)80005-5](https://doi.org/10.1016/S1570-002X(08)80005-5) (cit. on p. 21).
- Chen, C., Bornet, G., Bintz, M., Emperauger, G., Leclerc, L., Liu, V. S., Scholl, P., Barredo, D., Hauschild, J., Chatterjee, S., Schuler, M., Läuchli, A. M., Zaletel, M. P., Lahaye, T., Yao, N. Y., & Browaeys, A. (2023). Continuous Symmetry Breaking in a Two-dimensional Rydberg Array. *Nature*, 1–3. <https://doi.org/10.1038/s41586-023-05859-2> (cit. on pp. 41, 50, 70).
- Cheuk, L. W., Nichols, M. A., Lawrence, K. R., Okan, M., Zhang, H., Khatami, E., Trivedi, N., Paiva, T., Rigol, M., & Zwierlein, M. W. (2016). Observation of spatial charge and spin correlations in the 2D Fermi-Hubbard model. *Science*, 353(6305), 1260–1264. <https://doi.org/10.1126/science.aag3349> (cit. on p. 69).
- Cho, A. (2014). Quantum or not, controversial computer yields no speedup. *Science*, 344(6190), 1330–1331. <https://doi.org/10.1126/science.344.6190.1330> (cit. on p. 37).
- Choi, S., Bao, Y., Qi, X.-L., & Altman, E. (2020). Quantum Error Correction in Scrambling Dynamics and Measurement-Induced Phase Transition. *Physical Review Letters*, 125(3), 030505. <https://doi.org/10.1103/PhysRevLett.125.030505> (cit. on p. 28).
- Christiaen, B. (2018, May). *Modélisation multi-échelle de la déformation d’alliage de zirconium sous irradiation* [These de doctorat]. Université de Lille (2018-2021). (Cit. on p. 7).
- Coelho, W. d. S., D’Arcangelo, M., & Henry, L.-P. (2022). Efficient protocol for solving combinatorial graph problems on neutral-atom quantum processors. *arXiv:2207.13030* (cit. on pp. 58, 64).
- Coleman, P. (2015). *Introduction to Many-Body Physics*. Cambridge University Press. <https://doi.org/10.1017/CBO9781139020916> (cit. on p. 18).
- Colless, J. I., Ramasesh, V. V., Dahlen, D., Blok, M. S., Kimchi-Schwartz, M. E., McClean, J. R., Carter, J., de Jong, W. A., & Siddiqi, I. (2018). Computation of Molecular Spectra on a Quantum Processor with an Error-Resilient Algorithm. *Physical Review X*, 8(1), 011021. <https://doi.org/10.1103/PhysRevX.8.011021> (cit. on p. 32).
- Cong, I., Levine, H., Keesling, A., Bluvstein, D., Wang, S.-T., & Lukin, M. D. (2022). Hardware-Efficient, Fault-Tolerant Quantum Computation with Rydberg Atoms. *Physical Review X*, 12(2), 021049. <https://doi.org/10.1103/PhysRevX.12.021049> (cit. on p. 41).
- Dalyac, C., & Henriët, L. (2022). Embedding the mis problem for non-local graphs with bounded degree using 3d arrays of atoms. *arXiv:2209.05164* (cit. on p. 63).
- Dalyac, C., Henriët, L., Jeandel, E., Lechner, W., Perdrix, S., et al. (2020). Qualifying quantum approaches for hard industrial optimization problems. a case study in the field of smart-charging of electric vehicles. *quant-ph arXiv*, (2012.14859) (cit. on p. 51).
- Dalyac, C., Henriët, L., Jeandel, E., Lechner, W., Perdrix, S., et al. (2021). Qualifying quantum approaches for hard industrial optimization problems. A case study in the field of smart-charging of electric vehicles. *EPJ Quantum Technology*, 8(1), 1–27. <https://doi.org/10.1140/epjqt/s40507-021-00100-3> (cit. on pp. 11, 34, 56, 58, 59).
- Damascelli, A., Hussain, Z., & Shen, Z.-X. (2003). Angle-resolved photoemission studies of the cuprate superconductors. *Reviews of Modern Physics*, 75(2), 473–541. <https://doi.org/10.1103/RevModPhys.75.473> (cit. on p. 109).
- D’Ariano, G. M., Paris, M. G. A., & Sacchi, M. F. (2003, February). Quantum Tomography. <https://doi.org/10.48550/arXiv.quant-ph/0302028> (cit. on p. 28).

- de Léséleuc, S., Barredo, D., Lienhard, V., Browaeys, A., & Lahaye, T. (2018). Analysis of imperfections in the coherent optical excitation of single atoms to Rydberg states. *Physical Review A*, *97*(5), 053803. <https://doi.org/10.1103/PhysRevA.97.053803> (cit. on pp. 64, 82, 89).
- de Léséleuc, S., Lienhard, V., Scholl, P., Barredo, D., Weber, S., et al. (2019). Observation of a symmetry-protected topological phase of interacting bosons with Rydberg atoms. *Science*, *365*(6455), 775–780. <https://doi.org/10.1126/science.aav9105> (cit. on p. 48).
- de’Medici, L., Giovannetti, G., & Capone, M. (2014). Selective mott physics as a key to iron superconductors. *Phys. Rev. Lett.*, *112*, 177001. <https://doi.org/10.1103/PhysRevLett.112.177001> (cit. on p. 70).
- de’Medici, L., Georges, A., & Biermann, S. (2005). Orbital-selective Mott transition in multiband systems: Slave-spin representation and dynamical mean-field theory. *Physical Review B*, *72*(20), 205124. <https://doi.org/10.1103/PhysRevB.72.205124> (cit. on pp. 74, 87, 109, 114).
- Derby, C., & Klassen, J. (2020). A Compact Fermion to Qubit Mapping. *Physical Review B*, *104*(3), 035118. <https://doi.org/10.1103/PhysRevB.104.035118> (cit. on p. 70).
- Domain, C., & Becquart, C. S. (2001). Ab initio calculations of defects in fe and dilute fe-cu alloys. *Phys. Rev. B*, *65*, 024103. <https://doi.org/10.1103/PhysRevB.65.024103> (cit. on p. 8).
- Dorado, B., Freyss, M., Amadon, B., Bertolus, M., Jomard, G., & Garcia, P. (2013). Advances in first-principles modelling of point defects in uo2: F electron correlations and the issue of local energy minima. *Journal of Physics: Condensed Matter*, *25*(33), 333201 (cit. on p. 17).
- du Croo de Jongh, M. S. L., & van Leeuwen, J. M. J. (1998). Critical behavior of the two-dimensional Ising model in a transverse field: A density-matrix renormalization calculation. *Physical Review B*, *57*(14), 8494–8500. <https://doi.org/10.1103/PhysRevB.57.8494> (cit. on p. 117).
- Ebadi, S., et al. (2022). Quantum optimization of maximum independent set using rydberg atom arrays. *Science*, *376*(6598), 1209–1215. <https://doi.org/10.1126/science.abo6587> (cit. on pp. 50, 51, 56, 58, 59).
- Ebadi, S., Wang, T. T., Levine, H., Keesling, A., Semeghini, G., Omran, A., Bluvstein, D., Samajdar, R., Pichler, H., Ho, W. W., Choi, S., Sachdev, S., Greiner, M., Vuletić, V., & Lukin, M. D. (2021). Quantum phases of matter on a 256-atom programmable quantum simulator. *Nature*, *595*(7866), 227–232. <https://doi.org/10.1038/s41586-021-03582-4> (cit. on pp. 48, 70).
- Echenique, P., & Alonso, J. L. (2007). A mathematical and computational review of Hartree–Fock SCF methods in quantum chemistry. *Molecular Physics*, *105*(23-24), 3057–3098. <https://doi.org/10.1080/00268970701757875> (cit. on p. 14).
- Eckstein, M., Kollar, M., & Werner, P. (2009). Thermalization after an Interaction Quench in the Hubbard Model. *Physical Review Letters*, *103*(5), 056403. <https://doi.org/10.1103/PhysRevLett.103.056403> (cit. on p. 85).
- Ekholm, M., Zapolsky, H., Ruban, A. V., Vernyhora, I., Ledue, D., & Abrikosov, I. A. (2010). Influence of the Magnetic State on the Chemical Order-Disorder Transition Temperature in Fe-Ni Permalloy. *Physical Review Letters*, *105*(16), 167208. <https://doi.org/10.1103/PhysRevLett.105.167208> (cit. on p. 7).
- Elben, A., Vermersch, B., Roos, C. F., & Zoller, P. (2019). Statistical correlations between locally randomized measurements: A toolbox for probing entanglement in many-body quantum states. *Physical Review A*, *99*(5), 052323. <https://doi.org/10.1103/PhysRevA.99.052323> (cit. on p. 51).
- Endo, S., Cai, Z., Benjamin, S. C., & Yuan, X. (2021). Hybrid quantum-classical algorithms and quantum error mitigation. *J. Phys. Soc. Jpn.*, *90*, 032001. <https://doi.org/10.7566/JPSJ.90.032001> (cit. on p. 70).

- Endo, S., Kurata, I., & Nakagawa, Y. O. (2020). Calculation of the Green's function on near-term quantum computers. *Physical Review Research*, *2*(3), 033281. <https://doi.org/10.1103/PhysRevResearch.2.033281> (cit. on p. 90).
- Esler, K., Kim, J., Ceperley, D., & Shulenburger, L. (2012). Accelerating Quantum Monte Carlo Simulations of Real Materials on GPU Clusters. *Computing in Science & Engineering*, *14*(1), 40–51. <https://doi.org/10.1109/MCSE.2010.122> (cit. on p. 22).
- Esslinger, T. (2010). Fermi-Hubbard Physics with Atoms in an Optical Lattice. *Annual Review of Condensed Matter Physics*, *1*(1), 129–152. <https://doi.org/10.1146/annurev-conmatphys-070909-104059> (cit. on p. 69).
- Evered, S. J., Bluvstein, D., Kalinowski, M., Ebadi, S., Manovitz, T., Zhou, H., Li, S. H., Geim, A. A., Wang, T. T., Maskara, N., Levine, H., Semeghini, G., Greiner, M., Vuletic, V., & Lukin, M. D. (2023, April). High-fidelity parallel entangling gates on a neutral atom quantum computer. <https://doi.org/10.48550/arXiv.2304.05420> (cit. on pp. 41, 47).
- Ezratty, O. (2022). Understanding quantum technologies 2022. (Cit. on p. 9).
- Farhi, E., Goldstone, J., & Gutmann, S. (2014). A Quantum Approximate Optimization Algorithm. *arXiv:1411.4028* (cit. on pp. 34, 56).
- Fedorov, D. A., Peng, B., Govind, N., & Alexeev, Y. (2022). VQE method: A short survey and recent developments. *Materials Theory*, *6*(1), 2. <https://doi.org/10.1186/s41313-021-00032-6> (cit. on pp. 52, 117).
- Feynman, R. P. (1982). Simulating physics with computers. *International Journal of Theoretical Physics*, *21*(6-7), 467–488. <https://doi.org/10.1007/BF02650179> (cit. on pp. 8, 69).
- Finnila, A. B., Gomez, M. A., Sebenik, C., Stenson, C., & Doll, J. D. (1994). Quantum annealing: A new method for minimizing multidimensional functions. *Chemical Physics Letters*, *219*(5), 343–348. [https://doi.org/10.1016/0009-2614\(94\)00117-0](https://doi.org/10.1016/0009-2614(94)00117-0) (cit. on p. 37).
- Florens, S., & Georges, A. (2004). Slave-rotor mean-field theories of strongly correlated systems and the Mott transition in finite dimensions. *Physical Review B*, *70*(3), 035114. <https://doi.org/10.1103/PhysRevB.70.035114> (cit. on p. 110).
- Fokt, M. (2021, November). *Modelling microstructural evolution under irradiation and swelling of reactor internal structures* [These de doctorat]. universit  Paris-Saclay. (Cit. on p. 7).
- Fontana, E., Cerezo, M., Arrasmith, A., Rungger, I., & Coles, P. J. (2022). Non-trivial symmetries in quantum landscapes and their resilience to quantum noise. *Quantum*, *6*, 804. <https://doi.org/10.22331/q-2022-09-15-804> (cit. on p. 37).
- Fuhrmanek, A., Bourgain, R., Sortais, Y. R. P., & Browaeys, A. (2011). Free-Space Lossless State Detection of a Single Trapped Atom. *Physical Review Letters*, *106*(13), 133003. <https://doi.org/10.1103/PhysRevLett.106.133003> (cit. on p. 45).
- Gacon, J., Zoufal, C., Carleo, G., & Woerner, S. (2021). Simultaneous Perturbation Stochastic Approximation of the Quantum Fisher Information. *Quantum*, *5*, 567. <https://doi.org/10.22331/q-2021-10-20-567> (cit. on pp. 35, 51).
- Gentini, L., Cuccoli, A., Pirandola, S., Verrucchi, P., & Bianchi, L. (2020). Noise-resilient variational hybrid quantum-classical optimization. *Physical Review A*, *102*(5), 052414. <https://doi.org/10.1103/PhysRevA.102.052414> (cit. on p. 37).
- Georges, A. (2004). Strongly correlated electron materials: Dynamical mean-field theory and electronic structure. *AIP Conference Proceedings*, *715*(1), 3–74. <https://doi.org/10.1063/1.1800733> (cit. on p. 20).
- Georges, A., Kotliar, G., Krauth, W., & Rozenberg, M. J. (1996). Dynamical mean-field theory of strongly correlated fermion systems and the limit of infinite dimensions. *Reviews of Modern Physics*, *68*(1), 13–125. <https://doi.org/10.1103/RevModPhys.68.13> (cit. on p. 21).
- Georgescu, I. M., Ashhab, S., & Nori, F. (2014). Quantum simulation. *Reviews of Modern Physics*, *86*(1), 153–185. <https://doi.org/10.1103/RevModPhys.86.153> (cit. on pp. 26, 50).
- Gerrits, N., Smeets, E. W. F., Vuckovic, S., Powell, A. D., Doblhoff-Dier, K., & Kroes, G.-J. (2020). Density Functional Theory for Molecule–Metal Surface Reactions: When Does the

- Generalized Gradient Approximation Get It Right, and What to Do If It Does Not. *The Journal of Physical Chemistry Letters*, 11(24), 10552–10560. <https://doi.org/10.1021/acs.jpcclett.0c02452> (cit. on p. 17).
- Glaetzle, A. W., Dalmonte, M., Nath, R., Gross, C., Bloch, I., & Zoller, P. (2015). Designing Frustrated Quantum Magnets with Laser-Dressed Rydberg Atoms. *Physical Review Letters*, 114(17), 173002. <https://doi.org/10.1103/PhysRevLett.114.173002> (cit. on p. 70).
- González-Cuadra, D., Bluvstein, D., Kalinowski, M., Kaubruegger, R., Maskara, N., Naldesi, P., Zache, T. V., Kaufman, A. M., Lukin, M. D., Pichler, H., Vermersch, B., Ye, J., & Zoller, P. (2023). Fermionic quantum processing with programmable neutral atom arrays. *Proceedings of the National Academy of Sciences*, 120(35), e2304294120. <https://doi.org/10.1073/pnas.2304294120> (cit. on p. 70).
- GOOGLE AI QUANTUM AND COLLABORATORS, Arute, F., Arya, K., Babbush, R., Bacon, D., Bardin, J. C., Barends, R., Boixo, S., Broughton, M., Buckley, B. B., Buell, D. A., Burkett, B., Bushnell, N., Chen, Y., Chen, Z., Chiaro, B., Collins, R., Courtney, W., Demura, S., . . . Zalcman, A. (2020). Hartree-Fock on a superconducting qubit quantum computer [Publisher: American Association for the Advancement of Science]. *Science*, 369(6507), 1084–1089. <https://doi.org/10.1126/science.abb9811> (cit. on pp. 39, 40).
- Greiner, M., Mandel, O., Hänsch, T. W., & Bloch, I. (2002). Collapse and revival of the matter wave field of a Bose–Einstein condensate. *Nature*, 419, 51–54. <https://doi.org/10.1038/nature00968> (cit. on p. 85).
- Grover, L. K. (1996). A fast quantum mechanical algorithm for database search. *Proceedings of the twenty-eighth annual ACM symposium on Theory of Computing*, 212–219. <https://doi.org/10.1145/237814.237866> (cit. on p. 31).
- Guo, S., et al. (2022). Scalable quantum computational chemistry with superconducting qubits. *arXiv:2212.08006* (cit. on p. 64).
- Hadfield, C., Bravyi, S., Raymond, R., & Mezzacapo, A. (2020, June). Measurements of Quantum Hamiltonians with Locally-Biased Classical Shadows. <https://doi.org/10.48550/arXiv.2006.15788> (cit. on p. 35).
- Harrow, A. W., Hassidim, A., & Lloyd, S. (2009). Quantum Algorithm for Linear Systems of Equations. *Physical Review Letters*, 103(15), 150502. <https://doi.org/10.1103/PhysRevLett.103.150502> (cit. on p. 31).
- Hart, R. A., Duarte, P. M., Yang, T.-L., Liu, X., Paiva, T., Khatami, E., Scalettar, R. T., Trivedi, N., Huse, D. A., & Hulet, R. G. (2015). Observation of antiferromagnetic correlations in the Hubbard model with ultracold atoms. *Nature*, 519(7542), 211–214. <https://doi.org/10.1038/nature14223> (cit. on p. 69).
- Hashimoto, M., Vishik, I. M., He, R.-H., Devereaux, T. P., & Shen, Z.-X. (2014). Energy gaps in high-transition-temperature cuprate superconductors. *Nature Physics*, 10(7), 483–495. <https://doi.org/10.1038/nphys3009> (cit. on p. 109).
- Hashizume, T., McCulloch, I. P., & Halimeh, J. C. (2022). Dynamical phase transitions in the two-dimensional transverse-field Ising model. *Physical Review Research*, 4(1), 013250. <https://doi.org/10.1103/PhysRevResearch.4.013250> (cit. on p. 117).
- Hassan, S. R., & de’Medici, L. (2010). Slave spins away from half filling: Cluster mean-field theory of the Hubbard and extended Hubbard models. *Physical Review B*, 81(3), 035106. <https://doi.org/10.1103/PhysRevB.81.035106> (cit. on pp. 71, 74, 109, 110, 114).
- Haule, K., & Birol, T. (2015). Free Energy from Stationary Implementation of the DFT+DMFT Functional. *Physical Review Letters*, 115(25), 256402. <https://doi.org/10.1103/PhysRevLett.115.256402> (cit. on p. 21).
- Havlíček, V., Córcoles, A. D., Temme, K., Harrow, A. W., Kandala, A., Chow, J. M., & Gambetta, J. M. (2019). Supervised learning with quantum-enhanced feature spaces. *Nature*, 567(7747), 209–212. <https://doi.org/10.1038/s41586-019-0980-2> (cit. on p. 33).

- Hehre, W. J., Stewart, R. F., & Pople, J. A. (2003). Self-Consistent Molecular-Orbital Methods. I. Use of Gaussian Expansions of Slater-Type Atomic Orbitals. *The Journal of Chemical Physics*, *51*(6), 2657–2664. <https://doi.org/10.1063/1.1672392> (cit. on p. 40).
- Helgaker, T., Jørgensen, P., & Olsen, J. (2000). Coupled-cluster theory. In *Molecular electronic-structure theory* (pp. 648–723). <https://doi.org/https://doi.org/10.1002/9781119019572.ch13> (cit. on pp. 40, 55).
- Helgaker, T., Jørgensen, P., & Olsen, J. (2001, January). In Molecular Electronic-Structure Theory. In *Physics Today - PHYS TODAY* (Vol. 54). <https://doi.org/10.1002/9781119019572> (cit. on p. 15).
- Hempel, C., et al. (2018). Quantum Chemistry Calculations on a Trapped-Ion Quantum Simulator. *Physical Review X*, *8*(3), 031022. <https://doi.org/10.1103/PhysRevX.8.031022> (cit. on pp. 35, 40, 50, 52, 55, 56).
- Henelius, P., & Sandvik, A. W. (2000). Sign problem in Monte Carlo simulations of frustrated quantum spin systems. *Physical Review B*, *62*(2), 1102–1113. <https://doi.org/10.1103/PhysRevB.62.1102> (cit. on p. 22).
- Henriet, L. (2020). Robustness to spontaneous emission of a variational quantum algorithm. *Physical Review A*, *101*(1), 012335. <https://doi.org/10.1103/PhysRevA.101.012335> (cit. on p. 64).
- Henriet, L., Beguin, L., Signoles, A., Lahaye, T., Browaeys, A., Reymond, G.-O., & Jurczak, C. (2020). Quantum computing with neutral atoms. *Quantum*, *4*, 327. <https://doi.org/10.22331/q-2020-09-21-327> (cit. on pp. 42, 43, 48, 51, 53, 58, 70).
- Ho, A., McClean, J., & Ong, S. P. (2018). The promise and challenges of quantum computing for energy storage. *Joule*, *2*(5), 810–813 (cit. on p. 13).
- Holmes, Z., Sharma, K., Cerezo, M., & Coles, P. J. (2022). Connecting ansatz expressibility to gradient magnitudes and barren plateaus. *PRX Quantum*, *3*, 010313. <https://doi.org/10.1103/PRXQuantum.3.010313> (cit. on p. 64).
- Huang, B., Govoni, M., & Galli, G. (2022). Simulating the Electronic Structure of Spin Defects on Quantum Computers. *PRX Quantum*, *3*(1), 010339. <https://doi.org/10.1103/PRXQuantum.3.010339> (cit. on p. 89).
- Huang, H.-Y., Bharti, K., & Rebentrost, P. (2019). Near-term quantum algorithms for linear systems of equations. <https://doi.org/10.48550/arXiv.1909.07344> (cit. on p. 36).
- Huang, H.-Y., Kueng, R., & Preskill, J. (2020). Predicting many properties of a quantum system from very few measurements. *Nature Physics*, *16*(10), 1050–1057. <https://doi.org/10.1038/s41567-020-0932-7> (cit. on p. 36).
- Huang, H.-Y., Kueng, R., & Preskill, J. (2021). Efficient estimation of Pauli observables by derandomization. *Physical Review Letters*, *127*(3), 030503. <https://doi.org/10.1103/PhysRevLett.127.030503> (cit. on pp. 36, 51, 52, 61).
- The Hubbard model at half a century. (2013). *Nature Physics*, *9*(9), 523–523. <https://doi.org/10.1038/nphys2759> (cit. on p. 19).
- IPCC. (2022). *Climate change 2022: Impacts, adaptation and vulnerability*. (Cit. on p. 7).
- Isenhower, L., Urban, E., Zhang, X. L., Gill, A. T., Henage, T., Johnson, T. A., Walker, T. G., & Saffman, M. (2010). Demonstration of a Neutral Atom Controlled-NOT Quantum Gate. *Physical Review Letters*, *104*(1), 010503. <https://doi.org/10.1103/PhysRevLett.104.010503> (cit. on p. 47).
- Iyer, D., Mondaini, R., Will, S., & Rigol, M. (2014). Coherent quench dynamics in the one-dimensional Fermi-Hubbard model. *Physical Review A*, *90*(3), 031602. <https://doi.org/10.1103/PhysRevA.90.031602> (cit. on p. 85).
- Jandura, S., Thompson, J. D., & Pupillo, G. (2023). Optimizing Rydberg Gates for Logical-Qubit Performance. *PRX Quantum*, *4*(2), 020336. <https://doi.org/10.1103/PRXQuantum.4.020336> (cit. on p. 47).

- Johansson, J. R., Nation, P. D., & Nori, F. (2013). QuTiP 2: A Python framework for the dynamics of open quantum systems. *Computer Physics Communications*, *184*(4), 1234–1240. <https://doi.org/10.1016/j.cpc.2012.11.019> (cit. on pp. 80, 114).
- Jordan, P., & Wigner, E. (1928). Über das paulische äquivalenzverbot. *Z. Physik*, *47*, 631. <https://doi.org/10.1007/BF01331938> (cit. on pp. 38, 53, 70).
- Jördens, R., Strohmaier, N., Günter, K., Henning, M., & Esslinger, T. (2008). A Mott insulator of fermionic atoms in an optical lattice. *Nature*, (455), 204. <https://doi.org/10.1038/nature07244> (cit. on p. 69).
- Kadowaki, T., & Nishimori, H. (1998). Quantum annealing in the transverse Ising model. *Physical Review E*, *58*(5), 5355–5363. <https://doi.org/10.1103/PhysRevE.58.5355> (cit. on p. 37).
- Kairys, P., King, A. D., Ozfidan, I., Boothby, K., Raymond, J., Banerjee, A., & Humble, T. S. (2020). Simulating the Shastry-Sutherland Ising Model Using Quantum Annealing. *PRX Quantum*, *1*(2), 020320. <https://doi.org/10.1103/PRXQuantum.1.020320> (cit. on p. 37).
- Kalinowski, M., Maskara, N., & Lukin, M. D. (2023). Non-Abelian Floquet Spin Liquids in a Digital Rydberg Simulator. *Physical Review X*, *13*(3), 031008. <https://doi.org/10.1103/PhysRevX.13.031008> (cit. on p. 41).
- Kandala, A., Mezzacapo, A., Temme, K., Takita, M., Brink, M., Chow, J. M., & Gambetta, J. M. (2017). Hardware-efficient Variational Quantum Eigensolver for Small Molecules and Quantum Magnets. *Nature*, *549*(7671), 242–246. <https://doi.org/10.1038/nature23879> (cit. on pp. 32, 35, 36, 50, 55).
- Kim, Y., Eddins, A., Anand, S., Wei, K. X., van den Berg, E., Rosenblatt, S., Nayfeh, H., Wu, Y., Zaletel, M., Temme, K., & Kandala, A. (2023). Evidence for the utility of quantum computing before fault tolerance. *Nature*, *618*(7965), 500–505. <https://doi.org/10.1038/s41586-023-06096-3> (cit. on p. 76).
- Kittel, C., & Holcomb, D. F. (1967). Introduction to Solid State Physics. *American Journal of Physics*, *35*(6), 547–548. <https://doi.org/10.1119/1.1974177> (cit. on p. 13).
- Kokail, C., Maier, C., van Bijnen, R., Brydges, T., Joshi, M. K., Jurcevic, P., Muschik, C. A., Silvi, P., Blatt, R., Roos, C. F., & Zoller, P. (2019). Self-Verifying Variational Quantum Simulation of the Lattice Schwinger Model. *Nature*, *569*(7756), 355–360. <https://doi.org/10.1038/s41586-019-1177-4> (cit. on pp. 29, 35, 36, 51, 56, 70).
- Kollath, C., Läuchli, A. M., & Altman, E. (2007). Quench Dynamics and Nonequilibrium Phase Diagram of the Bose-Hubbard Model. *Physical Review Letters*, *98*(18), 180601. <https://doi.org/10.1103/PhysRevLett.98.180601> (cit. on p. 85).
- Kübler, J. M., Arrasmith, A., Cincio, L., & Coles, P. J. (2020). An Adaptive Optimizer for Measurement-Frugal Variational Algorithms. *Quantum*, *4*, 263. <https://doi.org/10.22331/q-2020-05-11-263> (cit. on p. 37).
- Lacki, M., & Heyl, M. (2019). Dynamical quantum phase transitions in collapse and revival oscillations of a quenched superfluid. *Physical Review B*, *99*(12), 121107. <https://doi.org/10.1103/PhysRevB.99.121107> (cit. on p. 85).
- Lanyon, B. P., Whitfield, J. D., Gillett, G. G., Goggin, M. E., Almeida, M. P., et al. (2010). Towards quantum chemistry on a quantum computer. *Nature Chemistry*, *2*(2), 106–111. <https://doi.org/10.1038/nchem.483> (cit. on p. 50).
- Lavrijsen, W., Tudor, A., Müller, J., Iancu, C., & de Jong, W. (2020). Classical Optimizers for Noisy Intermediate-Scale Quantum Devices. *2020 IEEE International Conference on Quantum Computing and Engineering (QCE)*, 267–277. <https://doi.org/10.1109/QCE49297.2020.00041> (cit. on p. 35).
- Lazzeri, M., Attaccalite, C., Wirtz, L., & Mauri, F. (2008). Impact of the electron-electron correlation on phonon dispersion: Failure of LDA and GGA DFT functionals in graphene and graphite. *Physical Review B*, *78*(8), 081406. <https://doi.org/10.1103/PhysRevB.78.081406> (cit. on p. 17).
- LeBlanc, J. P. F., Antipov, A. E., Becca, F., Bulik, I. W., Chan, G. K.-L., Chung, C.-m., Deng, Y., Ferrero, M., Henderson, T. M., Jiménez-Hoyos, C. A., Kozik, E., Liu, X.-w., Millis,

- A. J., Prokof'ev, N. V., Qin, M., Scuseria, G. E., Shi, H., Svistunov, B. V., Tocchio, L. F., ... Gull, E. (2015). Solutions of the Two-Dimensional Hubbard Model: Benchmarks and Results from a Wide Range of Numerical Algorithms. *Physical Review X*, 5(4), 041041. <https://doi.org/10.1103/PhysRevX.5.041041> (cit. on p. 69).
- Lechermann, F. (2018). Oxide Heterostructures from a Realistic Many-Body Perspective. In W. Andreoni & S. Yip (Eds.), *Handbook of Materials Modeling: Applications: Current and Emerging Materials* (pp. 1–20). https://doi.org/10.1007/978-3-319-50257-1_80-1 (cit. on pp. 21, 22).
- Leclerc, L., Ortiz-Guitierrez, L., Grijalva, S., Albrecht, B., Cline, J. R. K., et al. (2022). Financial risk management on a neutral atom quantum processor. *arXiv:2212.03223* (cit. on p. 58).
- Levine, H., Keesling, A., Omran, A., Bernien, H., Schwartz, S., Zibrov, A. S., Endres, M., Greiner, M., Vuletić, V., & Lukin, M. D. (2018). High-Fidelity Control and Entanglement of Rydberg-Atom Qubits. *Physical Review Letters*, 121(12), 123603. <https://doi.org/10.1103/PhysRevLett.121.123603> (cit. on p. 47).
- Li, L., Fan, M., Coram, M., Riley, P., & Leichenauer, S. (2020). Quantum optimization with a novel Gibbs objective function and ansatz architecture search. *Physical Review Research*, 2(2), 023074. <https://doi.org/10.1103/PhysRevResearch.2.023074> (cit. on p. 32).
- Li, W., Huang, Z., Cao, C., Huang, Y., Shuai, Z., Sun, X., Sun, J., Yuan, X., & Lv, D. (2022). Toward practical quantum embedding simulation of realistic chemical systems on near-term quantum computers. *Chemical Science*, 13(31), 8953–8962. <https://doi.org/10.1039/D2SC01492K> (cit. on p. 89).
- Lienhard, V., de Léséleuc, S., Barredo, D., Lahaye, T., Browaeys, A., Schuler, M., Henry, L.-P., & Läuchli, A. M. (2018). Observing the Space- and Time-Dependent Growth of Correlations in Dynamically Tuned Synthetic Ising Models with Antiferromagnetic Interactions. *Physical Review X*, 8(2), 021070. <https://doi.org/10.1103/PhysRevX.8.021070> (cit. on p. 82).
- Lucas, A. (2014). Ising formulations of many NP problems. *Frontiers in Physics*, 2 (cit. on pp. 37, 48).
- Ma, S., Liu, G., Peng, P., Zhang, B., Jandura, S., Claes, J., Burgers, A. P., Pupillo, G., Puri, S., & Thompson, J. D. (2023). High-fidelity gates and mid-circuit erasure conversion in an atomic qubit. *Nature*, 622(7982), 279–284. <https://doi.org/10.1038/s41586-023-06438-1> (cit. on p. 47).
- Ma, Y. (2018). Computer Simulation of Cathode Materials for Lithium Ion and Lithium Batteries: A Review. *ENERGY & ENVIRONMENTAL MATERIALS*, 1(3), 148–173. <https://doi.org/10.1002/eem2.12017> (cit. on p. 18).
- Mazurenko, A., Chiu, C. S., Ji, G., Parsons, M. F., Kanász-Nagy, M., Schmidt, R., Grusdt, F., Demler, E., Greif, D., & Greiner, M. (2017). A cold-atom Fermi–Hubbard antiferromagnet. *Nature*, 545(7655), 462–466. <https://doi.org/10.1038/nature22362> (cit. on p. 69).
- McArdle, S., Endo, S., Aspuru-Guzik, A., Benjamin, S. C., & Yuan, X. (2020). Quantum computational chemistry. *Reviews of Modern Physics*, 92(1), 015003. <https://doi.org/10.1103/RevModPhys.92.015003> (cit. on p. 32).
- McClellan, J. R., Boixo, S., Smelyanskiy, V. N., Babbush, R., & Neven, H. (2018). Barren plateaus in quantum neural network training landscapes. *Nature Communications*, 9(1), 4812. <https://doi.org/10.1038/s41467-018-07090-4> (cit. on pp. 36, 51).
- McClellan, J. R., Romero, J., Babbush, R., & Aspuru-Guzik, A. (2016). The theory of variational hybrid quantum-classical algorithms. *New Journal of Physics*, 18(2), 023023. <https://doi.org/10.1088/1367-2630/18/2/023023> (cit. on pp. 32, 34, 36, 50, 51, 54).
- Meitei, O., Gard, B., Barron, G., Pappas, D., Economou, S., et al. (2021). Gate-free state preparation for fast variational quantum eigensolver simulations. *npj Quantum Information*, 7(1). <https://doi.org/10.1038/s41534-021-00493-0> (cit. on pp. 51, 59).

- Metropolis, N., Rosenbluth, A. W., Rosenbluth, M. N., Teller, A. H., & Teller, E. (2004). Equation of State Calculations by Fast Computing Machines. *The Journal of Chemical Physics*, *21*(6), 1087–1092. <https://doi.org/10.1063/1.1699114> (cit. on p. 22).
- Michel, A., Grijalva, S., Henriët, L., Domain, C., & Browaeys, A. (2023). Blueprint for a digital-analog variational quantum eigensolver using rydberg atom arrays. *Phys. Rev. A*, *107*, 042602. <https://doi.org/10.1103/PhysRevA.107.042602> (cit. on pp. 11, 35, 36, 50, 70).
- Michel, A., Henriët, L., Domain, C., Browaeys, A., & Ayrat, T. (2023). Hubbard physics with rydberg atoms: Using a quantum spin simulator to simulate strong fermionic correlations. <https://doi.org/10.48550/arXiv.2312.08065> (cit. on p. 69).
- Montanaro, A. (2016). Quantum algorithms: An overview. *npj Quantum Information*, *2*(1), 1–8. <https://doi.org/10.1038/npjqi.2015.23> (cit. on p. 9).
- Monz, T., Nigg, D., Martinez, E. A., Brandl, M. F., Schindler, P., Rines, R., Wang, S. X., Chuang, I. L., & Blatt, R. (2016). Realization of a scalable Shor algorithm. *Science*, *351*(6277), 1068–1070. <https://doi.org/10.1126/science.aad9480> (cit. on p. 32).
- Moore, G. E. (2006). Cramming more components onto integrated circuits, Reprinted from *Electronics*, volume 38, number 8, April 19, 1965, pp.114 ff. *IEEE Solid-State Circuits Society Newsletter*, *11*(3), 33–35. <https://doi.org/10.1109/N-SSC.2006.4785860> (cit. on p. 19).
- Mott, N. F., & Peierls, R. (1937). Discussion of the paper by de Boer and Verwey. *Proceedings of the Physical Society*, *49*(4S), 72. <https://doi.org/10.1088/0959-5309/49/4S/308> (cit. on p. 19).
- Muller, R. (2022, June). PyQuante2. <https://github.com/rpmuller/pyquante2> (cit. on p. 61).
- Nam, Y., Chen, J.-S., Pienti, N. C., Wright, K., Delaney, C., Maslov, D., Brown, K. R., Allen, S., Amini, J. M., Apisdorf, J., Beck, K. M., Blinov, A., Chaplin, V., Chmielewski, M., Collins, C., Debnath, S., Hudek, K. M., Ducore, A. M., Keesan, M., . . . Kim, J. (2020). Ground-state energy estimation of the water molecule on a trapped-ion quantum computer. *npj Quantum Information*, *6*(1), 33. <https://doi.org/10.1038/s41534-020-0259-3> (cit. on pp. 32, 35, 36, 51).
- Nelder, J. A., & Mead, R. (1965). A Simplex Method for Function Minimization. *The Computer Journal*, *7*(4), 308–313. <https://doi.org/10.1093/comjnl/7.4.308> (cit. on p. 63).
- Nguyen, M.-T., Liu, J.-G., Wurtz, J., Lukin, M. D., Wang, S.-T., & Pichler, H. (2023). Quantum Optimization with Arbitrary Connectivity Using Rydberg Atom Arrays. *PRX Quantum*, *4*(1), 010316. <https://doi.org/10.1103/PRXQuantum.4.010316> (cit. on p. 34).
- Nielsen, M. A., & Chuang, I. L. (2011). *Quantum computation and quantum information: 10th anniversary edition*. Cambridge University Press. <https://doi.org/10.1017/CBO9780511976667> (cit. on pp. 23, 27, 46, 49).
- Nogrette, F., Labuhn, H., Ravets, S., Barredo, D., Béguin, L., Vernier, A., Lahaye, T., & Browaeys, A. (2014). Single-Atom Trapping in Holographic 2D Arrays of Microtraps with Arbitrary Geometries. *Physical Review X*, *4*(2), 021034. <https://doi.org/10.1103/PhysRevX.4.021034> (cit. on p. 44).
- Notarnicola, S., Elben, A., Lahaye, T., Browaeys, A., Montangero, S., et al. (2021). A randomized measurement toolbox for Rydberg quantum technologies. *arXiv:2112.11046* (cit. on p. 61).
- O’Malley, P. J. J., Babbush, R., Kivlichan, I. D., Romero, J., McClean, J. R., Barends, R., Kelly, J., Roushan, P., Tranter, A., Ding, N., Campbell, B., Chen, Y., Chen, Z., Chiaro, B., Dunsworth, A., Fowler, A. G., Jeffrey, E., Lucero, E., Megrant, A., . . . Martinis, J. M. (2016). Scalable Quantum Simulation of Molecular Energies. *Physical Review X*, *6*(3), 031007. <https://doi.org/10.1103/PhysRevX.6.031007> (cit. on pp. 32, 55).
- Onsager, L. (1944). Crystal Statistics. I. A Two-Dimensional Model with an Order-Disorder Transition. *Physical Review*, *65*(3-4), 117–149. <https://doi.org/10.1103/PhysRev.65.117> (cit. on p. 19).
- Orioli, A. P., Signoles, A., Wildhagen, H., Günter, G., Berges, J., Whitlock, S., & Weidemüller, M. (2018). Relaxation of an Isolated Dipolar-Interacting Rydberg Quantum Spin System.

- Physical Review Letters*, 120(6), 063601. <https://doi.org/10.1103/PhysRevLett.120.063601> (cit. on p. 45).
- Pan, G., & Meng, Z. Y. (2022, April). Sign Problem in Quantum Monte Carlo Simulation. <https://doi.org/10.48550/arXiv.2204.08777> (cit. on p. 22).
- Paré, C. (2022, December). *Prévisions de l'évolution micro structurale jusqu'à fin de vie sous irradiation d'alliages ferritiques par simulations numérique : Vers une simulation quantitative et la prise en compte des hétérogénéités* [These de doctorat]. Centrale Lille Institut. (Cit. on p. 7).
- Park, H., Haule, K., & Kotliar, G. (2008). Cluster Dynamical Mean Field Theory of the Mott Transition. *Physical Review Letters*, 101(18), 186403. <https://doi.org/10.1103/PhysRevLett.101.186403> (cit. on p. 21).
- Park, H., Millis, A. J., & Marianetti, C. A. (2014). Computing total energies in complex materials using charge self-consistent DFT + DMFT. *Physical Review B*, 90(23), 235103. <https://doi.org/10.1103/PhysRevB.90.235103> (cit. on p. 21).
- Parra-Rodriguez, A., Lougovski, P., Lamata, L., Solano, E., & Sanz, M. (2020). Digital-analog quantum computation. *Physical Review A*, 101(2), 022305. <https://doi.org/10.1103/PhysRevA.101.022305> (cit. on p. 52).
- Paul, A., & Birol, T. (2019). Applications of dft + dmft in materials science. *Annual Review of Materials Research*, 49(1), 31–52. <https://doi.org/10.1146/annurev-matsci-070218-121825> (cit. on p. 21).
- Peruzzo, A., McClean, J., Shadbolt, P., Yung, M.-H., Zhou, X.-Q., Love, P. J., Aspuru-Guzik, A., & O'Brien, J. L. (2013). A variational eigenvalue solver on a quantum processor. *Nature Communications*, 5(1), 4213. <https://doi.org/10.1038/ncomms5213> (cit. on pp. 32, 50, 70).
- Piochaud, J. B., Klaver, T. P. C., Adjanor, G., Olsson, P., Domain, C., et al. (2014). First-principles study of point defects in an fcc Fe-10Ni-20Cr model alloy. *Phys. Rev. B*, 89, 024101. <https://doi.org/10.1103/PhysRevB.89.024101> (cit. on pp. 7, 8, 18).
- Piskor, T., Reiner, J.-M., Zanker, S., Vogt, N., Marthaler, M., et al. (2022). Using gradient-based algorithms to determine ground-state energies on a quantum computer. *Physical Review A*, 105(6), 062415. <https://doi.org/10.1103/PhysRevA.105.062415> (cit. on pp. 35, 51).
- Powell, M. J. D. (1964). An efficient method for finding the minimum of a function of several variables without calculating derivatives. *The Computer Journal*, 7(2), 155–162. <https://doi.org/10.1093/comjnl/7.2.155> (cit. on p. 62).
- Preskill, J. (2018). Quantum Computing in the NISQ era and beyond. *Quantum*, 2, 79. <https://doi.org/10.22331/q-2018-08-06-79> (cit. on pp. 9, 28).
- Qiskit contributors. (2023). Qiskit: An open-source framework for quantum computing. <https://doi.org/10.5281/zenodo.2573505> (cit. on p. 61).
- Rader, M., & Läuchli, A. M. (2018). Finite Correlation Length Scaling in Lorentz-Invariant Gapless iPEPS Wave Functions. *Physical Review X*, 8(3), 031030. <https://doi.org/10.1103/PhysRevX.8.031030> (cit. on p. 121).
- Riegger, L., Orso, G., & Heidrich-Meisner, F. (2015). Interaction quantum quenches in the one-dimensional Fermi-Hubbard model with spin imbalance. *Physical Review A*, 91(4), 043623. <https://doi.org/10.1103/PhysRevA.91.043623> (cit. on p. 85).
- Roffe, J. (2019). Quantum error correction: An introductory guide. *Contemporary Physics*, 60(3), 226–245. <https://doi.org/10.1080/00107514.2019.1667078> (cit. on p. 28).
- Rohrbach, A., & Hafner, J. (2005). Molecular adsorption of NO on NiO(100): DFT and DFT + U calculations. *Physical Review B*, 71(4), 045405. <https://doi.org/10.1103/PhysRevB.71.045405> (cit. on p. 18).
- Rossmannek, M., Pavošević, F., Rubio, A., & Tavernelli, I. (2023). Quantum Embedding Method for the Simulation of Strongly Correlated Systems on Quantum Computers. *The Journal of Physical Chemistry Letters*, 14(14), 3491–3497. <https://doi.org/10.1021/acs.jpcclett.3c00330> (cit. on p. 89).

- Rudolph, M. S., Miller, J., Chen, J., Acharya, A., & Perdomo-Ortiz, A. (2022). Synergy between quantum circuits and tensor networks: Short-cutting the race to practical quantum advantage. *arXiv:2208.13673* (cit. on p. 63).
- Rüegg, A., Huber, S. D., & Sigrist, M. (2010). Z_2 -slave-spin theory for strongly correlated fermions. *Physical Review B*, *81*(15), 155118. <https://doi.org/10.1103/PhysRevB.81.155118> (cit. on pp. 70, 72, 73, 86, 109, 110).
- Saffman, M., Walker, T. G., & Mølmer, K. (2010). Quantum information with Rydberg atoms. *Reviews of Modern Physics*, *82*(3), 2313–2363. <https://doi.org/10.1103/RevModPhys.82.2313> (cit. on p. 44).
- Sandvik, A. W., & Kurkijärvi, J. (1991). Quantum Monte Carlo simulation method for spin systems. *Physical Review B*, *43*(7), 5950–5961. <https://doi.org/10.1103/PhysRevB.43.5950> (cit. on p. 22).
- Schachenmayer, J., Daley, A. J., & Zoller, P. (2011). Atomic matter-wave revivals with definite atom number in an optical lattice. *Physical Review A*, *83*(4), 043614. <https://doi.org/10.1103/PhysRevA.83.043614> (cit. on p. 85).
- Schäfer, T., Wentzell, N., Iv, F. Š., He, Y.-y., Hille, C., Klett, M., Eckhardt, C. J., Arzhang, B., Harkov, V., R, F.-m. L., Kirsch, A., Wang, Y., Kim, A. J., Kozik, E., Stepanov, E. A., Kauch, A., Andergassen, S., Hansmann, P., Rohe, D., ... Zhang, S. (2021). Tracking the Footprints of Spin Fluctuations : A MultiMethod , MultiMessenger Study of the Two-Dimensional Hubbard Model. *Physical Review X*, *11*(1), 11058. <https://doi.org/10.1103/PhysRevX.11.011058> (cit. on p. 69).
- Schiró, M., & Fabrizio, M. (2011). Quantum quenches in the Hubbard model: Time-dependent mean-field theory and the role of quantum fluctuations. *Physical Review B*, *83*(16), 165105. <https://doi.org/10.1103/PhysRevB.83.165105> (cit. on pp. 71, 73, 85, 86).
- Schlosser, N., Raymond, G., Protsenko, I., & Grangier, P. (2001). Sub-poissonian loading of single atoms in a microscopic dipole trap. *Nature*, *411*(6841), 1024–1027. <https://doi.org/10.1038/35082512> (cit. on p. 44).
- Schmitt, M., Rams, M. M., Dziarmaga, J., Heyl, M., & Zurek, W. H. (2022). Quantum phase transition dynamics in the two-dimensional transverse-field Ising model. *Science Advances*, *8*(37), eabl6850. <https://doi.org/10.1126/sciadv.abl6850> (cit. on p. 117).
- Schneider, U., Hackermüller, L., Will, S., Best, T., Bloch, I., Costi, T. A., Helmes, R. W., Rasch, D., & Rosch, A. (2008). Metallic and Insulating Phases of Repulsively Interacting Fermions in a 3D Optical Lattice. *Science*, *322*(5907), 1520–1525. <https://doi.org/10.1126/science.1165449> (cit. on p. 69).
- Schneider, U., Hackermüller, L., Ronzheimer, J. P., Will, S., Braun, S., Best, T., Bloch, I., Demler, E., Mandt, S., Rasch, D., & Rosch, A. (2012). Fermionic transport and out-of-equilibrium dynamics in a homogeneous Hubbard model with ultracold atoms. *Nature Physics*, *8*(3), 213–218. <https://doi.org/10.1038/nphys2205> (cit. on p. 69).
- Scholl, P., Williams, H. J., Bornet, G., Wallner, F., Barredo, D., Henriot, L., Signoles, A., Hainaut, C., Franz, T., Geier, S., Tebben, A., Salzinger, A., Zürn, G., Lahaye, T., Weidemüller, M., & Browaeys, A. (2022). Microwave Engineering of Programmable XXZ Hamiltonians in Arrays of Rydberg Atoms. *PRX Quantum*, *3*(2), 020303. <https://doi.org/10.1103/PRXQuantum.3.020303> (cit. on p. 41).
- Scholl, P. (2021, December). *Simulation quantique de modèles de spins avec des grandes matrices d'atomes de Rydberg* [Doctoral dissertation, Université Paris-Saclay]. (Cit. on pp. 42, 49).
- Scholl, P., Schuler, M., Williams, H. J., Eberharter, A. A., Barredo, D., Schymik, K.-N., Lienhard, V., Henry, L.-P., Lang, T. C., Lahaye, T., Läuchli, A. M., & Browaeys, A. (2021). Quantum simulation of 2D antiferromagnets with hundreds of Rydberg atoms. *Nature*, *595*(7866), 233–238. <https://doi.org/10.1038/s41586-021-03585-1> (cit. on pp. 37, 41, 48, 50, 62, 70, 113, 121).
- Schreiber, M., Hodgman, S. S., Bordia, P., Lüschen, H. P., Fischer, M. H., Vosk, R., Altman, E., Schneider, U., & Bloch, I. (2015). Observation of many-body localization of interacting

- fermions in a quasirandom optical lattice. *Science*, *349*(6250), 842–845. <https://doi.org/10.1126/science.aaa7432> (cit. on p. 69).
- Schuler, M., Whitsitt, S., Henry, L.-p., Sachdev, S., & Läuchli, A. M. (2016). Universal Signatures of Quantum Critical Points from Finite-Size Torus Spectra: A Window into the Operator Content of Higher-Dimensional Conformal Field Theories. *Physical Review Letters*, *117*(21), 210401. <https://doi.org/10.1103/PhysRevLett.117.210401> (cit. on pp. 83, 117).
- Schymik, K.-N., Ximenez, B., Bloch, E., Dreon, D., Signoles, A., et al. (2022). In situ equalization of single-atom loading in large-scale optical tweezer arrays. *Physical Review A*, *106*(2), 022611 (cit. on p. 63).
- Seeley, J. T., Richard, M. J., & Love, P. J. (2012). The bravyi-kitaev transformation for quantum computation of electronic structure. *The Journal of Chemical Physics*, *137*(22). <https://doi.org/10.1063/1.4768229> (cit. on pp. 38, 39).
- Senjean, B., Yalouz, S., & Saubanère, M. (2023). Toward density functional theory on quantum computers? *SciPost Physics*, *14*(3), 055. <https://doi.org/10.21468/SciPostPhys.14.3.055> (cit. on p. 90).
- Setia, K., Bravyi, S., Mezzacapo, A., & Whitfield, J. D. (2019). Superfast encodings for fermionic quantum simulation. *Physical Review Research*, *1*(3), 033033. <https://doi.org/10.1103/PhysRevResearch.1.033033> (cit. on p. 70).
- Shen, Y., Zhang, X., Zhang, S., Zhang, J.-N., Yung, M.-H., et al. (2017). Quantum implementation of the unitary coupled cluster for simulating molecular electronic structure. *Phys. Rev. A*, *95*, 020501. <https://doi.org/10.1103/PhysRevA.95.020501> (cit. on p. 50).
- Shi, H., Chu, M., & Zhang, P. (2010). Optical properties of UO₂ and PuO₂. *Journal of Nuclear Materials*, *400*(2), 151–156 (cit. on p. 17).
- Shor, P. (1994). Algorithms for quantum computation: Discrete logarithms and factoring. *Proceedings 35th Annual Symposium on Foundations of Computer Science*, 124–134. <https://doi.org/10.1109/SFCS.1994.365700> (cit. on pp. 8, 27, 31).
- Si, Q., Yu, R., & Abrahams, E. (2016). High-temperature superconductivity in iron pnictides and chalcogenides. *Nature Reviews Materials*, *1*(4), 16017. <https://doi.org/10.1038/natrevmats.2016.17> (cit. on p. 69).
- Signoles, A., Franz, T., Ferracini Alves, R., Gärttner, M., Whitlock, S., Zürn, G., & Weidemüller, M. (2021). Glassy Dynamics in a Disordered Heisenberg Quantum Spin System. *Physical Review X*, *11*(1), 011011. <https://doi.org/10.1103/PhysRevX.11.011011> (cit. on p. 48).
- Silvério, H., Grijalva, S., Dalyac, C., Leclerc, L., Karalekas, P. J., Shammah, N., Beji, M., Henry, L.-P., & Henriët, L. (2022). Pulser: An open-source package for the design of pulse sequences in programmable neutral-atom arrays. *Quantum*, *6*, 629. <https://doi.org/10.22331/q-2022-01-24-629> (cit. on pp. 50, 62, 80, 114).
- Sim, J.-H., Sarma, D. D., Tarascon, J.-M., & Biermann, S. (2023). Intra-atomic hund’s exchange interaction determines spin states and energetics of li-rich layered sulfides for battery applications. (Cit. on p. 21).
- Sim, S., Johnson, P. D., & Aspuru-Guzik, A. (2019). Expressibility and entangling capability of parameterized quantum circuits for hybrid quantum-classical algorithms. *Advanced Quantum Technologies*, *2*(12), 1900070. <https://doi.org/10.1002/qute.201900070> (cit. on p. 64).
- Stapmanns, J., Corboz, P., Mila, F., Honecker, A., Normand, B., & Wessel, S. (2018). Thermal Critical Points and Quantum Critical End Point in the Frustrated Bilayer Heisenberg Antiferromagnet. *Physical Review Letters*, *121*(12), 127201. <https://doi.org/10.1103/PhysRevLett.121.127201> (cit. on p. 22).
- Stewart, R. F. (2003). Small Gaussian Expansions of Slater-Type Orbitals. *The Journal of Chemical Physics*, *52*(1), 431–438. <https://doi.org/10.1063/1.1672702> (cit. on p. 15).
- Storn, R., & Price, K. (1997). Differential Evolution – A Simple and Efficient Heuristic for global Optimization over Continuous Spaces. *Journal of Global Optimization*, *11*(4), 341–359. <https://doi.org/10.1023/A:1008202821328> (cit. on p. 56).

- Tangpanitanon, J., Thanasilp, S., Dangniam, N., Lemonde, M.-A., & Angelakis, D. G. (2020). Expressibility and trainability of parametrized analog quantum systems for machine learning applications. *Phys. Rev. Res.*, *2*, 043364. <https://doi.org/10.1103/PhysRevResearch.2.043364> (cit. on p. 64).
- Tarruell, L., & Sanchez-Palencia, L. (2018). Quantum simulation of the Hubbard model with ultracold fermions in optical lattices. *Comptes Rendus Physique*, *19*(6), 365–393. <https://doi.org/10.1016/j.crhy.2018.10.013> (cit. on p. 69).
- Thouless, D. J. (1960). Stability conditions and nuclear rotations in the Hartree-Fock theory. *Nuclear Physics*, *21*, 225–232. [https://doi.org/10.1016/0029-5582\(60\)90048-1](https://doi.org/10.1016/0029-5582(60)90048-1) (cit. on p. 39).
- Tilly, J., Sriluckshmy, P. V., Patel, A., Fontana, E., Rungger, I., Grant, E., Anderson, R., Tennyson, J., & Booth, G. H. (2021). Reduced density matrix sampling: Self-consistent embedding and multiscale electronic structure on current generation quantum computers. *Physical Review Research*, *3*(3), 033230. <https://doi.org/10.1103/PhysRevResearch.3.033230> (cit. on p. 89).
- Toulouse, J., & Adamo, C. (2002). A new hybrid functional including a meta-GGA approach. *Chemical Physics Letters*, *362*(1), 72–78. [https://doi.org/10.1016/S0009-2614\(02\)00950-8](https://doi.org/10.1016/S0009-2614(02)00950-8) (cit. on p. 17).
- Verstraete, F., & Cirac, J. I. (2005). Mapping local Hamiltonians of fermions to local Hamiltonians of spins, 2–8. <https://doi.org/10.1088/1742-5468/2005/09/P09012> (cit. on p. 70).
- Verwey, E. J. W., & de Boer, J. H. (1936). Cation arrangement in a few oxides with crystal structures of the spinel type. *Recueil des Travaux Chimiques des Pays-Bas*, *55*(6), 531–540. <https://doi.org/10.1002/recl.19360550608> (cit. on p. 19).
- Virtanen, P., Gommers, R., Oliphant, T. E., Haberland, M., Reddy, T., Cournapeau, D., Burovski, E., Peterson, P., Weckesser, W., Bright, J., van der Walt, S. J., Brett, M., Wilson, J., Millman, K. J., Mayorov, N., Nelson, A. R. J., Jones, E., Kern, R., Larson, E., ... SciPy 1.0 Contributors. (2020). SciPy 1.0: Fundamental Algorithms for Scientific Computing in Python. *Nature Methods*, *17*, 261–272. <https://doi.org/10.1038/s41592-019-0686-2> (cit. on p. 78).
- Vorwerk, C., Sheng, N., Govoni, M., Huang, B., & Galli, G. (2022). Quantum embedding theories to simulate condensed systems on quantum computers. *Nature Computational Science*, *2*(7), 424–432. <https://doi.org/10.1038/s43588-022-00279-0> (cit. on p. 90).
- Wagner, L. K. (2007). Transition metal oxides using quantum Monte Carlo. *Journal of Physics: Condensed Matter*, *19*(34), 343201. <https://doi.org/10.1088/0953-8984/19/34/343201> (cit. on p. 22).
- Wagner, L. K. (2014). Quantum Monte Carlo for Ab Initio calculations of energy-relevant materials. *International Journal of Quantum Chemistry*, *114*(2), 94–101. <https://doi.org/10.1002/qua.24526> (cit. on p. 22).
- Wakaura, H., Tomono, T., & Yasuda, S. (2021). Evaluation on Genetic Algorithms as an optimizer of Variational Quantum Eigensolver(VQE) method. *arXiv:2110.07441 [quant-ph]* (cit. on pp. 35, 51).
- Wang, H., Ashhab, S., & Nori, F. (2011). Quantum algorithm for simulating the dynamics of an open quantum system. *Physical Review A*, *83*(6), 062317. <https://doi.org/10.1103/PhysRevA.83.062317> (cit. on pp. 27, 90).
- Wang, S., Fontana, E., Cerezo, M., Sharma, K., Sone, A., Cincio, L., & Coles, P. J. (2021). Noise-induced barren plateaus in variational quantum algorithms. *Nature Communications*, *12*(1), 6961. <https://doi.org/10.1038/s41467-021-27045-6> (cit. on p. 36).
- Wecker, D., Hastings, M. B., & Troyer, M. (2015). Progress towards practical quantum variational algorithms. *Phys. Rev. A*, *92*(4), 042303. <https://doi.org/10.1103/PhysRevA.92.042303> (cit. on pp. 34, 35, 51, 64).

- Weiss, P. (1907). L'hypothèse du champ moléculaire et la propriété ferromagnétique. *Journal de Physique Théorique et Appliquée*, 6(1), 661–690. <https://doi.org/10.1051/jphys:019070060066100> (cit. on p. 19).
- Welinq. (2022). *Welinq website*. <https://welinq.fr/> (cit. on p. 37).
- Wessel, S. (2013). 7 monte carlo simulations of quantum spin models. *Emergent Phenomena in Correlated Matter* (cit. on p. 22).
- Whitlock, S., Glaetzle, A. W., & Hannaford, P. (2017). Simulating quantum spin models using Rydberg-excited atomic ensembles in magnetic microtrap arrays. *Journal of Physics B: Atomic, Molecular and Optical Physics*, 50(7), 074001. <https://doi.org/10.1088/1361-6455/aa6149> (cit. on p. 48).
- Will, S., Iyer, D., & Rigol, M. (2015). Observation of coherent quench dynamics in a metallic many-body state of fermionic atoms. *Nature Communications*, 6(1), 6009. <https://doi.org/10.1038/ncomms7009> (cit. on p. 85).
- Wootters, W. K., & Zurek, W. H. (1982). A single quantum cannot be cloned. *Nature*, 299(5886), 802–803. <https://doi.org/10.1038/299802a0> (cit. on p. 28).
- Wu, B., Sun, J., Huang, Q., & Yuan, X. (2023). Overlapped grouping measurement: A unified framework for measuring quantum states. *Quantum*, 7, 896 (cit. on p. 65).
- Yang, W.-W., Luo, H.-G., & Zhong, Y. (2019). Benchmarking the simplest slave-particle theory with Hubbard dimer. *Chinese Physics B*, 28(10), 107103. <https://doi.org/10.1088/1674-1056/ab3dfe> (cit. on pp. 73, 85).
- Yang, Y.-T., & Luo, H.-G. (2023, January). First-Order Excited-State Quantum Phase Transition in the Transverse Ising Model with a Longitudinal Field. <https://doi.org/10.48550/arXiv.2301.02066> (cit. on p. 117).
- Yavuz, D. D., Kulatunga, P. B., Urban, E., Johnson, T. A., Proite, N., Henage, T., Walker, T. G., & Saffman, M. (2006). Fast Ground State Manipulation of Neutral Atoms in Microscopic Optical Traps. *Physical Review Letters*, 96(6), 063001. <https://doi.org/10.1103/PhysRevLett.96.063001> (cit. on p. 46).
- Yu, J., Devanathan, R., & Weber, W. J. (2009). First-principles study of defects and phase transition in uo2. *Journal of Physics: Condensed Matter*, 21(43), 435401 (cit. on p. 17).
- Zhang, H., Johansson, B., & Vitos, L. (2011). Density-functional study of paramagnetic iron. *Phys. Rev. B*, 84, 140411. <https://doi.org/10.1103/PhysRevB.84.140411> (cit. on p. 8).

Appendix A

LiH and BeH₂ Hamiltonians

In this section, examples of complete Hamiltonians of molecules LiH (for an inter-atomic distance of 1.5 Å) and BeH₂ (for an inter-atomic distance of 1.17 Å) obtained with the method described in Chap. 4 Sec. 4.3.1 are shown.

$$\begin{aligned}
 H_{\text{LiH}} = & -\mathbf{0.19975} + \mathbf{0.05393}Z_0 - \mathbf{0.12836}Z_1 - \mathbf{0.31773}Z_0Z_1 - \mathbf{0.31773}Z_3 + \mathbf{0.0605}Z_1Z_3 \\
 & + \mathbf{0.11409}Z_0Z_1Z_3 + \mathbf{0.05362}Z_4 + \mathbf{0.11434}Z_2Z_4 - \mathbf{0.03787}Z_2Z_3Z_4 + \mathbf{0.05362}Z_1Z_2Z_3Z_4 \\
 & + \mathbf{0.0836}Z_0Z_1Z_2Z_3Z_4 - \mathbf{0.03787}Z_5 + \mathbf{0.05666}Z_1Z_5 + \mathbf{0.11434}Z_0Z_1Z_5 + \mathbf{0.0836}Z_3Z_5 \\
 & + \mathbf{0.05666}Z_2Z_3Z_5 - \mathbf{0.12836}Z_4Z_5 + \mathbf{0.0847}Z_1Z_4Z_5 + \mathbf{0.0605}Z_0Z_1Z_4Z_5 + \mathbf{0.05393}Z_3Z_4Z_5 \\
 & + \mathbf{0.12357}Z_2Z_3Z_4Z_5 + \mathbf{0.01522}X_1 - \mathbf{0.01522}Z_0X_1 + \mathbf{0.01089}X_1Z_3 - \mathbf{0.01089}Z_0X_1Z_3 \\
 & + \mathbf{0.00436}X_1Z_2Z_3Z_4 - \mathbf{0.00436}Z_0X_1Z_2Z_3Z_4 + \mathbf{0.01273}X_1Z_5 - \mathbf{0.01273}Z_0X_1Z_5 - \mathbf{0.00901}X_1Z_4Z_5 \\
 & + \mathbf{0.00901}Z_0X_1Z_4Z_5 + \mathbf{0.00448}X_0X_2 - \mathbf{0.00479}X_0Z_1X_2 - \mathbf{0.03512}X_0Z_1X_2Z_3 - \mathbf{0.03512}Y_0Y_2Z_4 \\
 & - \mathbf{0.00479}Y_0Y_2Z_3Z_4 + \mathbf{0.00448}Y_0Z_1Y_2Z_3Z_4 - \mathbf{0.03306}X_0Z_1X_2Z_5 + \mathbf{0.00237}Y_0Y_2Z_3Z_5 + \mathbf{0.00237}X_0Z_1X_2Z_4Z_5 \\
 & - \mathbf{0.03306}Y_0Y_2Z_3Z_4Z_5 - (4 \times 10^{-5})X_0X_1X_2 - \mathbf{0.00277}Y_0Y_1X_2 + \mathbf{0.01054}X_0X_1X_2Z_3 + \mathbf{0.01054}X_0Y_1Y_2Z_4 \\
 & + \mathbf{0.00277}Y_0X_1Y_2Z_3Z_4 - (4 \times 10^{-5})X_0Y_1Y_2Z_3Z_4 + \mathbf{0.01173}X_0X_1X_2Z_5 - \mathbf{0.00154}X_0Y_1Y_2Z_3Z_5 \\
 & - \mathbf{0.00154}X_0X_1X_2Z_4Z_5 + \mathbf{0.01173}X_0Y_1Y_2Z_3Z_4Z_5 + \mathbf{0.01522}X_3X_4 - \mathbf{0.00901}Z_1X_3X_4 + \mathbf{0.01089}Z_0Z_1X_3X_4 \\
 & + \mathbf{0.00436}Y_3Y_4 - \mathbf{0.01273}Z_2Y_3Y_4 + \mathbf{0.00436}X_3X_4Z_5 - \mathbf{0.01273}Z_2X_3X_4Z_5 + \mathbf{0.01522}Y_3Y_4Z_5 - \mathbf{0.00901}Z_1Y_3Y_4Z_5 \\
 & + \mathbf{0.01089}Z_0Z_1Y_3Y_4Z_5 + \mathbf{0.00658}X_1X_3X_4 - \mathbf{0.00658}Z_0X_1X_3X_4 + \mathbf{0.00658}X_1Y_3Y_4Z_5 - \mathbf{0.00658}Z_0X_1Y_3Y_4Z_5 \\
 & - \mathbf{0.00776}X_0Z_1X_2X_3X_4 + \mathbf{0.00776}Y_0Y_2Y_3Y_4 + \mathbf{0.00776}Y_0Y_2X_3X_4Z_5 - \mathbf{0.00776}X_0Z_1X_2Y_3Y_4Z_5 \\
 & + \mathbf{0.00211}X_0X_1X_2X_3X_4 - \mathbf{0.00211}X_0Y_1Y_2Y_3Y_4 - \mathbf{0.00211}X_0Y_1Y_2X_3X_4Z_5 + \mathbf{0.00211}X_0X_1X_2Y_3Y_4Z_5 \\
 & + \mathbf{0.00004}X_5 + -\mathbf{0.00154}Z_1X_5 + \mathbf{0.01054}Z_0Z_1X_5 + \mathbf{0.00277}Z_3X_5 - \mathbf{0.01173}Z_2Z_3X_5 + \mathbf{0.00004}Z_4X_5 \\
 & + \mathbf{0.00154}Z_1Z_4X_5 + -\mathbf{0.01054}Z_0Z_1Z_4X_5 - \mathbf{0.00277}Z_3Z_4X_5 + \mathbf{0.01173}Z_2Z_3Z_4X_5 \\
 & + \mathbf{0.00211}X_1X_5 - \mathbf{0.00211}Z_0X_1X_5 + -\mathbf{0.00211}X_1Z_4X_5 + \mathbf{0.00211}Z_0X_1Z_4X_5 - \mathbf{0.00837}X_0Z_1X_2X_5 \\
 & + \mathbf{0.00837}Y_0Y_2Z_3X_5 + \mathbf{0.00837}X_0Z_1X_2Z_4X_5 \\
 & - \mathbf{0.00837}Y_0Y_2Z_3Z_4X_5 + \mathbf{0.00303}X_0X_1X_2X_5 - \mathbf{0.00303}X_0Y_1Y_2Z_3X_5 - \mathbf{0.00303}X_0X_1X_2Z_4X_5 \\
 & + \mathbf{0.00303}X_0Y_1Y_2Z_3Z_4X_5 + \mathbf{0.00448}X_3X_4X_5 + \mathbf{0.03306}Z_2X_3X_4X_5 - \mathbf{0.00479}Y_3Y_4X_5 + \mathbf{0.00237}Z_1Y_3Y_4X_5 \\
 & - \mathbf{0.03512}Z_0Z_1Y_3Y_4X_5 + \mathbf{0.00448}Y_3X_4Y_5 + \mathbf{0.03306}Z_2Y_3X_4Y_5 + \mathbf{0.00479}X_3Y_4Y_5 - \mathbf{0.00237}Z_1X_3Y_4Y_5 \\
 & + \mathbf{0.03512}Z_0Z_1X_3Y_4Y_5 - \mathbf{0.00776}X_1Y_3Y_4X_5 + \mathbf{0.00776}Z_0X_1Y_3Y_4X_5 + \mathbf{0.00776}X_1X_3Y_4Y_5 - \mathbf{0.00776}Z_0X_1X_3Y_4Y_5 \\
 & - \mathbf{0.03074}Y_0Y_2X_3X_4X_5 + \mathbf{0.03074}X_0Z_1X_2Y_3Y_4X_5 - \mathbf{0.03074}Y_0Y_2Y_3X_4Y_5 - \mathbf{0.03074}X_0Z_1X_2X_3Y_4Y_5 \\
 & + \mathbf{0.00837}X_0Y_1Y_2X_3X_4X_5 - \mathbf{0.00837}X_0X_1X_2Y_3Y_4X_5 + \mathbf{0.00837}X_0Y_1Y_2Y_3X_4Y_5 + \mathbf{0.00837}X_0X_1X_2X_3Y_4Y_5
 \end{aligned}
 \tag{A.1}$$

$$\begin{aligned}
H_{\text{BeH}_2} = & -1.90305 - 0.48894Z_0 + 0.14357Z_1 - 0.18803Z_0Z_1 + 0.12314Z_2 + 0.18326Z_0Z_2 \\
& + 0.10964Z_1Z_2 + 0.18222Z_0Z_1Z_2 - 0.48894Z_3 + 0.1288Z_0Z_3 + 0.1136Z_0Z_1Z_3 \\
& + 0.11249Z_2Z_3 + 0.11746Z_1Z_2Z_3 + 0.14357Z_4 - 0.18803Z_3Z_4 + 0.1136Z_0Z_3Z_4 \\
& + 0.10602Z_0Z_1Z_3Z_4 + 0.10306Z_2Z_3Z_4 + 0.10577Z_1Z_2Z_3Z_4 + 0.12314Z_5 + 0.11249Z_0Z_5 \\
& + 0.10306Z_0Z_1Z_5 + 0.10451Z_2Z_5 + 0.10785Z_1Z_2Z_5 + 0.18326Z_3Z_5 + 0.10964Z_4Z_5 \\
& + 0.11746Z_0Z_4Z_5 + 0.10577Z_0Z_1Z_4Z_5 + 0.10785Z_2Z_4Z_5 + 0.11352Z_1Z_2Z_4Z_5 + 0.18222Z_3Z_4Z_5 \\
& - 0.00743X_0X_1 - 0.00229Y_0Y_1 - 0.00229X_0X_1Z_2 - 0.00743Y_0Y_1Z_2 - 0.00711Y_0Y_1Z_3 \\
& - 0.00711X_0X_1Z_2Z_3 - 0.00875Y_0Y_1Z_3Z_4 - 0.00875X_0X_1Z_2Z_3Z_4 - 0.00352Y_0Y_1Z_5 - 0.00352X_0X_1Z_2Z_5 \\
& - 0.0072Y_0Y_1Z_4Z_5 - 0.0072X_0X_1Z_2Z_4Z_5 - 0.04165X_0X_2 + 0.03769X_0Z_1X_2 - 0.00396Y_0Y_2 \\
& + 0.00839X_1X_2 - 0.01015Z_0X_1X_2 - 0.01015Y_1Y_2 + 0.00839Z_0Y_1Y_2 + 0.01355Z_0X_1X_2Z_3 \\
& + 0.01355Y_1Y_2Z_3 + 0.01082Z_0X_1X_2Z_3Z_4 + 0.01082Y_1Y_2Z_3Z_4 + 0.00854Z_0X_1X_2Z_5 + 0.00854Y_1Y_2Z_5 \\
& + 0.01408Z_0X_1X_2Z_4Z_5 + 0.01408Y_1Y_2Z_4Z_5 + 0.03611X_0X_3 - 0.03611X_0Z_1X_3 - 0.03611X_0X_3Z_4 \\
& + 0.03611X_0Z_1X_3Z_4 - 0.02498X_1X_3 + 0.02498Z_0X_1Z_2X_3 + 0.02498X_1X_3Z_4 - 0.02498Z_0X_1Z_2X_3Z_4 \\
& - 0.03615X_2X_3 + 0.03615Z_1X_2X_3 + 0.03615X_2X_3Z_4 - 0.03615Z_1X_2X_3Z_4 - 0.01573X_0X_1X_2X_3 \\
& - 0.01573Y_0X_1Y_2X_3 + 0.01573X_0X_1X_2X_3Z_4 + 0.01573Y_0X_1Y_2X_3Z_4 - 0.02498X_0X_4 + 0.02498X_0Z_1X_4 \\
& + 0.02498X_0Z_3X_4Z_5 - 0.02498X_0Z_1Z_3X_4Z_5 + 0.02085X_1X_4 - 0.02085Z_0X_1Z_2X_4 - 0.02085X_1Z_3X_4Z_5 \\
& + 0.02085Z_0X_1Z_2Z_3X_4Z_5 + 0.02464X_2X_4 - 0.02464Z_1X_2X_4 - 0.02464X_2Z_3X_4Z_5 + 0.02464Z_1X_2Z_3X_4Z_5 \\
& + 0.01532X_0X_1X_2X_4 + 0.01532Y_0X_1Y_2X_4 - 0.01532X_0X_1X_2Z_3X_4Z_5 - 0.01532Y_0X_1Y_2Z_3X_4Z_5 \\
& - 0.00743X_3X_4 - 0.00229Y_3Y_4 - 0.00711Z_0Y_3Y_4 - 0.00875Z_0Z_1Y_3Y_4 - 0.00352Z_2Y_3Y_4 - 0.0072Z_1Z_2Y_3Y_4 \\
& - 0.00229X_3X_4Z_5 - 0.00711Z_0X_3X_4Z_5 - 0.00875Z_0Z_1X_3X_4Z_5 - 0.00352Z_2X_3X_4Z_5 - 0.0072Z_1Z_2X_3X_4Z_5 \\
& - 0.00743Y_3Y_4Z_5 + 0.01972Y_0Y_1Y_3Y_4 + 0.01972X_0X_1Z_2Y_3Y_4 + 0.01972Y_0Y_1X_3X_4Z_5 + 0.01972X_0X_1Z_2X_3X_4Z_5 \\
& - 0.0173Z_0X_1X_2Y_3Y_4 - 0.0173Y_1Y_2Y_3Y_4 - 0.0173Z_0X_1X_2X_3X_4Z_5 - 0.0173Y_1Y_2X_3X_4Z_5 - 0.03615X_0X_5 \\
& + 0.03615X_0Z_1X_5 + 0.03615X_0Z_4X_5 - 0.03615X_0Z_1Z_4X_5 + 0.02464X_1X_5 - 0.02464Z_0X_1Z_2X_5 \\
& - 0.02464X_1Z_4X_5 + 0.02464Z_0X_1Z_2Z_4X_5 + 0.04177X_2X_5 - 0.04177Z_1X_2X_5 - 0.04177X_2Z_4X_5 \\
& + 0.04177Z_1X_2Z_4X_5 + 0.01232X_0X_1X_2X_5 + 0.01232Y_0X_1Y_2X_5 - 0.01232X_0X_1X_2Z_4X_5 - 0.01232Y_0X_1Y_2Z_4X_5 \\
& - 0.04165X_3X_5 + 0.03769X_3Z_4X_5 - 0.00396Y_3Y_5 + 0.00839X_4X_5 - 0.01015Z_3X_4X_5 \\
& + 0.01355Z_0Z_3X_4X_5 + 0.01082Z_0Z_1Z_3X_4X_5 + 0.00854Z_2Z_3X_4X_5 + 0.01408Z_1Z_2Z_3X_4X_5 - 0.01015Y_4Y_5 \\
& + 0.01355Z_0Y_4Y_5 + 0.01082Z_0Z_1Y_4Y_5 + 0.00854Z_2Y_4Y_5 + 0.01408Z_1Z_2Y_4Y_5 + 0.00839Z_3Y_4Y_5 \\
& - 0.0173Y_0Y_1Z_3X_4X_5 - 0.0173X_0X_1Z_2Z_3X_4X_5 - 0.0173Y_0Y_1Y_4Y_5 - 0.0173X_0X_1Z_2Y_4Y_5 \\
& + 0.01858Z_0X_1X_2Z_3X_4X_5 + 0.01858Y_1Y_2Z_3X_4X_5 + 0.01858Z_0X_1X_2Y_4Y_5 + 0.01858Y_1Y_2Y_4Y_5 \\
& - 0.01573X_0X_3X_4X_5 + 0.01573X_0Z_1X_3X_4X_5 - 0.01573X_0Y_3X_4Y_5 + 0.01573X_0Z_1Y_3X_4Y_5 \\
& + 0.01532X_1X_3X_4X_5 - 0.01532Z_0X_1Z_2X_3X_4X_5 \\
& + 0.01532X_1Y_3X_4Y_5 - 0.01532Z_0X_1Z_2Y_3X_4Y_5 + 0.01232X_2X_3X_4X_5 - 0.01232Z_1X_2X_3X_4X_5 \\
& + 0.01232X_2Y_3X_4Y_5 - 0.01232Z_1X_2Y_3X_4Y_5 + 0.01415X_0X_1X_2X_3X_4X_5 + 0.01415Y_0X_1Y_2X_3X_4X_5 \\
& + 0.01415X_0X_1X_2Y_3X_4Y_5 + 0.01415Y_0X_1Y_2Y_3X_4Y_5
\end{aligned}$$

(A.2)

Appendix B

Slave-spin theory for the Mott transition in the triangular lattice

B.1 Forewords

In the main chapter (Chap. 5), we focus on the square lattice because of it is a bipartite lattice and therefore the constraint of the slave-spin method is useless. In addition, it is the most studied lattice. At first, we did not focus on this lattice but on the triangular lattice, (111) plane of the crystal structure of face-centered cubic materials like iron. The two main differences are the condition for half-filling and the constraint fulfillment. In order to keep the system at half-filling, we use an optimizer to find the good chemical potential for every values of U/t . Yet, the constraint is never satisfied in the following. Despite this strong approximation, I think it is interesting to see the result as the geometry is totally different and the cluster mean-field is not defined in the same way. The simulation are performed for cluster of 6 and 10 sites.

The out of equilibrium case is not studied here. The content of this chapter is extracted from a first version of the article on the Slave-Spin theory.

B.2 Solving the spin Hamiltonian H_S for Q : cluster mean-field

We now focus on the computation of $Q_{i,j}$. It requires the computations the spin-spin correlation function $\langle S_i^z S_j^z \rangle$. Many strategies are available. Most authors (de'Medici et al., 2005; Rüegg et al., 2010) handle H_S at the single-site mean-field level. This yields local observables, but neglects important spatial correlation effects, thereby limiting the scope of the method. In particular, spatial (or orbital) resolution in quasi-particle weights is a key factor to investigate e.g hot and cold spots observed in angle-resolved photoemission spectroscopy (Brown et al., 2020; Damascelli et al., 2003; Hashimoto et al., 2014).

One must thus go beyond single-site mean-field. A straightforward approach would be to directly diagonalize a finite-site version of H_S and compute the finite-size ground-state. However, finite-size effects would prevent us from observing the phase transition we are looking for, namely the transition from a Fermi liquid to a Mott insulator.

We thus tackle H_S (Eq. (5.2b)) with a cluster mean-field approach, as done in e.g (Hassan & de'Medici, 2010). Finite-size effects are thus reduced thanks to the influence of a self-consistent mean field $m = \langle S^z \rangle$ at the boundary of the cluster, at the same numerical price as the exact diagonalization (except the procedure needs to be repeated in a self-consistent fashion until convergence of the mean field).

The cluster mean-field approximation leads to

$$S_i^z S_j^z \approx \langle S_i^z \rangle S_j^z + \langle S_j^z \rangle S_i^z - \langle S_i^z \rangle \langle S_j^z \rangle, \quad (\text{B.1})$$

where i (j) is inside the cluster and j (i) is not. The mean-field parameter $\langle S^z \rangle$ is the same for all sites in the thermodynamic limit. As we consider finite-size systems, we numerically compute

$$m = \frac{1}{N_a} \sum_i^{N_a} \langle S_i^z \rangle \quad (\text{B.2})$$

With N_a being the number of sites. Eq. (5.2b) can be rewritten as

$$H_S^{(C)}(J, m) = H_S(J) + \sum_{i \in C} h_i S_i^z \quad (\text{B.3})$$

where C is the cluster and $h_i = \sum_j m J_{i,j}$

The shape of the cluster and the mean field are illustrated in Fig. B.1 for clusters of size 6 and 10.

For instance, for the 6-site cluster, sites 0, 3 and 5 have 2 nearest-neighbor whereas sites 1, 2 and 4 are connected to 4 sites respectively. If we consider a hopping term of value -1 for connected sites and 0 for the others, the matrix t can be written:

$$t = - \begin{pmatrix} 0 & 1 & 1 & 0 & 0 & 0 \\ 1 & 0 & 1 & 1 & 1 & 0 \\ 1 & 1 & 0 & 0 & 1 & 1 \\ 0 & 1 & 0 & 0 & 1 & 0 \\ 0 & 1 & 1 & 1 & 0 & 1 \\ 0 & 0 & 1 & 0 & 1 & 0 \end{pmatrix} \quad (\text{B.4})$$

This embedding will be the one studied in the rest of the article.

The self-consistent procedure to solve for the approximate ground state of H_S , $|\psi_0\rangle_C$, and hence $Q_{i,j}$, is illustrated in Fig. 5.1. The solution of the cluster Hamiltonian for a fixed mean field h , $H_S^{(C)}$, is described in section B.3.1.

B.3 Self-consistent outer cycle

We are now ready to describe the outer self-consistent loop. It is illustrated in Fig. 5.1.

In the regime of cluster mean-field theory, there is a difference between the quasi-particle weight Z and the effective mass renormalization $\frac{m}{m^*}$. across the Mott insulator phase, Z vanishes to 0 beside $g = \frac{m}{m^*}$ stays finite (Florens & Georges, 2004; Hassan & de'Medici, 2010; Rüegg et al., 2010). They are the order parameters of the Fermi-liquid/Mott insulator phase transition. The final output of our method is then the quasi-particle weight defined as

$$Z = h^2 = \langle S^z \rangle^2. \quad (\text{B.5})$$

It is the order parameter for the phase transition : it is $\neq 0$ before transition and should be $= 0$ after the phase transition. The effective mass

$$g = \frac{m}{m^*} = \langle S_i^z S_{i+1}^z \rangle \quad (\text{B.6})$$

on the other hand, does not reach 0 after the transition. These definitions are true (i.e do not depend on the site we choose) if we consider a system with an infinite number of size. Numerically,

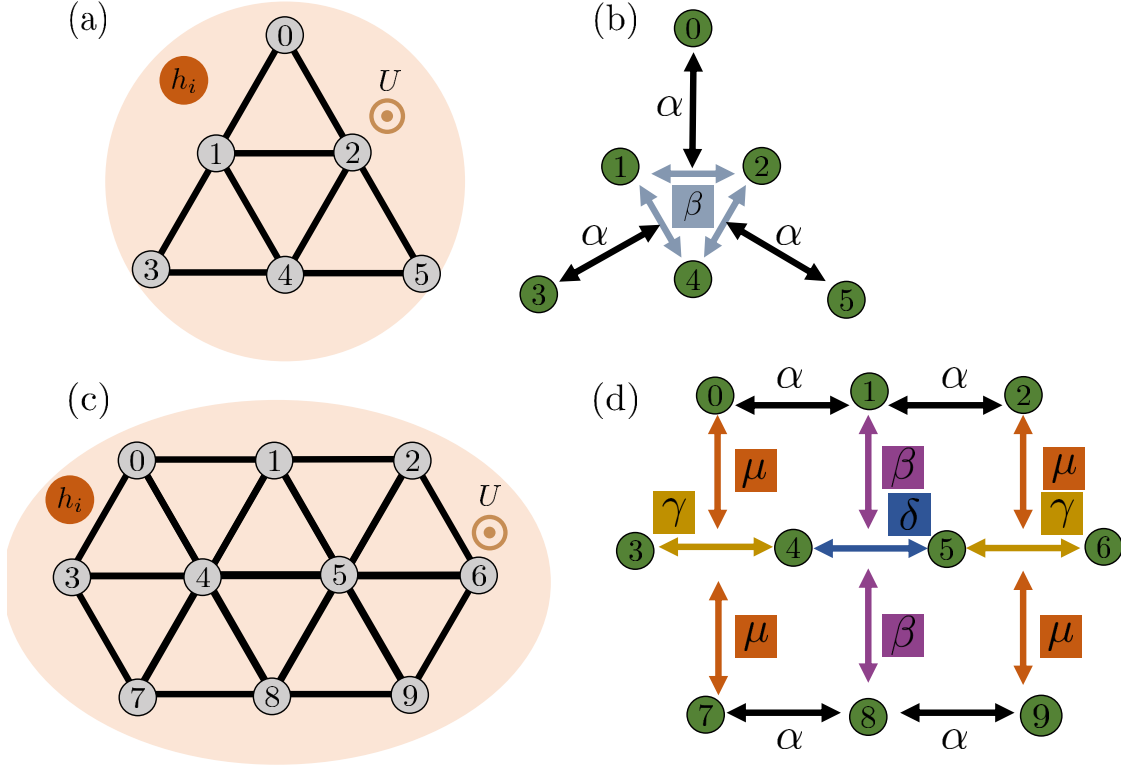


Figure B.1: *Cluster mean field and parameterized geometry of Rydberg atoms.* (a) Geometry of a 6-site cluster. After the slave spin mean field approach combined with the cluster mean field approach, all spins S_i^z are immersed in a mean-field bath h_i and undergo a transverse field $\propto U$. (b) Optimization of the geometry with parameters α and β to fulfill Eq.(B.12). (c-d) Same as (a-b), for a 10-site cluster.

these values are computed as mean values over all spins:

$$Z = h^2 = \left(\frac{1}{N_a} \sum_i^{N_a} \langle S_i^z \rangle \right)^2 \quad (\text{B.7a})$$

$$g = \frac{1}{(N_a - 1)} \sum_i^{N_a-1} \langle S_i^z S_{i+1}^z \rangle. \quad (\text{B.7b})$$

In the following, the whole procedure to find these two values is named SSMF-CMFT for Slave Spin Mean Field - Cluster Mean Field Theory.

B.3.1 Solving the embedded model

For a given value of the mean field h , we now need to compute $\langle S_i^z S_j^z \rangle$ and $\langle S_i^z \rangle$ with $\langle \dots \rangle = \langle \psi_0 | \dots | \psi_0 \rangle_{\mathbb{S}}$ to obtain g , Q and Z at the end of the loop. It is possible to compute these values without knowing the exact groundstate of the system but in our case, considering an implementation on a Rydberg quantum processor, it is simpler to get the groundstate of $H_S^{(C)}(J, h)$.

Exact diagonalization of the cluster Hamiltonian Eq. (B.3) is possible only for a few sites because of the exponential size of the corresponding Hilbert space. We therefore turn to our Rydberg platform, characterized by the Hamiltonian given in Eq. (3.6), to find the solution to our spin model Eq. (B.3).

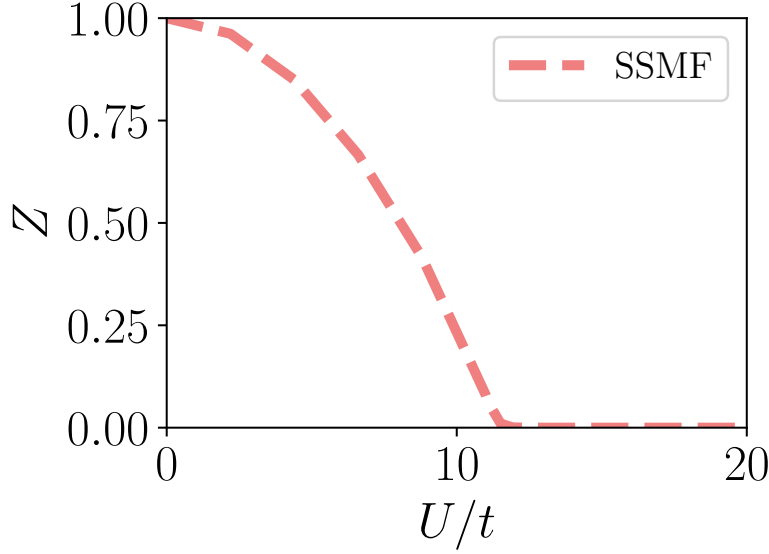


Figure B.2: *Quasiparticle weight and mass renormalization as a function of U/t with the SSMF-CMFT method.* Systems plotted here 10 sites triangular lattices. $H_S^{(C)}(J, h)$ is solved by exact diagonalization method.

These two Hamiltonians have a major difference: while the Rydberg Hamiltonian has an anti-ferromagnetic interaction, the auxiliary spin Hamiltonian has a ferromagnetic interaction as long as $t_{i,j} > 0$. We can nevertheless make use of the Rydberg platform: instead of looking for its ground state, we are going to be looking for its most excited state.

To this aim, we resort to an annealing procedure. The atomic register is prepared in a state

$$|\psi_{\text{start}}\rangle = |g\rangle^{\otimes N_a} \quad (\text{B.8})$$

where N_a is the number of atoms.

The adiabatic theorem states that a physical system remains in its instantaneous eigenstate if the Hamiltonian is driven slowly enough compare to the inverse square gap between the eigenvalue and the rest of the Hamiltonian's spectrum. In particular, this is true for the most excited state. We can rewrite (B.3) as:

$$H_{\text{target}} = \sum_{i,j,\sigma} (-J_{i,j}) S_i^z S_j^z - \sum_{i \in C} h_i S_i^z - \frac{U}{4} \sum_i S_i^x \quad (\text{B.9})$$

that is the target Hamiltonian. The first step is to calculate which experimental values should be obtained to go from Eq. (3.6) to Eq. (B.9). The Rabi frequency, detuning and the interaction matrix of the atoms have to fulfil the following relations at the end of the annealing procedure:

$$\Omega(t_{\text{max}}) = \frac{U}{2}, \quad (\text{B.10})$$

$$\delta_i(t_{\text{max}}) = \frac{1}{2} \sum_{j \neq i} \frac{C_6}{r_{i,j}^6} + 2h \sum_{j \neq i} J_{i,j}, \quad (\text{B.11})$$

$$\frac{C_6}{r_{i,j}^6} = -4J_{i,j}. \quad (\text{B.12})$$

In our embedding, sites can be described in two categories: those which have two nearest neighbours and those which have four nearest neighbours. It leads to a matrix $J_{i,j}$ of the form

$$\begin{pmatrix} 0. & a & a & 0. & 0. & 0. \\ a & 0. & b & a & b & 0. \\ a & b & 0. & 0. & b & a \\ 0. & a & 0. & 0. & a & 0. \\ 0. & b & b & a & 0. & a \\ 0. & 0. & a & 0. & a & 0. \end{pmatrix}. \quad (\text{B.13})$$

It means that only two parameters are needed to satisfy Eq. (B.12). The parameters α and β described in Fig. B.1 are then optimized in each outer loop of the algorithm (Fig. 5.1). The optimization of the geometry starts with an initial guess for parameters α and β . Then, a Nelder-Mead algorithm is used to minimize the value

$$\sum_{i,j} \left| \frac{C_6}{r_{i,j}^6} + 4J_{i,j} \right| \quad (\text{B.14})$$

It usually takes less than 50 steps to find the final parameters with very good results (see Sec.B.5.2). In the following, we describe the experimental procedure to solve (B.3). First, the atoms are prepared in the state (B.8) and in the optimised geometry. The following Hamiltonian is the one applied at $t = 0$

$$H_{\text{start}} = \sum_{i \neq j} \frac{C_6}{|\mathbf{r}_i - \mathbf{r}_j|^6} \hat{n}_i \hat{n}_j - \hbar \delta_{\text{start}} \sum_i n_i \quad (\text{B.15})$$

where δ_{start} is set so that $|\psi_{\text{start}}\rangle$ is the most excited state of Eq. (B.15). The Rabi frequency and the detuning are then driven during a time t_{max} to reach the Hamiltonian Eq. (B.9). A global addressing is performed for the Rabi frequency whereas a local one is used for the detuning. Following Eq. (B.10), the Rabi frequency starts at 0 MHz and is driven linearly to $\frac{U}{2}$. Similarly, the detunings are all prepared at a value δ_{start} and are driven separately to values Eq. (B.11). $h \in [0, 1]$ and Eq. (B.12) ensures that $\delta_i(t_{\text{max}})$ is always positive. Observables (Q , Z , g) are measured with a sample of shots obtained from the state of the atoms.

B.4 Discussion on units

Experimentally, the Rydberg states used impose a van der Waals coefficient $\frac{C_6}{h} = 1947.10^3$ MHz. μm^6 (Scholl et al., 2021). This leads to fix all parameters in our protocol. The Rabi frequency (Eq. (B.10)) can be driven up to a maximal value of $\frac{U}{2\pi} \approx 2.5$ MHz. Therefore, considering $U \in [0, 5]$ is tailored to our device. In addition, It is guessed that the phase transition is for $\frac{U}{t} \in [10, 15]$ (see Sec. B.5.1). We consider then $t = \frac{1}{3}$ such as all the interval is span. This yields to value distance between atoms $\approx 11\mu\text{m}$ for the closest ones and $\approx 23\mu\text{m}$ for unintended interactions. Interaction values are then between 10^{-2} MHz and ≈ 0.8 MHz. Frequencies of local detuning are then imposed by Eq. (B.11). It is important to note that for h values close to 1 (i.e. $\frac{U}{t} \ll \frac{U_c}{t}$), all $\delta_i(t_{\text{max}})$ are expected to reach 0 MHz¹. In our numerical simulation, optimization of geometry provides us $\delta_i(t_{\text{max}}) \approx 10^{-2}$ MHz. For values of $\frac{U}{t}$ at the phase transition and after, $h \approx 0$ and $\delta_i(t_{\text{max}}) = -2 \sum_{j \neq i} J_{i,j} \approx 0.8$ MHz.

¹We aim at $\frac{C_6}{r_{i,j}^6} = -4J_{i,j}$. If we consider this perfectly fulfilled, we can replace in Eq. (B.11) and we obtain $\delta_i(t_{\text{max}}) = \frac{1}{2}(-4 \sum_{i \neq j} J_{i,j}) + 2 \times 1 \times \sum_{j \neq i} J_{i,j} = -2 \sum_{j \neq i} J_{i,j} + 2 \sum_{j \neq i} J_{i,j} = 0$

Numerical tools

All numerical simulations are performed with the library qutip (Johansson et al., 2013) (exact diagonalization) and Quantum Learning Machine. The SPAM error is implemented with a code from Pulser (Silvério et al., 2022).

During the SSMF-CMFT procedure, the vector state obtained for each diagonalization of Eq. (B.3) is sampled to measure Q and Z . Sampling the vector state above 100 samples allows to see the Mott transition. If the maximum number of iterations is set to 5 for the SSMF loop and the CMFT loop, the maximal number of shots is $100 \times 25 = 2500$. The working rate of the device is ≈ 5 Hz. It means it would take 500 s to perform one complete run for a given U .

B.5 Results

B.5.1 Exact diagonalization method

This method is performed in Fig. B.4. The Mott transition appears for $U/t \approx 11.3$. The Mott insulating phase occurs between 10.5 and 16.2 for other numerical methods like DMFT-exact diagonalization ($\frac{U}{t} = 15$, 8 sites), exact diagonalization on 12 sites ($\frac{U}{t} = 12$) and CDMFT ($\frac{U}{t} = 10.5$) (Hassan & de'Medici, 2010): the difference lies in the number of sites taken in the cluster and the choice of gauge considered in the slave-spin theory (de'Medici et al., 2005).

B.5.2 Impact of experimental parameters

The evolution of h during the SSMF-CMFT procedure is shown Fig. B.3. Different starting points h^0 are tested. If $h^0 = 0$ or $h^0 = 1$, the value of h stays constant, it is therefore needed to choose $h^0 \in]0, 1[$. In this interval, h always converges towards the same value. Far from the phase transition, the convergence is relatively quick (less than 35 iterations in total). Near the phase transition, the convergence takes a lot more time as $h^2 = Z$ is an order parameter, but it finally reaches the same value regardless of initial guess for h^0 . The same protocol can be applied to check the evolution of Q during loops. The initial guess for Q is always t in all results.

Optimized geometry

The result of the optimization of atomic positions is shown Fig. B.4 (6 sites). The difference in Z values is under 0.1%. The norm of the difference Eq. (B.14) after optimization is ~ 0.18 for each value of $\frac{U}{t}$.

Dephasing noise

The time of annealing is $t_{max} = 5 \mu s$ and the exact state vector is considered to measure Z . The dephasing effect is shown in Fig. B.5. We can notice that for small γ (0.01 and 0.3 MHz), the phase transition is still present but with smaller values of $\frac{U}{t}$. For larger values, the phase transition disappears. Experimentally, γ is measured around 0.02 MHz. We will use this value in our simulations.

Measurement error

We show the effect of these errors in Fig. B.6. The trivial groundstate of Eq. (5.3) when $U = 0$ is Eq. (B.8). Therefore, a finite ϵ will have an impact on the measurement of this state.

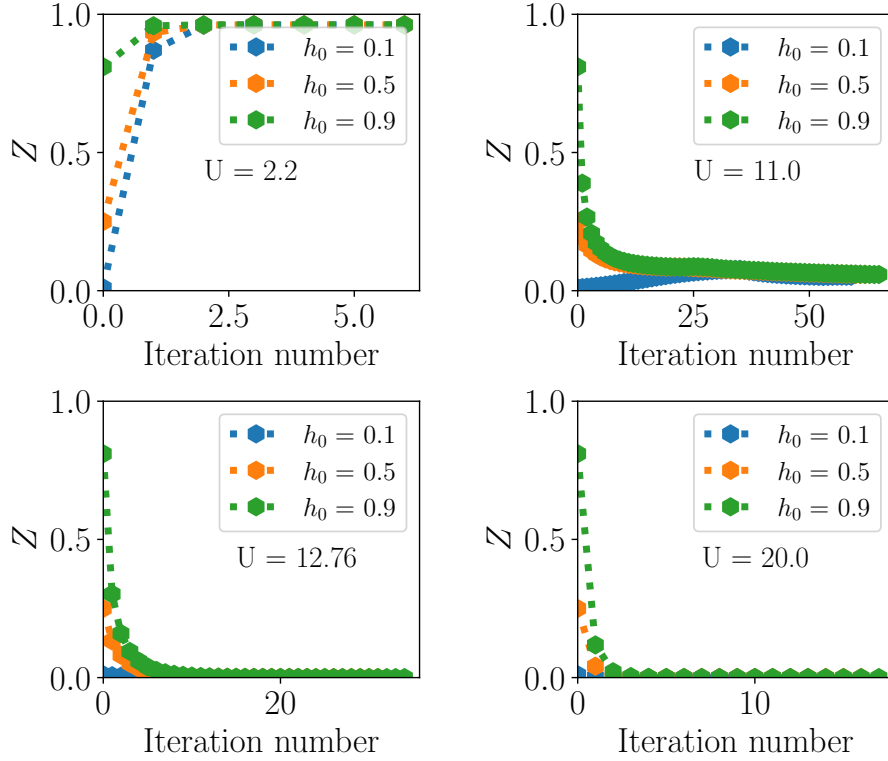


Figure B.3: *Evolution of Z as a function of loop iterations for a 6 sites embedding.* Different starting point h^0 (0.1, 0.5 and 0.9) are considered for each value of U/t (clockwise starting from upper left: $U/t = 2.2$, $U/t = 11.0$, $U/t = 20.0$ and $U/t = 12.76$). The solving method is exact diagonalization. The number of allowed iteration is increased to 2500 and the error accepted is $\eta = 10^{-3}$.

Shot noise

The effect of shot noise is shown in Fig. B.7. We clearly see that increasing the number of shot increases the precision of the result. In order to fit with experimental limitations and stay in the phase transition regime, we will impose $n_{\text{shot}} = 150$ for numerical simulations.

B.6 Discussion

B.6.1 Convergence of the method

Different initial guess of h (0.1, 0.5 and 0.9) for this method are tested in Fig. B.3. For $U \ll U_c$, $U \approx U_c$ and $U \gg U_c$, the convergent point is the same for all initial value, which confirms that this method is quite unrelated to the choice of the initial value of the mean field. In addition, when $U \approx U_c$, it takes more iteration steps to converge, which is normal close to the phase transition.

B.6.2 Experimental feasibility

The method proposed in this study offers several advantages with regard to experimental feasibility. First, it avoids non-local terms that occurs when usual method of solving fermionic systems are used (Jordan-Wigner or Bravyi-Kitaev for instance). This leads to a relatively simple experimental

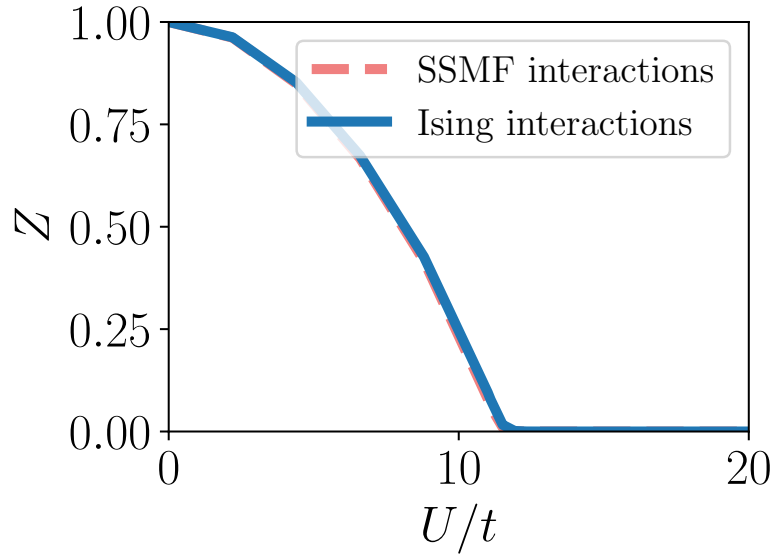


Figure B.4: *Impact of considering a realistic geometry.* Comparison of Z values between method with the real matrix J and the optimized one for 6 sites. In both cases, exact diagonalization method is performed to obtain the groundstate of $H_S^{(C)}$

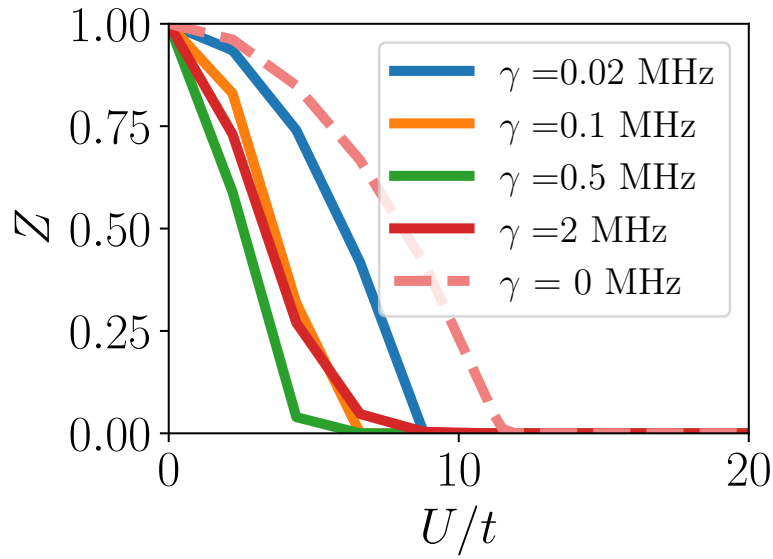


Figure B.5: *Impact of considering dephasing noise* A triangular lattice cluster of 6 sites is considered.

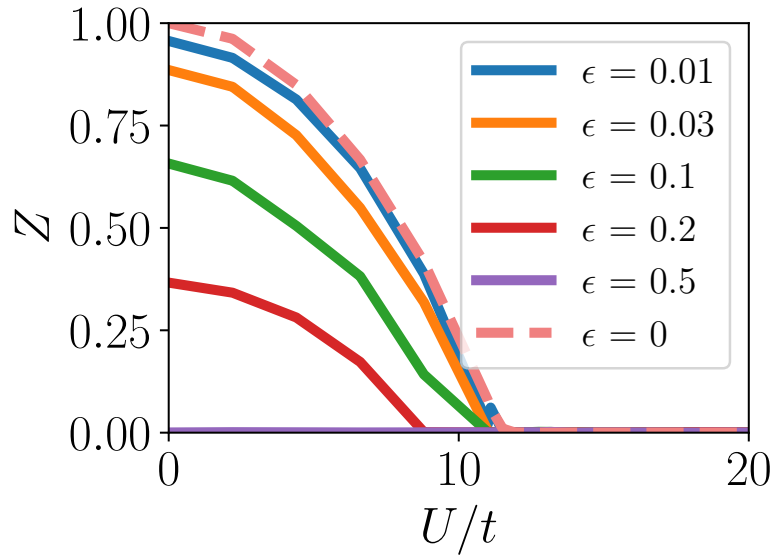


Figure B.6: *Impact of measurement error.* The top panel shows the effect of ϵ and the bottom panel shows the effect of ϵ' . The number of shots considered for each measurement is 1000. The time of annealing is $4 \mu\text{s}$.

setup where only annealing is performed. The scalability of annealing seems better compare to Variational Quantum Eigensolver algorithms for instance, where the number of parameters, the number of loop and the intractability of calculations increases with the system size (Cerezo, Arrasmith, Babbush, Benjamin, Endo, et al., 2021; Fedorov et al., 2022). Finding the good optimizer in the classical part of this kind of algorithm is still an active field of research. In the work presented here, annealing only needs a global detuning and Rabi frequency, which suits well with experimental device. The low number of loop needed (set to a maximum value of 25) leads to a short number of realizations. In addition, the classical part of the method only involves diagonalization of a free fermion system being scalable and easy to tract. For the quantum part of the algorithm, it solves the two-dimensional transverse-field Ising model that exhibits several interesting properties as it is equivalent with the anisotropic limit of the three-dimensional lattice Ising model (Blöte & Deng, 2002; du Croo de Jongh & van Leeuwen, 1998). In addition, The quantum phase transition of the 2D Ising transverse system is not quite well understood (Balducci et al., 2023; Hashizume et al., 2022; Schmitt et al., 2022) and some very recent works show a first-order phase transition for the first excited state of this model (Y.-T. Yang & Luo, 2023). For all these reasons, Rydberg atoms can help to solve actual issues in the 2D ferromagnetic transverse Ising model and thus gained a good understanding of the 2D Hubbard model through SSMF. Yet, the results above focus on the application of the slave-spin method applied to the half-filled, single-site Hubbard model and one should not expect them to prove any quantum advantage with respect to classical methods. Indeed, in this parameters regime, classical methods like diagrammatic Monte-Carlo are efficient in the absence of a sign problem and can essentially reach the exact solution in the thermodynamic limit (Schuler et al., 2016). This therefore constitutes the short-term quantitative target for the Rydberg platform, provided a sufficient quality can be attained.

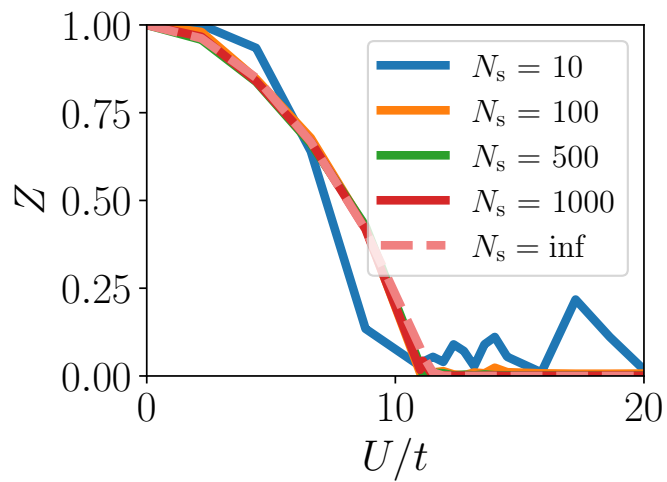


Figure B.7: *Impact of considering a realistic geometry.* Comparison of Z values between method with the real matrix J and the optimized one for 6 sites. In both cases, exact diagonalization method is performed to obtain the groundstate of $H_S^{(C)}$

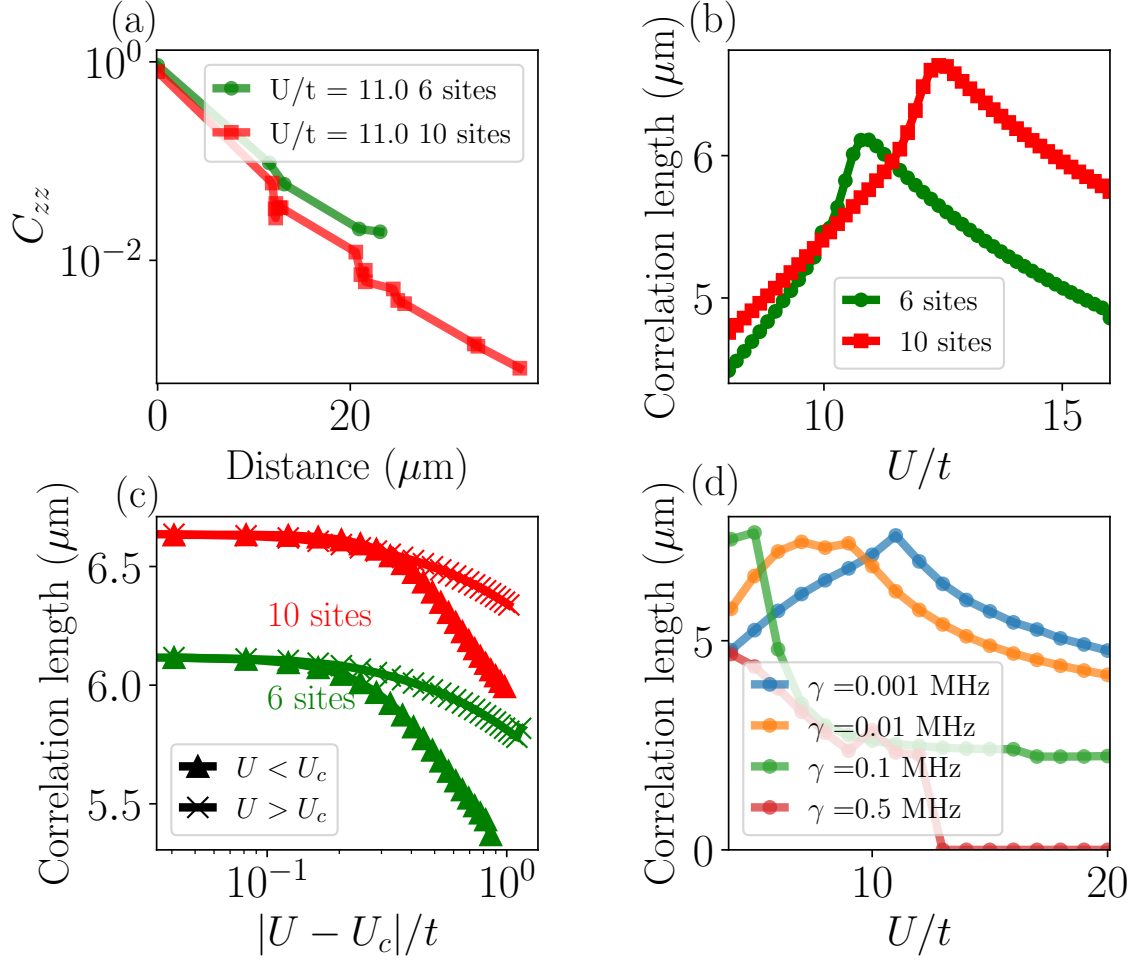


Figure B.8: Correlations $C_{zz}(l)$ and correlation length of spins in the final state for a triangular lattice. (a) correlations C_{zz} vs. distance between atoms for an exact diagonalization method with an optimized geometry. values are shown for several values of U/t and a system with 6 sites (circle dashed lines) and 10 sites (dotted square lines). (b) Correlation lengths vs. U/t for 6 sites (circle green line) and 10 sites (circle red line). The exact diagonalization method is used to solve the Ising Hamiltonian with an optimized geometry. (c) Correlation length for 6 sites vs. U/t for different dephasing noise (blue line $\gamma = 0.001$ MHz, orange line $\gamma = 0.01$ MHz, green line $\gamma = 0.01$ MHz and red line $\gamma = 0.5$ MHz). The annealing procedure is performed to obtain correlations. the dashed black line depicts the result without dephasing ($\gamma = 0.001$ MHz). (d) Correlation length as function of $|U - U_c|/t$ on a log-scale for 6 and 10 sites.

Appendix C

Discussion on the correlation length of the system

C.1 Forewords

Achieving a quantum advantage strongly relies being able to simulate strongly interacting state in the quantum simulator. This means that these states can not be reached by simulating small parts separately but the whole system is needed (all qubits are entangled). A good quantity to check if our system is interacting strongly is the correlation length. It describes the distance at which two spins interact in average. If the correlation length is small one spin "only sees" its nearest-neighbor and its state only depends of them. On the other hand, if the correlation length is very large, two very distant spins interact and it means that the state is very difficult to reach classically.

I propose therefore a little study of correlation length in the Ising with and without slave-spin theory and I focus on the difference between the ferromagnetic model and the antiferromagnetic model.

C.2 Correlation length with the slave-spin method implemented in a RQP

A concrete quantitative yardstick for telling if our problem generates strongly interacting states, is the correlation length ξ than can be achieved in the ground states prepared on the Rydberg platform. Essentially, the size of the problem that is effectively handled by the quantum processor is of order $O(\xi^2)$ (for a 2D geometry), say $N_c^{(Q)} = \pi\xi^2/4$ for concreteness. If one denotes by $N_c^{(C)}$ the number of spins that can be successfully handled by a classical algorithm (for solving H_S), it means one needs $\xi = (4N_c^{(C)}/\pi)^{1/2}$ to reach quantum advantage. Let us assess ξ for the platform under consideration. For this, we focus on the spin-spin correlation length, defined as

$$C_{zz}(l) = \langle S_0^x S_l^x \rangle - \langle S_0^x \rangle \langle S_l^x \rangle \propto e^{-l/\xi}. \quad (\text{C.1})$$

Correlation length and $C_{zz}(l)$ obtained with the SSMF-CMFT method for a triangular lattice (the results shown in this appendix) are shown in Fig. B.8. A maximum value of the correlation length is observed for different values of U/t which confirms the emergence of a phase transition. The dephasing noise has a strong impact on the value of the phase transition as notices in Fig. B.5. The phase transition value is shifted to small U/t values as the dephasing noise is increase. For very high values of γ , correlations become very close to 0. It appears that the correlation length is smaller than the minimum distance between atoms ($l \approx 7 \mu\text{m} < 11 \mu\text{m}$).

This result seems to be well known for the 2D-ferromagnetic Ising system with a transverse field (Rader & Läuchli, 2018), especially when the longitudinal field is non null.

In order to confirm this result for a square lattice, I have run simulation on the Ising transverse field model on a square lattice with a simple cluster mean-field approach.

The considered Hamiltonian is:

$$H = \sum_{\langle i,j \rangle} J_{i,j} S_i^z S_j^z + \bar{m} \sum_i S_i^z + U \sum_i S_i^z \quad (\text{C.2})$$

with $J_{i,j} = -1$ for the ferromagnetic phase and $J_{i,j} = 1$ for the antiferromagnetic phase and $\bar{m} = 1/N \sum_i \langle S_i^z \rangle$. The lattice spacing (and the distance) is set to one between nearest neighbors. Therefore, the distance between points is the Euclidean distance $\sqrt{|x_i - x_j|^2 + |y_i - y_j|^2}$ where (x_i, y_i) and (x_j, y_j) are the coordinates of the spins i and j respectively (see Fig. C.1 and Fig. C.2). The cluster mean-field resolution starts with a first guess of \bar{m} and the groundstate is calculated with an exact diagonalization method. Then \bar{m} is calculated with the system in this groundstate and the loop goes on until convergence. The last groundstate computed is the one used to calculate all correlators and then, ξ .

The computed values are shown in fig. C.1 for the ferromagnetic phase and in Fig. C.2 for the antiferromagnetic phase. In the case of ferromagnetic interactions, the correlation length goes to only one neighbor, in accordance with our result with the slave-spin theory whereas in the antiferromagnetic cases, the correlation length is more than 12 times the distance between atoms in accordance with experimental results (Scholl et al., 2021). In both cases, a phase transition is clearly seen as $\Delta Z/\Delta U$ diverges in both cases. The difference between this two transitions seems to not be clearly understood in the literature. The resolution of such a system with a cluster mean-field approach deserves more research for the slave-spin method to be more deeply understood.

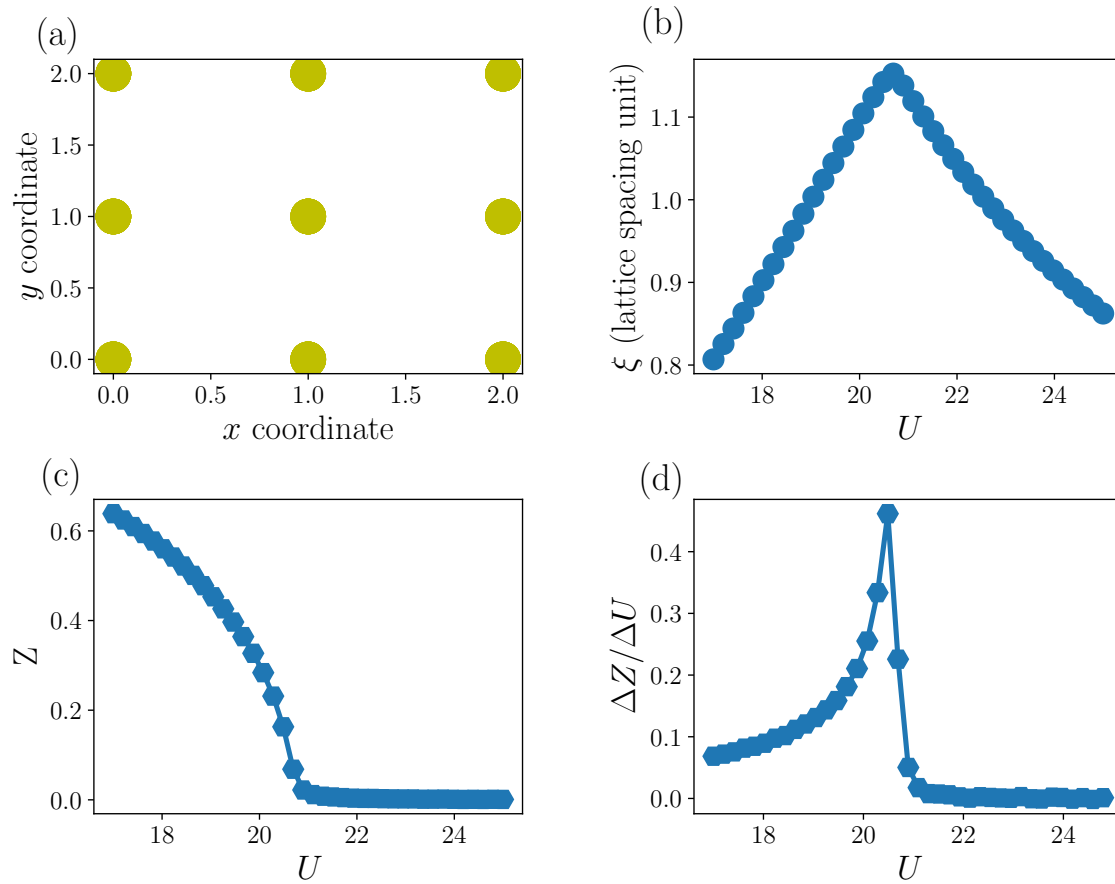


Figure C.1: *Correlations and phase transition for the ferromagnetic Ising transverse field model.* (a) A square lattice of 3×3 spins is used. (b) Correlation length as a function of U . The unit is the lattice spacing. The correlation length has a pic at 1.1. (c) Evolution of $Z = \langle S^z \rangle^2$ as a function of U . (d) Variation of Z with regard to variation U as a function of U .

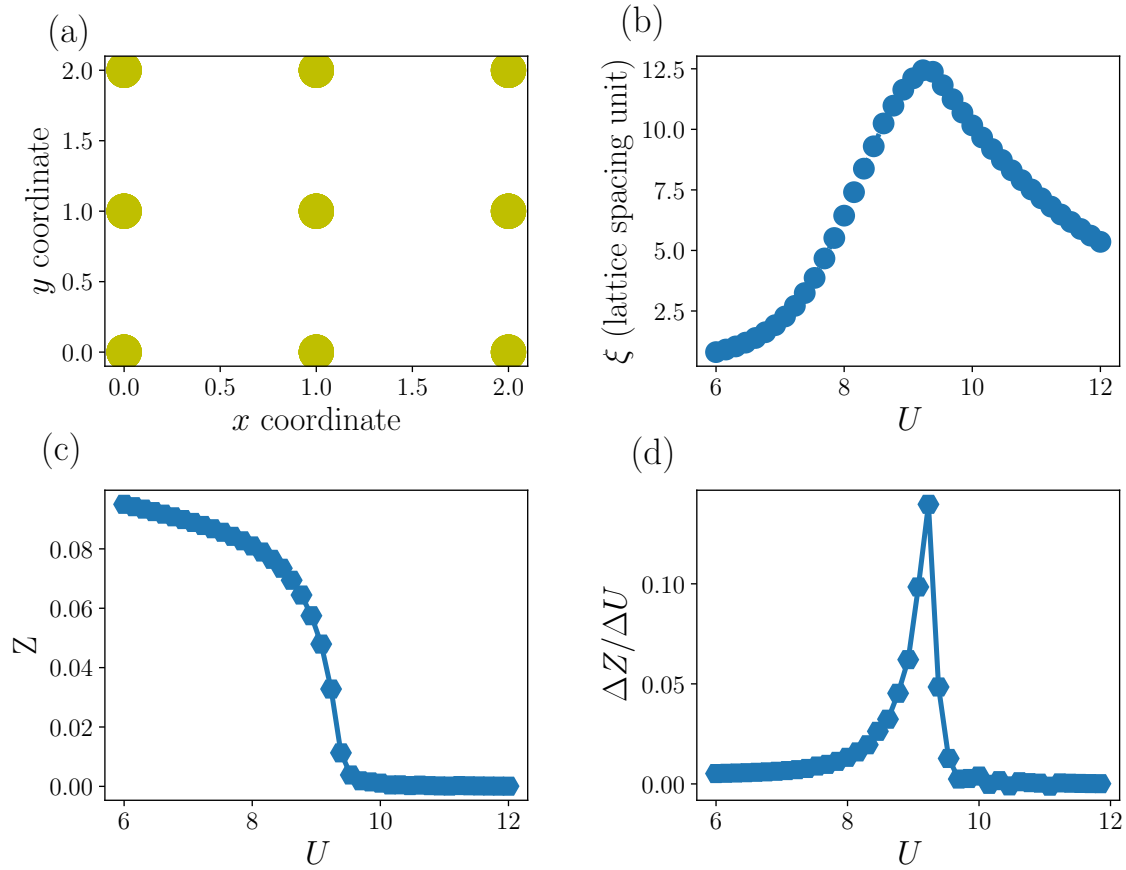


Figure C.2: *Correlations and phase transition for the antiferromagnetic Ising transverse field model.*(a) A square lattice of 3×3 spins is used. (b) Correlation length as a function of U . The unit is the lattice spacing. The correlation length has a pic at 12.5. (c) Evolution of $Z = \langle S^z \rangle^2$ as a function of U . (d) Variation of Z with regard to variation of U as a function of U .

Appendix D

Quasi-particle weight oscillations

D.1 Forewords

In this appendix, I show the data I have obtained with the slave spin method for a quench $0 \rightarrow U_f$ (see Chapter 5) and how we can extract information from it even when a noisy numerical simulation is considered.

D.2 Data of the signal

Quasi-particle response for different U_f is shown in Fig. D.1. The mean value of the oscillation converges to 0 when U_f increases.

D.3 Fourier transform

The frequency of the oscillations of the quasi-particle weight obtained with the slave-spin method is computed from the Fourier transform of the signal. The signal is a list of points $(Z(\tau_k))$ taken during a time τ_{\max} . The library NUMPY is used to perform the Fourier transform of the signal version. The result is shown in Fig. D.2. One can clearly see the shift in frequency as U_f increases. In addition we see two peaks at a frequency U_f and $U_f/2$ as explained in chapter 5.

D.4 Effect of noise

The effect of noise is shown in Fig. D.3. When $U_f \ll U_c$, the oscillations are too small and the noise interferes with the signal. However, when $U_f \geq U_c$, the Fourier transform can clearly be recovered even in the presence of noise.

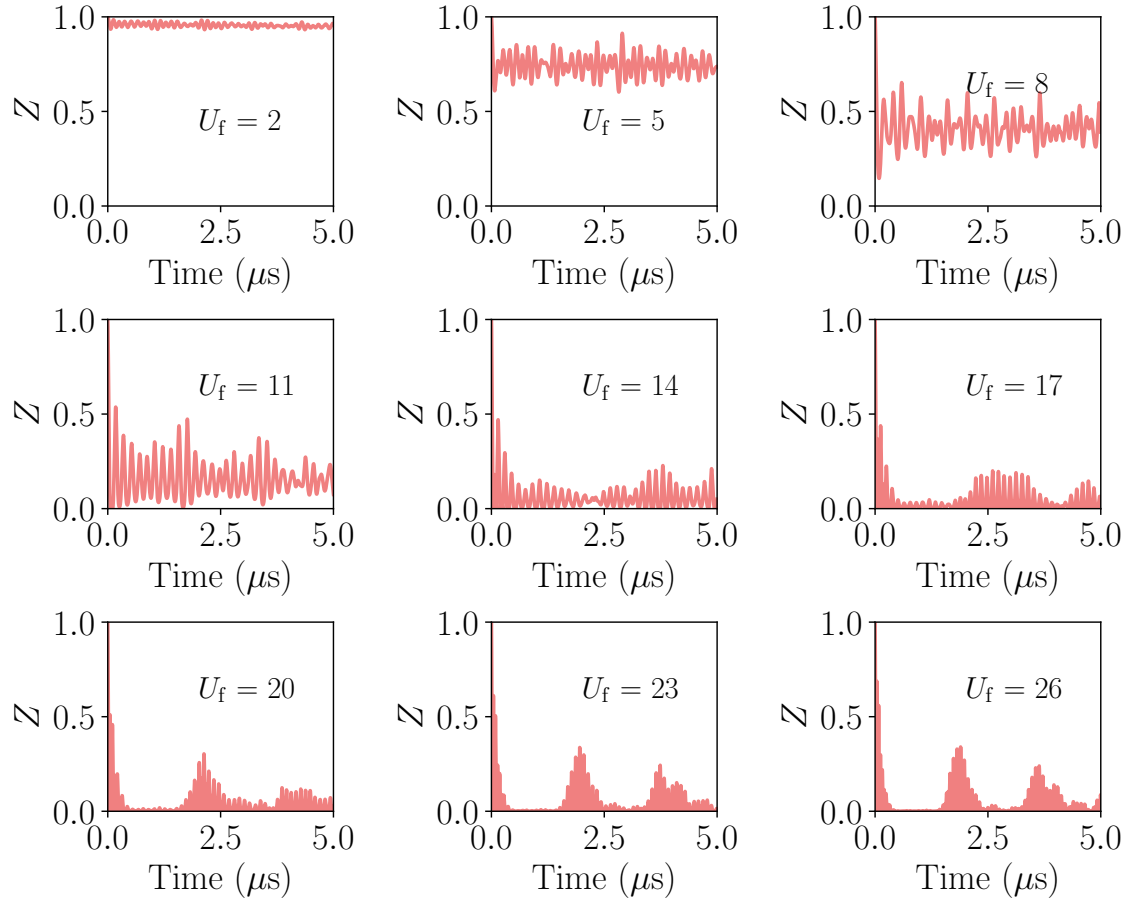


Figure D.1: Response of the quasi-particle weight after a quench $0 \rightarrow U_f$.

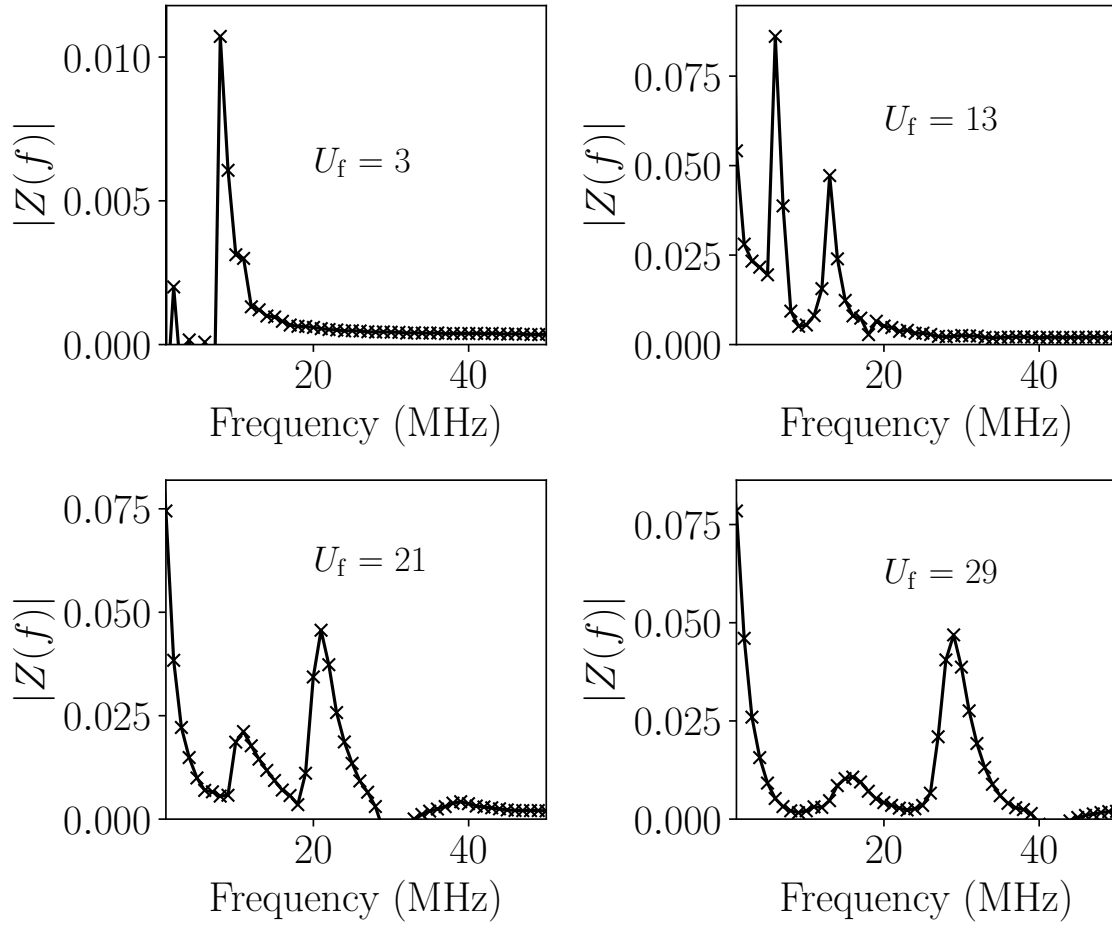


Figure D.2: Fourier transform of the response of the quasi-particle weight after a quench.

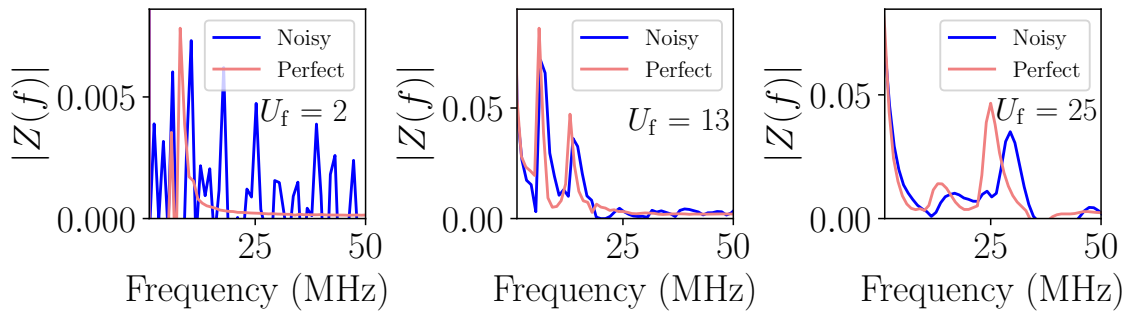


Figure D.3: Fourier transform of the response of the quasi-particle weight after a quench considering a noiseless (pink) or a noisy numerical simulation (blue).

Appendix E

Résumé en français

EDF a pour objectif de délivrer une énergie électrique, stable et à bas prix quels que soient les défis sociétaux, politiques ou scientifiques rencontrés. Pour ce faire, il est apparu nécessaire, dans le projet de créer un réseau énergétique totalement décarboné d'ici 2050, d'augmenter la durée de vie des centrales nucléaires actuelles (à réacteur à eau pressurisée) au-delà de 60 ans. Une très bonne compréhension du vieillissement des matériaux (batteries, panneaux photovoltaïques, matériaux de structure dans les centrales nucléaires) devient alors primordiale pour anticiper l'apparition de défauts, de gonflement ou de corrosion sous contrainte par exemple dans les différents éléments de la centrale. Comme il est très difficile d'observer directement le vieillissement des matériaux dans un milieu fortement irradié, être capable de simuler numériquement ou expérimentalement correctement les matériaux d'intérêts dans les conditions réelles est la voie prise aujourd'hui à EDF. À cet effet, plusieurs méthodes de simulation numérique à l'échelle atomique sont utilisées et développées au sein d'EDF comme la théorie de la fonctionnelle de densité, la dynamique moléculaire, le Monte-Carlo cinétique ou la dynamique d'amas avec un certain succès. Ces simulations font partie d'un plus grand ensemble de simulations multi-échelles pour comprendre les mécanismes de vieillissement des matériaux. Néanmoins, certains états physiques de ces matériaux peuvent être très difficiles à simuler : paramagnétisme, électrons fortement corrélés, états excités. Des améliorations de modélisation et la levée de certains verrous sont par conséquent nécessaires.

Dans le même temps, la recherche sur le calcul et la simulation quantique a connu un très grand essor ces dernières années, que ce soit dans la recherche publique ou dans le cadre d'investissements privés. Le calcul quantique pourrait être une "révolution" dans les années à venir en surpassant largement les capacités de calcul des méthodes dites "classiques" pour des problèmes ciblés tels que : des problèmes d'optimisation, d'équation aux dérivées partielles, de cryptographie et évidemment de simulation de matériaux. Une technologie en particulier semble être adaptée à la simulation de corps en interaction : les atomes neutres (ou atomes de Rydberg). En effet, cette technologie permet d'implémenter nativement des Hamiltoniens de spins, générant ainsi des états fortement corrélés et exotiques de la matière. Ce concept de simulation quantique fut introduit par le physicien Richard Feynman et propose de simuler des systèmes d'intérêts, par exemple des électrons en interaction, à l'aide de systèmes artificiels contrôlables comme les atomes de Rydberg. Cela est maintenant permis grâce aux développements expérimentaux et théoriques importants de ces dernières années. Cependant, les algorithmes quantiques pour simuler la matière sont encore en développement et les simulateurs actuels, bien que très bien contrôlés, sont encore bruités et ne possèdent pas de qubits parfaits. Il est alors nécessaire de tester numériquement les nouveaux algorithmes sur un petit nombre de qubits dans les conditions les plus proches d'une expérience afin de les optimiser en vue d'une implémentation sur un simulateur réel.

Ma thèse s'inscrit à la fois dans la problématique de simulation de matériaux d'EDF et dans la recherche et l'algorithmie en simulation quantique.

Dans ce manuscrit, après l'introduction, je décris dans le chapitre 1 les méthodes numériques

actuelles, dites de premier principe ou *ab initio*, pour la simulation de matériaux à l'échelle atomique. Je présente leurs succès, mais aussi leurs limitations ainsi que les méthodes classiques qui proviennent de la théorie quantique. Ces méthodes sont très répandues dans le monde académique, mais aussi industriel, et ont permis beaucoup d'avancées dans la compréhension des phénomènes quantiques au sein des matériaux. Enfin, je donne un aperçu de la théorie sur laquelle est basée la simulation quantique et les méthodes qui permettent de passer d'un problème électronique à un problème décrit par des qubits. Dans le chapitre 3, je présente la plateforme de Rydberg et les applications possibles de cette plateforme pour la simulation et le calcul quantique ainsi que les récents résultats très encourageants obtenus. Dans le chapitre 4, je montre les résultats numériques d'un nouvel algorithme variationnel pour la chimie implémentable sur les atomes de Rydberg. Enfin, dans le chapitre 5, j'implémente numériquement un algorithme basé sur la méthode slave-spin pour simuler le comportement d'un modèle de Fermi-Hubbard à l'équilibre et hors équilibre. Cet algorithme est aussi conçu pour les atomes de Rydberg.

Chapitre 2 Simuler la matière corrélée : du classique au quantique

Ce chapitre décrit les méthodes "classiques" actuelles pour simuler numériquement la matière ainsi que les bases théoriques pour le calcul quantique.

Tout d'abord, je présente la méthode Hartree-Fock puis la théorie de la fonctionnelle de la densité (DFT) qui a pour but de résoudre l'équation de Schrödinger à l'aide de la densité d'état électronique du système plutôt que la fonction d'onde au prix d'approximations pour le terme d'échanges et de corrélations. Plusieurs approximations existent (approches locales, à gradients) et toutes possèdent leurs avantages et inconvénients. Je présente des développements récents permettant d'étendre la DFT, notamment sur la simulation du magnétisme. J'aborde ensuite les approches se basant sur le formalisme de la physique quantique avec notamment la théorie du champ moyen dynamique (DMFT) après avoir décrit la fonction de Green. Cette méthode permet de décrire un système de Fermi-Hubbard et notamment le phénomène de transition de Mott avec une bonne précision. Je décris aussi brièvement la méthode DFT+DMFT et la méthode de Monte-Carlo quantique. Je finis ce chapitre en donnant les bases théoriques au calcul quantique et aux différentes approches possibles (digitales ou analogues). J'expose la méthode d'estimation de phase et les méthodes variationnelles. Un approfondissement est proposé pour appliquer ces méthodes aux fermions en interaction.

Chapitre 3 : Simulation quantique avec les atomes de Rydberg

Ce chapitre me permet de décrire le fonctionnement expérimental de ce simulateur quantique. La première étape est la préparation des atomes froids sous forme de matrices d'atomes contrôlées par des lasers. La géométrie des atomes peut être totalement contrôlée pour réaliser n'importe quel type de réseaux 2D et 3D. Des états électroniques de Rydberg de ces atomes sont contrôlés à l'aide de laser, et permettent de considérer les atomes comme des qubits ou des spins. Ces spins effectifs interagissent soit par interaction d'Ising, soit par une interaction XY en fonction des états de Rydberg choisis.

Enfin, l'état du système est mesuré grâce à la fluorescence des atomes. Cette architecture permet de faire de la simulation digitale et analogue jusqu'à plus de 200 qubits avec des résultats récents très prometteurs.

Chapitre 4 : Algorithme quantique variationnel analogue-digital pour la chimie

Dans ce chapitre, je décris, implémente et montre le résultat d'un algorithme que nous avons conçu pendant ma thèse, pour trouver l'énergie de l'état fondamental de molécules (H_2 , LiH et BeH_2) avec les atomes neutres. Après avoir expliqué comment j'ai transformé les Hamiltoniens moléculaires en Hamiltonien de qubits, je présente comment optimiser la géométrie des atomes de Rydberg en fonction de l'Hamiltonien cible, les séquences de pulses optimisées qui sont implémentées ainsi que la méthode de mesure qui utilise la "derandomization". Je compare les résultats de ma méthode avec la méthode naïve d'opérateurs alternatifs et je montre que j'obtiens de meilleurs résultats plus rapidement (avec moins de mesures). Je montre que l'énergie fondamentale peut être retrouvée avec 5% d'erreur lorsque nous imposons un certain nombre de mesures (le critère d'arrêt de l'algorithme variationnel) et donnons des pistes pour améliorer la méthode. Ce travail a

été publié dans *Physical review A*.

Chapitre 5 : Utilisation de la plateforme de Rydberg pour simuler de la physique d'électrons fortement corrélés dans le modèle de Hubbard 2D

Résoudre le modèle de Hubbard pourrait mener à l'explication de beaucoup de problématiques de matière condensée (par exemple, il devrait aider à décrire les supraconducteurs haute-température). Cependant, il est très difficile à résoudre classiquement avec certains types de dopage ou de modèles multi-orbitaux. Dans cette étude, nous proposons une méthode pour simuler le comportement d'un modèle de Hubbard 2D sur une plateforme de Rydberg. L'idée est d'utiliser la méthode des spins "esclaves" et d'un découplage des degrés de liberté avec une approche de champ moyen. En effet, les spins esclaves ajoutent artificiellement un degré de liberté aux fermions présents dans le système tout en restant dans un espace d'états physiques si une contrainte sur les opérateurs est appliquée. Un découplage en champ moyen est ensuite appliqué de façon à décorréler les degrés de liberté de charge (et de spin) de fermions et des spins esclaves. On obtient ainsi deux Hamiltoniens auto-cohérents :

- un Hamiltonien de fermions libres,
- un Hamiltonien d'Ising en champ transverse.

La résolution de ces Hamiltoniens est réalisable avec une boucle auto-cohérente où résoudre l'un des deux permet de résoudre l'autre. L'idée majeure de cette approche est qu'il est possible de résoudre classiquement l'Hamiltonien de fermions libres alors que toute la complexité du modèle de départ a été transférée dans l'Hamiltonien d'Ising, qui est implémentable directement sur la plateforme de Rydberg. Il s'agit d'un algorithme hybride mais non variationnel. Je teste cette méthode sur un réseau carré à demi-remplissage et je montre que l'on peut retrouver une transition de Mott dans le cas théorique, mais aussi en considérant une émulation d'expérience sur une vraie architecture. Plusieurs sources de bruits possibles sont considérées (bruit de shot, déphasage, temps d'anncaling, géométrie des atomes). De plus, la dynamique des électrons est étudiée dans ce paradigme avec des résultats correspondant aux résultats théoriques et numériques de la littérature.

Cet algorithme peut être implémenté sur les simulateurs actuels avec un possible avantage quantique pour la dynamique des électrons, très difficile à simuler avec les méthodes numériques et théoriques actuelles.